University of Alberta

Library Release Form

Name of Author: Chao Hu

Title of Thesis: Localization and Orientation System for Robotic Wireless Capsule Endoscope

Degree: Doctor of Philosophy

Year this Degree Granted: 2005

____

Chao Hu
11124-86 Av.
Edmonton, AB
Canada, T6G 0X2

Date:________________

To my grandparents,
for feeding my young body and soul;

To my parents,
for raising me and the ever-going standards;

To my wife,
for burning her immense love to energize me;

To my son,
for bringing me lucks and happiness.

University of Alberta

LOCALIZATION AND ORIENTATION SYSTEM FOR ROBOTIC WIRELESS CAPSULE ENDOSCOPE

by

Chao Hu

A thesis submitted to the Faculty of Graduate Studies and Research in partial fulfillment of the requirements for the degree of **Doctor of Philosophy**.

Department of Electrical and Computer Engineering

Edmonton, Alberta

Fall 2005

ABSTRACT

Medical doctors can access and visualize the gastrointestinal tract through an endoscope. However, existing endoscopes have several limitations such as inaccessibility to the entire intestine and high discomfort. The wireless capsule endoscope, with external guidance for interactive GI tract examination, tries to address some of these limitations. However, the current techniques do not provide good localization of the endoscope capsule.

In this thesis, I propose a new wireless robotic capsule endoscope that uses a magnet based localization and orientation system. Here, the capsule, which encloses a permanent magnet, moves in a patient's GI tract, and the magnet creates a magnetic field. The field intensities at some spatial points are measured by magnetic sensors placed around the patient's body. We have derived the magnetic intensities as nonlinear functions of magnet's 3D location and 2D orientation parameters, which can be solved by minimizing an objective error function. We have evaluated several optimization algorithms and found that the Levenberg-Marquardt method provides superior performance in terms of numerical accuracy and execution speed. Although a nonlinear method could be an approach to the problem, it requires a good initial guess of the unknown parameters, and its speed is low. Therefore, I propose a linear algorithm. With the data from five (or more) 3-axis magnetic sensors, this algorithm is realized through matrix computations. In most cases, it results in correct solution if the matrix is not singular, and its execution time is less than one-tenth that of the fastest nonlinear algorithm.

Finally, a real magnetic sensor array system has been built with sixteen Honeywell 3-axis AMR sensors. With a computer interface for 3D graphic and data display, real-time tracking is realized, and the results are satisfactory with an average localization error of about 3.3 mm and an orientation error of about 3.0º in case that the magnet moves within the area of the sensor array. The magnet's orientation misses the information of capsule's rotation along its own central axis, and hence a supplemental localization and orientation method is proposed by an imaging technique. Applying an 8-point algorithm on the images after distortion correction, we solve the 3D rotation and 2D transition parameters of the camera and this rotation can be further decomposed into two sub-rotations, the rotation of the camera's central axis and the rotation around this axis.

Keywords: Localization and orientation, Robotic wireless capsule endoscope, Magnetic tracking, Image processing and Computer vision.

Acknowledgements

I will soon complete my Ph.D program. I feel that I have gained pretty much knowledge through the four year study and research, and my research ability have been exceedingly improved. Here, I first wish to express sincere gratitude to Dr Max Q.-H. Meng, my supervisor, friend and mentor, for his masterly guidance, constant support, and intelligent inspiration throughout my graduate study at the University of Alberta, and my visiting research at the Chinese University of Hong Kong. I also wish to express sincere gratitude to my another supervisor, Dr. Mrinal Mandal, for his patient instruction, constant encouragement and friendly assistance to my thesis research. Their dedications to me are primarily responsible for the successful completion of my thesis, and the knowledge gained from their guidance will continue to be a tremendous influence on my future career.

I would like to thank Dr. Hong Zhang and Dr. Qing Zhao for their kind supports, insightful discussions to my researches, and invaluable suggestions to the thesis. I also thank Dr. Xing Ni for serving as the external examiner, Dr. Bruce Cockburn for serving as the exam committee member, for their proof-reading this thesis and offering invaluable expert suggestions.

I would offer my thanks to the faculty and staff members, the fellow graduate students for creating the friendly study and research environment. In particular, many thanks to Dr. Tongwen Chen and Dr. Alan Lynch, for the knowledge gained from their lectures and the discussions, to Peter Xiaoping Liu, Xiang Wang, Axel Von Bertoldi for their cooperation and assistance. Without this rich environment, I doubt that my study and research would be far from complete.

I would like to acknowledge the financial supports by the organizations through grants to professor Max Q.-H. Meng, professor Hong Zhang, and professor Mrinal Mandal; by University of Alberta through in the form of assistantship; by SPIE, the International Society for Optical Engineering, in the form of Education Scholarship.

Contents

List of Figures

List of Tables

List of Symbols

$(a, b, c)^{\mathrm{T}}$	Magnet's position vector
$\mathbf{B}$	Magnetic intensity vector
$\mathbf{B}_l$	Magnetic intensity vector in the l-th sensor position;
B_{lx}, B_{ly}, B_{lz}	3 projection components of magnetic intensity vector $\mathbf{B}_l$ in the l-th sensor position
$\widehat{B}_{lx}, \widehat{B}_{ly}, \widehat{B}_{lz}$	3 magnetic intensities calculated by the position and orientation Parameters
B_{T}	A constant related to magnetic intensity
$\mathbf{C}_1$, $\mathbf{C}_2$, $\mathbf{C}_3$	Column vectors in matrices
$\mathbf{D}_1$, $\mathbf{D}_2$, $\mathbf{D}_3$	Column vectors in matrices
$\mathbf{D}$	Matrix with diagonal elements
E	Define an error or a deviation
$\mathbf{E}$	Fundamental matrix
$\mathbf{E}_1$, $\mathbf{E}_2$, $\mathbf{E}_3$	Column vector of the fundamental matrix
$\overline{E}_P, \overline{E}_O$	Average localization and orientation error
$\mathbf{F}$	4 by 4 Matrix formed by $\mathbf{C}_i$ and D_i
$F(R, \hat{\theta})$	Magnetic potential of a spatial point. Here, $\hat{\theta}$ is the angle formed by magnet's central axis and the position vector
f	Focal length
$\mathbf{H}_0$	Magnet's orientation vector
$\mathbf{h}_k$	Outputs vector of the hidden layer neurons
$\hat{h}_i$	The i-th element in the fundamental matrix
i, j, k	Index number
i, j, k	Orthonormal basis components in quaternion (in Appendix A, B).
K_H	Hall sensitivity
K_X	Sampling sensitivity of the system
l	Index number of the sensor
l_{1k}, l_{21k}, l_3 l'_{1k}, l'_{2k}, l'_3	Distances between points (along a line) in the original and distortion images

$L_q(\mathbf{v})$	Quaternion rotation operator acting on vector $\mathbf{v}$
$(m, n, p)^T$	Orientation vector defined by the 3 projections
m', n', p'	Relative orientation parameters to m, or n, or p
M_0	Magnetism constant on the upper and lower magnet's surfaces
M_{T}	Magnet's magnetism
$\overline{\mathbf{m}}$	Magnetic dipole moment
$\overline{M}$	Sample number
$\hat{m}_{ij}$	The *i*-th row and *j*-th column element in a matrix
N	Number of sensors
$\overline{N}$	Degree of expansion polynomial
$\mathbf{P}$	Vector defining a spatial point with respect to the magnet's center
$_{\mathbf{a}}\mathbf{P}$	Position vector in the particular frame defined by the subscript
$_i\mathbf{P}^j$	The *j*-th spatial vector represented in *i*-th coordinate system
$\mathbf{q}$, $\tilde{q}$	Quaternion
$(q_0\ \ q_x\ \ q_y\ \ q_z)^T$	4 elements representation of a quaternion
R	The distance and θ the angle formed by magnet's central axis and the position vector
$\mathbf{R}$	Rotation Matrix
$_j^i\mathbf{R}$	Mapping rotation matrix from the *j*-th coordinate system to the *i*-th coordinate system
$\vec{\mathbf{r}}$	Vector defining the direction of a moving object, e.g., capsule direction, camera direction
r_i	The *i*-th (i=1,2, …5) element of the solution parameter vector $\mathbf{r}$
$\hat{r}_{1k}'$, $\hat{r}_{2k}'$, $\hat{r}_k$	Distances related to l_{1k}, l_{21k}, l_3 and l_{1k}', l_{2k}', l_3'
S_l	The *l*-th sensor position
s_{li}	The *j*-th row and *i*-th column element of matrix $\mathbf{\Omega}$
$\mathbf{T}, \mathbf{T}_0$	Transition vector
$t_{x0}\ \ t_{y0}\ \ t_{z0}$	3 components of the transition vector
$[\mathbf{T}]_x$	Matrix formed by vector T
$\mathbf{U}$	A matrix formed by vector $\boldsymbol{\omega}_i$ (i=1, 2, … $\overline{M}$)
U_H	Hall voltage
u, v	Position of a point in the image plane
$\mathbf{V}, \tilde{\mathbf{V}}$	Matrices resulted from singular value decomposition of the fundamental matrix

$V_S(j), \hat{V}_S(j)$	The j-th sample of the measured and theoretical data
V_X	Sampled sensor data
$\vec{\mathbf{v}}_X, \vec{\mathbf{v}}_Y, \vec{\mathbf{v}}_Z$	Unit vectors in 3 coordinate axes
$\mathbf{W}_1$, $\mathbf{W}_2$, $\mathbf{W}_3$	Vectors for calculating rotation matrix
w, v	Quaternion vectors
$(x, y, z)^T$	3D spatial coordinates
$(x_l, y_l, z_l)^T$	3D position coordinates of the lth sensor
$\{X_aY_aZ_a\}$	Definition of different coordinate system by the subscript
α, β, γ	Rotation angle along 3 specific axes
$\boldsymbol{\delta}$	Radius of the magnet
η	Order of the fitting function
θ	Rotation angle along a specific axis
$\kappa_{2l}, \kappa_{1l}, \kappa_{0l}$ $\hat{\kappa}_{2l}, \hat{\kappa}_{1l}, \hat{\kappa}_{0l}$	Coefficients of the 2-order equations for solving magnet's position parameter using the l-th sensor
μ_r	Relative magnetic permeability of the medium
μ_0	Air magnetic permeability
λ_1, λ_2	Coefficients for fitting nonlinear sensitivity function
ρ	The magnitude from a point in an image to the distortion center of the image
$\hat{\lambda}$	Coefficient for a fitting function
$\tilde{\lambda}_i$	Coefficients of an expansion polynomial related to magnitudes in original and distortion images
$\boldsymbol{\omega}_i$	A vector related to image correspondence point pairs (number=i)
ξ, ξ'	Inputs to the neural node in the hidden and output layers
$\mathbf{\Lambda}$	A vector formed by 9 elements of the fundamental matrix
$\mathbf{\Gamma}$	A vector defining 5 unknowns relative to the magnet's position and orientation
$\mathbf{\Omega}$	A matrix for solution of the magnet's position and orientation
$[\bullet]_l$, $[\bullet]_r$	A mapping from a rotation quaternion to a 4 by 4 matrix (l and r stand for left and right multiplication).

List of Abbreviations

GI	Gastrointestinal
CRT	Cathode Ray Tube
FDA	Food and Drug Administration
RF	Radio Frequency
CCD	Charge Coupled Device
CMOS	Complementary Metal Oxide Semiconductor
3D	3 Dimensional
CT	Computer Tomography
MRI	Magnetic Resonance Imaging
US	Ultrasound
MMM	Magnetic Marker Monitoring
DC	Direct Current
SQUID	Superconducting Quantum Interference Device
mm	millimeter
cm	centimeter
dm	one tenth of a meter
MCS	Multilevel Coordinate Search
mS	milli-Second
SNR	Signal to Noise Ratio
MR	Magneto-Resistive
AMR	Anisotropic Magneto-Resistive
GMR	Giant Magneto-Resistive
ADC	analog to digital converter
USB	Universal Serial Bus
DO	Digital Output
MSRE	Mean Square Root Error
T	Tesla

Chapter 1

Introduction

An arrangement that can send out information about conditions inside a living body can supply important diagnostic and clinical information. So many diagnoses of important pathologies are currently performed by exploiting minimally invasive techniques, which allow medical doctors to introduce a test instrument, to examine visually the interior of a bodily canal or a hollow organ, through natural orifices or small incisions. This technique is called as endoscopy [1]. Typically there are two kinds of gastrointestinal (GI) endoscopy, gastroscopy for the test of the upper digestive tract, and colonoscopy for the test of the colon and rectum.

The instrument used to perform this test is called as an endoscope: traditionally a long, thin, flexible tube. Within the end of this tube is a miniaturized color-TV camera or fiber-optic instrument [1, 2], with a wide-angle lens to acquire as much information as possible. After passing this "scope" through the GI tract, the doctor can directly examine the lining of patient's upper and lower digestive tract with a CRT monitor, or other types of displayer. However, difficulty exists in the inspection of the small intestine with this type of cabled endoscope. Attempts have been made to develop longer endoscopic instruments. This technique called push enteroscopy has had only limited success. The longer instruments are difficult to manipulate, because the commercial endoscopes have only limited capability to bend at their tip and lack means to actively control their shape along the rest of their length. Their inspection is limited since even in the best of operations by the skillful doctors the entire small intestine is not visualized. Nevertheless, the procedures used for endoscopy cause much discomfort because they require flexible, relatively wide cables to be pushed into bowel, which carry light, power and video signals. Sometimes it needs sedation or anesthesia or insufflation of the bowel. Therefore, it is desirable to develop a new endoscope that can directly access and visualize the entire GI tract. This goal can be reached by introducing actively controlled electro-mechanical articulation---an endoscopic robot. The robot can be a surgeon guided machine and can autonomously locomote in the small bowel to perform medical diagnosis. In addition, it can be used for therapeutic treatments, such as the removal of blockages, deliver drugs, and it should not cause much discomfort as conventional endoscope makes.

Efforts have been made to develop such an endoscopic robot, and lots of them introduced the designs of the robot structure and locomotion techniques. For instance, Ikuta et al. [3] introduced an active colon endoscope, whose shape can be adjusted according to the winding path of the colon using shape memory alloy actuator. Among the proposed locomotion methods of the self-propelling endoscope, the inchworm mode is a favorable approach. Based on the inchworm idea, Dario and Phee et al. [4, 5] proposed a micro robotic system instead of the rigid endoscope, which uses a pneumatic distributor and the shape memory alloy for the locomotion. They also proposed a theoretical model [6] for the locomotion of this endoscope robot moving in the colon. This model helps to understand the mechanics of the endoscope motion and to design the actuation system. Similarly, Slatkin et al. [7] tried to develop a robotic endoscope with some grippers to access the entire GI tract. Menciassi et al. [8] proposed the robots based on sliding clamper solutions for semi-autonomous colonoscopy, and the robots have the self-propelling and steering abilities. Kumar et al. [9] proposed a micro-robotic colonoscopy system and the corresponding method for path planning and guidance control. A locomotion mechanism by clamping the colon wall based on the passive vacuum devices is suggested, and the path planning of the robot is carried out based on the sensor fusion techniques utilizing the data from the captured images and the tactile sensors. Lim et al. [10] suggested a self-propelling endoscope which can travel forward and backward by controlling pneumatic valves under different duty ratios. Reynaerts et al. [11], Peirs et al. [12, 13] also proposed some prototypes of miniature manipulators for the integration of self-propelled endoscopes.

Above proposed endoscopic robots are more suitable for colonoscopy since they are driven by a pneumatic source, and some types of cables are required for connecting the endoscope robot to the workstation outside the patient's body. They are not widely accepted and applied clinically since their performance is still not satisfactory. Therefore, some techniques are expected that can thoroughly improve these abilities. A new exciting advance, the development of the wireless video capsule, is a potential solution. It has made it possible to transmit GI endoscopic images from the whole small intestine in living humans without causing much pain [14].

1.1 Wireless Capsule Endoscope

An example of an early radio transmitting capsule [15] for the GI tract examination was released by the Rockefeller Institute of New York in 1957. It comprises a plastic capsule, 1.125 inch long and 0.4 inch in diameter, and contains a tiny transistor oscillator operating at a frequency of about one megahertz. In one end of the capsule is housed a minute replaceable battery which is able to supply the electrical power of 15 hours. The other end of the capsule is sealed by a rubber membrane which transmits the body pressure variations to the armature of an inductance coil, and so changes the frequency of the radio signal. When the capsule is swallowed by a patient and pursues its course through the GI tract, it transmits frequency signals which are varied by the pressure changes in the tract. These signals from the capsule are picked up on a receiver with an antenna held close to the body. The output responses can be displayed on the CRT screen.

Almost at the same time, similar research was done in the University of California Medical Center [16]. They designed a passive telemetering transmitter in the form of a resonant transistor circuit, the reactance of which would change in response to the observation variable. The change in characteristic frequency (hundred-kilocycle range) was to be detected from outside the body by a 'grid-dip meter' that cyclically scanned the frequency range. This technique was used to test some variables, such as pressure, temperature and pH value. The capsule was 2.8 cm long and 0.9 cm in diameter. Although these radio transmitting capsules have limited clinical applications, they did help to give ideas for the invention of the video capsule endoscope.

In May 2000, Iddan et al. in Given Image Ltd, in Israel, reported a video-telemetry capsule endoscope (M2A Capsule) [2], which is small enough to be swallowed (11*28mm) and has no external wires or cables. Its composition is shown in Figure 1.1, including optical dome and lens, CMOS imager, illumination LEDs, RF transmitter and antennas, and two batteries. It was the only Food and Drug Administration (FDA) approved wireless video endoscopy system [20], but has captured wide attention from endoscopic doctors [17~22] and researchers, especially for its ability to test the small intestine [14]. Since then, some other companies, or institutes, such as RF SYSTEM lab [23] and Olympus Corporation [24] in Japan, the Intelligent Microsystem Center in Korea [25], have announced similar products and research achievements.

The M2A capsule endoscope system includes three stages: the capsule, the recorder, and the workstation, as shown in Figure 1.3. In the first stage, the capsule acquires the images. The image data are then transmitted outside the body by means of the transmitter and antenna. In the second stage, the antennae array, which consists of eight (or more) antennas and the receiver circuit system, collects the transmitted signals. The received data are subsequently processed and stored in the data storage unit of the recorder. In the third stage the data are retrieved from the recorder and transferred to the workstation for additional processing and presented on the display.

Figure 1.1 Wireless capsule endoscope [2]

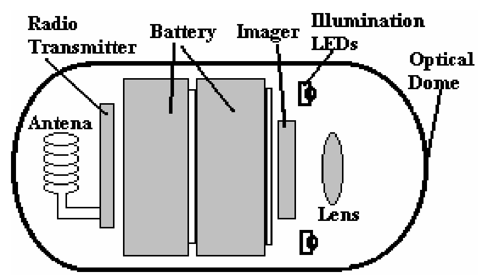

Figure 1.2 Configuration of M2A capsule

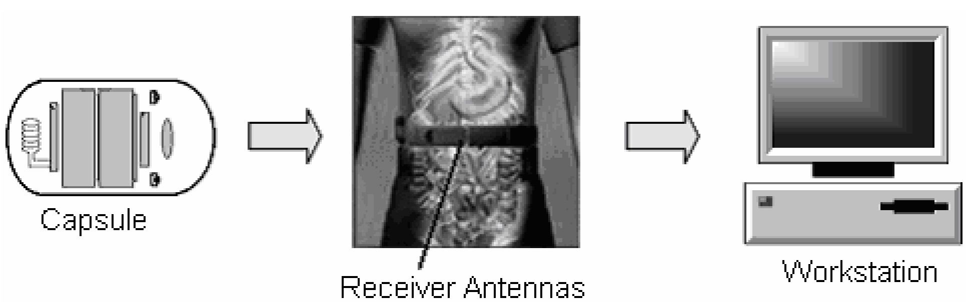

Figure 1.3 The capsule endoscope system
(3 stages: the capsule, the recorder, and the workstation) [2]

The M2A capsule endoscope represents one great breakthrough in gastrointestinal diagnosis in over 20 years. Comparing with the traditional endoscopy, however, it has some limitations. For one, the camera can not be pointed in a special observation direction, nor can it be made to linger at a site to get additional images, because it is propelled passively by peristalsis of the GI tract. Hence, it is possible to miss capturing images of some important spots. For two, it can not take biopsies or remove polyps as catheter endoscopes can. Finally, the duration of the batteries is not enough to allow imaging of the whole colon, because the capsule passage from mouth to elimination takes 20 to 48 hours, while the battery in the capsule can only last 8 hours. To address these limitations, a new type of wireless robotic capsule endoscope system should be proposed.

1.2 Robotic Capsule Endoscope

Because most drawbacks of M2A are associated with the inability to control the capsule's motion, it is a key point to give the capsule the specific motion ability under the guidance of the operation doctor [26]. Here, the robotic capsule can be guided to examine and stop at any important GI spots and can move through unimportant areas in a much faster pace than the natural peristaltic movement [27~30]. In addition, such a robotic capsule endoscope can realize biopsy, drug delivery, and other operations [23~25, 31].

The idea for the control on the motion of the capsule endoscope was also proposed by other researchers. Feng Gong et al. proposed their conceptual system [32] as shown in Figure 1.4, which is similar to M2A capsule. A joystick could be used to communicate with the wireless endoscope, and to control the light, image capture and transmission of the capsule. Alexander Mosse et al. [33] used an acrylic ovoid-shaped endoscope, which has 2 electrodes to apply electro-stimulation to the bowel wall. The stimulation causes circular muscle contraction, which might propel the endoscope within the GI tract. However, this stimulation device still needs electrical cord because the large electrical power is required for the stimulation, so it is difficulty for this device to be used in the wireless capsule endoscopy. Byungkyu Kim et al. [37] propose a locomotive mechanism for capsule-type endoscope based on the shape memory alloy actuator, but the operation of the shape memory alloy needs much energy for its temperature adjustment, which makes it impossible to currently apply it in wireless capsule endoscope.

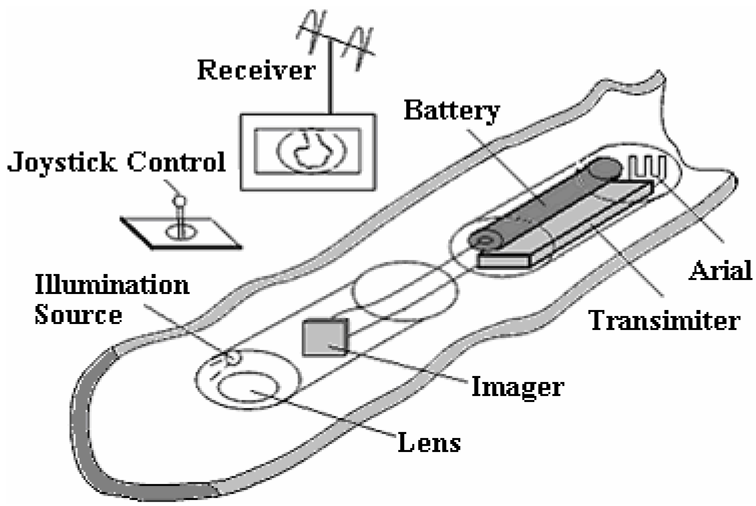

Figure 1.4 The concept schematic diagram of wireless endoscope by Feng Gong et al. [32]

A very promising prototype of robotic capsule endoscope is being proposed by a Japanese company "RF System Lab", known as NORIKA3 [23], as shown in Figure 1.5. The dimension of the capsule is 9 mm in diameter and 23mm in length and its case is made of resin. The NORIKA system consists of following main units:

1) **Micro capsule CCD camera.** This unit is comparable the optic system and image sensor in M2A, but a CCD imager is used instead of the CMOS imager, such that the image quality, e.g. color reproducibility, brightness, and dynamic range, is improved.

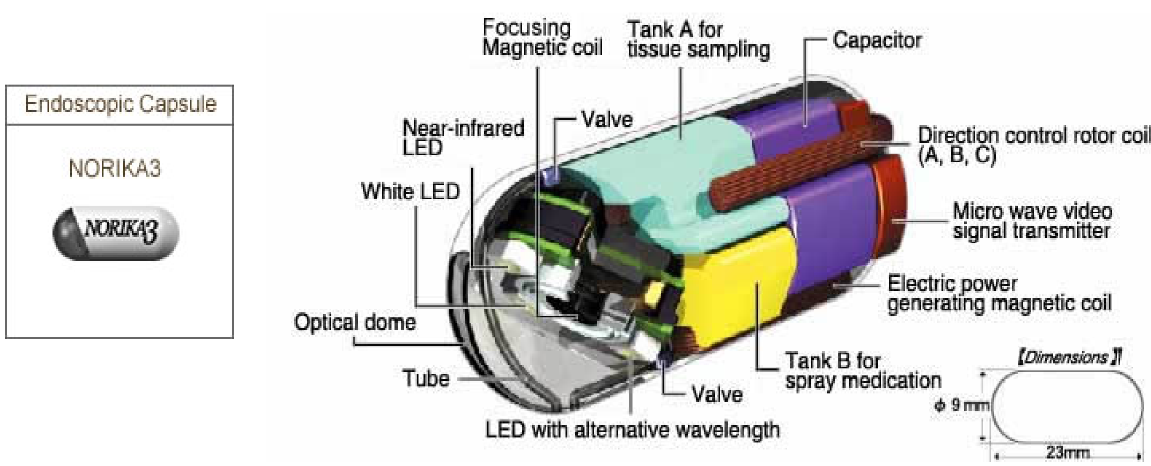

Figure 1.5 NORIKA3 wireless capsule endoscope system [23]

The disadvantage of the CCD imager is its larger power consumption.

2) **Wireless power transmission.** The typical battery power supply has its drawbacks, because it contains substances harmful to human body, and might not last enough time. Therefore, the wireless power transmission is a good choice for supplying power to the capsule.

3) **Locomotion by external driving rotation.** Three coils are placed at 60-degree interval inside the capsule, which play the role like that of rotor coils. Three coils embedded in a vest-like jacket act as stators. The rotation mechanism is similar to that of the 3-pole motor theory and strobe light emitting technology that is a repetition of constant current battery charge followed by a quick discharge. The capacitor in the capsule is charged with electric power transmitted wirelessly from the external unit. When the charged energy is quickly released to the rotor coil, a strong magnetic force is generated within a short period of time so as to rotate the capsule. The stator's magnetic field's direction decides the rotation direction, and thus driving the capsule forward or backward.

4) **Focus adjustment.** The movement mechanism for the focus adjustment of the camera lens is realized by a magnetic coil. The lens is placed in the center of the coil with a round paper cone and a pole piece. When an electric current is loaded through the coil, a magnetic field is developed. Repulsive force and attractive force are also generated between the pole piece and the coil. By controlling the current while monitoring live images on the screen, the lens is moved back and forth, and the focus is adjusted.

5) **Spray medication and tissue cutting manipulator.** The NORIKA has been developed mainly for image capture of affected areas. Future usage for medical treatments and operations are also being considered. Approximately 40% of the space in the capsule is unoccupied, which is separated into 2 tanks. One of the potential usages of the free space is to store medication to spray affected areas using air pressure. Another potential usage is to store surgical knives and scissors to get tissue samples or to store sensors such as a pH monitor.

NORIKA3 gives us ideas for the new robotic capsule endoscope. However, some of the proposed techniques, e.g., wireless power transmission, locomotion by external driving rotation, still need further investigation for their safety to be applied to the human body. Since it is presently difficult for the endoscope robot to be actuated by using some active propelling device attached to the capsule robot (the active locomotion), we try to apply actuation force in a passive mode. One possible method for the robot teleoperation is to use the force produced by magnetic field. This idea has been similarly proposed to be applied to the micro-robots which are used for pipe examinations reported by Shuxiang Guo et al. [34], and Toshio Fukuda et al. [35]. They used some kinds of magnetic micro-actuator, such as the giant magnetostrictive alloy actuator, to drive the robot to move through a pipe by the external revolution of the magnetic field. For the case of the capsule endoscope, we propose a design in which a small permanent magnet is enclosed in the capsule. When this capsule is swallowed, its locomotion can be controlled by an externally applied magnetic field. Two locomotion modes can be applied as shown in Figure 1.6. In the figure, the left one is the direct locomotion mode, which applies an external magnetic field with the direction parallel to that of the permanent magnet (whose direction is the same as that of the capsule). The right one was first proposed by Sendoh et al. [36], where the capsule works like a permanent magnetic motor. The magnet (Figure 1.6(b)) has a magnetic direction perpendicular to the central axis of the capsule that has a spiral structure. When an external rotation magnetic field is applied, the capsule is rotated to move forward or backward. In both of the systems, the actuation will not exhaust internal energy since the permanent magnet is used as the excitation source. Therefore, this magnetic actuation method has the advantage without any internal power consumption.

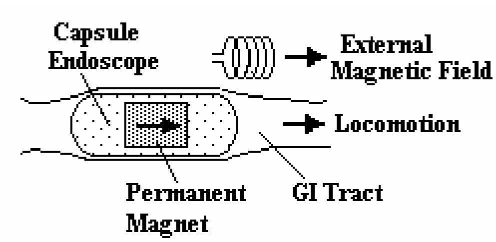

(a) Direct locomotion

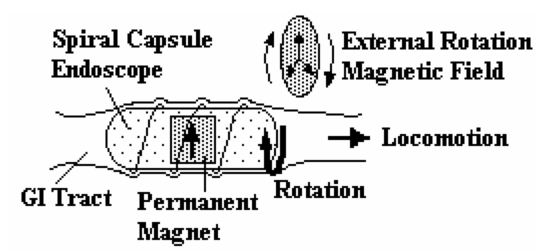

(b) Locomotion by rotation

Figure 1.6 Magnetic actuator for capsule endoscope locomotion

In 2004, another Japanese company, Olympus Medical Systems Corporation, also announced a prototype capsule endoscope [24]. Its basic (passive) capsule endoscope is 26mm long with an external diameter of 11mm, and Olympus initiated its clinical trials in the fall of 2004. Besides that, the company also proposed an external capsule guidance system, as shown in Figure 1.7. The principle behind the technology is similar to that of spiral capsule in Figure 1.6(b). It calls for the creation of a uniform magnetic field in any direction (N/S Poles) by an external magnetic field generator using three pairs of opposing electromagnets arranged in three directions (vertically, laterally and depths). The capsule endoscope can then be turned in any desired direction by means of its built-in magnet, generating thrust through the spiral structure. The direction of observation can also be adjusted. In addition to the technology of capsule endoscope and the guidance system, Olympus put forward some other techniques, e.g., wireless power supply, drug delivery, body fluid sampling, self-propelled capsule, and ultrasound capsule.

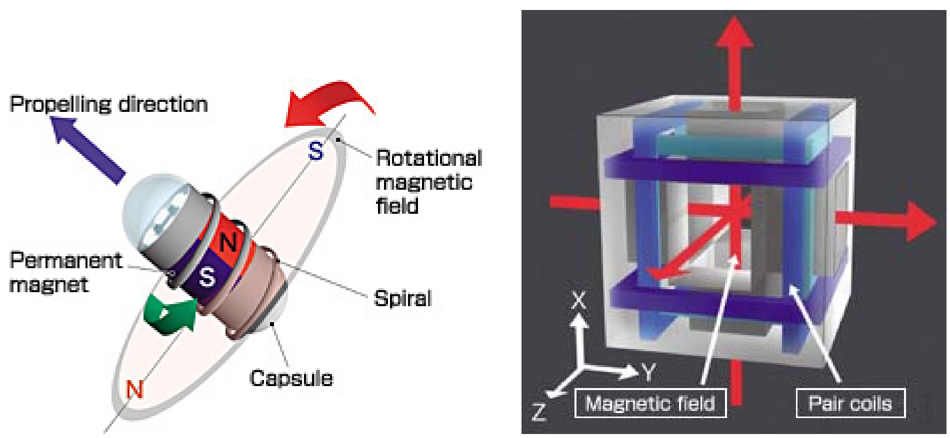

Figure 1.78 The external capsule guidance system proposed by Olympus Corp. [24]

In order to implement such an external driving system, many technical problems still have to be solved. One is the localization of the capsule, which can provide the doctor with information on the capsule's position and its movement locus to do the external guidance. Further, this external guidance can be performed more effectively if the information of the capsule's orientation can also be provided. Therefore, a localization and orientation system for the capsule's movement is desirable.

1.3 Objectives of the Proposal of the Capsule's Localization and Orientation System

The (3D) position or (6D) position/orientation information of the endoscope robot can provide very useful pathological messages in the GI tract and helps medical diagnosis tremendously. It makes the robot tracking possible so that the doctor can realize the external guidance and actuation, and determine other important medical treatments corresponding to the specific pathologic location. Nevertheless, based on the accurate localization/orientation information of the capsule, we can do the 3D image recovery of some interesting GI tissues, so that more accurate diagnosis can be made. Therefore, it will be an important and meaningful contribution to find a sound localization and orientation (sensing) technique that can track the capsule' position and orientation accurately. In this thesis, I present a localization/orientation system, which should have following properties:

1) **High localization and orientation accuracy**: Within the area of the capsule's movement, the proposed system should provide average localization accuracy within 10 mm in the 3D tracking space, and average orientation accuracy within 6° (about 10% of the orientation vector) comparing with true camera direction (in 2D space).
2) **Human body having no (or very little) effect or interference on the sensing signal used in the proposed technique:** Different persons have different body peculiarities, e.g., size, thickness, compositions, and etc. These specific properties might exert some kinds of effects on the sensing signal and lower the localization/orientation accuracy. Therefore, we need to find a proper sensing technique in which human body will induce no (or very little) interferences on the sensing signal.
3) **Low internal energy consumption**: As mentioned above, power supply is a key factor for the wireless capsule endoscope fulfilling the (long time) inspection of entire GI tract. It is demanded that the capsule should have as little energy consumption as possible used for the localization/orientation module.
4) **No negative effect to the human body**: The localization/orientation system should

avoid using some technique that might be harmful to human body, e.g., long time (X-ray and other) radiation.

5) **Easy realization**: The system does not impose special environment requirement, and can be realized in a regular hospital room. The sensors and the accessories should be easily purchased with low expense, and conventional products are preferable. The supporting hardware, associated devices, and the software should also be as simple as possible.
6) **Fast speed**: The execution time of the localization/orientation must match the time for the period of endoscopic image capture and the external actuation (<0.5 Second/sample).
7) **High robustness**: Since the capsule's localization/orientation is related to 6-dimensional computation problem, an appropriate algorithm must be found, and this algorithm must not fail to give a solution in any possible case. Furthermore, the system must possess high de-noising and anti-interference ability.

1.4 Contribution of this Thesis

To complete the objectives mentioned above, we propose a localization and orientation system, which uses magnetic technique complemented with imaging techniques. The contributions of this thesis can be summarized as follows.

1) Proposing a linear algorithm for magnetic localization and orientation

One important theoretical contribution of this thesis is the proposition of the new linear algorithm for finding the position and orientation of the magnet's capsule endoscope. Most existing techniques for the magnetic localization and orientation use a nonlinear algorithm, but a linear algorithm is preferable because of its computation simplicity and fast speed. Unlike other linear algorithms that derive their models upon some approximations, our algorithm is derived from the absolute vector computation and is realized by matrix computations. It doesn't need an initial guess for the magnet's the position and orientation as the nonlinear algorithm does, but has faster speed. The lab results show it to be reliable. No comparable such an algorithm has been reported in any other researchers.

2) Proposing a magnetic localization and orientation technique for the wireless capsule endoscope

Although there are some research reports with respect to the magnetic marker monitoring for a dosage transition in the GI tract, our design is the first proposal to apply magnetic localization/orientation technique in the wireless capsule endoscope. This technique uses a magnetic sensor array to track movement of a small magnet, which is included in the capsule. It is suitable for the localization and orientation of the capsule endoscope because the human body does not affect the static magnetic field, so that high tracking accuracy can be obtained. It does not need any power to build the magnetic field, and has very small volume. In addition, the expense of this system is lower comparing with other possible test techniques (CT, MRI, 3D-US). A real time magnetic sensing array is set up, and the test results show it possible to obtain higher localization/orientation accuracy, if there is enough number of the sensors and some appropriate signal processing techniques are applied to the sensor data.

3) Finding a robust nonlinear algorithm for magnetic localization and orientation

While the linear algorithm needs five 3-axis magnetic sensors, a nonlinear algorithm can be realized by using 5 (or more) single axis sensors with respect to the 5D localization/ orientation parameters. There are many nonlinear algorithms that could be applied to solve the nonlinear problem. These algorithms need a good initial guess of the parameters; otherwise the algorithm might fail to give correct results. Therefore, I tried several optimization methods to find a robust and fast algorithm, and found that the Levenberg-Marquardt method (nonlinear least square solution) is appropriate. Using this algorithm, different sensor arrays were investigated for their de-noising ability, and the sensor array with sixteen 3-axis magnetic sensors is found to have good results.

1.5 The organization of this thesis

The organization of this thesis is as follows. In Chapter 2, I review the existing and possible localization and orientation methods for the capsule endoscope. In Chapter 3, I present the spatial descriptions for capsule position and orientation, their coordinate transformations, and the capsule's rotation decomposition. In Chapter 4, I present the mathematical model of the magnetic field produced by a permanent magnet, and the nonlinear (optimization) algorithm for localization and orientation of the (magnet) capsule. In Chapter 5, I propose the linear algorithm for absolute localization and orientation of the capsule, and its performance by simulation. In Chapter 6, I present the real magnetic sensing (array) system, including the hardware and the software, and evaluate the system performance by real experimental tests. In Chapter 7, I present the relative localization/ orientation technique based on the imaging technique, and examples to apply this method and rotation decomposition technique on some real images. Finally conclusions and future work will be given in Chapter 8.

Chapter 2

Review of Existing Potential Localization and Orientation Methods

There are several techniques that could be used to localize the capsule: X-ray Radiograph [38], computer tomography (CT), magnetic resonance imaging (MRI), and 3D Ultrasonic (US) test [39~41]. Although X-ray radiograph, or CT test, can provide images with good visual resolution for the localization of the capsule, they are not desirable for the long duration capsule endoscopic test, because it may come into conflict with the radiation protection. Making use of modern, fast-imaging procedures, MRI provides good imaging of the abdominal tests. However, its application is limited by the necessity to perform multiple scans for each sampling point, and its high expense is another factor to avoid their applications.

Another approach of the capsule localization is to fuse 2D medical ultrasonic images with the 3D spatial data of the US scanhead [42~44]. Ultrasonic imaging is an appropriate technique for finding the position of the endoscope capsule robot that moves inside the patient abdomen. However, it is difficult to get message of the 3D capsule position just using an ultrasonic transducer, because the US transducer must maintain direct contact with the test body to efficiently transfer acoustic energy. As a result, its position and orientation are variable so that it makes accurate 3D-reconstruction impossible, unless we know the spatial information of the scanhead. A popular method to realize 3D US imaging is to equip hand-held US scanhead with position and orientation locating sensor [45]. If the 6D position and orientation messages of the scanhead are found, the 3D imaging reconstruction of the test body can be realized. Figure 2.1 shows an example of such a system [41], where a magnetic 6D measurement system is attached the US scanhead. The transmitter in the system generates pulsed DC (or low frequency) magnetic field, and the receiver senses the magnetic field and gives 6D position/orientation messages in the space with respect to the origin of the transmitter. Based on the 6D information of the scanhead, 2D US image data can be transformed into 3D image data, and then the capsule robot can be located with these 3D reconstruction images. However, such a US system is still inconvenient since it must continuously contact the patient's abdomen, and the quality of the US imaging on the small capsule needs further improvement. A more suitable localization technique should be found for higher accuracy and easier realization. Several possible approaches are: RF signal, magnetic localization and orientation, and the computer vision methods.

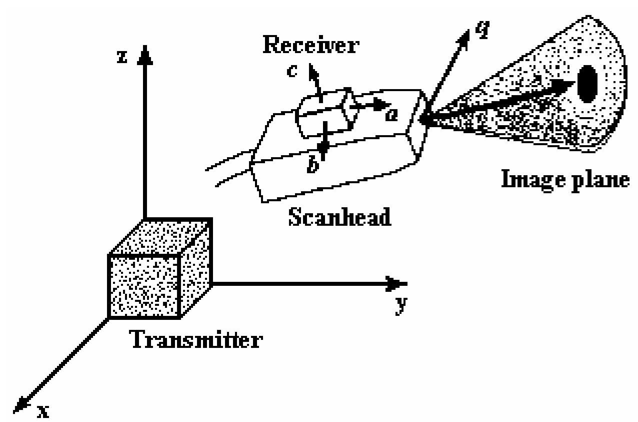

Figure 2.1 Coordinate system of a magnetic 6D measurement system [41]

2.1 Localization by RF signal

The M2A wireless capsule endoscope system includes a localization module [28, 46, 47]. The module is based on the RF (radio frequency) signals emitted by the capsule and received by eight antennas, as shown in Figure 2.2, on the exterior of the human abdomen. The localization algorithm is based on the assumption that the closest sensor (antenna) receives the strongest signal, such that the location of the capsule can be computed using the RF signal intensities in the eight antennas. Because the RF system is also used to transmit the captured images, this localization module has the advantage that it does not require any additional equipment. However, the measurement accuracy seems to be too low. It has been reported [46, 47] that 62.0% samples have 40 mm or better accuracy; 87.0% samples have 60 mm or better accuracy; the average error is 37.7 mm.

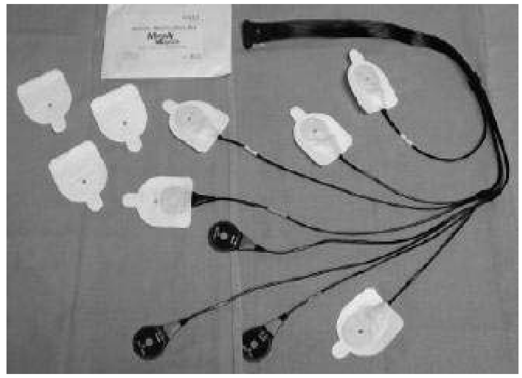

Figure 2.2 Eight receiving antennas (sensors) used for transmitting images and doing localization [19]

2.2 Magnetic Localization

As the RF localization system has a lower accuracy, a more efficient localization and orientation technique is desirable. Here we propose a method to perform the localization of the endoscope capsule by using magnetic technique. Human body has the compositions very similar to air, water, and other non-ferromagnetic materials. Since these materials have the magnetic permeability very close to that of the vacuum, as shown in Table 2.1, they have very little influence on the static magnetic field. Therefore, human body will not change the distribution of the static magnetic field, and it is possible to achieve higher localization accuracy with static magnetic field method.

A. Magnetic coil technique [48~51]

Usually, magnetic tracking techniques are based on a mapping from a magnetic source to the sensors. An earlier system was proposed by Kalmus[50]. This system was used for one vehicle to track another. It has a transmitter and a receiver, both made of coils. The transmitter consists of two coils with horizontal axes that are arranged at right angles to each other. A rotating magnetic field is produced as low-frequency alternating current passing through the excitation coils. The receiver again contains two coils in space quadrant, measuring the corresponding magnetic component. With the algorithm related to the phase measurement, the distance of the two vehicles, as well as their relative direction, can be determined. This system actually solves the 2D localization problem since the two

Table 2.1 Permeability of Different Materials

Material	Group Type	Relative Permeability
vacuum	non-magnetic	1.000000000
air	paramagnetic	1.0000004
water	diamagnetic	0.999991
copper	diamagnetic	0.999991
silver	diamagnetic	0.99998
lead	diamagnetic	0.999983
aluminum	paramagnetic	1.00002
cobalt	ferromagnetic	250
nickel	ferromagnetic	600
mild steel	ferromagnetic	2000
purified iron	ferromagnetic	200000

vehicles are located on the same ground. A more complete system was proposed by Raab et al., which can track 6D position and orientation of the target [48]. This system used both a three-axis magnetic-dipole (made of 3 small coils) source and a three-axis magnetic sensor. Linear rotation transformations (derived by some approximations) are applied to both the source excitation and sensor output vectors, yielding quantities that are proportional to small changes in the position and orientation of the target (the sensor relative to the source). An interesting aspect of the system is that all the large angle effects have been reduced to small angle approximately, and the algorithm is therefore linear.

One simplification of above magnetic tracking technique is to use only two excitation coils [49]. The coils are mutually orthogonal and fed with phase-quadrature currents, thus comprising the excitation source that is equal to a mechanically rotating magnetic dipole. In the sensor position, three magnetic excitation components can be measured. Then the position of the target (sensor relative to the source) can be computed by the minima and the maxima of the excitation field, and the orientation can further be determined by comparing the phase and amplitude of the measured signals against the phase and amplitude of the excitation field at the sensor's position.

B. Magnet marker monitoring technique

Above coil dipole methods provide us ideas how to build the magnetic localization/ orientation system, as well as the computation algorithms. However, the coil excitation system is not appropriate to tracking the capsule endoscope, because the excitation coils should have enough number of turns and enough current in order to set up enough intensity of magnetic excitation signal. It is difficult to put the coils inside the small capsule, which has limited space and power supply. Therefore, we propose a localization and orientation technique using a small permanent magnet, which can establish a magnetic dipole similar to the magnetic excitation coil, but no excitation current is required. This magnet can also be used for external actuation of the capsule, as mentioned in Chapter 1.

There are also some reports for magnetic tracking systems being used for medical applications. Yoshiaki et al. [52] used a magnetic system consisting of a small magnet and four magnetic sensors, to measure both tooth rotation and rectilinear movements. Similarly, Akutagawa et al. [53] used a magnet to measure the mandibular movement. A multi-layered artificial neural network was used for estimation of the magnet location and orientation. Some researchers have developed 3D ultrasonic imaging system using an ultrasonic instrument and a magnetic 6D position and orientation system [42, 54].

In magnetic localization/orientation system, the magnet produces a magnetic field whose spatial intensity and direction are determined by the magnet's location (3D) and orientation (2D). We measure the magnetic intensities and directions in some definite spatial positions using a few properly arranged (5 or more) sensors outside of the patient abdomen, and compute the location and orientation of the capsule (magnet) by these measured sensor data [55**,** 56].

This idea is similar to the magnetic tracking methods that are used to investigate the GI transit of the solid magnetized drug dosage [57~62], which are called as Magnetic Marker Monitoring (MMM) techniques. In 1970, Ephraim et al. [57] reported a technique for measuring the emptying of the stomach by using two pickup coils situated symmetrically to an exciting coil. When a tracer material (magnesium ferrite) passes through this system, it will unbalance the coupling between the pickup coils and produce a signal. Obviously, this system can only provide one-dimensional information (of stomach emptying).In 1994, Weitschies et al. [59] investigated the GI transit of magnetically marked drug dosage that was enclosed in a cylindrical capsule (16.1 mm × 5.7 mm) of silicone rubber. The magnetic detector is a commercial seven-channel DC-SQUID (Superconducting Quantum Interference Device) gradiometers with 20 mm coil diameter and 80 mm baseline. The marker positions with respect to the sensor were adjusted by moving the sliding bed in the horizontal plane in two orthogonal directions x and y, such that 21 (3×7) field data were yielded to provide more accurate localization of the magnetic moment, but the test speed is decreased to 5 seconds. Later, they improved their system by more advanced SQUID magnetometers. In 1997, they reported a system that used 37-channel SQUID such that it is possible to observe the GI transit of magnetically marked dosage forms with high temporal resolution (≤100ms) and spatial resolution (a few millimeters) [60]. In 2001, they proposed a new system [61] with 83-channel SQUID first-order gradiometer [62]. The system was applied to the monitor the disintegrating magnetically marked dosage capsules, which have no longer a constant magnetic moment. Their system was tested in phantom experiments, and the calculated coordinates of the capsules deviated between 2~8 mm from the expected position values depending on the distance between the capsule and the sensors. Similar to the system proposed by Weitschies et al., Osmanoglou et al. [58] made their esophageal transit studies using 63-channel flat SQUID device to track magnetically marked capsules (16.1 mm × 5.5 mm), which were applied by 5 volunteers and tested with different amount of water.

The above MMM systems in [58~62] are based on the multi-channel SQUID magnetometers. These systems have high sensitivity and are able to detect small variation of the magnetic dipole's position and orientation. This is especially important for detecting the dipole far away from the sensing system. However, the SQUID measurements have to be performed in a magnetically shielded room, and the systems are rather complicated and expensive. Therefore, it is desirable to find a more applicable technique that can be realized in a normal environment of patients' or doctors' rooms in hospital. Researches have been done to develop such a system, as proposed in [63~65].

Prakash et al. [63] presented a paper, in which a system was introduced to localize a magnetic marker (e.g., 7.8×25 mm magnet) in GI motility studies. Here the localization and orientation was based on the measurement data of eight fluxgate magnetometer sensors, which are arranged on a plane as shown in Figure 2.3. The test results reported that the eight-single-channel megnetometer system can localize the magnetic marker with accuracy within a few millimetres. However, we can not find the detailed realization scheme in this paper, and more investigations should be made to use such a system.

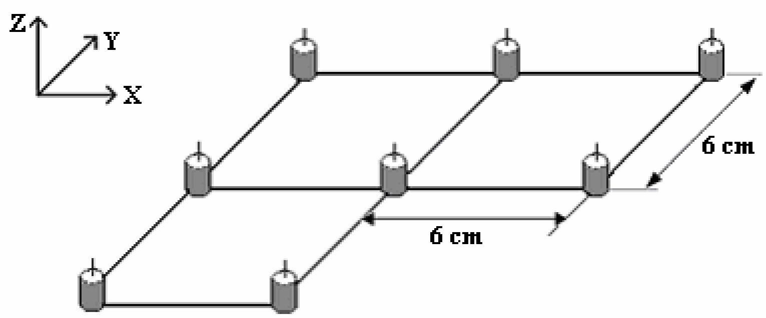

Figure 2.3 Fluxgate magnetometer sensor system [63]

Schlageter et al. [64] proposed a system built with a 2D-array of 16 Hall sensors (as shown in Figure 2.4), for tracking a magnetic marker made of rare earth cylindrical magnet (ϕ6 mm × 7 mm). For the 4 × 4 Hall sensors, integrated flux-concentrators are added to magnify the sensing signal and increase the signal-noise-ratio. Each sensor measures one component of the magnetic field in the plane of the matrix, the x-component for half of them and y-component for the others. The experimental results show that the localization error increases with the distance between the magnet and the sensor plane, and approximately a few millimeters for the test distance up to 14 cm. This technique was applied to a real system for tracing a swallowed magnetic pill throughout the entire digestive tract [65]. The 16 sensors located over the abdomen, and the magnet position, orientation, and trajectory are displayed in real time. Ten young healthy volunteers were followed during the test of 34 hours. The results are satisfactory. However, their localization algorithm is based on the nonlinear fitting method, and the execution speed might be low, and utilization of the integrated flux-concentrators makes the system complex.

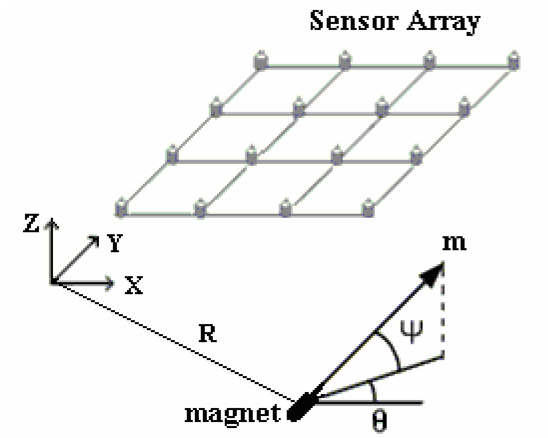

Figure 2.4 Magnetic tracking with 2D-array of 16 cylindrical Hall sensors [65]

Andra et al. [66] developed an interesting magnetic marker and testing system. Here, the marker is realized by a homogeneously magnetized sphere, as shown in Figure 2.6. This magnetic sphere marker (diameter = 3.5 mm, in a hollow sphere with diameter = 4 mm) has its moment aligned to be parallel to the z-axis through the external magnetic (coils) fields, as shown in Figure 2.5. Since the magnet's moment direction is fixed, always along the z-axis, we only need to consider the localization (no orientation) problem, which is in 3-dimensions. Therefore, the system uses a commercial 3-axis magneto-resistive sensor (HMR 2300; Honeywell, USA) to measure the three components of the stray field in a spatial point, and the magnet's position can be calculated by three predetermined equations. This technique has very simple algorithm (three equations) to calculate the position of the magnet, but it requires a mechanism to keep the external magnetic coils as close as possible to the position of the moving marker. Two stepping motors are used to shift the coil axes. In addition, this method misses the information of the capsule orientation if it is applied to the capsule endoscope.

Array technique: As discussed above, for localizing the magnetic dipole, the sensing systems (or magnet) often adopt more than 5 sensors for testing 5D localization/orientation parameters, e.g., the multi-channel SQUID technique, and the systems in Figure 2.3 and Figure 2.4. These sensors can be arranged as an array in a plane,

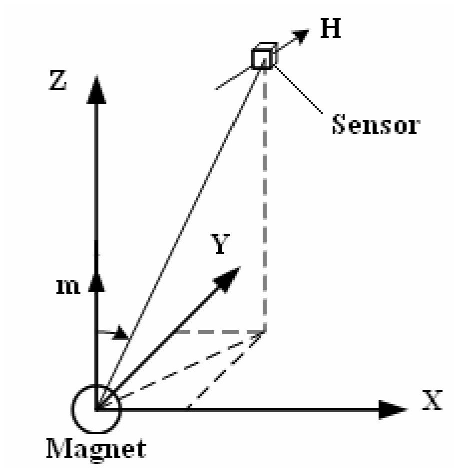

Figure 2.5 Scheme of the marker (magnet) and sensor [66]

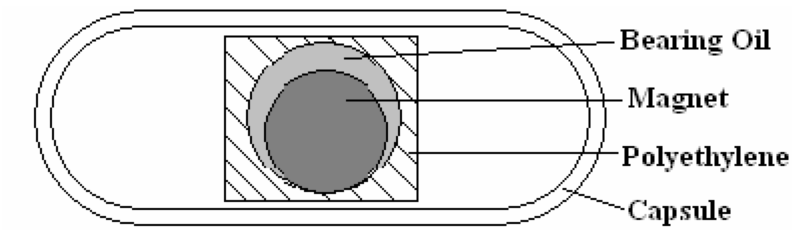

Figure 2.6 The sphere magnet (marker) in the bearing liquid box [66]

or in particular spatial positions. Since sensor number is more than that of the localization/ orientation parameters, the data are over-sampled. With an appropriate algorithm, we can compute the localization/orientation parameters with the over-sampled sensor data, and obtain higher accuracy comparing with those gotten by only 5 sensors. It is observed that the sensor array is an effective technique to improve the localization and orientation accuracy.

C. Localization and Orientation Algorithm

An algorithm is always companied a localization method. Typically, the algorithm for magnetic localization and orientation is built on the assumption that the magnetic excitation source (coil or magnet) works as a dipole, such that the magnetic field around this dipole can be expressed as [65, 66] (detailed derivation will be given in Chapter 3):

$$\mathbf{B} = \frac{\mu_r \mu_0 M_T}{4\pi}\left(\frac{3(\mathbf{H}_0 \cdot \mathbf{P})\mathbf{P}}{R^5} - \frac{\mathbf{H}_0}{R^3}\right)$$

where μ_r is the relative permeability of the medium; μ_0 is the air magnetic permeability (T·m/A); M_T is a constant defining the magnetic intensity of the dipole; $\mathbf{H}_0$ is a vector defining the direction of the dipole, which is in 2 dimension because it can be defined by 2 angles; **P** is a vector defining a spatial point with respect to the dipole, which is in 3 dimensions; R is a scalar defining the length of **P**. Obviously, the magnetic intensity **B** (in a spatial point) is a high-order nonlinear function of the 3D position and 2D orientation parameters of the dipole. For the localization and orientation, we need to solve the inverse problem: finding **P** and $\mathbf{H}_0$ from the measured data of **B** in some (5 or more) spatial points.

Nonlinear fitting: A common method to determine the dipole parameters is the nonlinear least squares fitting technique [58, 60, 69]. If the measured data of the magnetic field are represented by B_{meas} and the calculated field data by B_{culc} , the least-square varies both **P** (3D) and $\mathbf{H}_0$ (2D) to minimize the deviation given by

$$E = \sum_{l=1}^{N} (B_{meas}^{(l)} - B_{calc}^{(l)})^2$$

where N is the number of the sensors. Hence, an appropriate minimization algorithm should be found to solve this problem. In Chapter 4, several optimization algorithms will be tested for their calculation accuracy and execution speed, and the best one is found to be the Levenberg-Marquardt method, which was also proposed by other researchers [56, 64, 69].

There are some measures to improve the performance of the algorithm, In [63], the authors used 8 sensors as shown in Figure 2.3. For the computation, they first simplify the equations of the magnetic field given by a dipole, such that resultant equations have only position (3D) parameters. Then, Newton's method (based on 4 different seeds) was used to solve the nonlinear equations for the magnet's position, and finally computed the orientation parameters (2 direction angles). One other improvement is to use first order gradients of the magnetic intensities, instead of the absolute magnetic intensities, to do the nonlinear least squares fitting, as used for the SQUID gradiometers [59, 61, 62]. Since the background magnetic flux is removed out from the sensor (gradient) signals, the gradiometers can provide better detection performance, in case of the background with changeable magnetic field [70].

Linear algorithm: Linear algorithm is always desirable since it can provide unique solution (in nonsingular case), fast speed, and no requirement for the initial (guess) seeds. The system proposed by Raab et al. [48] is based on the linear algorithm. However, this algorithm was derived on the condition of some approximations and assumptions that are only suitable to small changes occur in the position an orientation. Error might be accumulated when too many steps are applied to the calculation. In addition, their algorithm is only used for the system composed of 3-axis excitation and receiving coils. Therefore, it is preferable to find a linear algorithm for the case of the permanent magnet dipole, and the derivation of this algorithm does not depend on the approximation. Here, we propose a linear algorithm that is based on measurement data from five or more 3-axis magnetic sensors. In Chapter 5, I will discus such a linear algorithm and corresponding measurement system.

2.3 Localization and orientation by imaging

The true capsule endoscope movement is in both 3D position and 3D orientation space. The magnetic orientation technique discussed above can only provide 2D orientation information. It misses the information of the capsule's rotation along its own central axis. Sometimes, this information is helpful for locating the pathology in the GI tract, and other applications, e.g., 3D recovery of the GI tract. Here, I propose a supplemental localization/ orientation method that is realized by computer vision (image processing) technique. This technique does not require any additional device, but only images that presented by the capsule endoscope camera. The drawback of imaging method is its low speed in the case of existing technique.

Because the current capsule endoscope has single camera, the localization and orientation must be realized by the images taken at different camera position or orientation. Two computer vision techniques can be applied to calculate the localization/orientation parameters. One is optic flow method [71~73], and another one is two-projection motion method [71, 74~77]. In the optic flow technique, the camera's position and orientation can be computed by finding the coordinates of some pixels and their transition velocities. These transition velocities can be found by matching some corresponding feature points in the two successive images. However, these two images must have small variation relative to the camera's position and orientation; otherwise there will be large error. Contrarily, a two-projection motion method, named as 8-point algorithm [75~78], does not have this limitation, and is realized by finding 8 or more correspondent points in the two successive images. Therefore, I choose the latter method, and detailed discuss will be given in Chapter 7.

This imaging method results in a relative orientation, which gives a rotation matrix from one camera's direction changing to another one, and is in true three dimensions. Sometimes, we are interested to know the rotation of the capsule's central axis (this axis can be also determined by the magnetic localization/orientation method), and the rotation around this axis. Therefore, we need to decompose the rotation gotten by imaging method into these 2 sub-rotations. A very clear decomposition method is based on the calculation of the quaternions [79~84] (see Section 3.3), which can represent above two rotations with two sets of quaternion parameters. Using an appropriate algorithm, we can solve the quaternion parameters from the rotation matrix, and compute the two angles corresponding to the two sub-rotations.

2.4 Conclusion

Because wireless capsule endoscope is a new endoscopic technique, there is only one method having been used for capsule (M2A) localization, the RF technique. This RF system is also used to transmit the captured images, so the localization module has the advantage that the capsule does not need any additional device. However, its measurement accuracy is low (average error: 37.7 mm). Therefore, we try to find more accurate approach and the magnetic localization/orientation technique is a good choice. It uses magnet as the excitation source, which does not require internal power supply, and can also be used for external actuation on the capsule. In addition, human body applies little effect on the sensing (static magnetic) signal so that high accuracy can be reached.

The magnetic localization technique has been used in many applications. Some commercial products use coils as the excitation and receiving components. Although they are not suitable for the localization of the capsule endoscope, they give us ideas how the system works. For the medical research of GI transit of drug dosage, Magnetic Marker Monitoring (MMM) techniques have been applied, and typically these techniques use multi-channel SQUID magnetometers and are able to detect small variation of the magnetic dipole's position and orientation. However, the SQUID measurements have to be performed in a magnetically shielded room, and the systems are rather complicated and expensive. Although there are other magnet's localization techniques using conventional magnetic sensors, a more efficient localization and orientation technique is desirable, which is of higher accuracy and robustness, faster speed, more effective algorithm, and more easily realization. Because the magnetic localization/orientation technique can only supply 2D orientation information, we present a supplementary method, the imaging localization/orientation technique, for obtaining the true 3D rotation parameters.

Chapter 3

Spatial Descriptions, Coordinate Transformations, and Rotation Decomposition

In order to do the localization and orientation of the capsule endoscope, an appropriate coordinate system must be created, such that some parameters related to the transition and the rotation of the capsule can be defined in this coordinate system, and be determined using an appropriate algorithm. This chapter introduces the coordinate systems in Cartesian coordinate system, their transformations, and the orientation decomposition with quaternion.

3.1 Description of position and orientation

3.1.1 Position description

The most common coordinate system for representing positions in space is the Cartesian coordinate system [85, 86] based on three perpendicular spatial axes generally designated x, y, and z, as shown in Figure 3.1. Often a position vector **P** can be expressed in terms of the coordinate values and associated unit vectors $\vec{\mathbf{v}}_X$, $\vec{\mathbf{v}}_Y$, and $\vec{\mathbf{v}}_Z$ along the 3 axes of the coordinate system

$$\mathbf{P} = x\vec{\mathbf{v}}_X + y\vec{\mathbf{v}}_Y + z\vec{\mathbf{v}}_Z \tag{3.1}$$

This vector can also be represented by $(x, y, z)^T$. Although the entire coordinate system can be rotated, the relationship between the axes is fixed in the right-handed coordinate system.

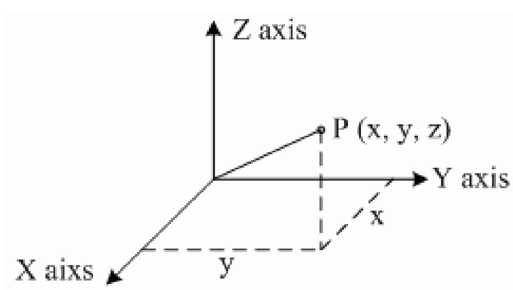

Figure 3.1 Cartesian coordinate system

3.1.2 Orientation description

The complete capsule's movement includes not only in the position but also the orientation, so here we make a description on the capsule's orientation (or rotation).

The orientation implies a second "inertial" frame with respect to a reference frame [84]. We can attach a coordinate system to the frame (with the capsule) and then give a description of this coordinate system relative to the reference system. In Figure 3.2, coordinate system $\{b\}=\{X_bY_bZ_b\}$ has been attached to the capsule relative to coordinate system $\{a\}=\{X_aY_aZ_a\}$. To simplify the problem, we can here deal with the orientation only. That is, assume {a} and {b} have the same origin, as in Figure 3.3.

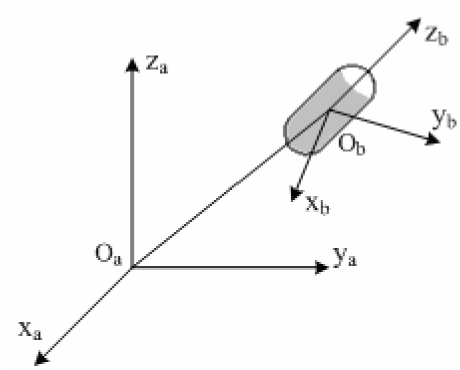

Figure 3.2 Locating the position and orientation

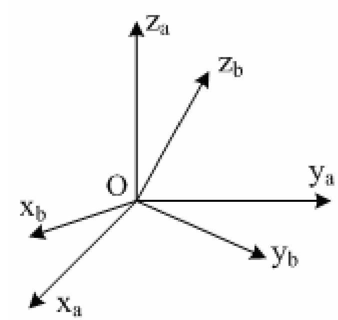

Figure 3.3 Locating the orientation

A rotation matrix is the most common method to represent rotation (another representation is quaternion referred in Appendix A). If a spatial point is represented in the coordinate vector ${}_a\mathbf{P}$ with respect to the frame {a}, and ${}_b\mathbf{P}$ with respect to the frame {b}, then we have

$$ {}_a\mathbf{P} = \mathbf{R} \cdot {}_b\mathbf{P} \quad , \quad \text{or} \quad \begin{pmatrix} {}_a p_x \\ {}_a p_y \\ {}_a p_z \end{pmatrix} = \mathbf{R} \begin{pmatrix} {}_b p_x \\ {}_b p_y \\ {}_b p_z \end{pmatrix} \tag{3.2} $$

where $\mathbf{R}$ is a 3 by 3 matrix, which is called rotation matrix. Typically, this transformation is defined orthogonal linear, and it satisfies $\mathbf{R}^T\mathbf{R} = \mathbf{R}\mathbf{R}^T = 1$. This implies that

$$ \mathbf{R}^{-1} = \mathbf{R}^T \tag{3.3} $$

3.1.3 Euler angles

Euler angles describe an orientation as a sequence of three rotations about moving frame axes. Around 1750, Euler proved that the relative orientation of coordinate systems can be specified by a set of three independent angles [87]. With these independent angles, we can describe rotation more easily, and there are typically several methods of describing the orientation. Here, I discuss the X-Y-Z fixed angles.

X-Y-Z fixed angles: The X-Y-Z fixed angles is described as follows:

Start with the frame coincident with a known reference frame {a}. Rotate {b} first about $\hat{X}_a$ by an angle γ (represented by $R(X,\gamma)$), then about $\hat{Y}_a$ by an angle β (represented by $R(Y,\beta)$), and finally about $\hat{Z}_a$ by an angle α (represented by $R(Z,\alpha)$).

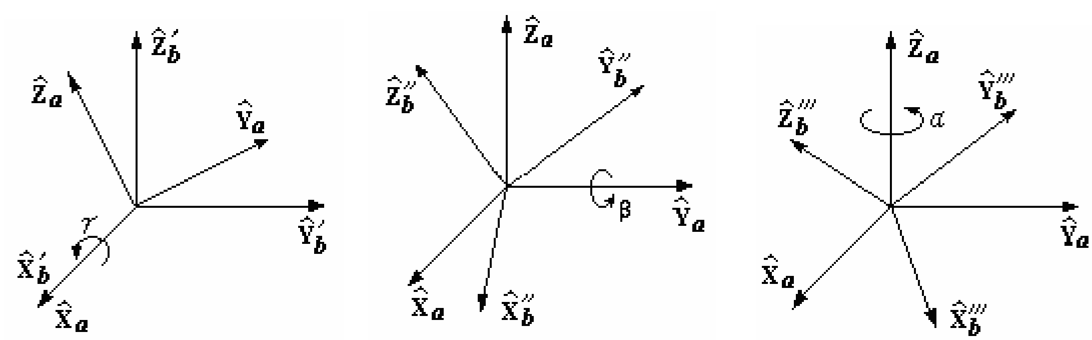

Figure 3.4 X-Y-Z fixed angles. Rotations are performed in the order $\mathbf{R}(X,\gamma)$, $\mathbf{R}(Y,\beta)$, $\mathbf{R}(Z,\alpha)$

Each of the three rotations takes place about an axis in the fixed reference frame {a}. Sometimes this rotation convention is referred to as roll, pitch, and yaw angles. The derivation of the equivalent rotation matrix ${}^b_a\mathbf{R}(XYZ,\gamma,\beta,\alpha)$ is straightforward, because all the rotations occur about axes of the reference frame, that is

$$
\begin{aligned}
{}^b_a\mathbf{R}(XYZ,\gamma,\beta,\alpha) &= \mathbf{R}(Z,\alpha)\mathbf{R}(Y,\beta)\mathbf{R}(X,\gamma) \\
&= \begin{bmatrix} c\alpha & -s\alpha & 0 \\ s\alpha & c\alpha & 0 \\ 0 & 0 & 1 \end{bmatrix} \begin{bmatrix} c\beta & 0 & s\beta \\ 0 & 1 & 0 \\ -s\beta & 0 & c\beta \end{bmatrix} \begin{bmatrix} 1 & 0 & 0 \\ 0 & c\gamma & -s\gamma \\ 0 & s\gamma & c\gamma \end{bmatrix}
\end{aligned}
$$

$$=\begin{bmatrix} c\alpha c\beta & c\alpha s\beta s\gamma - s\alpha c\gamma & c\alpha s\beta c\gamma + s\alpha s\gamma \\ s\alpha c\beta & s\alpha s\beta s\gamma + c\alpha c\gamma & s\alpha s\beta c\gamma - c\alpha s\gamma \\ -s\beta & c\beta s\gamma & c\beta c\gamma \end{bmatrix} \tag{3.4}$$

where $c\alpha$ is the shorthand for $\cos\alpha$, $s\alpha$ for $\sin\alpha$, and so on.

3.2 Capsule's direction transformation in different coordinate systems

For the capsule endoscopy, we might be interested to know the capsule direction in which the endoscopic imager captures images. Typically we define the current image coordinate with respect to a coordinate system in wich one axis is in the imager's direction, so this coordinate representation changes when capsule moves. Obviously, it is clearer to represent the direction with respect to a fixed coordinate system. Here, I introduce the method to do the direction transformation from current image coordinate system to the global reference coordinate system, while knowing the relative rotation sequences.

As shown in Figure 3.5, the capsule direction is defined by unit vector $\vec{\mathbf{r}}_1 = (m_1 \;\; n_1 \;\; p_1)^T$ in (XYZ) universe coordinate system, and another Cartesian coordinate system ($X^1Y^1Z^1$) is defined with the Z^1-axis along the vector $\vec{\mathbf{r}}_1$. Transforming a vector from $X^1Y^1Z^1$ to *XYZ*, we have

$$\mathbf{P}^1 = {}^1\mathbf{R} \cdot {}_1\mathbf{P}^1 \tag{3.5}$$

where $\mathbf{P}^1 = (x \;\; y \;\; z)^T$ is a vector in *XYZ* coordinate system, ${}_1\mathbf{P}^1 = ({}_1x^1 \;\; {}_1y^1 \;\; {}_1z^1)^T$ the same vector in $X^1Y^1Z^1$ coordinate system, and ${}^1\boldsymbol{R}$ the mapping matrix from $X^1Y^1Z^1$ to *XYZ* coordinate system. ($\vec{\mathbf{r}}_1$ can be defined by $(0, 0, 1)^T$ in $X^1Y^1Z^1$ coordinate system, and it changes to ${}^1\boldsymbol{R}\,(0, 0, 1)^T$ in *XYZ* coordinate system).

If the capsule direction is $\vec{\mathbf{r}}_2 = ({}_1m^2 \;\; {}_1n^2 \;\; {}_1p^2)^T$ in $X^1Y^1Z^1$ coordinate system and $(m_2 \; n_2 \; p_2)^T$ in *XYZ* coordinate system, then

$$\begin{bmatrix} m_2 \\ n_2 \\ p_2 \end{bmatrix} = {}^1\mathbf{R} \cdot \begin{bmatrix} {}_1m^2 \\ {}_1n^2 \\ {}_1p^2 \end{bmatrix} \tag{3.6}$$

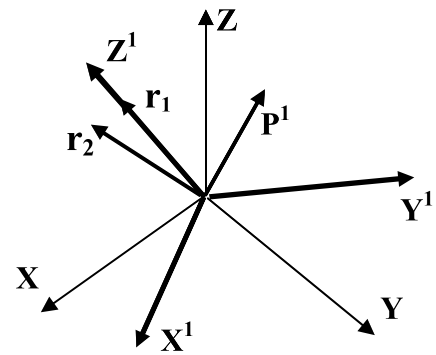

Figure 3.5 Rotation in universe and relative coordinate system

Now a new coordinate system ($X^2Y^2Z^2$) is built with Z^2-axis is along the vector $\vec{\mathbf{r}}_2$. From $X^2Y^2Z^2$ system to $X^1Y^1Z^1$ system, we have

$$ {}_1\mathbf{P}^2 = {}_1^2\mathbf{R} \cdot {}_2\mathbf{P}^2 \tag{3.7} $$

where ${}_1\mathbf{P}^2$ =(${}_1x^2 \quad {}_1y^2 \quad {}_1z^2$) is a vector represented in $X^1Y^1Z^1$ coordinate system, and ${}_2\mathbf{P}^2$ =(${}_2x^2 \quad {}_2y^2 \quad {}_2z^2$) the same vector in $X^2Y^2Z^2$ coordinate system. ${}_1^2\mathbf{R}$ is the mapping matrix from $X^2Y^2Z^2$ coordinate system to $X^1Y^1Z^1$ coordinate system. If the capsule direction is changed to (${}_2m^3 \quad {}_2n^3 \quad {}_2p^3$) in $X^2Y^2Z^2$ coordinate system and $(m_3 \ n_3 \ p_3)^T$ in *XYZ* coordinate system, then

$$ \begin{bmatrix} m_3 \\ n_3 \\ p_3 \end{bmatrix} = {}^1\mathbf{R} \cdot {}_1^2\mathbf{R} \cdot \begin{bmatrix} {}_2m^3 \\ {}_2n^3 \\ {}_2p^3 \end{bmatrix} = {}^2\mathbf{R} \cdot \begin{bmatrix} {}_2m^3 \\ {}_2n^3 \\ {}_2p^3 \end{bmatrix} \tag{3.8} $$

where ${}^2\mathbf{R} = {}^1\mathbf{R} \cdot {}_1^2\mathbf{R}$. Repeat this procedure we can get the capsule imager direction in step i-1.

$$ \begin{bmatrix} m_i \\ n_i \\ p_i \end{bmatrix} = {}^{i-2}\mathbf{R} \cdot {}_{i-2}^{i-1}\mathbf{R} \cdot \begin{bmatrix} {}_{i-1}m^i \\ {}_{i-1}n^i \\ {}_{i-1}p^i \end{bmatrix} = {}^{i-1}\mathbf{R} \cdot \begin{bmatrix} {}_{i-1}m^i \\ {}_{i-1}n^i \\ {}_{i-1}p^i \end{bmatrix} \tag{3.9} $$

where i is the step number for the capsule imager fulfilling relative rotation; $[m_i \ n_i \ p_i]^T$ is capsule imager direction represented in XYZ universe coordinate system;

$[{}_{i-1}m^i \quad {}_{i-1}n^i \quad {}_{i-1}p^i]^T$ is the direction coordinate in $X^{i-1}Y^{i-1}Z^{i-1}$ coordinate system; to change the representation from $[{}_{i-1}m^i \quad {}_{i-1}n^i \quad {}_{i-1}p^i]^T$ to $[m_i \; n_i \; p_i]^T$, we have the mapping matrix

$$^{i-1}\mathbf{R} = {}^{i-2}\mathbf{R} \cdot {}^{i-1}_{i-2}\mathbf{R} = {}^{1}\mathbf{R} \cdot {}^{2}_{1}\mathbf{R} \cdots {}^{i-2}_{i-3}\mathbf{R} \cdot {}^{i-1}_{i-2}\mathbf{R} \tag{3.10}$$

Therefore, in order to change the representation of capsule direction in $X^{i-1}Y^{i-1}Z^{i-1}$ coordinate system to that in XYZ coordinate system, we need to know $^{i-2}\mathbf{R}$, the mapping matrix from $X^{i-2}Y^{i-2}Z^{i-2}$ coordinate system to XYZ coordinate system, and ${}^{i-1}_{i-2}\mathbf{R}$, $X^{i-1}Y^{i-1}Z^{i-1}$ coordinate system to $X^{i-2}Y^{i-2}Z^{i-2}$ coordinate system.

3.3 Rotation decomposition using quaternions

The rotation matrix represents the transform representation of the spatial points' rotation from one coordinate system to another coordinate system. In the case of capsule endoscope, this rotation is composed of the rotation of the capsule (camera's) central axis and the rotation around this axis. In this section, I try to decompose these two rotations, that is, to find the resultant orientation (unit) vector $\vec{\mathbf{r}}_2 = (m_2 \; n_2 \; p_2)^T$ of the capsule's central axis and the rotation angle around this central axis, using the data of initial (unit) vector $\vec{\mathbf{r}}_1 = (m_1 \; n_1 \; p_1)^T$ of the capsule's central axis and the rotation transform matrix **R**.

It is more convenient to do the rotation decomposition using quaternion [79~84], because a quaternion $\mathbf{q} = (q_0 \; q_x \; q_y \; q_z)^T$ represents a rotation along vector $(q_x \; q_y \; q_z)^T$, whose rotation angle is determined by $2\cos^{-1}(q_0)$. In Appendix A, I present the detailed quaternion algebra. In this section, I focus on the computations for the rotation decomposition.

3.3.1 Conversion between rotation matrix and quaternion

Let a quaternion $\mathbf{q} = (q_0 \; q_x \; q_y \; q_z)^T$ represent a rotation, then we have the corresponding rotation matrix **R**:

$$\mathbf{R} = \begin{pmatrix} q_0^2 + q_x^2 - q_y^2 - q_z^2 & 2q_xq_y - 2q_0q_z & 2q_xq_z + 2q_0q_y \\ 2q_xq_y + 2q_0q_z & q_0^2 - q_x^2 + q_y^2 - q_z^2 & 2q_yq_z - 2q_0q_x \\ 2q_xq_z - 2q_0q_y & 2q_yq_z + 2q_0q_x & q_0^2 - q_x^2 - q_y^2 + q_z^2 \end{pmatrix} \tag{3.11}$$

Reversely, when the rotation matrix $\mathbf{R}$ is as $\mathbf{R} = \begin{pmatrix} \hat{m}_{11} & \hat{m}_{12} & \hat{m}_{13} \\ \hat{m}_{21} & \hat{m}_{22} & \hat{m}_{23} \\ \hat{m}_{31} & \hat{m}_{32} & \hat{m}_{33} \end{pmatrix}$, we can calculate the quaternion $\mathbf{q} = [q_0 \;\; q_x \;\; q_y \;\; q_z]^T$ with

$$q_0 = \sqrt{\frac{1 + \hat{m}_{11} + \hat{m}_{22} + \hat{m}_{33}}{4}} \tag{3.12}$$

$$q_x = \frac{\hat{m}_{32} - \hat{m}_{23}}{4q_0} \tag{3.13}$$

$$q_y = \frac{\hat{m}_{13} - \hat{m}_{31}}{4q_0} \tag{3.14}$$

$$q_z = \frac{\hat{m}_{21} - \hat{m}_{12}}{4q_0} \tag{3.15}$$

3.3.2 Order Problem

For the capsule's rotation (let $\mathbf{R}$ denote this rotation), we can assume that it has two sub-rotations: one is the rotation (let $\mathbf{R}_1$ denote this rotation) of capsule's central axis from $\vec{\mathbf{r}}_1 = (m_1 \; n_1 \; p_1)^T$ to $\vec{\mathbf{r}}_2 = (m_2 \; n_2 \; p_2)^T$, and the other one is its rotation (let $\mathbf{R}_2$ denote this rotation) around this central axis. To simplify the problem, we also assume that rotation $\mathbf{R}_1$ (from $\vec{\mathbf{r}}_1$ to $\vec{\mathbf{r}}_2$) is around the axis formed by $\vec{\mathbf{r}}_3 = \vec{\mathbf{r}}_1 \times \vec{\mathbf{r}}_2$ (the shortest route). Here, I introduce Theorem 3.1, by which we can see that the transform order of the two rotations will not affect the results of the rotation transforms.

Theorem 3.1: As shown in Figure 3.7, assume that the capsule central (orientation) axis is changed from $\vec{\mathbf{r}}_1 = (m_1 \; n_1 \; p_1)^T$ to $\vec{\mathbf{r}}_2 = (m_2 \; n_2 \; p_2)^T$, both of which are unit vectors, and meanwhile there is a rotation around its central axis, whose angle is $\boldsymbol{\alpha}$. Let

$$\vec{\mathbf{r}}_3 = \frac{\vec{\mathbf{r}}_1 \times \vec{\mathbf{r}}_2}{\left\| \vec{\mathbf{r}}_1 \times \vec{\mathbf{r}}_2 \right\|} \tag{3.16}$$

and θ is the rotation angle from $\vec{\mathbf{r}}_1$ to $\vec{\mathbf{r}}_2$ around $\vec{\mathbf{r}}_3$. We can show that the same coordinate transform can be realized by rotation (***θ)*** from $\vec{\mathbf{r}}_1$ to $\vec{\mathbf{r}}_2$ around $\vec{\mathbf{r}}_3$ first and rotation (α) around its central axis second; or equally by rotation (α**)** around the central axis first and rotation (***θ)*** from $\vec{\mathbf{r}}_1$ to $\vec{\mathbf{r}}_2$ around $\vec{\mathbf{r}}_3$ second. (Its proof is given in Appendix B.1)

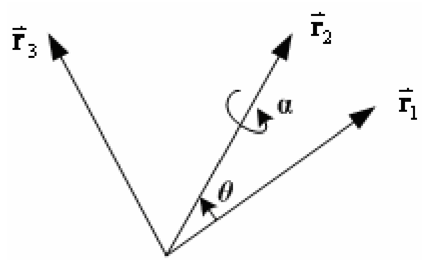

Figure 3.6 Central axis rotation ($\mathbf{R}_1$ with angle θ) and rotation around the axis (R2 with angle α)

Example 3.1: Let $\vec{\mathbf{r}}_1 = (1\ \ 0\ \ 0)^T$, $\vec{\mathbf{r}}_2 = (0\ \ 1\ \ 0)^T$, and rotation around the central axis is $\mathbf{R}_2$ with α ***= 90°***. Obviously, ***θ = 90°*** such that rotation around $\vec{\mathbf{r}}_3$ results in quaternion

$$\mathbf{q}_3 = \frac{\sqrt{2}}{2} + \frac{\sqrt{2}}{2}\mathbf{k}$$

And the rotation matrix

$$\mathbf{R}_3 = \begin{pmatrix} 0 & -1 & 0 \\ 1 & 0 & 0 \\ 0 & 0 & 1 \end{pmatrix}.$$

For the rotation α around the central axis, we first assume it rotates around $\vec{\mathbf{r}}_2$ so that

$$\mathbf{q}_2 = \frac{\sqrt{2}}{2} + \frac{\sqrt{2}}{2}\mathbf{j}$$

And the rotation matrix

$$\mathbf{R}_2 = \begin{pmatrix} 0 & 0 & 1 \\ 0 & 1 & 0 \\ -1 & 0 & 0 \end{pmatrix}.$$

The capsule's rotation $\mathbf{R}$ can be calculated with quaternion

$$\mathbf{q} = \mathbf{q}_2\mathbf{q}_3 = \frac{1}{2} + \frac{1}{2}\mathbf{i} + \frac{1}{2}\mathbf{j} + \frac{1}{2}\mathbf{k}$$

And rotation matrix (θ first, α second)

$$\mathbf{R} = \mathbf{R}_2\mathbf{R}_3 = \begin{pmatrix} 0 & 0 & 1 \\ 1 & 0 & 0 \\ 0 & 1 & 0 \end{pmatrix}$$

If we assume that rotation α is around $\vec{\mathbf{r}}_1$, then

$$\mathbf{q}_1 = \frac{\sqrt{2}}{2} + \frac{\sqrt{2}}{2}\mathbf{i}$$

And the rotation matrix

$$\mathbf{R}_1 = \begin{pmatrix} 1 & 0 & 0 \\ 0 & 0 & -1 \\ 0 & 1 & 0 \end{pmatrix}.$$

Then, the capsule's rotation $\mathbf{R}$ can be calculated with quaternion

$$\mathbf{q}' = \mathbf{q}_3\mathbf{q}_1 = \frac{1}{2} + \frac{1}{2}\mathbf{i} + \frac{1}{2}\mathbf{j} + \frac{1}{2}\mathbf{k}$$

And rotation matrix (α first, θ second)

$$\mathbf{R}' = \mathbf{R}_3\mathbf{R}_1 = \begin{pmatrix} 0 & 0 & 1 \\ 1 & 0 & 0 \\ 0 & 1 & 0 \end{pmatrix}.$$

Therefore, $\mathbf{R}' = \mathbf{R}$.

3.3.3 Rotation Decomposition

Now we determine the angle α and the resultant orientation $\vec{\mathbf{r}}_2 = (m_2\ n_2\ p_2)^T$ using $\vec{\mathbf{r}}_1 = (m_1\ n_1\ p_1)^T$ and the known rotation matrix $\boldsymbol{R}$ (or the quaternion $\mathbf{q} = [q_0\ \ q_x\ \ q_y\ \ q_z]^T$). Here, I introduce Theorem 3.2 (its proof is referred to Appendix B.2).

Theorem 3.2: If a rotation is represented by a quaternion $\mathbf{q} = [q_0 \ \ q_x \ \ q_y \ \ q_z]^T$ and the initial capsule central axis is represented by $\vec{\mathbf{r}}_1 = (m_1 \ n_1 \ p_1)^T$, then when the rotation ends, the sub-rotation angle $\boldsymbol{\alpha}$ around the central axis can be determined by

$$\alpha = 2\tan^{-1}(\frac{m_1 q_x + n_1 q_y + p_1 q_z}{q_0}) \tag{3.17}$$

and the rotation angle $\boldsymbol{\theta}$ that is formed by $\vec{\mathbf{r}}_1$ and the resultant axis vector $\vec{\mathbf{r}}_2 = (m_2 \ n_2 \ p_2)^T$ around the axis $\vec{\mathbf{r}}_3 = \vec{\mathbf{r}}_1 \times \vec{\mathbf{r}}_2$ is given by

$$\theta = 2\cos^{-1}(q_0 / \cos(\alpha / 2)) \tag{3.18}$$

Furthermore, the resultant orientation of the central axis can be determined by

$$\vec{\mathbf{r}}_2 = (m_2 \ n_2 \ p_2)^T = \frac{(q_{2x} \ \ q_{2y} \ \ q_{2z})^T}{\sin(\alpha / 2)} \tag{3.19}$$

Where

$$\begin{pmatrix} q_{2x} \\ q_{2y} \\ q_{2z} \end{pmatrix} = \begin{pmatrix} \cos(\theta/2) & q_{3z} & -q_{3y} \\ -q_{3z} & \cos(\theta/2) & q_{3x} \\ q_{3y} & -q_{3x} & \cos(\theta/2) \end{pmatrix}^{-1} \cdot \begin{pmatrix} q_x - \cos(\alpha/2)\cdot q_{3x} \\ q_y - \cos(\alpha/2)\cdot q_{3y} \\ q_z - \cos(\alpha/2)\cdot q_{3z} \end{pmatrix} \tag{3.20}$$

with

$$\begin{pmatrix} q_{3x} \\ q_{3y} \\ q_{3z} \end{pmatrix} = \begin{pmatrix} 1 & tg(\alpha/2)p_1 & -tg(\alpha/2)n_1 \\ -tg(\alpha/2)p_1 & 1 & tg(\alpha/2)m_1 \\ tg(\alpha/2)n_1 & -tg(\alpha/2)m_1 & 1 \end{pmatrix}^{-1} \cdot \begin{pmatrix} q_x \cos(\alpha/2) - q_0 \sin(\alpha/2)m_1 \\ q_y \cos(\alpha/2) - q_0 \sin(\alpha/2)n_1 \\ q_z \cos(\alpha/2) - q_0 \sin(\alpha/2)p_1 \end{pmatrix} \tag{3.21}$$

To show how the theorem works, here I introduce Example 3.2.

Example 3.2: assume that the rotation matrix

$$\mathbf{R} = \begin{pmatrix} 0.8783 & -0.4532 & 0.1522 \\ 0.4755 & 0.8607 & -0.1816 \\ -0.0487 & 0.2319 & 0.9715 \end{pmatrix}$$

and the initial vector of the central axis is

$$\vec{\mathbf{r}}_1 = (m_1 \ n_1 \ p_1) = (\frac{1}{\sqrt{3}} \quad \frac{1}{\sqrt{3}} \quad \frac{1}{\sqrt{3}})^T$$

Now, we need to calculate the angle $\boldsymbol{\alpha}$ and orientation vector $\vec{\mathbf{r}}_2 = (m_2 \ n_2 \ p_2)^T$. From **R**, we get the rotation quaternion using (3.12)~(3.15):

$$\mathbf{q} = [q_0 \ q_x \ q_y \ q_z]^T = \begin{bmatrix}0.9631 & 0.1073 & 0.0521 & 0.2411\end{bmatrix}^T$$

Using (3.17), we have

$$\alpha = 2\tan^{-1}(\frac{m_1 q_x + n_1 q_y + p_1 q_z}{q_0}) = 27.00°$$

Using (3.18), we have

$$\theta = 2\cos^{-1}(q_0 / \cos(\alpha/2)) = 15.79°$$

Up to now, we get the 2 sub-rotation angles. In the following we find the resultant orientation. From (3.21), we have

$$[q_{3x} \ q_{3y} \ q_{3z}]^T = [0.0000 \quad -0.0971 \quad 0.0971]^T$$

Using (3.20), we calculate

$$[q_{2x} \ q_{2y} \ q_{2z}]^T = [0.0778 \quad 0.1556 \quad 0.1556]^T$$

Finally, we get the vector $\vec{\mathbf{r}}_2$:

$$\vec{\mathbf{r}}_2 = (m_2 \ n_2 \ p_2)^T = \frac{[q_{2x} \ q_{2y} \ q_{2z}]^T}{\sin(\alpha/2)} = [0.3333 \quad 0.6667 \quad 0.6667]^T$$

We can verify that

$$\begin{aligned}\mathbf{q}_2\mathbf{q}_3 &= (q_{20} \quad q_{2x} \quad q_{2y} \quad q_{2z})^T (q_{30} \quad q_{3x} \quad q_{3y} \quad q_{3z})^T \\ &= (0.9724 \quad 0.0778 \quad 0.1556 \quad 0.1556)^T (0.9905 \quad 0.0000 \quad -0.0971 \quad 0.0971)^T \\ &= (0.9631 \quad 0.1073 \quad 0.0521 \quad 0.2411)^T\end{aligned}$$

This is exactly the values of the quaternion **q**.

3.4 Conclusion

A spatial point and its transition can be simply represented by its three projections in the Cartesian coordinate system. Contrarily, the orientation or rotation of an objective is a relative concept, and it is typically represented by transformation matrix for a coordinate vector **P** in a frame to be changed to another coordinate vector **P’** in a reference frame. Euler proved that the relative orientation of coordinate systems can be specified by a set of three independent angles. With Euler angles, we can describe rotation more easily.

Assume that the capsule direction is represented by three projections along the 3 axes of the current coordinate system, and we know the relative rotation transformation matrices between the different frames, then we can compute the direction vector with respect to the reference frame.

The true rotation of an object is in 3 dimensions. In the capsule endoscope’s case, this rotation is composed of the rotation of the capsule central axis and the rotation around this axis. For some applications, we might need to decompose these two rotations, that is, to find the resultant orientation vector of the capsule’s central axis and the rotation angle around this central axis, using the data of initial vector of the capsule’s central axis and the rotation transform matrix **R**. To do this decomposition, I use quaternion technique, since a quaternion can more clearly define a rotation, and present the approach by Theorem 3.1 and Theorem 3.2.

Chapter 4

Nonlinear Magnetic Localization and Orientation Technique

We propose a localization and orientation technique using a permanent magnet enclosed in the capsule to function as the excitation source. The magnetic field produced by the magnet is determined by the position (3D) and orientation (2D) of the capsule. Therefore, we can measure the magnetic intensity and direction using a few properly arranged sensors outside of the patient abdomen, and calculate the position and orientation parameters of the magnet with the algorithm. In this chapter, I will introduce the mathematic model for the magnetic field created by a permanent magnet, and propose the method to solve the 5D localization/orientation parameters using an optimization algorithm. Because there are several optimization algorithms, I evaluate them with respect to the calculation accuracy and execution time to determine the best one for capsule localization and orientation.

In section 4.1, we present the mathematical model for the magnetic field created by the permanent magnet. In section 4.2, we evaluate several optimization algorithms to determine the best one for capsule localization and orientation. In section 4.3, the system de-noising ability will be investigated by the simulation results, and discussions will be given in section 4.4.

4.1 Mathematic Model for the Magnetic Field created by a Permanent Magnet

4.1.1 The Magnetic Dipole

Figure 4.1 shows a cylindrical magnet with length L, diameter δ, and a uniform magnetization M_0 (Amp/meter) on its upper and bottom surfaces. Let us define a Cartesian coordinate system with the magnet at the origin. Let **P** be a vector representing a spatial point. We need to find the magnetic intensity and direction in this point. Assume that the size of the magnet is small enough comparing with the distance between the magnet and the point, then we can consider the magnet to be a magnetic dipole with the magnetism pair $+M$ and $-M$ with $M = \pi\delta^2 M_0$ at the two points with distance $L=2\bar{l}$, as shown in Figure 4.2. The distance from the point to the origin is R, and the distances from the point to $+M$ and $-M$ are R_1 and R_2 respectively. The magnetic potential at the point is given by [67, 68]

$$F(R,\theta) = M(\frac{1}{R_1} - \frac{1}{R_2}) \tag{4.1}$$

where θ is the angle between dipole vector and the vector **P**.

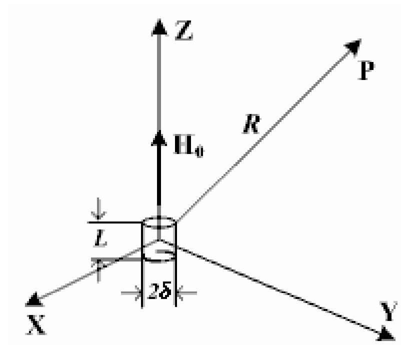

Figure 4.1 Magnetic field produced by a permanent magnet

Since the magnetic moment is axially symmetric, the magnetic potential must be independent of the azimuthal angle. Using cosine law, we may write

$$R_1^2 = R^2 + \bar{l}^2 - 2R\bar{l}\cos\hat{\theta} = R^2\left[1 + \left(\frac{\bar{l}}{R}\right)^2 - 2\frac{\bar{l}}{R}\cos\hat{\theta}\right] \tag{4.2}$$

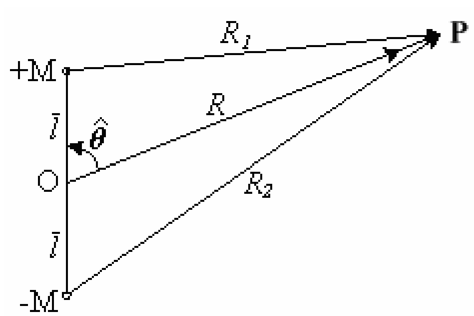

Figure 4.2 Magnetic dipole and its magnetic field

Thus,

$$\frac{1}{R_1} = \frac{1}{R}\left[1 + \left(\frac{\bar{l}}{R}\right)^2 - 2\frac{\bar{l}}{R}\cos\hat{\theta}\right]^{-1/2}$$

$$= \frac{1}{R}\left[1 + \left(\frac{\bar{l}}{R}\right)\cos\hat{\theta} + \frac{1}{2}\left(\frac{\bar{l}}{R}\right)^2\left(3\cos^2\hat{\theta} - 1\right) + \frac{1}{2}\left(\frac{\bar{l}}{R}\right)^3\left(5\cos^3\hat{\theta} - 3\cos\hat{\theta}\right) + \cdots\right]$$

where we have assumed that $l << R$. Therefore, we have approximately

$$\frac{1}{R_1} = \frac{1}{R} + \frac{\bar{l}}{R^2}\cos\hat{\theta} + \frac{1}{2}\frac{\bar{l}^2}{R^3}(3\cos^2\hat{\theta} - 1) \tag{4.3}$$

$$\frac{1}{R_2} = \frac{1}{R} - \frac{\bar{l}}{R^2}\cos\hat{\theta} + \frac{1}{2}\frac{\bar{l}^2}{R^3}(3\cos^2\hat{\theta} - 1) \tag{4.4}$$

Thus the magnetic potential becomes approximately

$$F(R,\hat{\theta}) = M\left(\frac{1}{R_1} - \frac{1}{R_2}\right) = 2M\bar{l}\,\frac{\cos\hat{\theta}}{R^2} \tag{4.5}$$

We define the magnetic dipole moment as the product of M and $2l$:

$$\overline{\mathbf{m}} = 2M\bar{l}\,\mathbf{H}_0 = ML\mathbf{H}_0 \tag{4.6}$$

The dipole moment is a vector whose direction is defined as the direction from negative to the positive magnetism; $\mathbf{H_0}$ is the unit vector in this direction. Clearly, the magnetic potential may be expressed as

$$F = \frac{\overline{\mathbf{m}} \bullet \mathbf{P}}{R^3} \tag{4.7}$$

The magnetic field vector **B** may be calculated by taking the gradient of F:

$$\mathbf{B} = -\frac{\mu_r\mu_0}{4\pi}\mathbf{grad}(F) = -\frac{\mu_r\mu_0}{4\pi}\mathbf{grad}\left(\frac{\overline{\mathbf{m}} \bullet \mathbf{P}}{R^3}\right) \tag{4.8}$$

where μ_r is the relative magnetic permeability of the medium, μ_0 is the air magnetic permeability (T·m/A). Expanding the gradient of the product of two scalar functions ($\overline{\mathbf{m}} \bullet \mathbf{P}$ and $\frac{1}{R^3}$), we obtain

$$\mathbf{B} = -\frac{\mu_r \mu_0}{4\pi} \frac{1}{R^3} \mathbf{grad}(\overline{\mathbf{m}} \bullet \mathbf{P}) - \frac{\mu_r \mu_0}{4\pi} (\overline{\mathbf{m}} \bullet \mathbf{P}) \mathbf{grad}(\frac{1}{R^3}) \tag{4.9}$$

Because $\mathbf{grad}(\overline{\mathbf{m}} \bullet \mathbf{P}) = \overline{\mathbf{m}}$, and $\mathbf{grad}(\frac{1}{R^3}) = -\frac{3\mathbf{P}}{R^5}$, we have

$$\mathbf{B} = -\frac{\mu_r \mu_0}{4\pi} (\frac{\overline{\mathbf{m}}}{R^3} - \frac{3(\overline{\mathbf{m}} \bullet \mathbf{P})\mathbf{P}}{R^5}) \tag{4.10}$$

Since $\overline{\mathbf{m}} = ML\mathbf{H}_0 = \pi \delta^2 LM_0 \mathbf{H}_0$, the magnetic flux density can be calculated using the following equation

$$\mathbf{B} = \frac{\mu_r \mu_0 M_T}{4\pi} \left(\frac{3(\mathbf{H}_0 \cdot \mathbf{P})\mathbf{P}}{R^5} - \frac{\mathbf{H}_0}{R^3} \right) = B_T \left(\frac{3(\mathbf{H}_0 \cdot \mathbf{P})\mathbf{P}}{R^5} - \frac{\mathbf{H}_0}{R^3} \right) \tag{4.11}$$

where $M_T = \pi \delta^2 LM_0$, $B_T = \frac{\mu_r \mu_0 M_T}{4\pi}$.

In the above derivation, we assume that the radius of the magnet dipole is small enough so that two surfaces of the dipole can be considered as point sources. One concern is the error induced by this assumption. We can prove this error is related to $\frac{1}{\sqrt{1+(\delta / R)^2}}$.

So if magnet has a radius of 3 mm and we control the distance *R* with 40mm or larger, then the error will be smaller than 0.3%, and this error is minor.

4.1.2 Mathematical model for localization and orientation

As the capsule endoscope traverses through the GI tract, the position of the magnet changes. Defining a coordinate system with location of the magnet at the origin makes the analysis difficult as the origin changes with time. Therefore, we propose to use a fixed coordinate system, shown in Figure 4.3. In the new coordinate system, the magnet's location is represented by $(a, b, c)^T$ and the magnet's orientation is represented by $\mathbf{H}_0 = (m, n, p)^T$, the projections on the three axes of the coordinate system. Assume that there are *N* sensors, with *l*-th sensor located at $(x_l, y_l, z_l)^T$, $1 \le l \le N$. The vectors connecting the *l*-th sensor to the magnet can then be represented by $\mathbf{P}_l = (x_l - a, y_l - b, z_l - c)^T$, and the magnetic flux density at the *l*-th sensor location can be represented by

$$\mathbf{B}_l = B_{lx}\vec{\mathbf{v}}_X + B_{ly}\vec{\mathbf{v}}_Y + B_{lz}\vec{\mathbf{v}}_Z \qquad (1 = 1,2,\ldots,N) \tag{4.12}$$

with three orthogonal components along the 3 coordinate axes:

$$B_{lx} = B_T\left\{\frac{3[m(x_l-a)+n(y_l-b)+p(z_l-c)]\cdot(x_l-a)}{R_l^{\,5}} - \frac{m}{R_l^{\,3}}\right\} \tag{4.13}$$

$$B_{ly} = B_T\left\{\frac{3[m(x_l-a)+n(y_l-b)+p(z_l-c)]\cdot(y_l-b)}{R_l^{\,5}} - \frac{n}{R_l^{\,3}}\right\} \tag{4.14}$$

$$B_{lz} = B_T\left\{\frac{3[m(x_l-a)+n(y_l-b)+p(z_l-c)]\cdot(z_l-c)}{R_l^{\,5}} - \frac{p}{R_l^{\,3}}\right\} \tag{4.15}$$

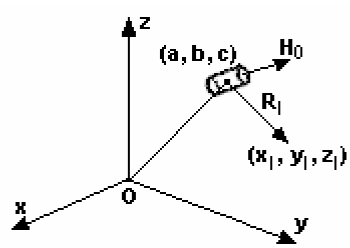

Figure 4.3 Coordinate system for magnetic localization

(magnet location is changeable with respect to a fixed coordinate system)

where $R_l = \sqrt{(x_l-a)^2 + (y_l-b)^2 + (z_l-c)^2}$,

In the proposed sensing system, the flux intensities B_{lx}, B_{ly}, and B_{lz} are measured using magnetic sensors that are arranged around (outside) the human abdomen, and $(x_l, y_l, z_l)^T$, the position of the *l*-th sensor, are known in advance. Note that there are six unknown parameters (*a, b, c, m, n, p*). The flux intensity is invariant to the rotation of the magnet along its central axis. Hence the magnet's orientation $\mathbf{H}_0$ is in two dimensions, in other words, the length of vector $(m, n, p)^T$ can be any fixed value. Therefore we add following constraint for $(m, n, p)^T$:

$$m^2 + n^2 + p^2 = 1 \tag{4.16}$$

Equations (4.13)~(4.15) show the relationship between the magnetic flux intensities at l-th sensor and the magnet location and orientation. For each sensor, we measure three magnetic intensities B_{lx}, B_{ly}, and B_{lz}. For N sensors, we obtain $3 \times N$ measured flux intensity values. Therefore, with two 3-axis magnetic sensors or five 1-axis sensors, the six parameters of the magnet location and orientation could be calculated by solving (4.13)~(4.16).

An example is shown as below with two 3-axis sensors. For the 1st sensor, let $x_1 = 0.1$, $y_1 = 0$, $z_1 = 0$, and $B_{1x} = -431.1 B_T$, $B_{1y} = -335.3 B_T$, $B_{1z} = 47.9 B_T$. For the 2nd sensor, let $x_2 = 0$, $y_2 = 0$, $z_2 = 0$, and $B_{2x} = 47.9 B_T$, $B_{2y} = 47.9 B_T$, $B_{2z} = 814.3 B_T$.

Then we have six equations as below

$$-431.1 = \frac{3\left[m(0.1-a) - nb - pc\right](0.1-a)}{\left[\sqrt{(0.1-a)^2 + b^2 + c^2}\right]^5} - \frac{m}{\left[\sqrt{(0.1-a)^2 + b^2 + c^2}\right]^3} \tag{4.17}$$

$$-335.3 = \frac{3\left[m(0.1-a) - nb - pc\right](-b)}{\left[\sqrt{(0.1-a)^2 + b^2 + c^2}\right]^5} - \frac{n}{\left[\sqrt{(0.1-a)^2 + b^2 + c^2}\right]^3} \tag{4.18}$$

$$-431.1 = \frac{3\left[m(0.1-a) - nb - pc\right](-c)}{\left[\sqrt{(0.1-a)^2 + b^2 + c^2}\right]^5} - \frac{p}{\left[\sqrt{(0.1-a)^2 + b^2 + c^2}\right]^3} \tag{4.19}$$

$$47.9 = \frac{3(ma + nb + pc)a}{\left[\sqrt{a^2 + b^2 + c^2}\right]^5} - \frac{m}{\left[\sqrt{(a)^2 + b^2 + c^2}\right]^3} \tag{4.20}$$

$$47.9 = \frac{3(ma + nb + pc)b}{\left[\sqrt{a^2 + b^2 + c^2}\right]^5} - \frac{n}{\left[\sqrt{(a)^2 + b^2 + c^2}\right]^3} \tag{4.21}$$

$$814.3 = \frac{3(ma + nb + pc)c}{\left[\sqrt{a^2 + b^2 + c^2}\right]^5} - \frac{p}{\left[\sqrt{(a)^2 + b^2 + c^2}\right]^3} \tag{4.22}$$

The six parameters can be solved by choosing five equations out of the equations (4.17)~(4.22) and (4.16). Although five sensors is the minimum to solve the 5 unknown localization/orientation parameters, more sensor can applied to get higher localization/

orientation accuracy. When N>5, the solution is not unique (in the presence of noise), and we try to obtain a solution that minimizes an objective function. Here, we define an error function corresponding to three orthogonal components of the magnetic intensity as follows:

$$E_x = \sum_{l=1}^{N} \left\{ B_{lx} - B_T \left[\frac{3\left[m(x_l - a) + n(y_l - b) + p(z_l - c)\right] \cdot (x_l - a)}{R_l^{\ 5}} - \frac{m}{R_l^{\ 3}} \right] \right\}^2 \qquad (4.23)$$

$$E_y = \sum_{l=1}^{N} \left\{ B_{ly} - B_T \left[\frac{3\left[m(x_l - a) + n(y_l - b) + p(z_l - c)\right] \cdot (y_l - b)}{R_l^{\ 5}} - \frac{n}{R_l^{\ 3}} \right] \right\}^2 \qquad (4.24)$$

$$E_z = \sum_{l=1}^{N} \left\{ B_{lz} - B_T \left[\frac{3\left[m(x_l - a) + n(y_l - b) + p(z_l - c)\right] \cdot (z_l - c)}{R_l^{\ 5}} - \frac{p}{R_l^{\ 3}} \right] \right\}^2 \qquad (4.25)$$

The total objective error is the summation of above three errors.

$$E = E_x + E_y + E_z \qquad (4.26)$$

The solution is the least square error problem that can be solved by several known optimization algorithms. When there are more equations than the number of the unknowns, we determine a solution that minimizes E as given by (4.23)~(4.26). To evaluate the performance of an algorithm, we define two parameters, localization error E_p and orientation error E_o as follows:

$$E_p = \sqrt{(a_c - a_t)^2 + (b_c - b_t)^2 + (c_c - c_t)^2} \qquad (4.27)$$

$$E_o = \sqrt{(m_c - m_t)^2 + (n_c - n_t)^2 + (p_c - p_t)^2} \qquad (4.28)$$

where $(a_c\ b_c\ c_c\ m_c\ n_c\ p_c)$ represent the calculated location and orientation parameters, and $(a_t\ b_t\ c_t\ m_t\ n_t\ p_t)$ represent the true location and orientation parameters of the magnet.

4.2 Localization and Orientation Algorithms

The Equations (4.23)~(4.25) are high-order nonlinear equations. To solve them, we can use an appropriate nonlinear minimization algorithm. There exist several nonlinear minimization algorithms, e.g., Powell's [88], Downhill Simplex [88, 89], DIRECT [90~92], Multilevel Coordinate Search [93, 94], and Levenberg-Marquardt method [95]. To choose an appropriate minimization method, following factors must be considered.

1) The nonlinear optimization algorithms normally need an initial guess of the parameters, or their bounds, to begin the search for the minimum. If the initial parameters (or bounds) are chosen with large error, the algorithms may fail to give correct (global minimization) solution because there might be many local minima. Therefore, the proposed minimization algorithm should have large tolerance of the initial guess of the parameters.

2) The minimization algorithm should be fast enough to enable real time implementation.

3) The algorithm and system implementation should be robust to the noises in the sensor data.

We compare the performance of several algorithms with respect to the localization error, orientation error, and execution time. Our main objective here is to show how these parameters change with the error level of the initial guess of the localization/orientation parameters. We do the simulation with five x-axis scheme as shown in Figure 4.4, where S_1~S_5 [S_1=(0 0 0), S_2=(0.1 0 0), S_3=(0 0.1 0), S_4=(-0.1 0 0), S_5=(0 -0.1 0)] (in meter) are the locations of the five sensors, $\mathbf{P_i}$ is the initial guess of the magnet's location, and $\mathbf{P_t}$ [we chose $\mathbf{P_t}$=(0.1, 0.1, 0.12)] is the true magnet's location. The error in the initial guess for magnet's location is d=|| $\mathbf{P_i}$-$\mathbf{P_t}$ ||. In addition, the error in the initial guess of orientation is a fixed value with an angle error 20°.

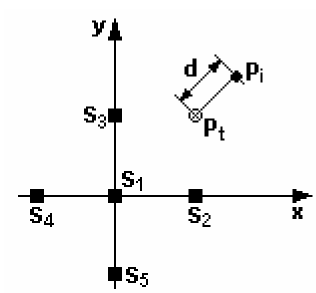

Figure 4.4 Localization using 5 sensors under initial guess of magnet's location with error *d* relative to true magnet's location. (S_1~S_5 represent sensor locations in x- and y- plane, P_t is the true magnet's location and P_i is the initial guess of the magnet's location)

4.2.1 Powell's algorithm

Powell's algorithm is a local minimization method with fast searching speed. In this algorithm, some searching directions are defined based on quadratically convergent method. With these directions, the multi-dimensional minimization problem is changed to one-dimensional search problem, and minimized parameters are found when the search along these directions is completed. However, in our trials, the calculation error of Powell's algorithm is too large to be acceptable. It is observed that the localization error, orientation error and execution time as shown in Figure 4.6, Figure 4.7, and Figure 4.8. The localization error reaches 8 cm under different error levels (0.1~20 cm) of the initial location guess. The orientation error reaches 30%. The average execution time is 0.367 second.

4.2.2 Downhill simplex algorithm

The downhill simplex method is also a local minimization method. Starting with an initial guess for the parameters, and applying operation steps, e.g. reflection, expansion, contraction and multi-contraction, the algorithm is then supposed to make its own way downhill until it encounters a minimum. As shown in Fig. 7, the results with downhill simplex method are acceptable (with localization error smaller than 5mm) only when the initial guess error is smaller then 1.7 cm. When the initial guess error is larger than 2.3 cm, the results are unacceptable. The average execution time of downhill simplex method is 0.290 second.

Both Powell's and downhill simplex methods are not appropriate for solving the problem. This is because Equations(23)-(25) are high-order nonlinear equations, such that there might exist a lot of local minima in the objective function. An example is shown in Figure 4.5, where the real magnet position is in (*a, b, c*). Assume that the searching line (for minimum) is along the y-coordinate: $b'=b+0.005$**,** and z-coordinate: $c'=c+0.001$, and also fix the orientation parameters, then the error E_x will changed with x-coordinate parameter *a',* as shown in Figure 4.5. Obviously, there are 3 minima between -*0.3 dm* and *3 dm* (*1 dm=0.1 m*). Since the local minimization methods are not suitable for multi-minima problem, we find some global optimization algorithms to solve the problem.

4.2.3 DIRECT algorithm

DIRECT is an algorithm for finding the global minimum of a multi-variant function subject to simple bounds. The algorithm is a modification of the standard Lipschitzian approach that eliminates the need to specify a Lipschitz constant. The algorithm is called DIRECT because it is a ***direct*** search technique and is an acronym for ***di****viding* ***rect****angles*, a key step in the algorithm. As shown in Figure 4.6, the localization error is smaller than 10 mm under the location level 0~20 cm of the search bounds. Also in Figure 4.7 and Figure 4.8, we can see the orientation error is within 16%, and the average execution time is 0.503 second.

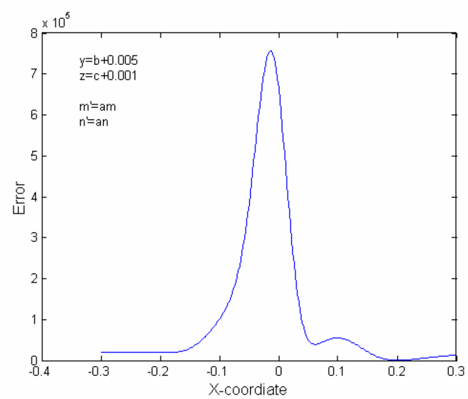

Figure 4.5 Minima in the objective error function

4.2.4 Multilevel Coordinate Search (MCS)

MCS is similar to the DIRECT method for global optimization based on multilevel coordinate search. Some shortcomings of DIRECT are remedied in MCS so that it can provide higher accuracy and faster convergence. The calculation errors using this method are pretty small. As shown in Figure 4.6 and Figure 4.7, the localization error is smaller than 0.2 mm, and orientation error is smaller than 0.5%, under different levels (0~20 cm) of the location bounds. However, the average execution time is 0.688 second, as shown in Figure 4.8, which is longer than other methods.

4.2.5 Levenberg-Marquardt method

The Levenberg-Marquardt method is a general non-linear downhill minimization algorithm. It dynamically mixes Gauss-Newton and gradient iterations. Both the

MATLAB functions "lsqnonlin", the nonlinear least squares solution, and "fsolve", solving for roots of the nonlinear equations, can provide the calculation of Levenberg-Marquardt method. In our simulations, we have found that "lsqnonlin" provides a marginally better accuracy than "fsolve". Excellent localization and orientation accuracy is obtained with this algorithm. As shown in Figure 4.6 and Figure 4.7, the localization and orientation errors are zero when the error levels of the initial guess of location are within 20 cm. Moreover, the method provides faster execution speed, as shown in Figure 4.8. The average execution time is 0.106 second.

Comparing above results, we can conclude that:

1) The local minimization methods, e.g. Powell's and downhill simplex, are not suitable because Powell's method results in large error and downhill simplex has too small tolerance for initial guess parameters.
2) The global minimization methods, e.g. DIRECT and MCS, can provide high search accuracy, but their execution speed is low.
3) The Levenberg-Marquardt method is an appropriate algorithm for our case. It provides satisfactory tolerance for initial guess parameters, and faster speed (<0.11 Second).

4.3 Simulation for de-noising ability

The techniques discussed in section 4.2 are typically valid when there is no noise in the sensors. However, in a practical system, there are always some noises due to the influences of human body and the environment. In this section, we present the simulation results for de-noising abilities of different sensor arrays. We use the MATLAB function "lsqnonlin" (Levenberg-Marquardt method) to perform the optimization. Although five sensors is the minimum to solve the 5 unknown localization/ orientation parameters, the noise response of 5-sensor implementation is often unacceptable. The noise distribution is close to the normal distribution (be discussed in Chapter 6). Here, to simplify the problem in the simulation program, we use noise with uniform distribution, which is a stricter condition than that of normal distribution. Figure 4.11 shows the localization and orientation errors using 5-sensors via noise level 0.1 to 25 (25 is about 2~3 % full sensing

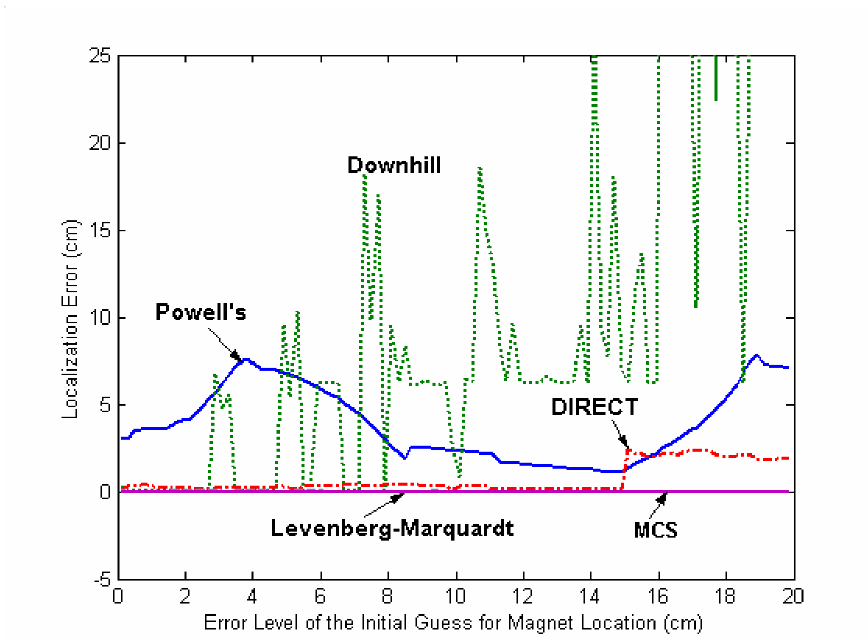

Figure 4.6 Localization errors of minimization algorithms under different error level of the initial guess of magnet location. Note that MCS and Levenberg-Marquardt methods have very small localization errors (<0.5 mm)

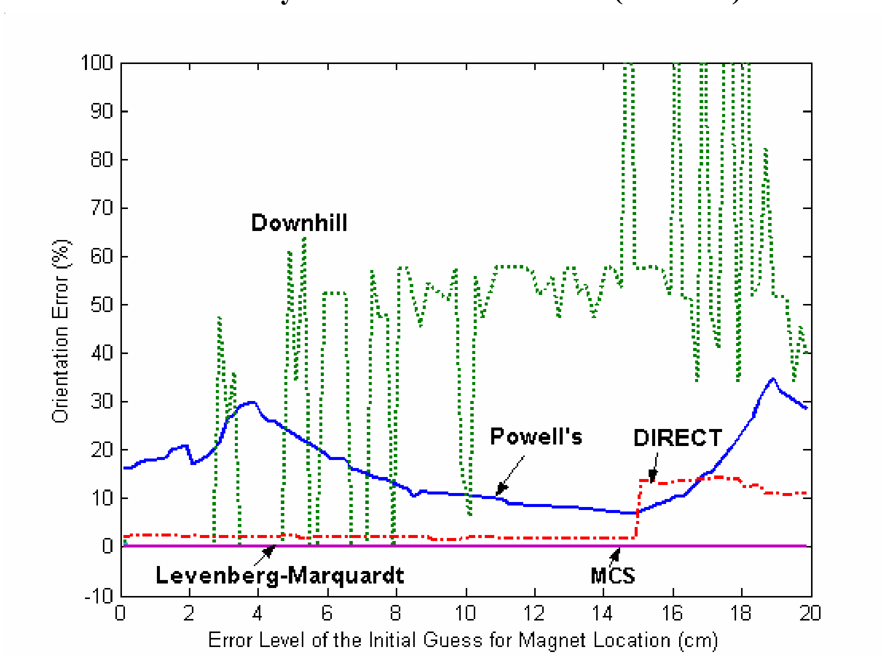

Figure 4.7 Orientation errors of minimization algorithms under different error level of the initial guess of magnet location. Note that MCS and Levenberg-Marquardt methods have very small orientation errors (<0.5%). Here orientation error is defined by (4.28) and error of 100% is equal to 60°.

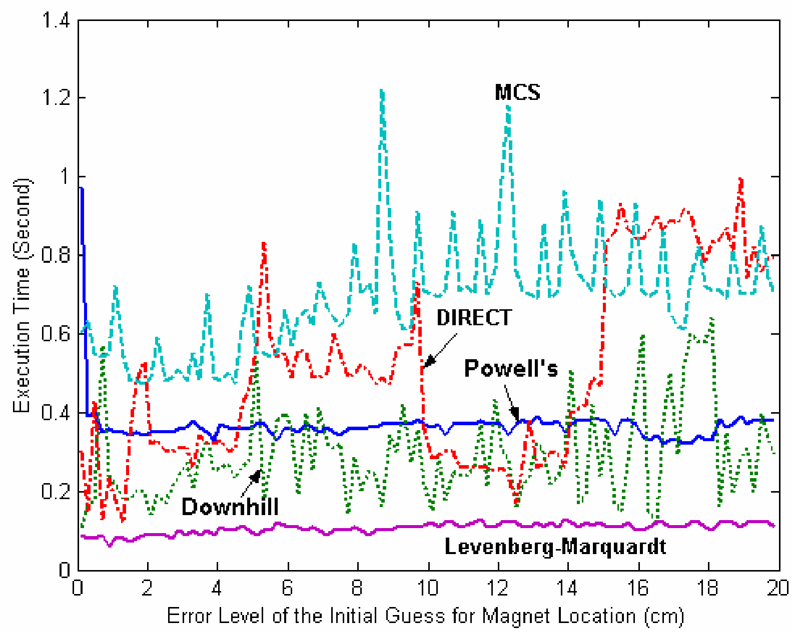

Figure 4.8 Execution time (Second) of minimization algorithms under different error level of the initial guess of magnet location.

range). The localization error might reach 200 mm. To improve the accuracy, we use a denser sensor arrangement to do the localization. In our implementation, nine and sixteen 1-, 2-, and 3-axis sensors are also tried. For nine-sensor case, the sensors are uniformly arranged on the 200mm×200mm square area as shown in Figure 4.9, whereas for 16-sensors' case, the sensors are uniformly arranged on the 240mm×240mm square area as shown in Figure 4.10. Table 4.1 shows the resulting average localization/orientation errors via levels (0.1~25) of random noises. Figure 4.12~4.14 show the localization and orientation errors with five, nine, and sixteen 3-axis sensors. It is observed that higher localization accuracy is obtained with larger number of sensors. For the case of sixteen 3-axis sensors, the localization error is within 15mm and the average errors are 4.6mm for localization and 4.5% for orientation.

4.4 Shortcomings of the nonlinear algorithms

In above sections, we present to determine the localization/orientation parameters of the magnet by the nonlinear optimization algorithms. Although a properly selected algorithm can be applied to the localization and orientation system, the nonlinear algorithm has its limitations:

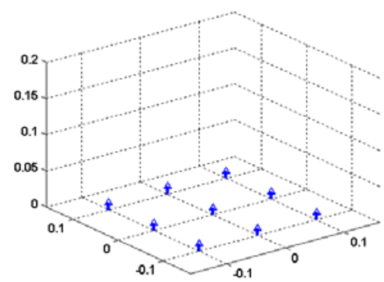

Figure 4.9 Nine sensor distribution

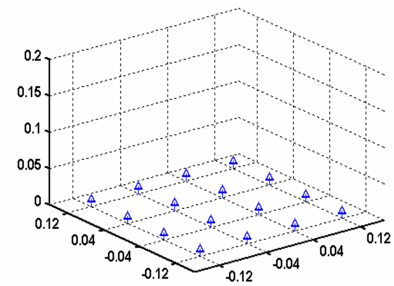

Figure 4.10 Sixteen sensor distribution

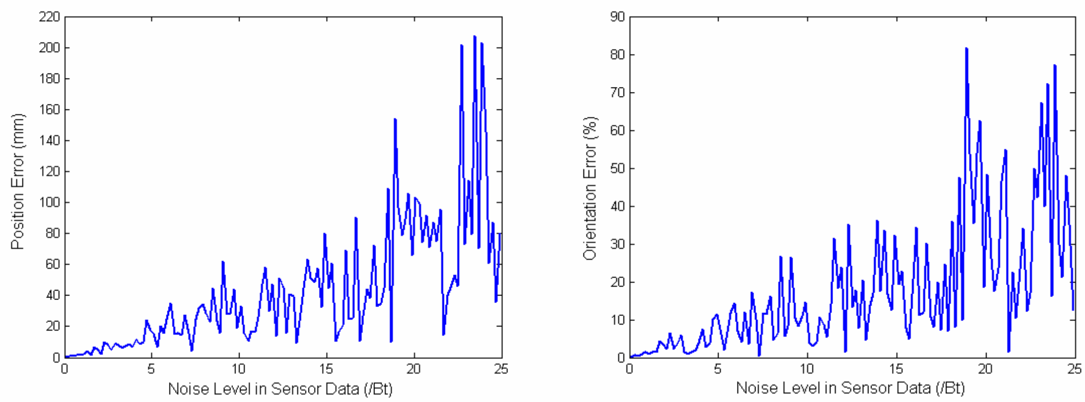

(a) Localization error **(b) Orientation error (90% ≈ 54°)**

Figure 4.11 Localization and orientation error via noise level using five 1-axis (x-axis) sensors

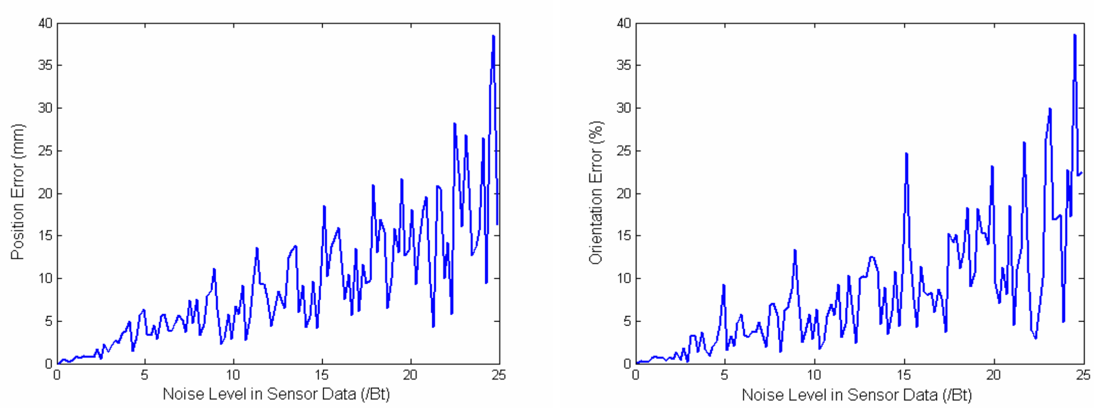

(a) Localization error **(b) Orientation error (40% ≈ 23°)**

Figure 4.12 Localization and orientation error via noise level using five 3-axis sensors

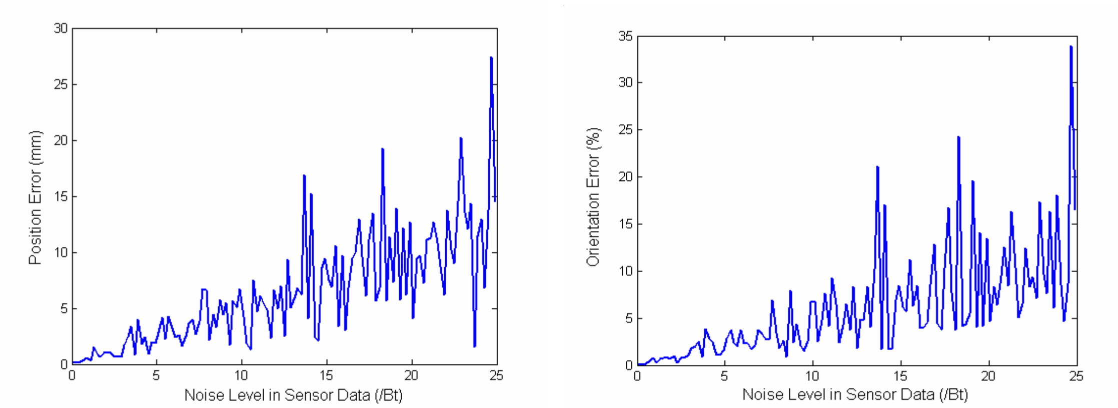

(a) Localization error **(b) Orientation error (35% ≈ 20°)**

Figure 4.13 Localization and orientation error via noise level using nine 3-axis sensors

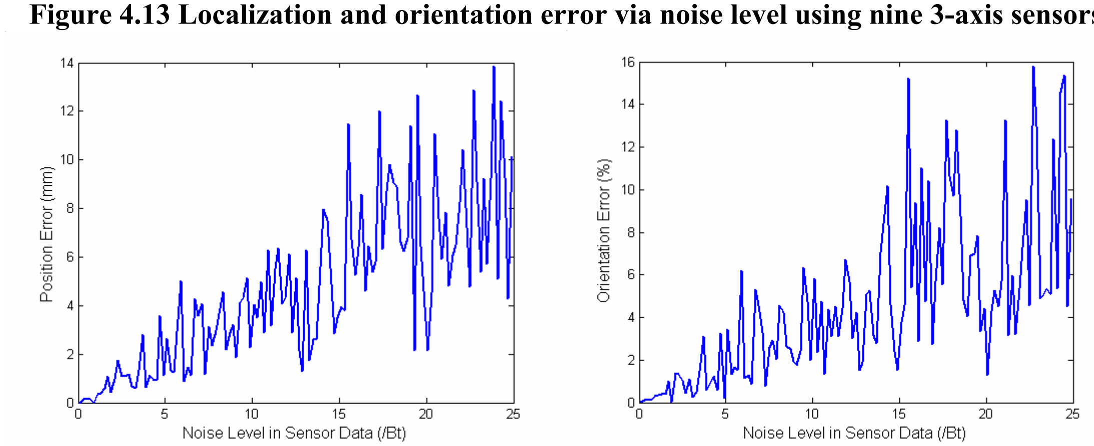

(a) Localization error **(b) Orientation error (16% ≈ 9.2°)**

Figure 4.14 Localization and orientation error via noise level using sixteen 3-axis sensors

Table 4.1 Average Localization/Orientation Errors via Noise Level 0.1:0.2:25

	1-axis sensor (x-axis)	2-axis sensor (x- & y-axes)	3-axis sensor (x-, y-, z-axes)
5-sensors	42.7mm; 17.9%	16.8mm; 16.6%	9.1mm; 8.2%
9-sensors	26.4mm; 27.1%	10.8mm; 9.3%	6.4mm; 6.0%
16-sensors	14.2mm; 15.8%	6.6mm; 5.8%	4.6mm; 4.5%

1) The optimization algorithm always needs some good initial guess or bounds for searching the global solution. Otherwise, they might fail to give correct solution. Figure

4.15 and Figure 4.16 show the searching (localization and orientation) errors of Levenberg-Marquardt method via initial guess of position and orientation. It is observed that the localization/orientation error is near zero when initial guess of position is within (*-9cm, 20cm*), or initial guess of orientation is within 155°. However, the algorithm fails to give correct solution when the initial guess of position is lower than -9 cm, or initial guess of orientation is larger than 155°. Although these values are relatively large so that we can adopt some measures to avoid its occurrence, we cannot say this algorithm will always be correct.

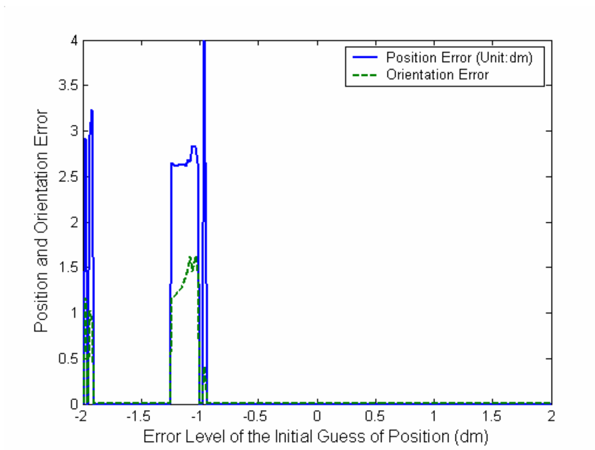

Figure 4.15 Searching errors via initial guess of position

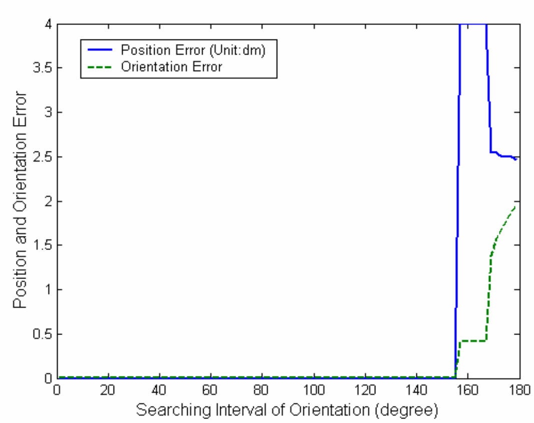

Figure 4.16 Searching errors via initial guess of orientation

2) Nonlinear optimization algorithms use space division, gradient, or downhill searching techniques, and the solution is found by recursions. Because the magnetic localization and orientation is related to 5D problem, the computation complexity is high.

3) The execution speed of the nonlinear algorithm might be too slow, (around 100 millisecond, as shown in Figure 4.8), to be applied to real time signal processing and the tracking of the magnet.

Therefore, a more fast, robust localization/orientation algorithm is desirable, and in the next chapter, we introduce a linear algorithm that does not need the initial guess of the parameters and can provide much faster execution speed.

4.5 Conclusion

The magnetic flux density at a spatial point created by a permanent magnet can be defined by equation $\mathbf{B}_l = B_{lx}\vec{\mathbf{v}}_X + B_{ly}\vec{\mathbf{v}}_Y + B_{lz}\vec{\mathbf{v}}_Z = B_T\left(\frac{3(\mathbf{H}_0 \cdot \mathbf{P})\mathbf{P}}{R^5} - \frac{\mathbf{H}_0}{R^3}\right)$ $(l = 1, 2, \cdots, N)$. In the magnetic localization and orientation system, we measure 3 components B_{lx}, B_{ly}, and B_{lz} of the magnetic flux, using some magnetic sensors. Then, we can calculate the localization/orientation parameters (*a, b, c, m, n, p*) inversely by a nonlinear optimization method to minimize the objective (square) error function.

Several nonlinear optimization algorithms can be applied to solve such a problem, e.g., Powell's, Downhill Simplex, DIRECT, Multilevel Coordinate Search (MCS), and Levenberg-Marquardt method. With the simulation results, we find that Levenberg-Marquardt method is the best, with respect to localization and orientation accuracy and the execution speed. We evaluate de-noising ability of algorithms. On the simulation results on the arrays with five 1-axis, five 3-axis, nine 3-axis, and sixteen 3-axis sensors, it is found that the localization and orientation accuracy is much improved with more sensor number.

Chapter 5

Linear Algorithm for Magnetic Localization and Orientation

Although it is possible to find the solution of the magnet's localization and orientation by the nonlinear methods discussed in Chapter 4, the nonlinear algorithms do need some good initial guess or bounds for searching the global solution. Otherwise, they might fail to give correct solution. Another problem of the nonlinear algorithm is its high computation complexity such that the execution speed might be too slow for system to apply signal processing and realize fast tracking of the magnet.

The above problems companied with nonlinear algorithms can be solved by introducing a linear algorithm. In the linear algorithm, some types of unknowns relative to (or including) magnet's location parameters *a, b, c,* and orientation parameters *m, n, p,* can be solved using matrix computation. Therefore, in most situations, the solution is unique unless singularity occurs. Furthermore, the execution speed is fast because the main computation is to find the inverse of the matrix. In this chapter, a new linear algorithm is proposed for solving 5D magnet's position and orientation parameters. In section 5.1, I propose the linear algorithm, its derivation and calculation steps. In section 5.2 I give some examples and singularity analysis. In section 5.3, I present the simulation results for the algorithm's de-noise ability and some signal processing methods, and followed by the conclusion in section 5.4.

5.1 Linear Localization and Orientation Algorithm

The magnetic flux density in the position of the i^{th} sensor group is given by (4.11)

$$\mathbf{B}_l = B_{lx}\vec{\mathbf{v}}_X + B_{ly}\vec{\mathbf{v}}_Y + B_{lz}\vec{\mathbf{v}}_Z = B_T\left(\frac{3(\mathbf{H_0}\cdot\mathbf{P}_l)\mathbf{P}_l}{R_l^{\,5}} - \frac{\mathbf{H_0}}{R_l^{\,3}}\right) \qquad (l=1,2,\ldots,N) \qquad (5.1)$$

As mentioned in Chapter 4, the magnetic orthogonal components B_{lx}, B_{ly}, and B_{lz} can be measured through some 3-axis magnetic sensors; and $(x_l, y_l, z_l)^T$, the positions of the sensors, are known in advance. If the position differences among the x, y, and z sensing elements in each of the 3-axis sensor are negligible, we can build a linear model to solve the 6 parameters of the magnet's position and orientation.

5.1.1 Derivation of the linear model

Cross product of (5.1) with $\mathbf{P}_l$, we have

$$\mathbf{B}_l \times \mathbf{P}_l = -B_T \frac{\mathbf{H_0} \times \mathbf{P}_l}{R_l^3} \qquad l = (1, 2, \cdots N)$$

Then, dot product of above equation with $\mathbf{H_0}$, we have

$$(\mathbf{B}_l \times \mathbf{P}_l) \cdot \mathbf{H_0} = 0 \qquad l = (1, 2, \cdots N) \tag{5.2}$$

That is

$$\begin{pmatrix} B_{lx} \\ B_{ly} \\ B_{lz} \end{pmatrix} \times \begin{pmatrix} x_l - a \\ y_l - b \\ z_l - c \end{pmatrix} \cdot \begin{pmatrix} m \\ n \\ p \end{pmatrix} = 0 \qquad l = (1, 2, \cdots N) \tag{5.3}$$

such that

$$\begin{aligned} &B_{lx}bp - B_{lx}y_l p + B_{lx}z_l n - B_{lx}cn + B_{ly}cm - B_{ly}z_l m + B_{ly}x_l p \\ &- B_{ly}ap + B_{lz}an - B_{lz}x_l n + B_{lz}y_l m - B_{lz}bm = 0 \end{aligned} \qquad (l = 1, 2, \cdots N) \tag{5.4}$$

The equation can be further simplified as

$$[(B_{lx} \;\; B_{ly} \;\; B_{lz} \;\; (B_{lz}y_l - B_{ly}z_l)\,(B_{lx}z_l - B_{lz}x_l))] \begin{bmatrix} b - cn' \\ cm' - a \\ an' - bm' \\ m' \\ n' \end{bmatrix} = B_{lx}y_l - B_{ly}x_l \qquad (l = 1, 2, \cdots N) \tag{5.5}$$

where $m'=m/p$, $n'=n/p$. This is a linear equation with unknown variables $(b - cn')$, $(cm' - a)$, $(an' - bm')$, m', and n'. With five 3-axis sensors, these variables can be solved, and then *a, b, c, m, n,* and *p* can further be solved, too.

Define a vector $\mathbf{\Gamma} = \begin{bmatrix} r_1 & r_2 & r_3 & r_4 & r_5 \end{bmatrix}^T = \begin{bmatrix} b - cn' & cm' - a & an' - bm' & m' & n' \end{bmatrix}^T$, and a matrix $\mathbf{\Omega}$ with elements $s_{l1} = B_{lx}$, $s_{l2} = B_{iy}$, $s_{l3} = B_{lz}$, $s_{l4} = B_{lz} y_l - B_{ly} z_l$, $s_{l5} = B_{lx} z_l - B_{lz} x_l$, (for *l=1…5*), and a vector $\overline{\mathbf{T}} = \begin{bmatrix} t_1 & t_2 & t_3 & t_4 & t_5 \end{bmatrix}^T$ with $t_l = B_{lx} y_l - B_{ly} x_l$ (for *l=1…5*). We can get the solution

$$\mathbf{\Gamma} = \mathbf{\Omega}^{-1} \overline{\mathbf{T}} \tag{5.6}$$

One property of (5.5) is that it is irrelevant to the magnetization of the magnet and the relative permeability μ_r of the medium. So the results solved from (5.5) are relatively more accurate. The cost of this method is that more (five 3-axis) magnetic sensors are required. In case that $\mathbf{\Omega}$ is singular, we define n*'=n/m*, and p*'=p/m*, and the model is modified as

$$[(B_{lx}\ B_{ly}\ B_{lz}\quad (B_{lx} z_l - B_{lz} x_l)\ (B_{ly} x_l - B_{lx} y_l))] \begin{bmatrix} bp' - cn' \\ c - ap' \\ an' - b \\ n' \\ p' \end{bmatrix} = B_{ly} z_l - B_{lz} y_l \quad (l = 1, 2, \cdots N) \tag{5.7}$$

Or define m*'=m/n*, and p*'=p/n*, and we have

$$[(B_{lx}\ B_{ly}\ B_{lz}\quad (B_{lz} y_l - B_{ly} z_l)\ (B_{ly} x_l - B_{lx} y_l))] \begin{bmatrix} bp' - c \\ cm' - ap' \\ a - bm' \\ m' \\ p' \end{bmatrix} = B_{lz} x_l - B_{lx} z_l \quad (l = 1, 2, \cdots N) \tag{5.8}$$

5.1.2 Linear Algorithm for Magnetic Sensor Array

Although five 3-axis magnetic sensors are sufficient for the solution, more sensors are preferable for higher accuracy, because there are interferences in the signals of the magnetic sensors, especially in the case of weak magnetic signal, or low SNR (Signal to Noise ratio). From (5.1), we know that magnetic intensity is an inverse function of power of three of the distance from the magnet to the sensors. In order to obtain stronger signals for higher SNR, we need to control the distance with more densely distributed sensors, and the sensor array scheme is an appropriate approach.

Assume there are totally N ($N \geq 5$) sensor groups, from (5.6) we define the calculation error in the summation of square error:

$$E = \sum_{i=1}^{N} (s_{l1}r_l + s_{l2}r_2 + s_{l3}r_3 + s_{l4}r_4 + s_{l5}r_5 - t_l)^2 \tag{5.9}$$

The optimal solution for $\mathbf{\Gamma} = [r_1 \ \ r_2 \ \ r_3 \ \ r_4 \ \ r_5]^T$, which make E minimum is

$$\mathbf{\Gamma} = \mathbf{\Omega}_B^{-1} \cdot \overline{\mathbf{T}}_L \tag{5.10}$$

where the elements of $\mathbf{\Omega}_B$ are defined by $s_{B\,lk} = \sum_{l=1}^{N} s_{lj} \cdot s_{lk}$ *(j=1…5; k=1…5; N≥5)* and the elements of $\overline{\mathbf{T}}_L$ are defined by $t_{Lj} = \sum_{l=1}^{N} t_l m_{lj}$ (j=1…5).

5.1.3. Solution for Magnet Position (a, b, c) and Orientation (m, n, p)

Now we have that the solution $\mathbf{\Gamma} = [r_1 \ \ r_2 \ \ r_3 \ \ r_4 \ \ r_5]^T$. Since $m' = r_4$, $n' = r_5$ *and* $m^2 + n^2 + p^2 = (m'p)^2 + (n'p)^2 + p^2 = 1$, we get the orientation (*m, n, p*)

$$p = \pm \frac{1}{\sqrt{1 + r_4^2 + r_5^2}} \tag{5.11}$$

$$m = r_4 p \tag{5.12}$$

$$n = r_5 p \tag{5.13}$$

Here, the orientation parameters (*m, n, p*) might have the positive or negative symbols. We will discuss how to determine it a little later. For the solution of magnet position (*a, b, c*), from (5.5) we have

$$\begin{bmatrix} 0 & 1 & -n' \\ -1 & 0 & m' \\ n' & -m' & 0 \end{bmatrix} \begin{bmatrix} a \\ b \\ c \end{bmatrix} = \begin{bmatrix} r_1 \\ r_2 \\ r_3 \end{bmatrix} \tag{5.14}$$

We observe that the matrix is singular, and

$$a r_1 + b r_2 + c r_3 = 0 \tag{5.15}$$

Obviously, one parameter, among *a, b, c*, can be represented by the linear combination of two other parameters. We also observe that the matrix's rank is two, so we can get two independent equations

$$a = r_4 \cdot c - r_2 \tag{5.16}$$

$$b = r_1 + r_5 \cdot c \tag{5.17}$$

To solve the parameters (*a, b, c*), we should find another equation. From (4.13)~(4.15), we have

$$B_{lx} = B_T \left\{ \frac{3[m(x_l - a) + n(y_l - b) + p(z_l - c)] \cdot (x_l - a)}{R_l^5} - \frac{m}{R_l^3} \right\} \tag{5.18}$$

$$B_{ly} = B_T \left\{ \frac{3[m(x_l - a) + n(y_l - b) + p(z_l - c)] \cdot (y_l - b)}{R_l^5} - \frac{n}{R_l^3} \right\} \tag{5.19}$$

$$B_{lz} = B_T \left\{ \frac{3[m(x_l - a) + n(y_l - b) + p(z_l - c)] \cdot (z_l - c)}{R_l^5} - \frac{p}{R_l^3} \right\} \tag{5.20}$$

Dividing (5.18) and (5.19) with (5.20), we get

$$\begin{aligned} &B_{lx}\{3[m(x_l - a) + n(y_l - b) + p(z_l - c)] \cdot (z_l - c) - R_l^2 p\} \\ &= B_{lz}\{3[m(x_l - a) + n(y_l - b) + p(z_l - c)] \cdot (x_l - a) - R_l^2 m\} \end{aligned} \quad (l=1,2,\ldots N) \tag{5.21}$$

$$\begin{aligned} &B_{ly}\{3[m(x_l - a) + n(y_l - b) + p(z_l - c)] \cdot (z_l - c) - R_l^2 p\} \\ &= B_{lz}\{3[m(x_l - a) + n(y_l - b) + p(z_l - c)] \cdot (y_l - b) - R_l^2 n\} \end{aligned} \quad (l=1,2,\ldots N) \tag{5.22}$$

Substitute (5.16) and (5.17) into (5.21), we get a 2-order equation with one unknown variable *c*

$$\kappa_{2l} c^2 + \kappa_{1l} c + \kappa_{0l} = 0 \qquad (l=1,\ 2,\ \ldots\ N) \tag{5.23}$$

where κ_{2l}, κ_{1l}, and κ_{0l} are functions of the known parameters $[r_1\ r_2\ r_3\ r_4\ r_5]^T$, sensor positions $(x_l, y_l, z_l)^T$, and measurable data (B_{lx}, B_{ly}, B_{lz}).

A. Solve the unknown by selecting 2 equations

If κ_{2l} is zero, we can directly get

$$c = -\frac{\kappa_{0l}}{\kappa_{1l}} \tag{5.24}$$

If κ_{2l} are not zero, we can get

$$c^2 + \kappa_{1l}/\kappa_{2l} \cdot c + \kappa_{0l}/\kappa_{2l} = 0 \tag{5.25}$$

Select any two equations (let *l=i and j*), and then we have $c^2 + \kappa_{1i}/\kappa_{2i} \cdot c + \kappa_{0i}/\kappa_{2i} = 0$ and $c^2 + \kappa_{1j}/\kappa_{2j} \cdot c + \kappa_{0j}/\kappa_{2j} = 0$. Then solve them for c:

$$c = -(\frac{\kappa_{0i}}{\kappa_{2i}} - \frac{\kappa_{0j}}{\kappa_{2j}})/(\frac{\kappa_{1i}}{\kappa_{2i}} - \frac{\kappa_{1j}}{\kappa_{2j}}) \tag{5.26}$$

If $(\frac{\kappa_{1i}}{\kappa_{2i}} - \frac{\kappa_{1j}}{\kappa_{2j}}) \neq 0$, c exists.

B. Solve the unknown by optimal (least square error) algorithm

A more accurate method to determine *c* is to apply optimal (least square error) method. We already have equation (5.23). Substitute (5.16) and (5.17) into (5.22), we get another equation

$$\hat{\kappa}_{2l}c^2 + \hat{\kappa}_{1l}c + \hat{\kappa}_{0l} = 0 \qquad (l=1,\ 2,\ \ldots\ N) \tag{5.27}$$

Define error to be

$$E = \sum_{l=1}^{N}[(\kappa_{2l}c^2 + \kappa_{1l}c + \kappa_{0l})^2 + (\hat{\kappa}_{2l}c^2 + \hat{\kappa}_{1l}c + \hat{\kappa}_{0l})^2] \tag{5.28}$$

Take derivative of *E* via *c,* we have

$$\begin{aligned}\frac{\partial E}{\partial c} = 2[2(\sum_{i=1}^{N}\kappa_{2l}^2 + \hat{\kappa}_{2l}^2)c^3 + 3[\sum_{i=1}^{N}(\kappa_{2l}\kappa_{1l} + \kappa_{2l}\kappa_{1l})]c^2 \\ + \sum_{i=1}^{N}(\kappa_{1l}^2 + 2\kappa_{2l}\kappa_{0l} + \hat{\kappa}_{1l}^2 + 2\hat{\kappa}_{2l}\hat{\kappa}_{0l})c + \sum_{i=1}^{N}(\kappa_{1l}\kappa_{0l} + \hat{\kappa}_{1l}\hat{\kappa}_{0l})]\end{aligned} \tag{5.29}$$

To get minimum value of *E*, let $\partial E/\partial c = 0$, and solve it for *c*, we get 3 roots, which normally includes two imaginary roots and one real root. So we get the solution with

a) Choose solution to be the real root if there are two imaginary roots;

b) If all three roots are real, substitute these 3 roots into (26), we can find the solution the one with the minimum value of E.

With this c, we can compute a and b by (5.16) and (5.17).

5.1.4 Determination of the Symbol of the Orientation

From (5.11), we know that the resultant orientation parameter p (and m, n) could be positive or negative. This is not true in real case, where the magnet has its unique magnetic direction from one surface to another surface. Hence, we need to determine the symbol of the orientation. Here, we first show that the symbol of the orientation does not affect the calculation of the location parameters (a, b, c).

Using $r_4 = \dfrac{m}{p}$ and $r_5 = \dfrac{n}{p}$, equations (5.21) and (5.22) can be rewritten as

$$\begin{aligned} & B_{lx}\{3[r_4(x_l-a)+r_5(y_l-b)+(z_l-c)]\cdot(z_l-c)-R_l^2\} \\ & \quad = B_{lz}\{3[r_4(x_l-a)+r_5(y_l-b)+(z_l-c)]\cdot(x_l-a)-R_l^2 r_4\} \end{aligned} \tag{5.30}$$

$$\begin{aligned} & B_{ly}\{3[r_4(x_l-a)+r_5(y_l-b)+(z_l-c)]\cdot(z_l-c)-R_l^2\} \\ & \quad = B_{lz}\{3[r_4(x_l-a)+r_5(y_l-b)+(z_l-c)]\cdot(y_l-b)-R_l^2 r_5\} \end{aligned} \tag{5.31}$$

Because (a, b, c) are calculated using these two equations and the solution of $[r_1 \ r_2 \ r_3 \ r_4 \ r_5]^T$, the symbol of p does not affect the calculation results of (a, b, c).

Now, we can determine the symbol of the orientation (m, n, p) by using the results of (a, b, c) and (r_4, r_5). We define and calculate

$$\widehat{B}_{lx} = \frac{3[r_4(x_l-a)+r_5(y_l-b)+(z_l-c)]\cdot(x_l-a)}{R_l^{\,5}} - \frac{r_4}{R_l^{\,3}} \qquad (l=1,2,\ldots N) \tag{5.32}$$

$$\widehat{B}_{ly} = \frac{3[r_4(x_l-a)+r_5(y_l-b)+(z_l-c)]\cdot(y_l-b)}{R_l^{\,5}} - \frac{r_5}{R_l^{\,3}} \qquad (l=1,2,\ldots N) \tag{5.33}$$

$$\widehat{B}_{lz} = \frac{3[r_4(x_l-a)+r_5(y_l-b)+(z_l-c)]\cdot(z_l-c)}{R_l^{\,5}} - \frac{1}{R_l^{\,3}} \qquad (l=1,2,\ldots N) \tag{5.34}$$

From (5.18)~(5.20), we have

$$\frac{B_{lx}}{B_T} = p\widehat{B}_{lx} \tag{5.35}$$

$$\frac{B_{ly}}{B_T} = p\widehat{B}_{ly} \tag{5.36}$$

$$\frac{B_{lz}}{B_T} = pB_{lz} \tag{5.37}$$

Then, it is clear that

$$\sum_{l=1}^{N}[\frac{B_{lx}}{B_T}p\widehat{B}_{lx} + \frac{B_{ly}}{B_T}p\widehat{B}_{ly} + \frac{B_{lz}}{B_T}p\widehat{B}_{lz}] = p\sum_{l=1}^{N}[\frac{B_{lx}}{B_T}\widehat{B}_{lx} + \frac{B_{ly}}{B_T}\widehat{B}_{ly} + \frac{B_{lz}}{B_T}\widehat{B}_{lz}] \geq 0 \tag{5.38}$$

Therefore, the symbol can be determined as: if $\sum_{l=1}^{N}[\frac{B_{lx}}{B_T}\widehat{B}_{lx} + \frac{B_{ly}}{B_T}\widehat{B}_{ly} + \frac{B_{lz}}{B_T}\widehat{B}_{lz}] \geq 0$, $p\geq 0$; else $p<0$. When the symbol of p is determined, the symbols of m and n can also be adjusted, and all the six localization/orientation parameters (a, b, c, m, n, p) are solved.

5.2 Example and singularity analysis

An example is for five 3-axis sensors to be applied to the localization and orientation. The positions of the five sensors are located in S_1=(0 0 0), S_2=(0.1 0.1 0), S_3=(-0.1 0.1 0), S_4=(-0.1 -0.1 0), and S_5=(0.1 -0.1 0) (in meter). Figure 5.1 shows sensor distribution in x-y plane and the magnet M's position and orientation is assumed to be [0.05, 0.055, 0.12, -0.7071, 0.7071, 0]. From (5.18)~(5.20), we get 5-sensor outputs (relative to B_T):

$$\mathbf{B}_1 = [B_{1x}\ B_{1y}\ B_{1z}]^T = [260.88\ \ -241.00\ \ 22.71]^T$$

$$\mathbf{B}_2 = [B_{2x}\ B_{2y}\ B_{2z}]^T = [260.84\ \ -281.29\ \ 25.83]^T$$

$$\mathbf{B}_3 = [B_{3x}\ B_{3y}\ B_{3z}]^T = [-115.49\ \ -29.80\ \ -166.05]^T$$

$$\mathbf{B}_4 = [B_{4x}\ B_{4y}\ B_{4z}]^T = [48.76\ \ -45.23\ \ 1.39]^T$$

$$\mathbf{B}_5 = [B_{5x}\ B_{5y}\ B_{5z}]^T = [21.23\ \ 113.53\ \ 154.02]^T$$

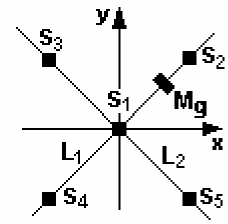

Figure 5.1 Sensor distribution in x-y plane

Using the sensor positions and above sensor outputs, we get the matrix $\overline{\mathbf{S}}$ in (5.6), or $\overline{\mathbf{S}}_B$ in (5.10). Either $\overline{\mathbf{S}}$ or $\overline{\mathbf{S}}_B$ is singular because *p=0,* such that *m'*(=*m/p*) and *n'*=(*n/p*) are infinite. Hence we cannot obtain the correct solution using (5.6) or (5.10). Here, we adopt (5.7), and the solutions of $[r_1\ r_2\ r_3\ r_4\ r_5]^T$ is [*0.1200 0.1200 -0.1050 -1.0000 -0.0000*]$^{\mathrm{T}}$. Then the orientation is calculated as

$$m = \frac{1}{\sqrt{1 + r_4^2 + r_5^2}} = 0.7071;$$

$$n = r_4 m = -0.7071;$$

$$p = r_5 m = 0;$$

where the symbol of orientation is wrong, and we will adjust it later. With this orientation, we calculate the parameter *a* by the optimal algorithm (5.29). Three roots are 0.0756 + 0.2309i, 0.0756- 0.2309i, and 0.0500. Choose the solution to be the real root, we obtain the parameter *a=0.05*. Then, other 2 position parameters can be solved as: $b = r_4 a - r_3 = 0.055$, and $c = r_5 a + r_2 = 0.12$. These values (*a, b, c*) are the same as the assumed magnet position. With these parameters, we can determine the symbol of the orientation using (5.32)~(5.34), and $\sum_{l=1}^{5}[\frac{B_{lx}}{B_T}\widehat{B}_{lx} + \frac{B_{ly}}{B_T}\widehat{B}_{ly} + \frac{B_{lz}}{B_T}\widehat{B}_{lz}] = -5.0596E+05$ <0, such that *m* is negative. That is

$$m = -0.7071;$$

$$n = r_4 m = 0.7071;$$

$$p = r_5 m = 0;$$

Therefore, the resultant localization and orientation parameters are $[0.05 \quad 0.055 \quad 0.120 \quad -0.707 \quad 0.707 \quad 0.000]$, which are exactly same as those assumed.

From this example, we can see that the problem of singularity can be solved by choosing equation of (5.5), or (5.7), or (5.8). However, we also found that in some special cases, singularity (or close to singularity) might occur in all the matrices formed by (5.5), or (5.7), or (5.8). For example, the singularity occurs in case that following conditions are conformed:

1) 5 sensors are arranged symmetrically in the center and four corners of a square, as that shown in Figure 5.1;

2) The magnet Mg's position is at the line L_1, or L_2, which connects three sensors**;**

3) The magnet's orientation conforms to $m=\pm n$ and $p=0$, or $m=n=0$.

Because singularity brings about wrong results or large error, we must find a method to avoid its occurrence. Following approaches can be applied:

1) Adjust the sensor positions such that no single line can connect three sensors in the x-y plane;

2) Add one (or more) sensor whose position is different from 5 sensors in the x-y plane. To show this, we add a sensor whose position is in (0.2 0 0.01). Then the condition number of the matrix $\overline{\mathbf{S}}_B$ formed by (5.7) is 673.43 changed from that of the infinite, and the correct solution can be obtained. Further, if there are six or more sensors, we can obtain six equations defined by (5.4), and solve the problem by the least square error method, such that the singular problem can be avoided.

3) Use new reduced order equations. In real application, there are always some noises in the sensor signals, such that the singularity will not happen. If we find large condition number and one orientation component (assume it to be p) is close to zero, substitute p with 0 into (5.4) we have

$$B_{lx}z_l n - B_{lx}cn + B_{ly}cm - B_{ly}z_l m + B_{lz}an - B_{lz}x_l n + B_{lz}y_l m - B_{lz}bm = 0 \tag{5.39}$$

Define n'=n/m, we get reduced order equation

$$[(B_{lx} \quad B_{ly} \quad B_{lz} \quad (B_{lx} z_l - B_{lz} x_l) \begin{bmatrix} -cn' \\ c \\ an' - b \\ n' \end{bmatrix} = B_{ly} z_l - B_{lz} y_l \qquad (l=1,\ldots N) \tag{5.40}$$

With 4 (out of *N*) above equations, we can solve for *c, an'-b,* and *n'*, and then for (*a, b, c*) and (*m, n*).

5.3 Simulation

5.3.1 De-noise ability of the sensor array

The algorithm was tested in Matlab with the simulation programs. To evaluate the de-noise ability of the algorithm, the random noise (uniform distribution as shown in Figure 5.2) was added in the simulated sensor signals (B_{lx}, B_{ly} and B_{lz}). The algorithm was run under different number of 3-axis sensors. For 5-sensor case, the sensors are arranged on a square plane with 200mm×200mm size, as that shown in Figure 5.1. For 9-sensor case and 16-sensor case, the sensors distributions are shown in Figure 4.9 and Figure 4.10. Figure 5.3 shows the resultant localization and orientation error E_P and E_O (defined by (4.27) and (4.28)) corresponding to different noise level (with respect to the magnet's constant B_T). We observe that, for 5-sensor case, the error can be acceptable when the noise level is smaller than 10, but it is too large for the noise level exceeds 20, in which the localization error is over 15mm. For the 9-sensor case, the accuracy is much improved, and for 16-senosr case, the localization/orientation error is within 3mm/4% for the noise level smaller than 65.

The accuracy can be improved using some signal processing methods. A simple method is the averaging technique (or fitting technique discussed later). Figure 5.4 shows simulation results of by averaging 100 samples of each the localization and orientation parameter (*a, b, c, m, n, p*). We can see that the accuracy is improved pretty much. The localization (position) errors are within 23mm, 2.5mm, and 0.35mm, and orientation errors are within 23%, 2.6%, and 0.7%, for 5, 9, and 16-sensor scheme respectively.

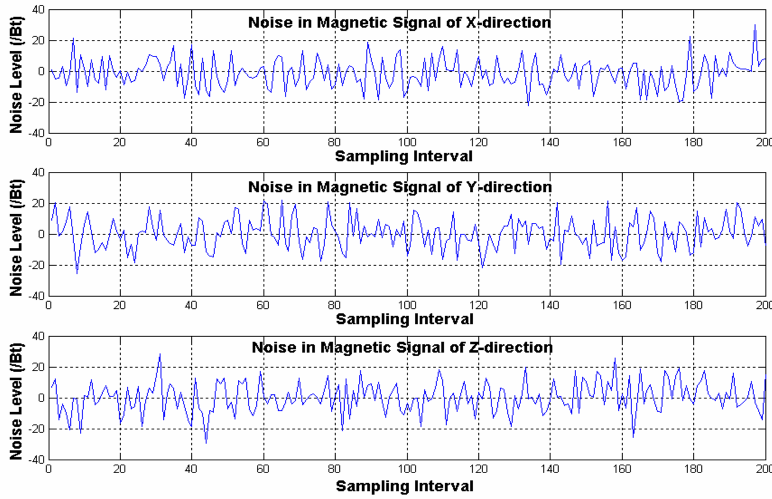

Figure 5.2 Noises in the 3 axis sensor

Because white noise has the random property, we tried this process many (ten) times for testing the repeatability of the algorithm. Here, the average position error $\overline{E}_P$ and orientation error $\overline{E}_O$ are presented for the noise level within (0, 65).

$$\overline{E}_P = [0.092, 0.094, 0.100, 0.100, 0.095, 0.101, 0.094, 0.097, 0.094, 0.095] \text{ (mm)}$$

$$\overline{E}_O = [0.190, 0.197, 0.197, 0.203, 0.201, 0.215, 0.188, 0.194, 0.206, 0.198] \text{ (\%)}$$

Figure 5.5 shows the results. In the figure, "Optimal-2" denotes the method that uses the algorithm for sensor array (in subsection 5.1.2) and solves the unknowns by the procedure discussed in subsection 5.1.3*B)*. "Optimal-1" denotes the method that uses the algorithm for sensor array (in subsection 5.1.2) and solves the unknowns by procedure discussed in subsection 5.1.3*A*). "5-Max" denotes the method that solves the five equations by selecting five sensors with maximum values of magnetic intensities (this means that these five sensors are the nearest to the magnet) and solves the unknowns by the procedure discussed in subsection 5.1.3*A*). Obviously, "Optimal-2" is the best choice of the three methods. On the Table 5.1, the execution time (in Matlab) is listed for a single "Optimal-2" execution period for 5, 9, and 16 sensor cases. It is around 4.22 mS, 6.46 mS, and 10.50 mS for 5, 9, 16 sensor schemes respectively.

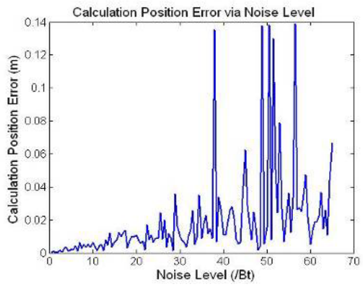

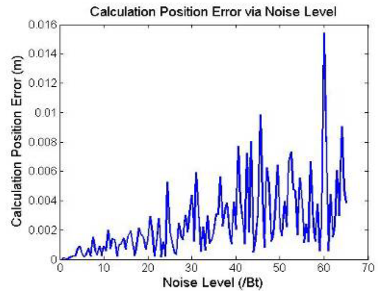

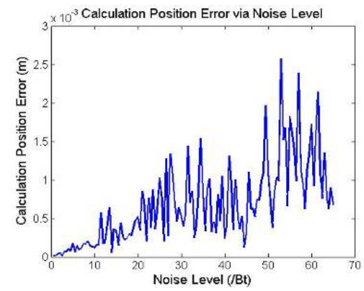

(a) 5-sensor localization **(b) 9-sensor localization** **(c) 16-sensor localization**

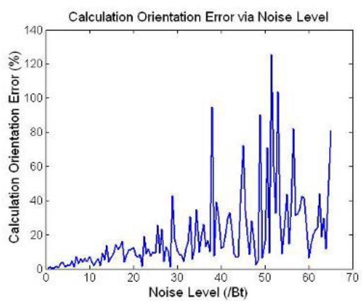

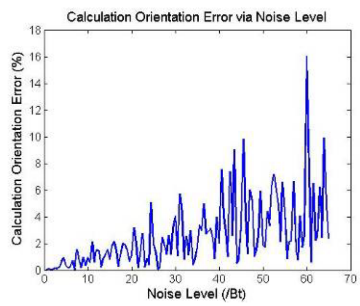

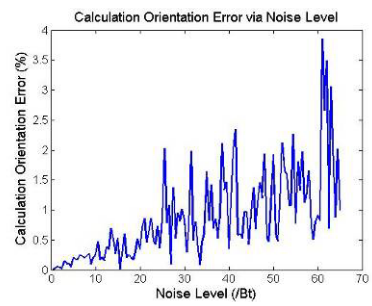

(d) 5-sensor orientation (140%≈89°) **(e) 9-sensor orientation (18%≈10°)** **(f) 16-sensor orientation (4%≈2.3°)**

Figure 5.3 Localization/orientation accuracy via noise level under 5, 9, and 16 sensors

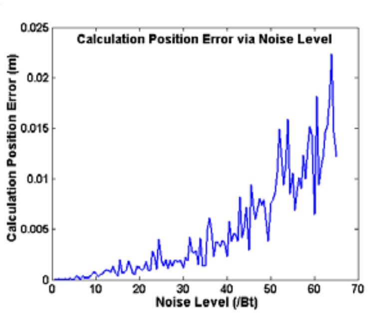

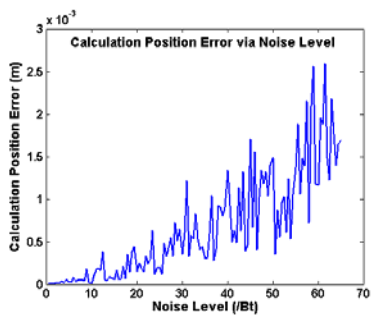

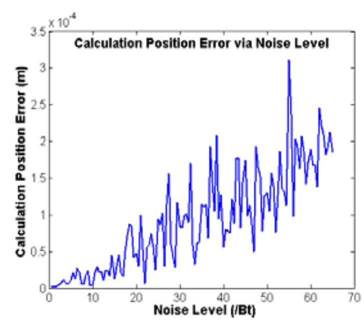

(a) 5-sensor localization **(b) 9-sensor localization** **(c) 16-sensor localization**

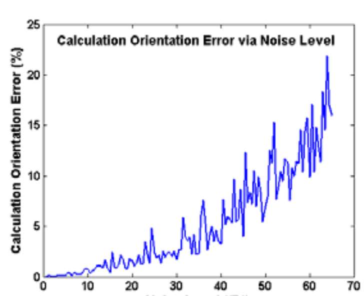

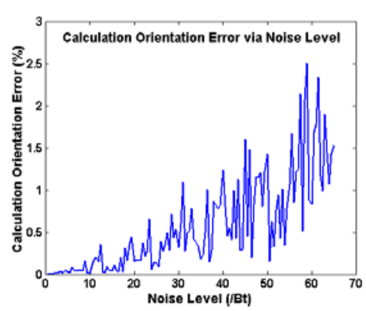

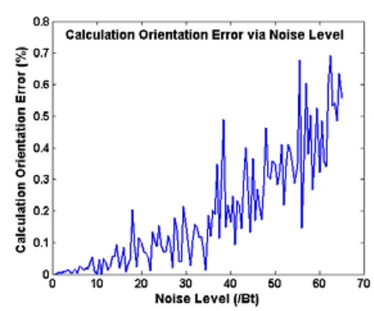

(d) 5-sensor orientation (25%≈14°) **(e) 9-sensor orientation (3%≈1.7°)** **(f) 16-sensor orientation (0.8%≈0.46°)**

Figure 5.4 Localization/orientation accuracy via noise level after averaging 100 samples

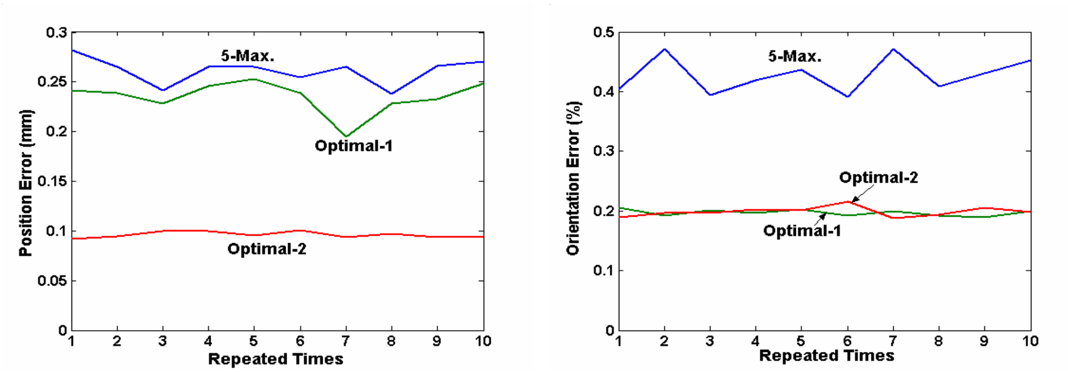

Figure 5.5 Position and orientation error under noise level [0, 65] and 16 sensor groups

Table 5.1 Average execution time (single loop of getting solution, for optimal-2)

Sensor Number	Trial 1 (ms)	Trial2 (ms)	Trial 3 (ms)	Trial 4 (ms)	Trial 5 (ms)	Trial 6 (ms)	Trial 7 (ms)	Trial 8 (ms)	Average time(ms)
5	4.19	4.21	4.14	4.34	4.26	4.15	4.26	4.22	4.22
9	6.46	6.47	6.50	6.50	6.48	6.40	6.39	6.44	6.46
16	10.43	10.52	10.45	10.43	10.63	10.53	10.46	10.58	10.50

5.3.2 Tracking property

To investigate the tracking performance of the system, we let the magnet move in specific pre-designed loci: Inverted conic spiral locus (Figure 5.6) and conic spiral locus (Figure 5.7). In addition, the orientation parameters are set up with $\mathrm{m} = \frac{1}{\sqrt{3}}$; $n = -\frac{1}{\sqrt{3}}; p = \frac{1}{\sqrt{3}}$.

With the magnet's locus, sensor data are created by adding white noises with a particular noise level. Then, the localization/orientation parameters are computed by the algorithm discussed in above. Figure 5.6 ~ Figure 5.9 show the results for the system to track the inverted conic spiral locus and the conic spiral locus with noise level of 20, using the 9-sensor and16-sensor array, which are placed on the plane at *z=0*. To compare the results, we define two parameters $\overline{E}_P$ and $\overline{E}_O$ to be root mean square errors of the position and orientation. We observe that the 16-sensor array has better tracking accuracy than the 9-senosr array, and the tracking error increases with the z-distance to the sensor plane.

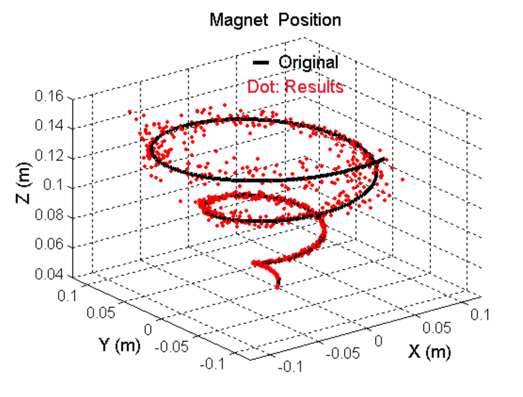

Figure 5.6 Inverted conic spiral locus (9-sensor) ($\overline{E}_P$ =5.60 mm, $\overline{E}_O$ =0.0438)

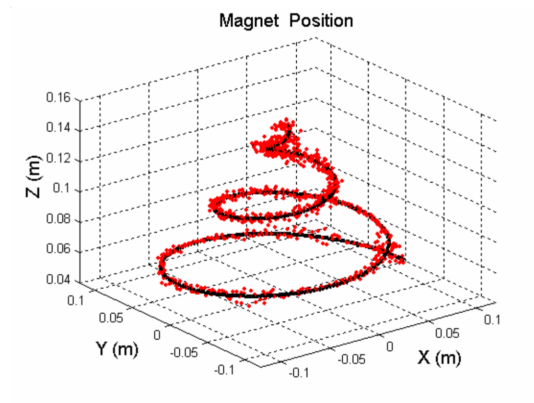

Figure 5.7 Conic spiral locus (9-sensor) ($\overline{E}_P$ =3.96 mm, $\overline{E}_O$ =0.0330)

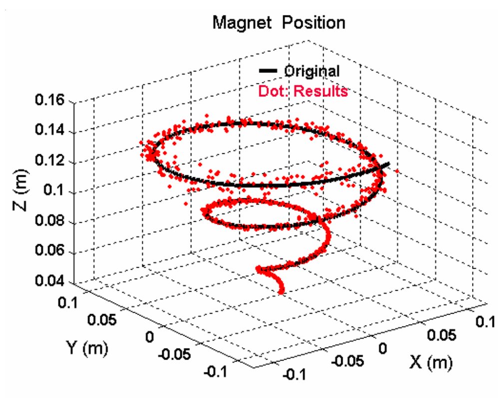

Figure 5.8 Inverted conic spiral locus (16-sensor) ($\overline{E}_P$ =3.49 mm, $\overline{E}_O$ =0.0286)

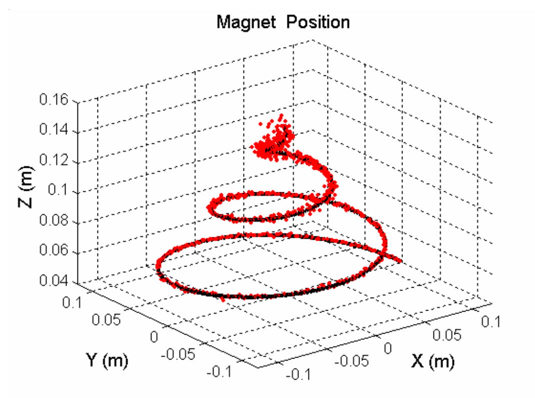

Figure 5.9 Conic spiral locus (16-sensor) ($\overline{E}_P$ =2.60m., $\overline{E}_O$ =0.0217)

A. Optimal tracking (post-processing)

The idea to apply the optimal tracking is to calculate each magnet's position (a_j, b_j, c_j) and orientation (m_j, n_j, p_j) at the *j-th* sampling instant from a fitting function using previous sampled data, such that $\overline{E}_P$ and $\overline{E}_O$ are minimized. For convenient computation, we use square error instead of root-mean square errors:

$$E = \sum_{k=j-\overline{M}+1}^{j} (\Delta a_k^2 + \Delta b_k^2 + \Delta c_k^2) \tag{5.43}$$

where $\Delta a_k = a_k - f_a(k\Delta t)$, $\Delta b_k = b_k - f_b(k\Delta t)$, and $\Delta c_k = c_k - f_c(k\Delta t)$ for time interval $t = k\Delta t$, and *f*() define the fitting function; $\overline{M}$ is the fitting number (=16, 32, 64, …) of samples used for calculation; $j>\overline{M}$ and j is the newest sample. In order to minimize E, we need to find optimal fitting functions $f_a(k\Delta t)$, $f_b(k\Delta t)$ and $f_c(k\Delta t)$, which can represented by some polynomials

$$f_r(t) = \sum_{i=0}^{\eta} \hat{\lambda}_{\zeta i} t^i \tag{5.44}$$

where $\zeta = a$, b, or c; η is the order of the polynomials, and $\hat{\lambda}_{\zeta i}$ are the polynomial coefficients. Since $f_a(t)$, $f_b(t)$ and $f_c(t)$ are not correlated, minimum value of ΔE can be rewritten as

$$\min(E) = \min(\sum_{k=j-\overline{M}+1}^{j} (\Delta a_k^2) + \min(\sum_{k=j-\overline{M}+1}^{j} (\Delta b_k^2) + \min(\sum_{k=j-\overline{M}+1}^{j} (\Delta c_k^2) \tag{5.45}$$

Therefore, we can find the optimal coefficients $\hat{\lambda}_{\zeta i}$ (ς=a, b, c; and $i=1,2,...$) independently. This is also a 2-norm problem to make following equation to minimum:

$$\begin{aligned} E_\zeta &= \sum_{k=j-\overline{M}+1}^{j} (\zeta_k - f_a(k \cdot \Delta t))^2 \\ &= \sum_{k=j-\overline{M}+1}^{j} [\zeta_k - \hat{\lambda}_{\zeta 0} - \hat{\lambda}_{\zeta 1}(k \cdot \Delta t) - \hat{\lambda}_{\zeta 2}(k \cdot \Delta t)^2 + ...]^2 \end{aligned} \qquad (\varsigma = a,\ b,\ c) \tag{5.46}$$

This is the problem of polynomial regression. Let its derivative of $\hat{\lambda}_{\zeta i}$ to be zeros, we get

$$\begin{bmatrix} \overline{M} & \sum_k (k\Delta t) & \sum_k (k\Delta t)^2 & \cdots & \sum_k (k\Delta t)^\eta \\ \sum_k (k\Delta t) & \sum_k (k\Delta t)^2 & \sum_k (k\Delta t)^3 & \cdots & \sum_k (k\Delta t)^{\eta+1} \\ \vdots & & & & \\ \sum_k (k\Delta t)^\eta & \sum_k (k\Delta t)^{\eta+1} & \sum_k (k\Delta t)^{\eta+2} & \cdots & \sum_k (k\Delta t)^{2\eta} \end{bmatrix} \begin{bmatrix} \hat{\lambda}_{\zeta 0} \\ \hat{\lambda}_{\zeta 1} \\ \vdots \\ \hat{\lambda}_{\zeta \eta} \end{bmatrix} = \begin{bmatrix} \sum_k \zeta_k \\ \sum_k \zeta_k (k\Delta t) \\ \vdots \\ \sum_k \zeta_k (k\Delta t)^\eta \end{bmatrix} \tag{5.47}$$

Solve this equation, we get solution for the polynomial coefficients $\hat{\lambda}_{\zeta i}$, and calculate optimized values a_j, b_j and c_j by $f_a(j\Delta t)$, $f_b(j\Delta t)$, and $f_c(j\Delta t)$. Figure 5.10 ~ Figure 5.12 show the results for computing localization parameters a_j, b_j, and c_j with $\overline{M}=64$. Figure 5.13 shows the tracking locus. In the simulation, the noise level is 30(/B_T)

and the sensor number is 16. We observe that the tracing accuracy is much improved, but the locus is still not smooth in case of low SNR.

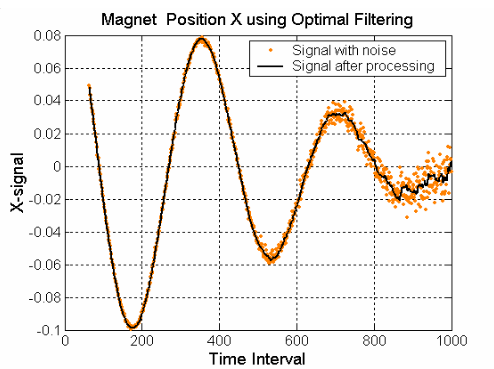

Figure 5.10 Fitting the parameter a_j

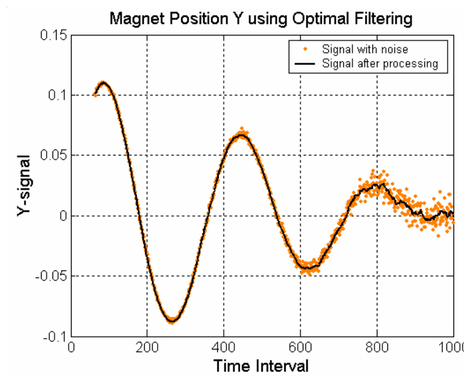

Figure 5.11 Fitting the parameter b_j

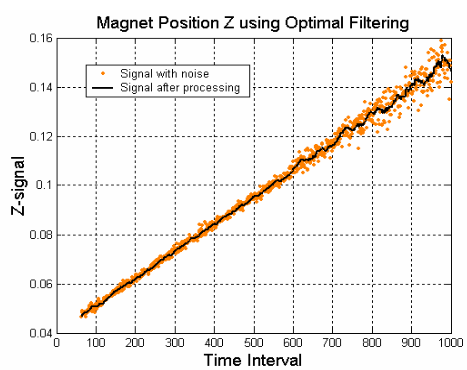

Figure 5.12 Fitting the parameter c_j

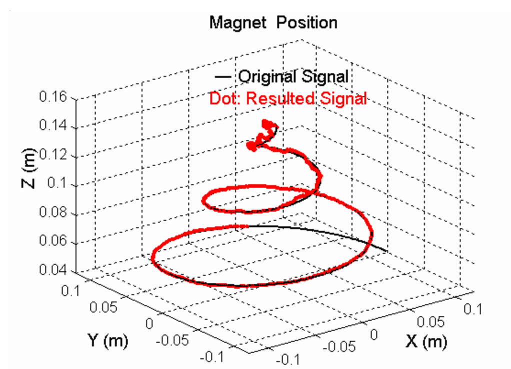

Figure 5.13 Tracking locus with $\overline{M}$ =64

Table 5.2 shows the average tracking accuracy under different order of optimal coefficients $\hat{\lambda}_{ri}$ and fitting number $\overline{M}$. 2-order with sample number 64 is good choice for the polynomial fitted regression, which results in position error 2.23mm and orientation error 1.68% from original position error 4.15mm and orientation error 3.4%. We can conclude that low order fitting is suitable for small number of the samples, when the locus is smooth. Otherwise high order should be used.

Above processing are applied to the signals *a, b,* and *c*, the resultant position. So we call it as post-processing. Post-processing takes the advantage of small number of data, but it is difficult for the fitting regression to achieve high accuracy. As shown in Figure 5.13, the deviation still exists in case of low magnetic signal SNR. Therefore, a further method should be found to improve it.

Table 5.2 Tracing accuracy comparison (16 sensors, noise level=30 (/BT))

	No processing	1-order ($\overline{M}$ =16)	1-order ($\overline{M}$ =32)	1-order ($\overline{M}$ =64)
$\overline{E}_P$ (mm)	4.15	2.39	2.73	3.56
$\overline{E}_O$ (%)	3.43 (2.0°)	1.93 (1.1°)	1.61 (0.92°)	1.52 (0.87°)
		2-order ($\overline{M}$ =16)	2-order ($\overline{M}$ =32)	2-order ($\overline{M}$ =64)
$\overline{E}_P$ (mm)	4.15	2.94	2.48	2.23
$\overline{E}_O$ (%)	3.43 (2.0°)	2.44 (1.4°)	2.01 (1.15°)	1.68 (0.96°)
		3-order ($\overline{M}$ =16)	3-order ($\overline{M}$ =32)	3-order ($\overline{M}$ =64)
$\overline{E}_P$ (mm)	4.15	3.57	2.86	2.43
$\overline{E}_O$ (%)	3.43 (2.0°)	2.92 (1.7°)	2.36 (1.35°)	1.91 (1.09°)

B. Signal processing on the magnetic signals (pre-processing)

In this subsection, we apply some signal processing methods on the original measured magnetic signals B_{lx}, B_{ly}, and B_{lz}, to filter the noise, and then calculate the magnet's position and orientation parameters (*a, b, c, m, n, p*). Also we use the optimal fitting method discussed in above subsection A. Here, we can use two sampling methods:

1) Method-A: Calculate the resulted signal by computing previous $\overline{M}$ ($\overline{M}>1$) samples;
2) Method-B: Get the resulted signal by computing previous $\overline{M}/2$ ($\overline{M}\geq 2$) samples and successive $\overline{M}/2$ samples in case that fast sampling is realizable.

Figure 5.14~ Figure 5.16 show the results for sensor data B_{15x}, B_{15y} and B_{15z}. We observe that Method-B provides higher fitting accuracy, especially for fast variation signal. Figure 5.18 shows the result of tracking the conic spiral locus by using pre-processing (Method-B) with 16 sensors. We observe that the tracking property is much improved (average localization error $\overline{E}_P$ =1.13 mm), comparing with that ($\overline{E}_P$ =4.08 mm) as shown in Figure 5.17 without signal processing. The tracking accuracy can be further improved by applying post-processing, and Figure 5.19 shows the result ($\overline{E}_P$ =0.683 mm). For the case of the inverted conic spiral locus, Figure 5.20 ~ Figure 5.22 show the tracking results, where $\overline{E}_P$=5.59 mm is the case without the signal processing, $\overline{E}_P$=1.30 mm (maximum error=10.15 mm) with the pre-processing, and $\overline{E}_P$=0.887 mm (maximum error=4.94 mm) with both the pre-processing and the post-processing.

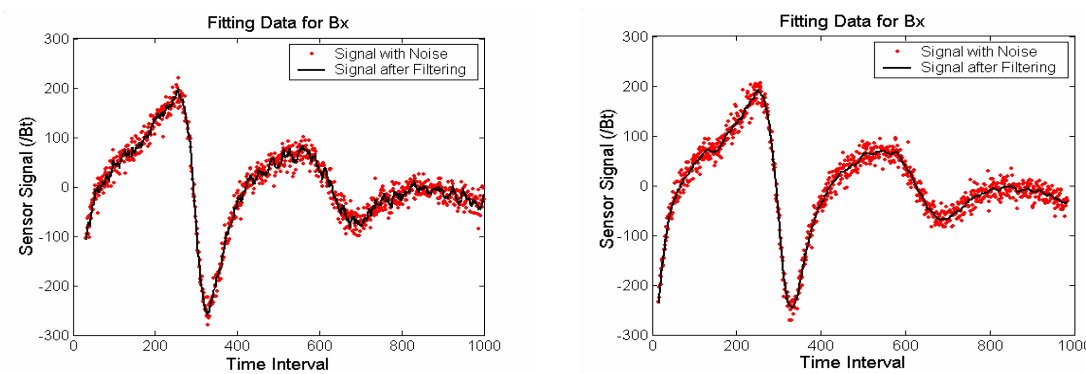

(a) Method-A **(b) Method-B**

Figure 5.14 Fitting the signal B_{15x}

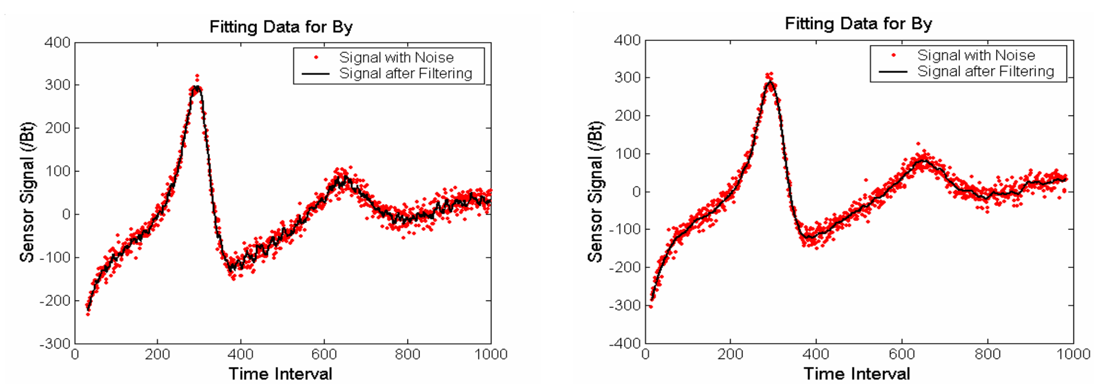

(a) Method-A **(b) Method-B**

Figure 5.15 Fitting the signal B_{15y}

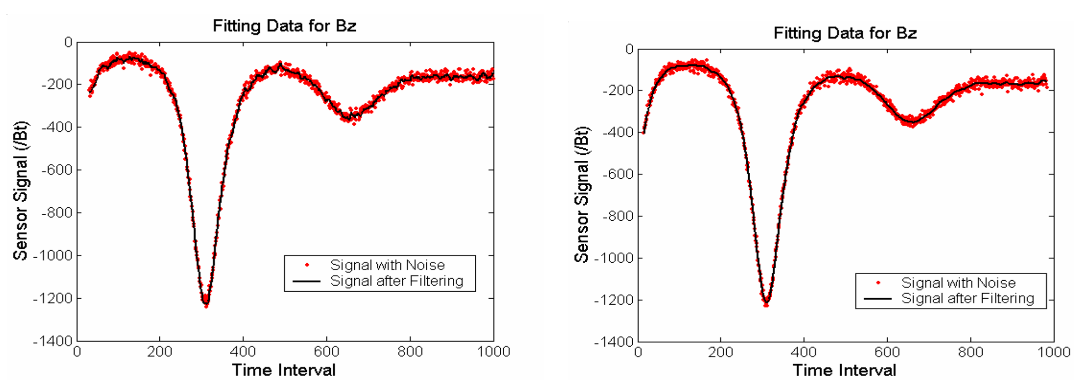

(a) Method-A **(b) Method-B**

Figure 5.16 Fitting the signal B_{15z}

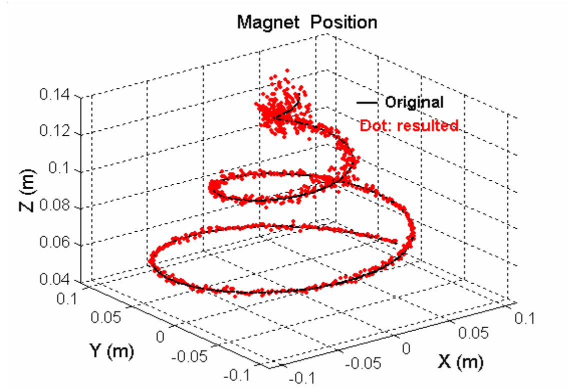

Figure 5.17 Tracking without signal processing ($\overline{E}_P$=4.08 mm, $\overline{E}_O$=3.36%)

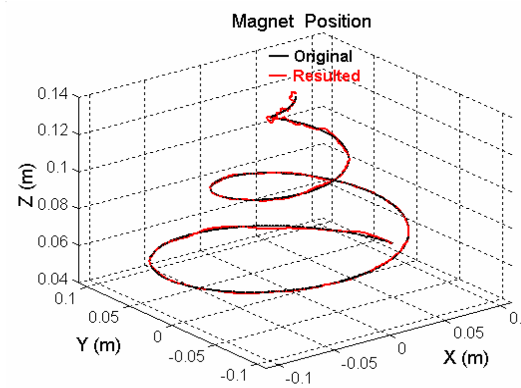

Figure 5.18 Tracking with pre-processing ($\overline{E}_P$ =1.13 mm, $\overline{E}_O$=0.830%, <5.76 mm)

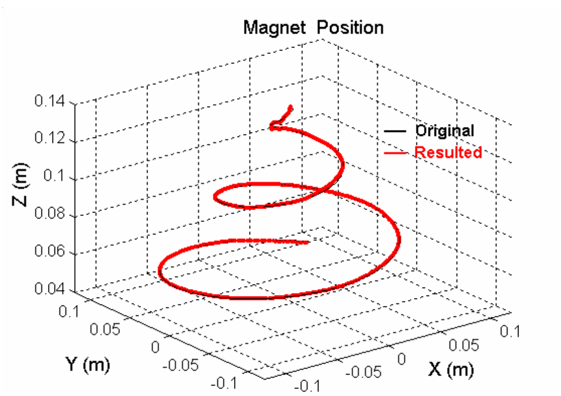

Figure 5.19 Tracking with pre-processing and post-processing ($\overline{E}_P$ =0.683 mm, $\overline{E}_O$=0.532%, max_error=3.15 mm)

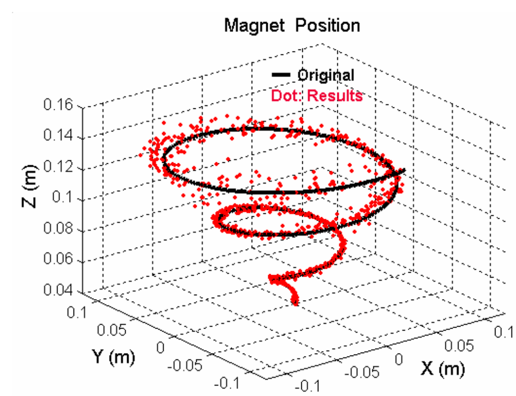

Figure 5.20 Tracking without signal processing ($\overline{E}_P$=5.59 mm, $\overline{E}_O$=4.78%)

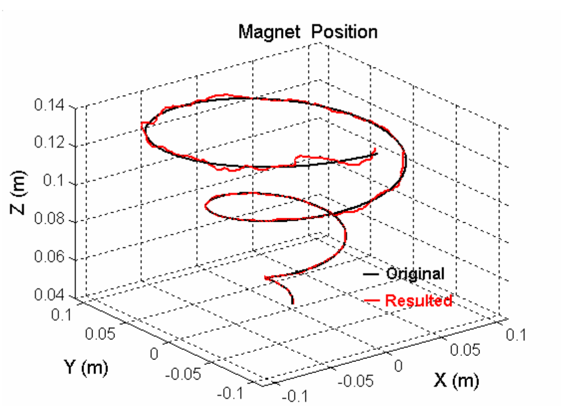

Figure 5.21 Tracking the inverted conic spiral locus with Pre_processing ($\overline{E}_P$=1.30 mm, $\overline{E}_O$=1.05%, <10.15 mm)

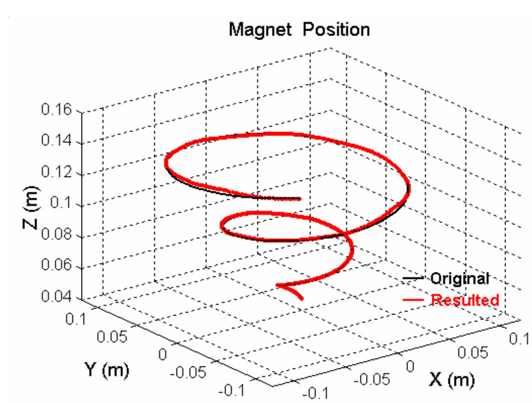

Figure 5.22 Tracking the inverted spiral locus with Pre_processing and Post_processing, ($\overline{E}_P$=0.887 mm, $\overline{E}_O$=0.708%, <4.94 mm)

5.4 Conclusion

Using the vector computations, a linear algorithm is derived from the model equation of the magnetic flux in a spatial position with respect to the magnet's position and direction. In the algorithm, five unknown vector $[r_1 \ r_2 \ r_3 \ r_4 \ r_5]^T$, composed of magnet's position and orientation parameters (*a, b, c, m, n, p*), can be determined by the measured data B_{lx}, B_{ly}, and B_{lz} (l=1, 2, …, N; for $N \geq 5$) and pre-determined sensor positions (x_l, y_l, z_l). Based on the solution of $[r_1 \ r_2 \ r_3 \ r_4 \ r_5]^T$, we can further solve for

1) The absolute values of orientation parameters (*m, n, p*), using $r_4 = \frac{m}{p}$, $r_5 = \frac{n}{p}$, and equation $m^2 + n^2 + p^2 = 1$;
2) The localization parameters (*a, b, c*), using equations of the magnetic flux components B_{lx}, B_{ly}, and B_{lz} with respect to the localization/orientation parameters.
3) The symbol of the orientation, using the results of the localization parameters (a, b, c) and (r_4, r_5).

The system was tested with its de-noise ability respect to different number of the 3-axis sensors and by the properties for tracking spiral conic and inverted conic locus. When the distance from the magnet to the sensor plane increases, the accuracy decreases obviously. To improve the accuracy, a signal processing method, the optimal fitting methods, is applied on the sensor signals and the data of localization and orientation parameters. The results show that the localization and orientation accuracy is significantly improved by applying this method and more (16) sensors.

Comparing with the nonlinear method discussed in Chapter 5, the linear algorithm is simpler and faster because it is mainly related the computations of the matrix, so this method is preferable.

Chapter 6

Real Time Sensor System and Test Results

In this chapter, I discuss the design of the real time sensor system to track the capsule. In section 6.1, I discuss the appropriate magnetic sensor that can be used. In section 6.2, I present the hardware system and sensor circuits. In section 6.3, I present the design of the software and interface. In section 6.4, I propose the calibration methods for the sensor system. In section 6.5, I present the test results and give some data analysis, followed by the conclusion in section 6.6.

6.1 Magnetic Sensor

A good selection of the magnetic sensors is the key factor to build a successful magnetic localization and orientation system. In this section, I discuss how to select the appropriate magnetic sensors for the proposed system.

6.1.1 Sensor specifications

To be used for the localization of the capsule endoscope, the magnetic sensor must have following properties:

1) High sensitivity: Because the magnet is expected to be as small as possible, the variation in the magnet's location and orientation may result in small changes in the magnetic field. Therefore, high sensing resolution is preferable to obtain required accuracy. Then, with properly chosen amplification and sampling circuit, a suitable sensing range is adjusted to match the possible magnetic variation range.

2) High linearity: It is desirable that the output of the sensor system have a linear relationship to the tested magnetic intensity within the possible sensing range. Good sensing linearity simplifies the test circuit and processing software.

3) Small size: We assume that 3-axis sensors are in the same position for the computations in the linear algorithm. The position differences in the these centers will bring about localization/orientation error, so the 3-axis sensor should have small size, and the internal 3 sensors should have center positions as close to each other as possible.

4) Low interference: The sensor should have low noise, a low temperature coefficient, and low signal drift and offset, for obtaining small measurement uncertainty.

5) Easy realization: It does not impose special requirement and restriction for the sensors' spatial arrangement such that the test-bed for the patient can easily be setup. In addition, the sensors are conveniently connected to the computer and other equipment.

6) Low cost. The cost of the whole sensing system should be low. As mentioned in chapter 4 and chapter 5, the localization and orientation accuracy is relevant to the number of the sensors used for the sensor array. We should find a suitable number of sensors with respect to the acceptable accuracy.

6.1.2 Selection of the magnetic sensor

There are many types of magnetic sensors (see Appendix D), e.g., search-coil magnetometer, Superconducting Quantum Interference Device (SQUID), fluxgate, Magneto-inductive magnetometers, Lorentz force devices (Hall sensor and Magnetoresistor), Giant magnetoresistive (GMR) devices, Anisotropic Magnetoresistive (AMR) devices, optic fiber, magnetodiode, magnetotransistor, and etc. Figure 6.1 shows the sensing range of different magnetic sensors. Among them, AMR, GMR and Hall

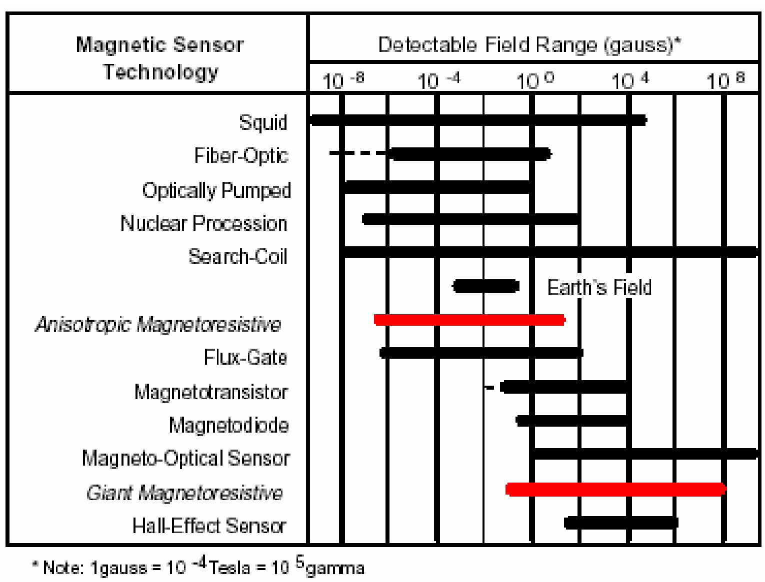

Figure 6.1. Detectable field range of different magnetic sensors

sensors have the advantages of small size, good linearity, ease of realization, and low cost. Based on the experiments, we found that magnet's magnetic intensity is smaller than that of the Earth's field (0.5~0.6 Gauss), when the small magnet (smaller than $\phi\, 8\times 12$ mm) has a distance 10 cm away from the sensor. From Figure 6.1, we observed that the AMR and GMR sensors possess the appropriate sensing range, while the Hall sensor has lower sensitivity unless a bigger magnet or magnetic concentrators are applied.

We have tried GMR sensors (ST302) [104] produced by Shenzhen Huaxia Magneto-electronic T&D Co., Ltd. It has good response, but there is remanent magnetism in the sensor if it is exposed to a magnet. The intensity of this remanent magnetism is changed relative to the distance between the sensor and the magnet. Therefore an additional external device (de-magnetic coil) is needed to remove this magnetism for correct measurement. This makes the system implementation more complex. While expecting new and simple commercial GMR devices in near future, we currently use the Hall sensor and AMR 3-axis senor, Honeywell HMC1053, to build the sensor system, and the real experiments show that HMC1053 sensors are suitable for the system.

6.2 Hardware system and sensor circuits

The sensing system is shown in Figure 6.2, including a magnetic sensor array, amplifier and control circuits, analog to digital converter (ADC), power supply, and computer. Figure 6.3 is the block diagram. In the system, the magnetic sensors, sixteen 3-axis sensors, receive the magnetic signals and change them to electrical signals. The amplifiers amplify (or adjust) the signal magnitude suitable to the range for AD conversion. Then, the computer selects the particular signal channel, and samples the signal using a 12-Bit ADC (we tried PCL-818L data acquisition card [ISA bus, 16 channels] made by the AdvanTech Co.; and ZTIC-USB-7130 [USB interface, 16 channels, 12 bits] by Beijing Zhong-tai R&D Limited.). Some sensors (e.g., HMC1053) may have controls, and there are 48 (16 3-axis) signal channels, so digital outputs are used for these controls and switching the multiplexer CD4052 such that 48 channel sampling is realized by 12 ADC channels. In addition, a highly stable power supply is used for these sensors and

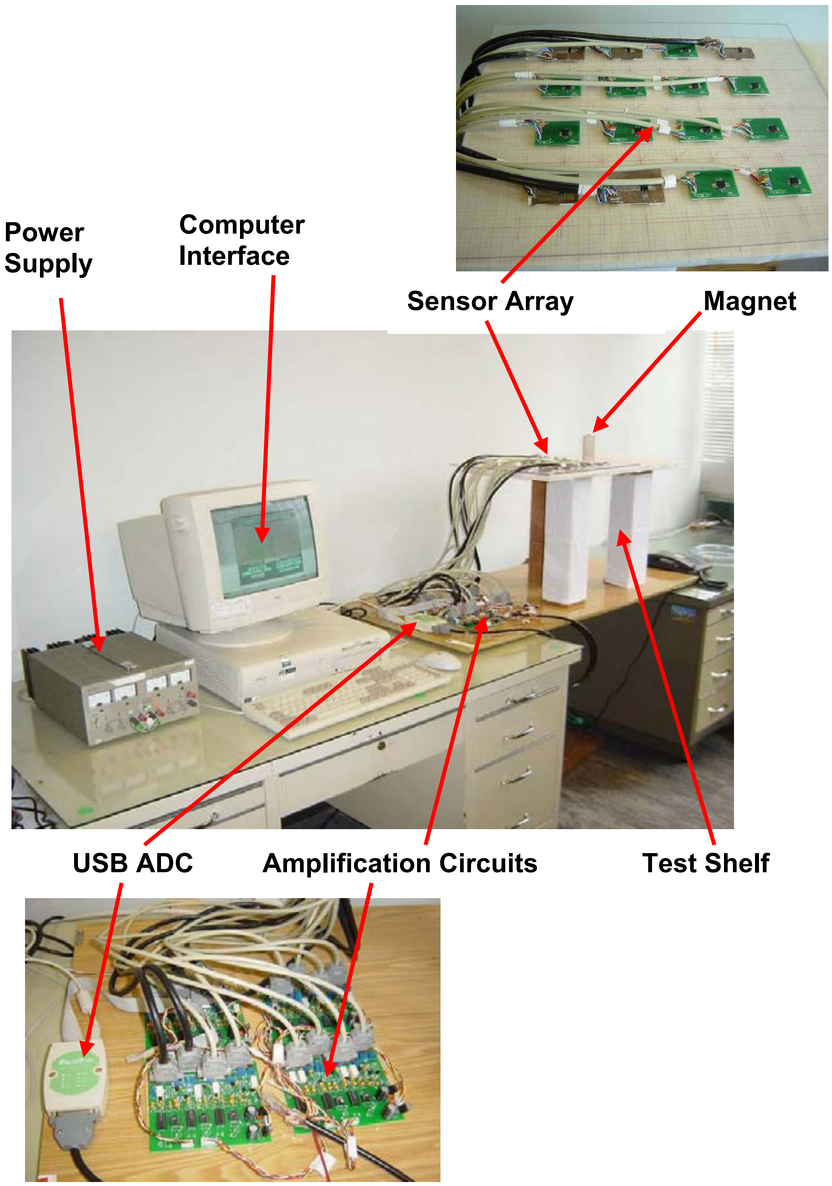

Figure 6.2 Hardware of the Sensing System

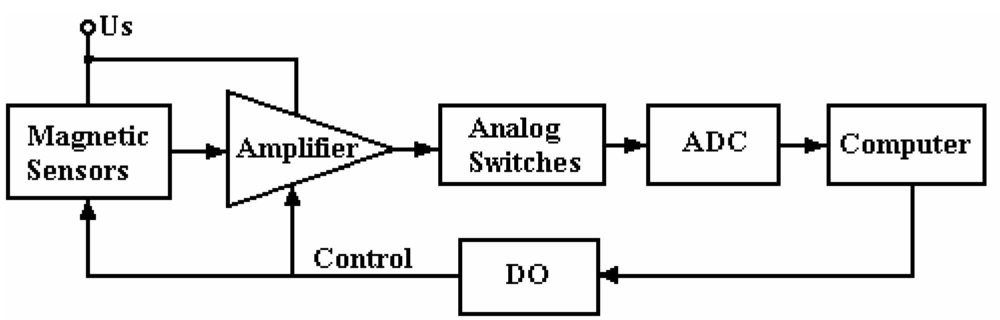

Figure 6.3 Block diagram of the hardware system

their circuits. In the following subsections, the circuits for the magnetic sensors, Hall sensor and AMR sensor (Honeywell 3-axis sensor HMC1053), will be discussed.

6.2.1 Amplifier Circuit for Hall sensor

A Hall sensor has four terminals, as shown in Figure 6.4. Two of these terminals are connected to a power (current or voltage) source, and other two terminals output the Hall e.m.f. signal U_H, which is proportional to product of the input current I and magnetic flux density **B**, if **B** vector is orthogonal to the sensor plane. When **B** vector is not orthogonal to the sensor plane, Hall voltage is

$$U_H = K_H I B \cos\theta \tag{6.1}$$

where K_H is the Hall sensitivity, θ is the angle between **B**-vector and the normal of the sensor plane.

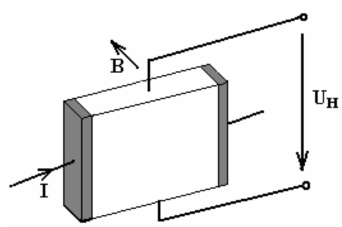

Figure 6.4 Hall sensor: output is the product of the magnetic intensity and current

Because the test signal is not high enough, we need to amplify the Hall output signal. Figure 6.5 is the amplifier circuit. In the circuit, $\mathbf{U_S}$ is a constant voltage source. R_N is used to adjust current for Hall sensor. R_{P1} is a potential meter, which is used to adjust the zero deviation of the output of the Hall sensor because of the possible unsymmetrical property in the element. The outputs of the Hall sensor are isolated from successive circuits by two voltage followers (A_1 and A_2). A differential amplifier then amplifies the Hall voltage. Since $R_{F1} = R_{F2}$ and $R_3 = R_4$, the output U_0 becomes

$$U_0 = U_H \frac{R_{F1}}{R_3} = K_H IB \cos\theta \frac{R_{F1}}{R_3} = K_H \frac{U_S}{R_I} \frac{R_{F1}}{R_3} B \cos\theta \tag{6.2}$$

where R_I is the resistance of the input loop of the Hall sensor, which consists of R_N and input resistance of the Hall sensor. For the differential amplifier, the R_{P2} is used to adjust the offset of the amplifier, and capacitor C is used to filter the noise of the sensor signals. From (6.2), we can see that the different amplification ratios can be chosen for different values of I, R_F and R_1.

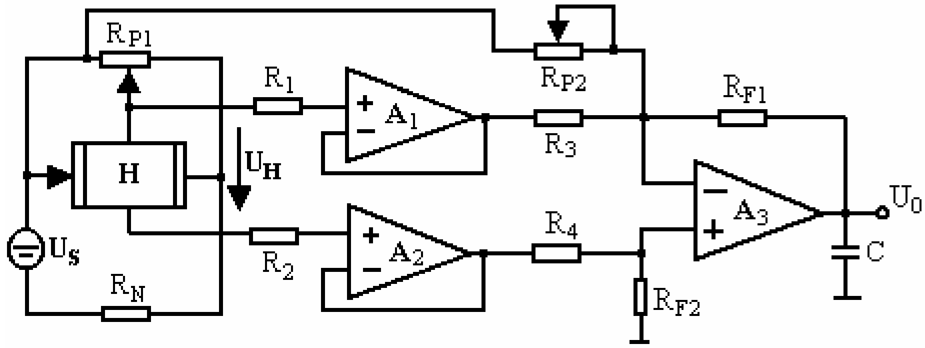

Figure 6.5 Amplifier circuit for the Hall sensor

Another type of Hall sensor, Honeywell's SS490B series sensors [105], has an internal integrated circuit, which can provide good sensitivity, high temperature stability, and small size. Figure 6.6 shows the component and the block diagram. This device can be directly used for testing a magnetic field with the sensitivity about 3 (mv/Gauss) under the range of ±600 Gauss.

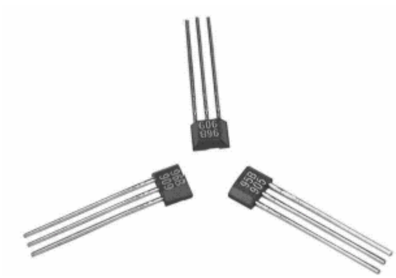

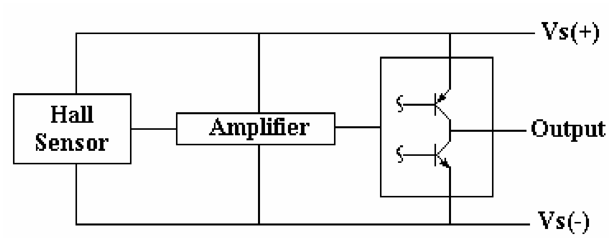

(a) Sensor package (b) Block diagram of the sensor composition

Figure 6.6 Honeywell SS490B series (Hall) sensors

In real applications, we observed that Hall sensor (SS490B series) is not appropriate for directly testing the field when the magnet is small (for instance, Φ6mm×10mm) because of its low sensitivity. Although some types of magnetic concentrators can be used to magnify the test signal, it makes system composition complex. Therefore, a higher sensitivity magnetic sensor is desirable, and Honeywell 3-axis magnetic sensor, e.g., AMR sensor HMC1053, is a good choice.

6.2.2 AMR sensor HMC1053 [106] and its Circuit

The Honeywell magnetic sensor**,** HMC1053**,** is a 3-axis AMR sensor, which has a resolution 100 μGauss and a range ±6 Gauss. Figure 6.7 shows its package (16 pins) and pin-out. In the sensor, each of the 3-axis sensors has four resistors made by thin films on the silicon base. When the magnetization has ideal alignment in the Permalloy film, these four resistors work in a differential mode. The resistance in two of them (in the opposite side) increases, while that of other two resistors decreases, with the input magnetic intensity, and this differential resistance variation will linearly produce a voltage output change in the Wheatstone bridge.

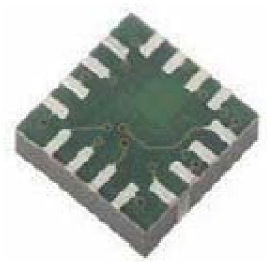

(a) LCC Package ($7.4\times7.4\times2.8mm^3$)

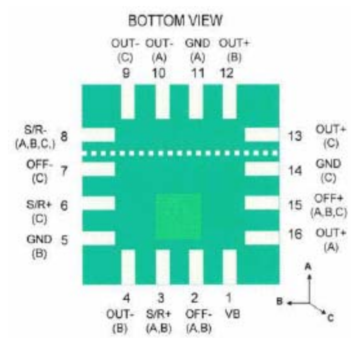

(b) 16 Pin-out (Bottom view)

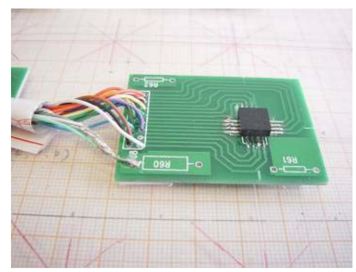

(c) PCB circuited (Fixed in sensor array)

Figure 6.7 Honeywell 3-axis AMR sensor HMC1053

To make use of the sensor, an amplification and control circuit is required. Figure 6.8 shows the amplifier circuit. The Wheatstone bridge is power-supplied by a high-stable power source (5V~6V). The outputs of the three bridges (A, B, C) are amplified using instrumentation amplifier AD623. Because we choose AD623 to work in differential common mode, it has high input impedance with 2 GΩ, such that the sensor bridge is isolated from the successive circuit. The amplification gain can be determined by following equation:

$$V_O = \left(1 + \frac{100k\Omega}{R_I}\right) V_C \tag{6.3}$$

where V_C is the input differential voltage from two outputs of the sensor bridge, V_O is the

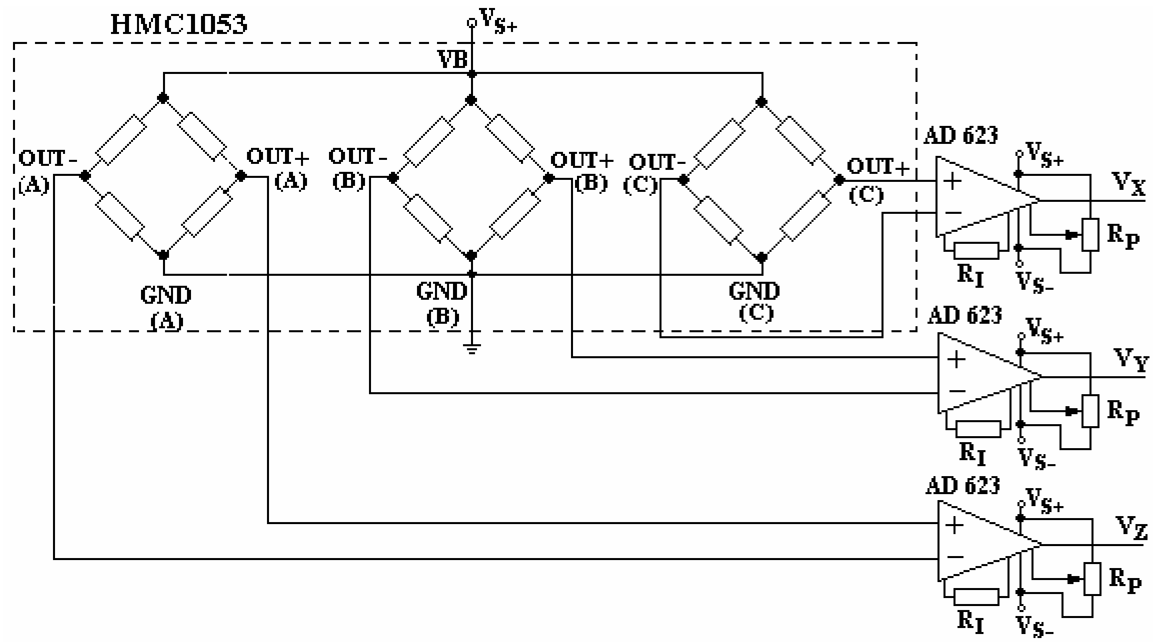

Figure 6.8 Amplification circuit for HMC1053

output of the amplifier, and R_I is the gain resistor with a value larger than 100Ω. The input magnetic intensity in our system is controlled within ±0.5 Gauss. Because HMC1053 has sensitivity of 1mV/V/Gauss, the bridge has an output range within ±0.5×5=±2.5 mV when the power supply is 5V. We choose R_I to be 110Ω, such that the amplifier AD623 has an amplification ratio 910. Then the amplifiers' outputs range with ±2.5 mV×910=±2.275V. In the circuit, the potential-meter is used for adjusting the offset of the amplifier.

To make better use of the sensors, we should use other built-in functions of the sensor, e.g., Set/Reset and Offset adjustment. The magnetic domain orientation in AMR thin films might be broken down when it is exposed to a strong interference magnetic field, and it is critical to the sensor operation. Honeywell's AMR sensor has a patented onchip strap that can create the set and reset fields to rebuild the ideal magnetization alignment. To do the set or reset, a 3~4A and 2μS pulse is applied to the set/reset strap. The set pulse has the same effect as the reset pulse, but the reverse the symbol of output. Figure 6.9 shows the control circuit, where relays S_1 and S_2 are used for the set and reset operations. When the circuit is powered, capacitor C is charged to 15V within one second. During the set operation, the computer sends controls "1" and "0" to digital output DO_1 and DO_2.

These signals are amplified so they that can apply enough current to the control coils of the relays through NPN transistors. Because relay S_1 is "on" and S_2 is "off", the capacitor C_1 discharges a current through the sensor's set/reset straps. The discharge time constant is around 9.2 μS. It is enough to rebuild the magnetization alignment. During the reset operation, the computer sends controls "0" and "1" to digital output DO_1 and DO2, such that relay S1 is "off" and S2 is "on". The set/reset straps have reversed current and the reset operation is done.

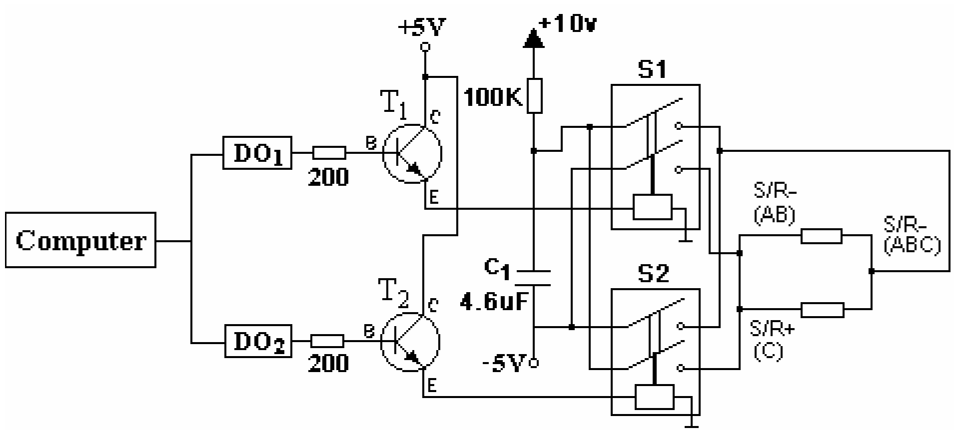

Figure 6.9 Set/reset control for the HMC1053

Honeywell's AMR sensor has a patented on-chip offset strap to accomplish offset adjustment. Figure 6.10 is the circuit for adjusting the offset by applying a current through the strap. Typically, the offset magnetism is within ±0.5 Gauss. Because the offset constant is 10mA/Gauss, a current within ±5mA is needed, and this is realized by adjusting the potential meters for the offset straps (AB) and (C), respectively.

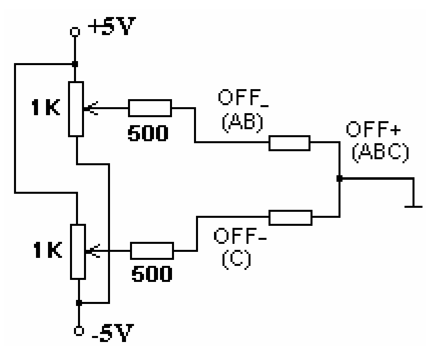

Figure 6.10 Offset adjustment circuit

6.3 Software

The software includes three main parts: data acquisition, the localization and orientation algorithm, and display interface. The data acquisition software completes the task of hardware control, sensor signal sampling, and data storage. Figure 6.11 shows an example for sensor data acquisition and display on the data and diagram format, where the 3-axis sensor signals are sampled and displayed on the numerical and diagram modes. In addition, the sampled data is averaged to filter some noises such that more stable data are displayed.

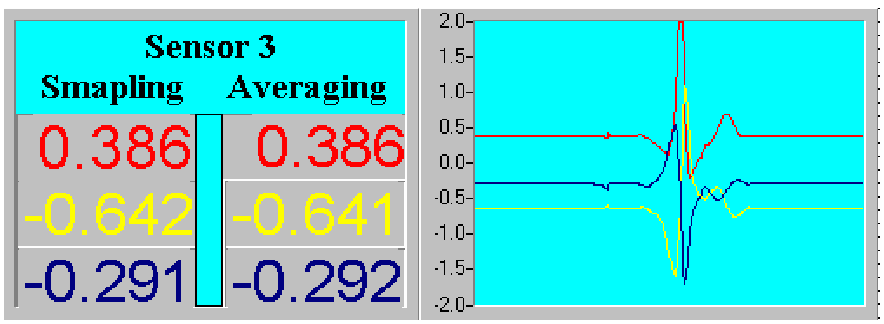

Figure 6.11 Data acquisition by ADC PCL-818L and VisiDAQ software

6.3.1 Interface of the real-time sensing system

Figure 6.12 shows the interface for the real-time magnetic localization and orientation system. When the system starts to work, some information is displayed in this interface, including the 3D localization coordinates for the magnet's position, 3 orientation (projection) parameters, 3D and 2D (X and Y coordinates) plots, initiation or working, and etc. There are two command items marked with yellow color, "Start/Stop Plot" and "Sensor Set". When "Start/Stop Plot" is clicked, 3D and 2D plots will be started or stop. When "Sensor Set" is clicked, all the sensors will be set to rebuild the magnetization alignment.

6.3.2 Main program modules in the real-time tracking system

We use AD converter ZTIC-USB-7130, and Visual Basic language for developing the software of the real time sensing system. The main modules include:

A. Initialization

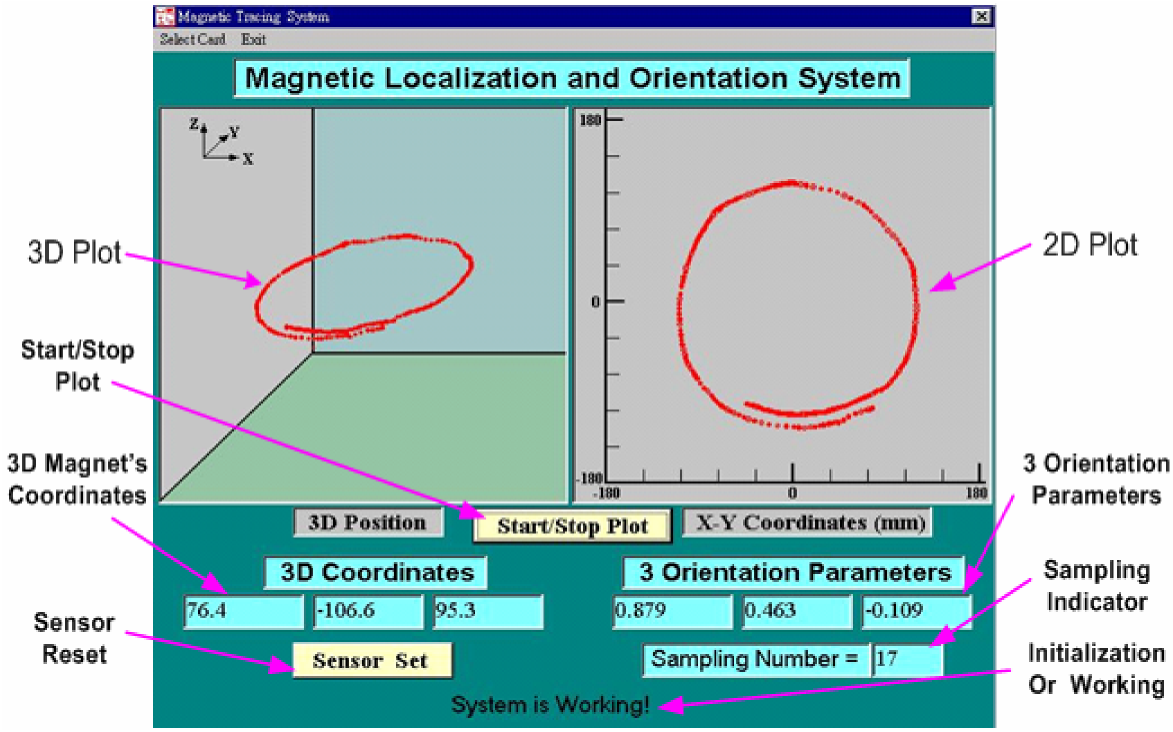

Figure 6.12 Interface for the real time magnetic localization and orientation system

When the system is started, initialization is necessary. It includes the loading of the sensor sensitivities and positions, sensor orientation adjustment matrix, timer and counter preset, ADC channel preset, and other preparations for later operations. Nevertheless, before the magnet is applied, all the sensor data are sampled and stored as the "zero signals". In the later real sampling process, these "zero signals" will be subtracted, which is called as "zero point adjustment", and the resultant data is only related to the magnet's movement.

B. Timer and main execution

Because of the demands of real-time tracking, the sensing system presents the measurement results continuously. We use a timer to control the time interval of the test and display. Once when the timer is trigged (around 0.2~0.3 Second), the program will complete all the operations of the data (ADC) sampling, calculation for the magnet's localization and orientation, and the data display and the 3D and 2D plots.

C. AD Conversion

For the specific ADC, "USB-7130", there is a special program module that completes the required hardware setup and declarations corresponding to a library file "usb7kC.dll". When the declarations are done, the program can realize AD sampling by software calls. Because there are 48 (sixteen 3-axis) sensors, we use digital outputs to control the multiplexer CD4052 to select the sensor channels and sample all the signals by using 16 ADC channels.

D. Localization and orientation algorithm

In the real-time system, we use the linear localization and orientation algorithm as discussed in Chapter 5. After the (sixteen 3-axis) sensor data are adjusted using sensitivity, position, and direction adjustment, we calculate the magnet's position and orientation parameters (a, b, c, m, n, p) by the procedures given by Section 5.1. Because the singularity might occur in equations (5.5), (5.7), and (5.8) owing to the zero orientation component ($m=0$, or $n=0$, or $p=0$), we use all the 3 equations to get 3 solutions. Then, the final solution is selected with that one with the largest value among the 3 orientation projections, which is used for the denumerator in the 3 equations obtained by defining ($n'=n/m$, and $p'=p/m$), ($m'=m/n$, and $p'=p/n$), and ($n'=n/p$, and $m'=m/p$).

E. Other software modules

Other programs include signal processing module with the optimal fitting method discussed in Sub-section 5.3.1., 3D and 2D (X-Y plane, same as sensor array plane) plots, finding the inverse of a matrix, data saving, sensor reset, and etc.

6.4 Calibration of the Magnetic Sensors

When the sensor system is built, calibration is necessary for the parameters related to the sensitivity, positions and orientation of each sensor. When these parameters are correctly determined, we can use apply some implementation measures to achieve higher localization and orientation accuracy. For the calibration, we put the magnet in some specific spatial positions and directions over a scale plane using a pillar (referring to Figure 6.2), and record the position and orientation data by vision. Therefore, we can calculate the three magnetic components for a specific sensor. In the same time, we measure the three components using real magnetic sensors. There are differences in the calculated and measured data, and we must find some adjustment methods to make these differences as small as possible.

6.4.1 Sensitivity calibration

For the 3-axis sensor, the sensing inputs are the three components of the magnetic signals along the orthogonal axes, which can be represented by (4.11)

$$\mathbf{B} = B_T\left(\frac{3(\mathbf{H}_0 \cdot \mathbf{P})\mathbf{P}}{R^5} - \frac{\mathbf{H}_0}{R^3}\right) = (B_{lX}\vec{\mathbf{v}}_X + B_{lY}\vec{\mathbf{v}}_Y + B_{lZ}\vec{\mathbf{v}}_Z) \quad (l = 1, 2, \cdots, N) \tag{6.4}$$

Assume that the sensor has a constant sensitivity and its outputs (the relative change of the differential magnetic resistors) are amplified by a linear amplifier (in our case, the AD623). Then the acquired data by the computer through the AD converters are proportional to the three magnetic components. Let V_X represent the measured data of the x-axis sensor, and magnet's position is in $(a, b, c)^T = (0, 0, 0)^T$, then we have

$$V_X = K_X \frac{B_X}{B_T} = K_X\left[\frac{3(\mathbf{H_0} \cdot \mathbf{P})x}{R^5} - \frac{m}{R^3}\right] \tag{6.5}$$

Now, we need to determine sensitivity factor K_X through the calibration. To simplify the problem, we measure sensor output by moving the magnet along, or perpendicular to, the sensor axis. For example, we move the magnet along the sensor axis, such that $\mathbf{P} = (x, 0, 0)^T$**,** and $\mathbf{H_0} = (1, 0, 0)^T$, and then

$$V_X = K_X\left[\frac{3(\mathbf{H_0} \cdot \mathbf{P})x}{R^5} - \frac{m}{R^3}\right] = K_X \frac{2}{x^3} \tag{6.6}$$

If the magnet moves perpendicular to the sensor axis, such that $\mathbf{P} = (0, y, 0)^T$ and $\mathbf{H_0} = (1, 0, 0)^T$, then we have

$$V_X = K_X\left[\frac{3(\mathbf{H_0} \cdot \mathbf{X})y}{R^5} - \frac{m}{R^3}\right] = -\frac{K_X}{y^3} \tag{6.7}$$

Therefore, the sensor sensitivity along the sensor's x-axis is negative double of that perpendicular to the x-axis. During calibration, we record the sensor output (V_X) and the displacement between magnet and sensor, and the sensitivity parameter is calculated as $K_X = V_X \cdot x^3 / 2$ (or $K_X = -V_X \cdot y^3$). To improve the accuracy, we expect as many samples as possible. In case that two or more samples are presented, we can calculate the sensitivity by averaging or fitting methods using the following equation:

$$K_X = \sum_{j=1}^{\overline{M}} (V_{Xj} / x_j^3) \Big/ \sum_{j=1}^{\overline{M}} (2 / x_j^6) \tag{6.8}$$

where $\overline{M}$ is the number of the samples. Figure 6.13 shows the fitting results using Hall sensor and the magnet (ϕ15*20) via 25 samples at relative positive and negative distance (60~300 mm). The calculated sensitivity K_X=3.5137, and the fitting error is 0.0121 (V), which is evaluated by the mean square root error

$$MSRE = \sqrt{\frac{1}{\overline{M}} \sum_{j=1}^{\overline{M}} [V_S(j) - \hat{V}_S(j)]^2} \tag{6.9}$$

where subscript "*s*" represents *X, Y*, or *Z;* $V_S(j)$ and $\hat{V}_S(j)$ are the *j*th (*j=1,2,…,* $\overline{M}$) sample of the measured and theoretical data.

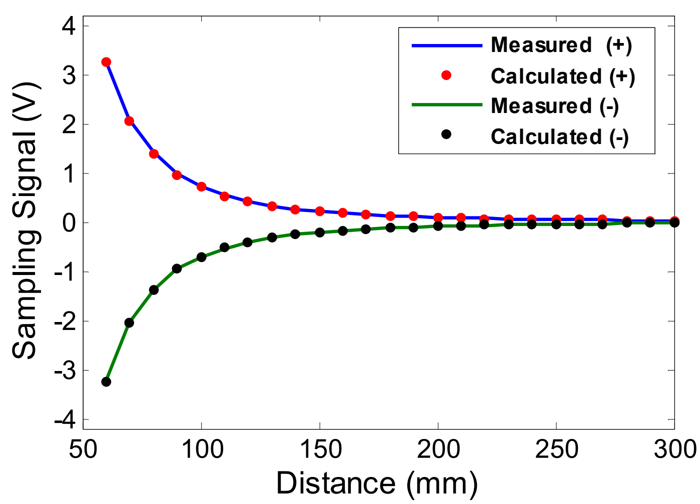

Figure 6.13 Fitting results with calculated sensitivity K_X

Table 6.1 shows the results with four Honeywell 3-axis sensors and a small magnet (Φ5.5mm*L 6.0 mm). We observe that the *Kx* values for different sensors range from 0.5979 to 0.6598, and the variation is about 10%.

Table 6.1 Sensitivity of the 3-axis sensors using magnet No.3
(No.3 Magnet: Φ 5.5 mm * L 6.0 mm; Sensitivity unit: 10^{-3} V*m^3)

Sensor1			Sensor2			Sensor3			Sensor4		
x	y	z	x	y	z	x	y	z	x	y	z
0.6268	0.6191	0.6598	0.6242	0.6123	0.6123	0.5979	0.6209	0.6415	0.6501	0.6216	0.6392

6.4.2 Sensor Position Adjustment

Although the Honeywell 3-axis magnetic sensor HMC1053 has small size, we found that the deviation exists in the sensing central position. This deviation originates from the asymmetrical disposition error of the 3 sensors inside the package. In order to decrease the measurement error, we should adjust the sensor positions that are applied to the computation of the localization and orientation program.

When sensors are fixed in the test-bed, we measure their 3D positions. During the calibration, we recorded the sensor outputs via different magnet's positions and orientations. With these sensors' positions, and the magnet's positions and orientations, the values of the sensor outputs can be calculated. The calculated values are different from measured values of the real sensor outputs since the errors exist in the sensor and measurement data. Here, we define an error objective function to be

$$E_S = \sum_{j=1}^{\overline{M}} [V_S(j) - \hat{V}_S(j)]^2 \tag{6.10}$$

Now we try to adjust the sensor positions to minimize E_S. Table 6.2 shows an example for adjusting the positions of sensor 1. On the table, the 1st column is the original sensor position. The 2nd, 3rd, and 4th columns are the adjustment for the position of the *x*- axis, *y*-axis, and *z*-axis sensor, while the 5th column is the results for adjusting the central position of the whole 3-axis senor, on which we minimize the error $E_X + E_Y + E_Z$.

Table 6.2 Sensor position adjustment

Sensor Position (mm)	x-axis Sensor (mm)	y-axis Sensor (mm)	z-axis Sensor (mm)	Adjustment of 3-axis sensor Centre (mm)
94.5, -37, 11.5	0.0, -2.8, -1.1	-1.2, 2.7, -0.9	1.5, -0.5, -0.8	0.6, 1.1, 0.0

6.4.3 Adjustment of the sensitivity and its nonlinearity

Because noise exists in the samples, the sensitivity still has error. In addition, the magnetic sensors (AMR) have some nonlinearity via input magnetic intensity, especially when the magnetic intensity has a large range. Figure 6.14 shows the difference between the measured data (red dots) and the calculated data. In ideal condition, these outputs should be identical to those in the blue line. To further improve the measurement accuracy, we can apply a step to adjust the sensitivity and the nonlinearity.

As mentioned in 6.4.2, we have $V_S(j)$ and $\hat{V}_S(j)$ ($j=1\ldots\overline{M}$), the measured and calculated sensor outputs. Now, we need to adjust $V_S(j)$ to best fit to $\hat{V}_S(j)$. Here, we assume that the resultant function $\overline{V}_S(j)$ is

$$\overline{V}_S(j) = \lambda_1 V_S(j) + \lambda_2 [V_S(j)]^3 \tag{6.11}$$

The function is symmetrical to the coordinate origin. We also define the fitting error as

$$E_{Sf} = \sum_{j=1}^{\overline{M}} \{\hat{V}_S - \lambda_1 V_S(j) - \lambda_2 [V_S(j)]^3\}^2 \tag{6.12}$$

To minimize E_{Sf}, we can find the optimal parameters

$$\begin{bmatrix} \lambda_1 \\ \lambda_2 \end{bmatrix} = \begin{bmatrix} \sum_{j=1}^{\overline{M}} V_S^2(j) & \sum_{j=1}^{\overline{M}} V_S^4(j) \\ \sum_{j=1}^{\overline{M}} V_S^4(j) & \sum_{j=1}^{\overline{M}} V_S^6(j) \end{bmatrix}^{-1} \begin{bmatrix} \sum_{j=1}^{\overline{M}} \hat{V}_S(j) \cdot V_S(j) \\ \sum_{j=1}^{\overline{M}} \hat{V}_S(j) \cdot V_S^4(j) \end{bmatrix} \tag{6.13}$$

Figure 6.15 shows the fitting results using (6.13). In this example, $\lambda_1 = 1.0313$,

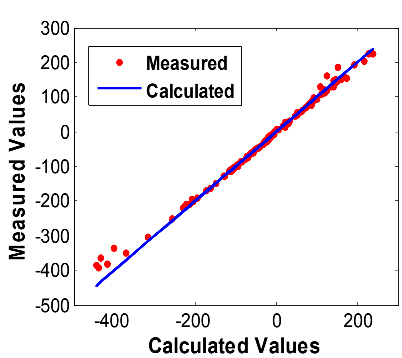

Figure 6.14 Sensitivity error

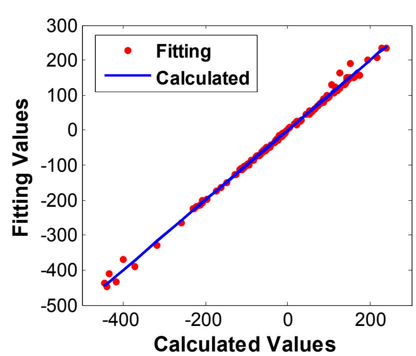

Figure 6.15 Adjustment (fitting) results

$\lambda_2 = \text{-2.9575e-007}$. Obviously, the data after fitting is closer to the calculated values.

6.4.4 Adjustment of sensor orientation

Another factor that affects the measurement accuracy is the error in the sensor orientation. We fix the sensors on the sensor plane based on the observation on their shape. The true orientation of a sensor corresponding to an axis (X-, Y-axis, or Z-axis) might not be exactly parallel to that axis, and this brings about measurement errors in the magnetic intensities (B_X, B_Y, or B_Z). To compensate for this orientation error, we can manually adjust the sensor direction, but it is difficult to accurately adjust it. Therefore, we propose an adjustment method by vector transformation.

Let $\boldsymbol{B_X}$ represent the measured data for an X-axis sensor. The sensor's orientation might not in the same X-axis of the coordinate system. As a result, $\boldsymbol{B_X}$ produces 3 projections onto the 3 axes of the coordinate system, and can be given by $\begin{bmatrix} B_{XX} & B_{YX} & B_{ZX} \end{bmatrix}^T = \begin{bmatrix} \hat{m}_{11} & \hat{m}_{21} & \hat{m}_{31} \end{bmatrix}^T \cdot B_X$. Similarly, for Y and Z-axis sensor data $\boldsymbol{B_Y}$ and $\boldsymbol{B_Z}$, there are also 3 projections $\begin{bmatrix} B_{XY} & B_{YY} & B_{ZY} \end{bmatrix}^T = \begin{bmatrix} \hat{m}_{12} & \hat{m}_{22} & \hat{m}_{32} \end{bmatrix}^T \cdot B_Y$ and $\begin{bmatrix} B_{XZ} & B_{YZ} & B_{ZZ} \end{bmatrix}^T = \begin{bmatrix} \hat{m}_{13} & \hat{m}_{23} & \hat{m}_{33} \end{bmatrix}^T \cdot B_Z$. Finally, the summations of the magnetic intensities along 3 coordinate axes can be represented by

$$\begin{bmatrix} \hat{B}_X \\ \hat{B}_Y \\ \hat{B}_Z \end{bmatrix} = \begin{bmatrix} \hat{m}_{11} & \hat{m}_{12} & \hat{m}_{13} \\ \hat{m}_{21} & \hat{m}_{22} & \hat{m}_{23} \\ \hat{m}_{31} & \hat{m}_{32} & \hat{m}_{33} \end{bmatrix} \begin{bmatrix} B_X \\ B_Y \\ B_Z \end{bmatrix} \tag{6.14}$$

Therefore, for any 3-axis sensor, we can find a matrix $\begin{bmatrix} \hat{m}_{11} & \hat{m}_{12} & \hat{m}_{13} \\ \hat{m}_{21} & \hat{m}_{22} & \hat{m}_{23} \\ \hat{m}_{31} & \hat{m}_{32} & \hat{m}_{33} \end{bmatrix}$, to change the sensor data to those along the 3 coordinate axes, such that the sensor orientation errors are adjusted. Figure 6.16 shows the results of the sensor orientation adjustment. We observe that the results points (red "*") in the right plot are more convergent to the ideal line (blue line). Nevertheless, in the real-time tracking experiments, we found the localization accuracy to be improved, especially in some test areas.

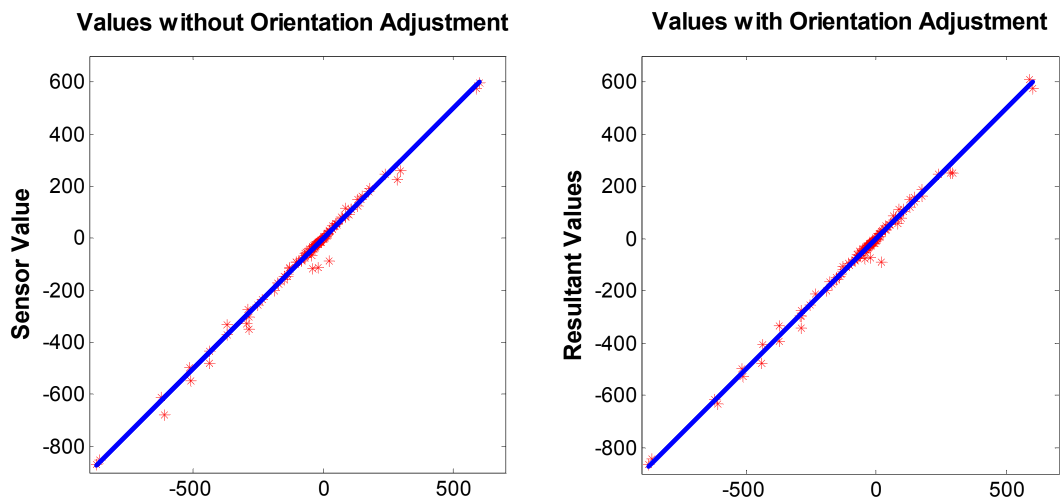

Figure 6.16 An example of sensor orientation adjustment: the left one is the plot without adjustment, the right one shows the results with orientation adjustment.

6.5 Results and data analysis

6.5.1 Results with Hall sensor

Using the sensor array with Hall sensors (and a big magnet Φ16mm × 19mm), the magnet's localization and orientation are realized. Figure 6.17 shows the results (32 samples) by the nonlinear algorithm. We see that the localization and orientation errors are smaller than (21mm, 33%), (16mm, 25%), and (12.6mm, 12%) and the average localization/orientation errors are (7.8mm, 6.14%), (7.3mm, 5.35%), and (5.6mm, 4.26%) for sixteen 1, 2, and 3-axis sensors respectively.

The same 32 samples are applied to the linear algorithm using sixteen 3-axis Hall sensor array. Figure 6.18 shows the localization and orientation errors. We observe that the localization error is within 8 mm, and orientation error is within 7%. The average localization error is 5.6 mm and the average orientation error is 2.9%, which are similar to those obtaied with the nonlinear algorithm.

6.5.2 Results with the AMR sensor system

A. Error distribution

Because the sensor system is affected by different types of interferences and errors

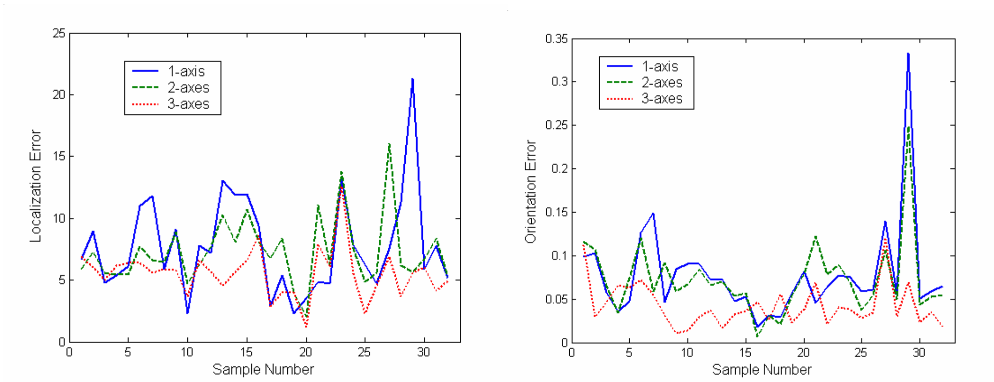

Figure 6.17 Localization and orientation errors using the nonlinear algorithm via 32 (location and orientation) samples for 1, 2, & 3-axis sensors (orientation error 0.35≈20°)

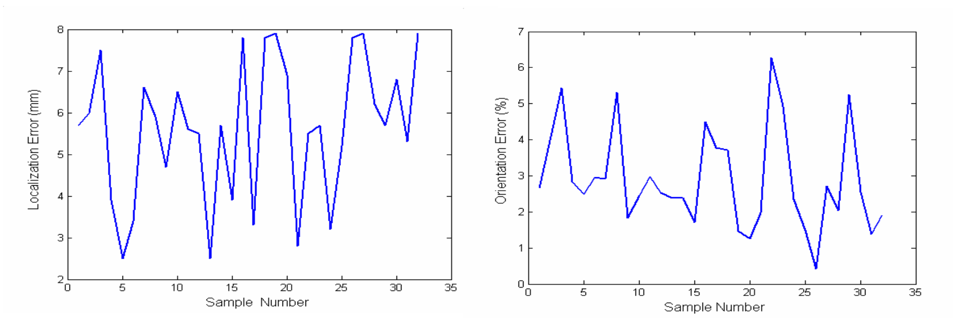

Figure 6.18 Localization and orientation error using linear algorithm via different (location and orientation) samples for 3-axis sensors (orientation error 7% ≈ 4.0°)

that exist in the sensor's sensitivity, position, and orientation, the sampling data might be inconsistent to the calculation data given by the mathematic model. This inconsistency brings about errors in final localization and orientation results, so we need to investigate the characteristics of the sensor errors and devise an appropriate signal processing method to decrease these errors. Figure 6.19 shows the sampling data of the X-axis sensor, and Figure 6.20 is the error distribution of the 3-axis sensor data. The distribution has the features of the normal distribution in the sampling error range from -16 to 22.

Figure 6.21 shows the error (histogram) distribution in all sixteen sensors in specific magnet's positions. Because the sensor signal changes with the magnet's position, the error also changes, so the error distribution has a larger range. From these figures, we observe that the distribution is close to normal distribution, and the error level is within 60 (Bt) for 98% samples.

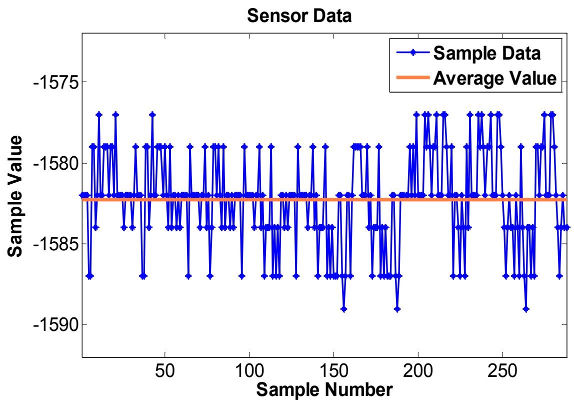

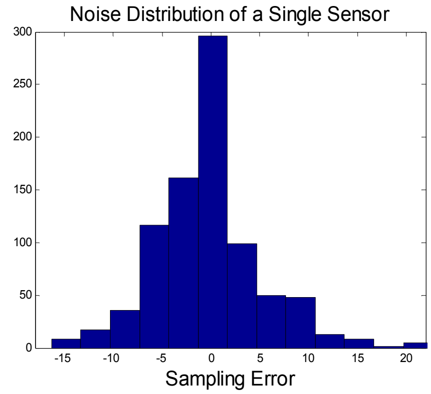

Figure 6.19 Sampling data of the X-axis sensor

Figure 6.20 Sensor error distribution

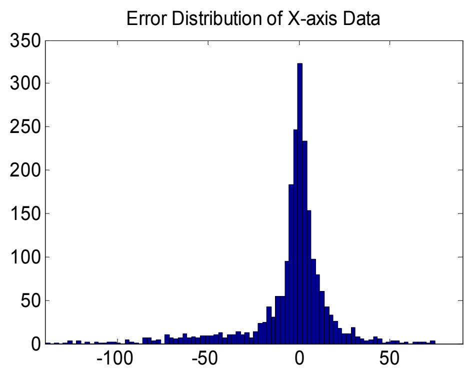

(a) Error distribution in X-axis sensors

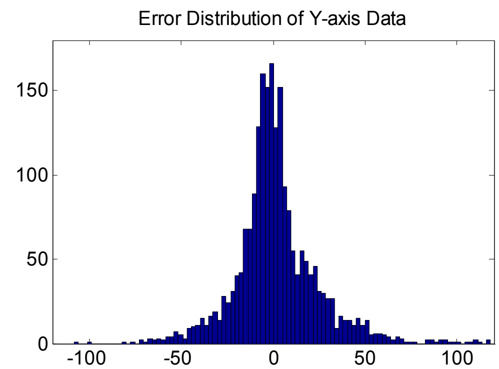

(b) Error distribution in Y-axis sensors

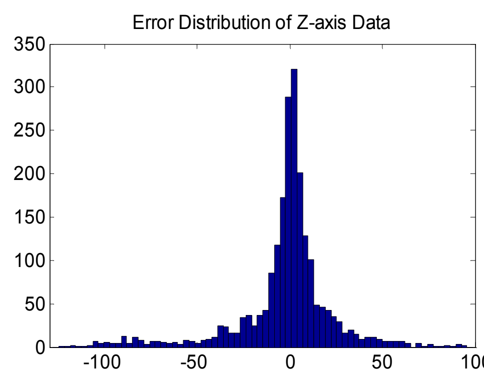

(c) Error distribution in Z-axis sensors

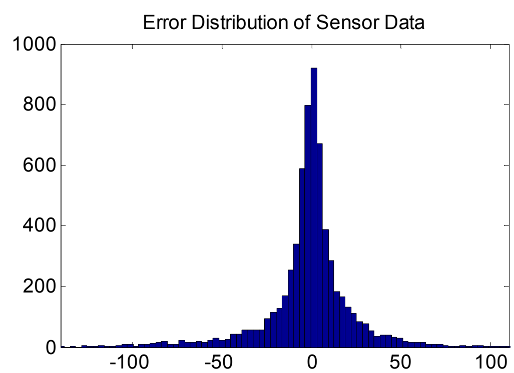

(d) Error distribution in all 3-axis sensors

Figure 6.21 Error distribution (Unit: Bt) in sensor data: the error is taken by real sensor data comparing with ideal calculated data in the specific magnet positions.

B. Accuracy via sensor number

For testing the effect of the sensor number, we fix the magnet's position and orientation (-0.0775, 0.049, 0.1078, 0, 1, 0), and test the localization and orientation accuracy with different sensor number. The results are shown in Figure 6.22. Furthermore, Figure 6.23 shows the average localization and orientation error for 12 sampling points. We observe that localization and orientation accuracy is improved with more sensors, and the accuracy is related to the condition number of the calculation matrix which decreases with the sensor number. Figure 6.24 shows the localization and orientation errors with 5, 10, 15 sensors respectively.

C. Localization and orientation accuracy by real time sensor system

After the sensor array system is built, the localization and orientation accuracy has been tested in different spatial positions under some predetermined orientations, e.g.,

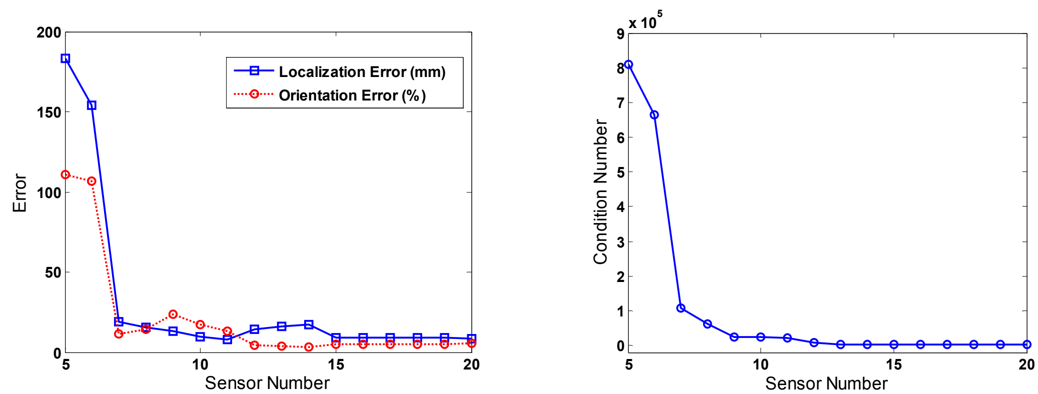

Figure 6.22 Localization error, orientation error, and condition number of the calculation matrix versus sensor number in magnet's position and orientation (-0.0775, 0.049, 0.1078, 0, 1, 0). (orientation error 100% = 60°)

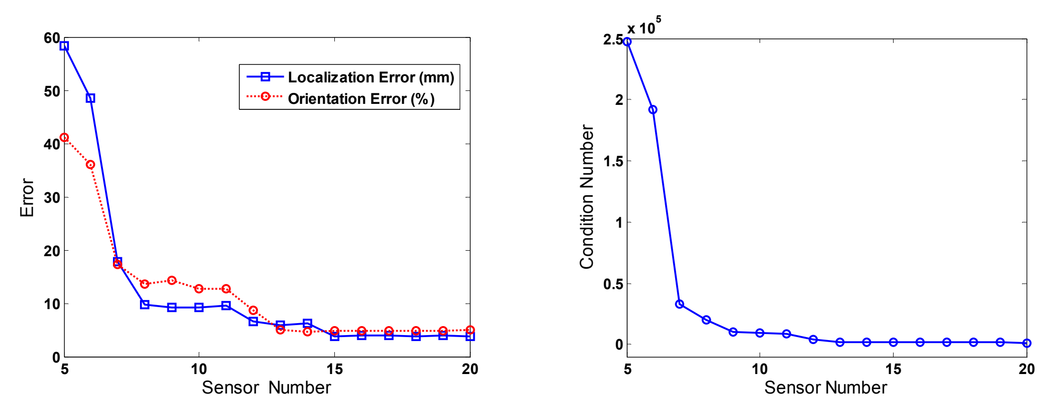

Figure 6.23 Average localization error, orientation error, and condition number of the calculation matrix versus sensor number (orientation error 40% = 23°)

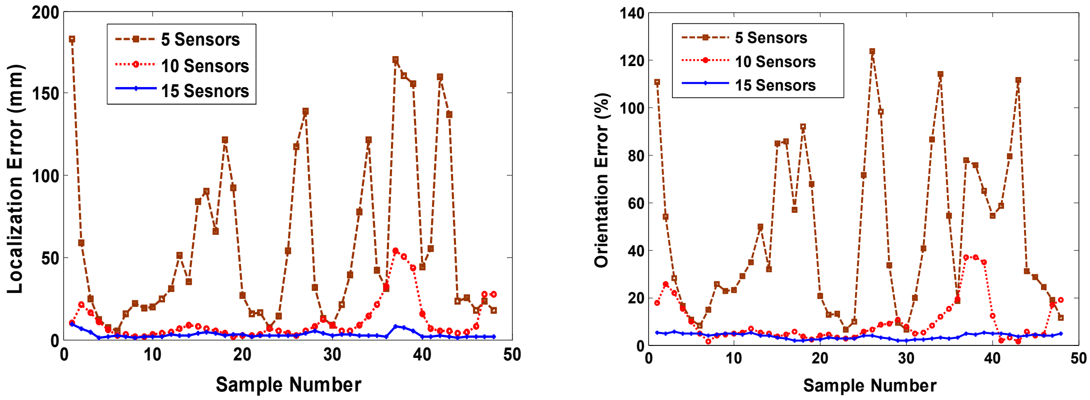

Figure 6.24 Localization and orientation error with 5, 10, and 15 sensors

(m=1, n=0, p=0), (m=n=0.7071, p=0), (m=0, n=1, p=0), (m=0, n=0, p=1), etc. Figure 6.25 shows the localization and orientation errors via 105 samples which were taken on the condition that the magnet (Φ4.5mm×9mm) moves within the square area (-120mm, -120mm to 120mm, 120mm) of the sensor array. We observe that almost all the samples have the localization accuracy within 10mm and orientation accuracy within 0.1 (about 5.7°). The average localization error is 3.3 mm and average orientation error is 0.051 (about 3.0°)

Figure 6.26 displays 3D and 2D (X and Y coordinates) plots in the different magnet's orientations: (*m=1, n=p=0*), (*m=0.7071, n=-0.7071, p=0*), (*m=0, n=1, p=0*), and (*m=0, n=0, p=1*). There are 21 positions and the test area is within the area of the sensor array, we observe that all the points are close to the true positions and the errors are small.

We also made the test for the cases that the magnet moves in the area outside the sensor array. Figure 6.27 shows the errors when the magnet moves along the square of (-160mm, -160mm to 160mm, 160mm). Obviously, the error distribution is much larger than that as the magnet moves within the area of the sensor array. Many samples have the errors larger than 10 mm, and some are even larger than 20 mm. The average localization error is 9.8 mm, and average orientation error is 0.079 (4.5°). Therefore, for real applications, we should design the sensor array with a larger area than that of the magnet's movement.

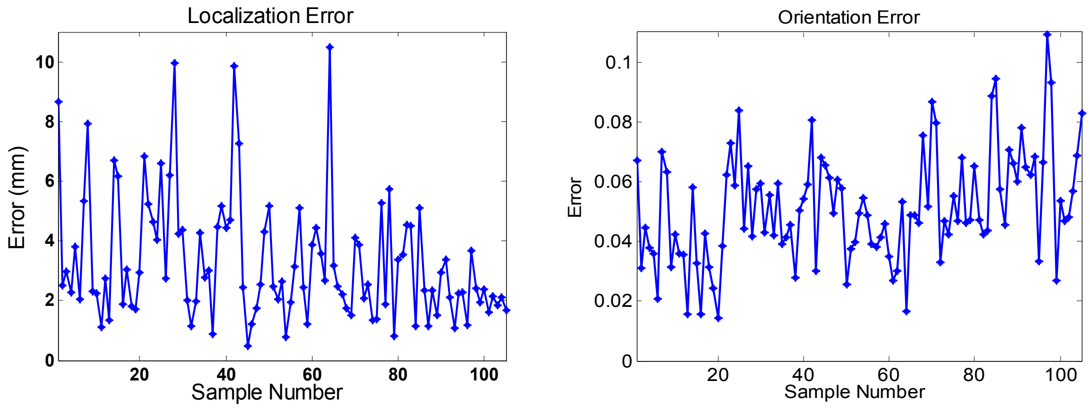

(a) Localization error: average 3.3 mm **(b) Orientation error: average 0.051(3.0°)**

Figure 6.25 Localization and orientation errors via 105 samples: magnet Φ4.5mm ×9mm) moves within the square area (-120mm, -1200mm to 120mm, 120mm) of the sensor array.

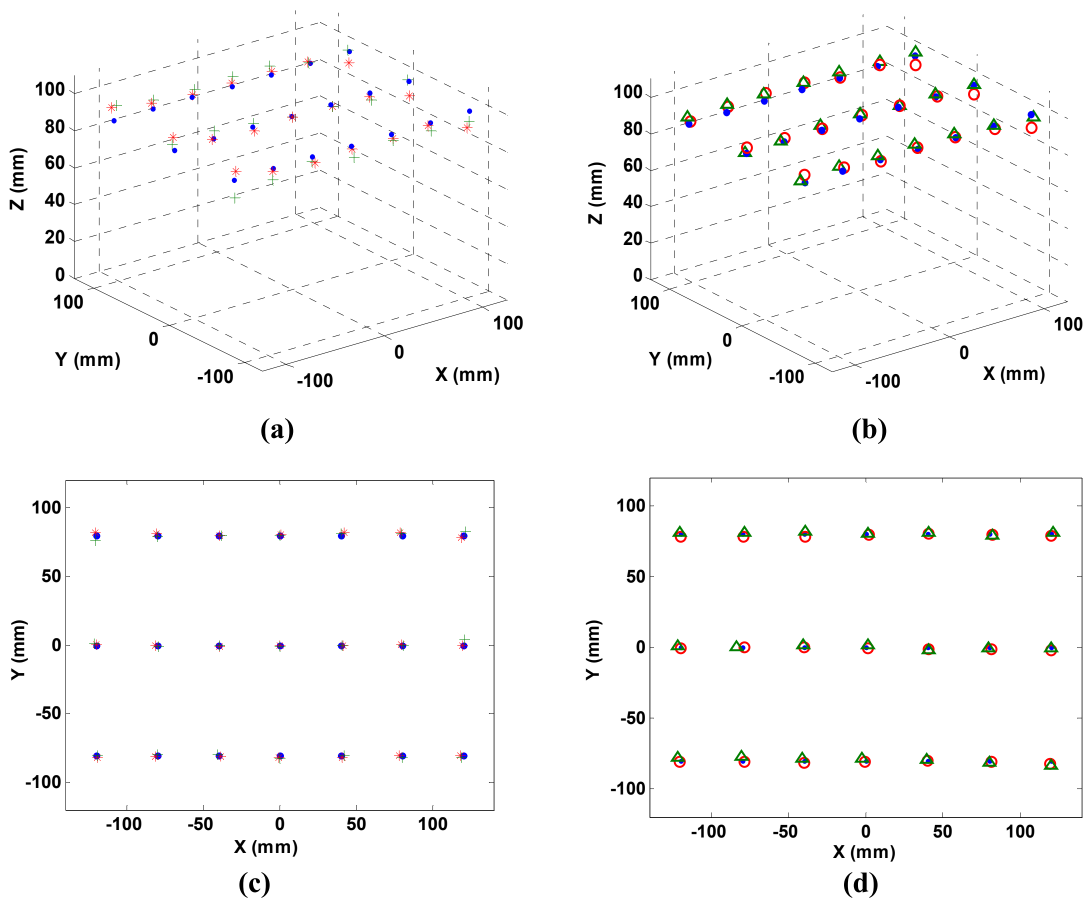

Figure 6.26 Resultant 3D and 2D positions in different magnet's orientations:
(a) and (c): blue dots ("•"): the true magnet's positions; red stars ("*"): magnet's positions in orientation (m=1, n=p=0); green pluses ("+"): (m=0.707, n=-0.707, p=0).
(b) and (d): pink circles ("○"): (m=0, n=1, p=0) ; green triangles ("Δ"): (m=0, n=0, p=1).

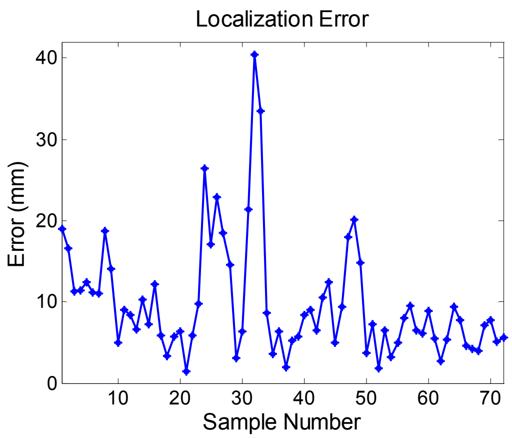

(a) **Localization error: average 9.8 mm**

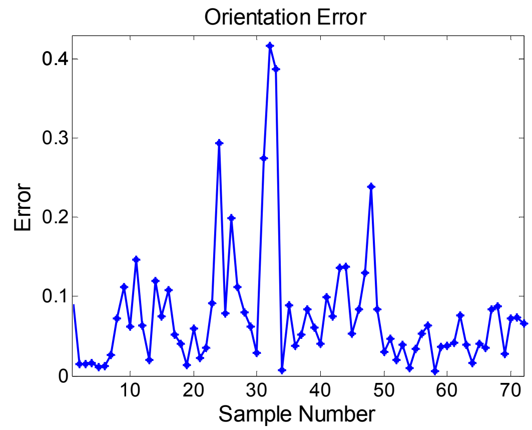

(b) Orientation error: average 0.079 (4.5°)

Figure 6.27 Localization and orientation errors: magnet (Φ4.5mm×9mm) moves in the square edges (-160mm, -160mm to 160mm, 160mm) outside the sensor array area.

D. Tracking properties

Figure 6.28 shows the results of the real-time tracking for the system to trace the magnet moving along a plastic circular tube with diameter about 240 mm, which was placed 98 mm over the plane of the sensor array. Figure 6.29 shows the locus for the magnet moving along some lines which are 94 mm above the sensor plane. We observe that the tracing lines are almost straight when the magnet moves inside the area of the sensor array. However, the lines are not so straight when the magnet moves outside the area of the sensor array. This indicates the tracing accuracy is higher when the magnet's movement is within the area of the sensor area.

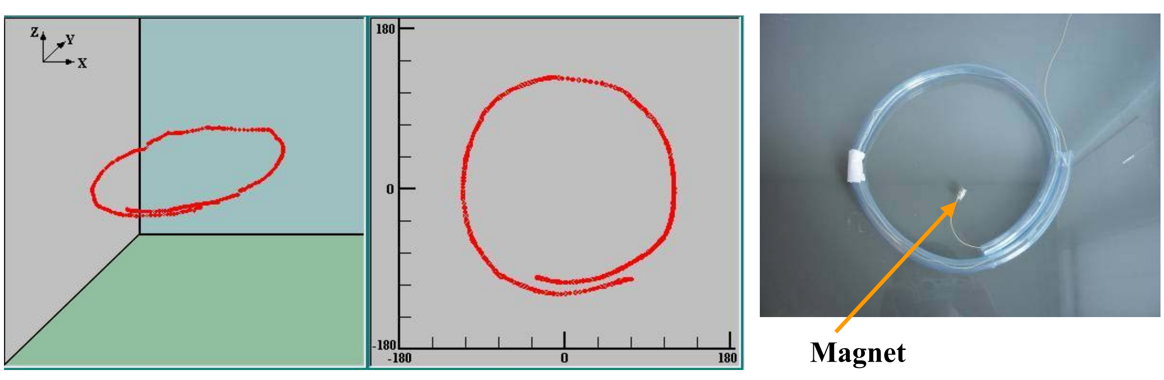

Figure 6.28 3D and 2D locus (red color) for tracking a circular tube: the magnet moves in the tube which is 98 mm above the sensor array.

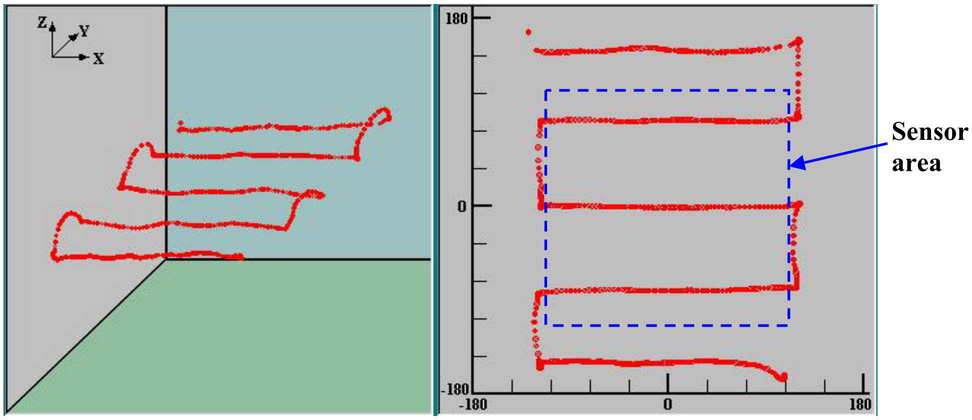

Figure 6.29 3D and 2D locus for tracking lines: the magnet moves along the lines 94 mm above the sensor array.

E. Influence of the medium material

One concern in the magnetic localization and orientation system is the influences of human body and surrounding objects on the sensing system. Therefore we investigated the influence of different materials by putting them between the magnet and the sensor array. Figure 6.30 shows the localization accuracy under different materials. For most non-ferromagnetic materials, the influence is minor. As shown in the figure, adding non-ferromagnetic material, e.g., human body, books, copper plate, and aluminum plate, does

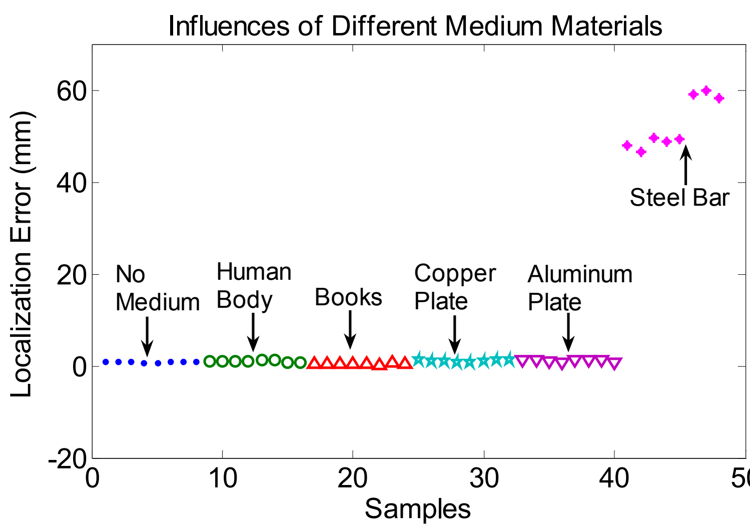

Figure 6.30 Influences of different medium materials: in localization errors

not change the localization results. However, when there is ferromagnetic material, even a small steel bar, the localization will fail. This indicates that we should use non-ferromagnetic metal to fix the sensor system, but avoiding any ferromagnetic material around the sensing system.

6.6 Conclusion

A real-time sensing system, magnetic sensor array, has been built for the localization and orientation of the magnet. For the appropriate magnetic sensors, we considered and tried the Hall sensor, GMR device, and AMR device, and finally chose the Honeywell AMR 3-axis sensor, HMC1053, because of its high sensitivity, high linearity, low offset, small size and easy realization. In case of variation of the magnetic signal, the sensors send out electrical signals through Wheatstone bridge. These signals are amplified to a range ±5V by the precision amplifiers, AD623s, and the computer samples the sensor signals through the AD converters.

Before putting the system into use, calibrations are required for determining the sensitivity of the sensors, finding and adjusting the sensor’s position and orientation errors, and the nonlinear errors. In the computer, the software (using Visual Basic) complete the signal processing and all other required operations on these data, and compute the magnet operations position and orientation via localization and orientation algorithm. Then the tracing results are displayed with 6 localization parameters, and 3D and 2D plots via a computer graphic interface.

Finally, the tracking accuracy is evaluated by moving the magnet in the possible positions and orientations, e.g., some fixed points above the sensor array, some specific spatial lines, or the circular locus. From the experiments, we conclude:

1) When the magnet’s movement within the area of the sensor array, the localization accuracy is smaller than 10mm and the orientation accuracy smaller than 0.1 (about 5.7°). The average localization error is 3.3 mm and the average orientation error is 0.051 (about 3.0°). These results are satisfactory.

2) Five sensors are not enough to obtain the required accuracy. The more sensors that are used, the higher is the achievable accuracy. The selection of the sensor number depends on the objective accuracy and the test area. Twelve or more sensors are suggested for tracking the capsule endoscope.

3) The tracking accuracy is higher when the magnet is located in the central area. When the magnet moves outside the area of the sensor array, the accuracy decreases obviously. Therefore, we should design a magnetic sensor array with an area larger than that of the magnet's movement.

4) The system performance is also relevant to the placement of the sensors. We used the uniform arrangement (on a plane) scheme in our system. For suitable application in endoscopy, we should investigate the distribution characteristics of the GI tract, and design sensor position based on the motion path of the capsule endoscope. One effective method to improve the system accuracy is to increase SNR by reducing the average distance from the magnet to the sensors. This can be realized by the scheme of putting sensors in 3D space. The ring structure of the sensors is a good choice, and further investigations should be made to find the optimal spatial sensor arrangement.

5) The non-ferromagnetic material medium between the magnet and sensors has very little influences on the test accuracy. However, the ferromagnetic material medium has the obvious effect on the test results, and should be avoided close to the system.

6) The system execution speed is about 0.2~0.3 second. It is limited by the AD conversion. To further improve the tracking accuracy by getting more samples for the signal processing, a faster AD converter should be found.

Chapter 7

Localization and Orientation by Imaging

The endoscopic system produces images continuously. Each of these images has been taken as the endoscope camera locates in a particular position and has a special direction, so the images contain the location and orientation (or their variation) information of the endoscope. We can compute the camera's motion parameters from image sequence [71, 74, 108, 109]. The problem is then to estimate the transition and rotation from two perspective views [77, 78, 110]. Since there exist some identical areas in the successive two images such that the correspondent observed point pairs can be found in these two images. Using these image correspondences, we can estimate the camera motion (rotation and translation) parameters with an appropriate algorithm. This approach can be a complementary method applied for the improvement of the magnetic localization and orientation method. Typically, the proposed approach can be divided into several steps:

(*a*) Adjusting camera parameters, e.g., nonlinear distortion correction. This step is done in the procedure of camera calibration [111].

(*b*) Establishing feature correspondence for all pairs of the consecutive images.

(*c*) Estimating motion and rotation parameters based on the correspondence point pairs.

(*d*) Recurring the step b) and c) from the calculated motion and rotation parameters to improve the accuracy.

In the following sections, I will discuss step (*a*) in section 7.1 and step (*c*) in section 7.2, which gives an idea and approach as to how to realize localization and orientation by image sequences taken by a monocular camera. These methods are applied to some real calibration images as presented in section 7.3. While step (*b*) is also important and interesting for finding some specific visional characteristics (for image correspondences) of the GI tract, it needs much more research and should be done in future work.

7.1 Nonlinear Distortion Correction

For the capsule endoscope, the camera captures images that provide the operator with information of the surrounding tissues. The view angle of the camera lens is so wide that it can provide as much information as possible in a single image. However, this lens will bring about some spatial ("barrel-type") distortion, as shown in Figure 7.1, which causes difficulties to do the token matching for finding correspondence pairs for the localization. In addition, it might bring about estimation error in the diagnosis of area and perimeter of pathological tissues. So it is a prerequisite to correct the nonlinear distortion.

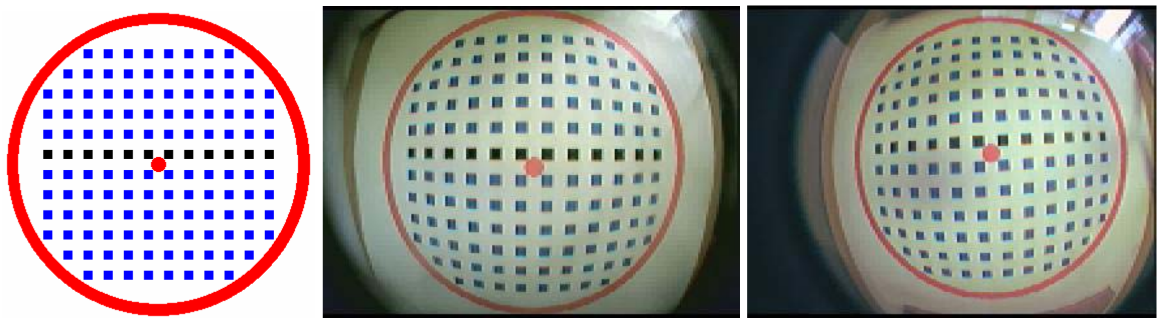

(a) Original pattern (b) Captured image (140° Camera) (c) Captured image (175° Camera)

Figure 7.1 Nonlinear image distortion

Various techniques [112~118] have been presented to find the mathematic models of the distortion and the procedures to complete the distortion correction. Among these techniques, the assumption was made that the distortion was to be purely radial, and some polynomial mapping is proper for changing the distortion image to the corrected image. Typically, the correction is based on a calibration template, which might be a dot pattern [112, 114, 116, 118], or a grid pattern [113, 117], or a chess board pattern [120]. When the template image is captured by the endoscope, some feature points on the captured image are extracted. Comparing these points with those in original standard pattern, we can compute the correction parameters: distortion image center, corrected image center, and the mapping polynomials. Here, I will discuss several methods for correcting the distortion, especially on a color circle-dot image pattern, and the neural network method, which can be applied to any type of spatial distortion, besides the "barrel-type" spatial distortion.

7.1.1 Calibration patterns

The correction of the distortion is based on a calibration template which includes a lot of samples with some special features. The position correspondences of these samples in the captured image and the original patterns can be set up to do the calibration. Some examples of the calibration patterns are shown in Figure 7.2~7.4.

Figure 7.2 shows a chess board pattern. The samples are extracted from the corners of the white and black squares. Figure 7.3 is a dot pattern, on which the samples are found to be the centers of the dots. Figure 7.4 is a grid pattern on which the samples are extracted by finding the cross points of the black lines. For these patterns, the chess board pattern provides higher position accuracy than other 2 patterns, but fewer samples can be extracted. A dot pattern can provide more sample points, and Figure 7.5 shows an example of distorted image with "barrel-type", which was taken from the calibration pattern as in Figure 7.3. Another calibration pattern is setup by the circles, on which some special properties can be found, and then the correction be realized. It will be discussed in 7.1.2 *B*.

7.1.2 Correction Methods based on the uniform pattern and circular pattern

The distortion is normally assumed purely radial about the distortion center [112, 114, 115, 117], and its parameters can be determined by orthogonal Chebyshev polynomials. Let (u', v') denote the point in distorted image space, and ρ' and θ' the magnitude and angle from this point to the distortion center (u_c', v_c'). We have

$$\rho' = \sqrt{(u'-u'_c)^2 + (v'-v'_c)^2} \tag{7.1}$$

$$\theta' = \arctan\left(\frac{v'-v'_c}{u'-u'_c}\right) \tag{7.2}$$

where (u'_c, v'_c) is the distortion center. Let the same point be assigned to a new location (u,v) in the corrected image space and the magnitude ρ and angle θ from this point to the corrected center (u_c, v_c). We have

$$\rho = \sqrt{(u-u_c)^2 + (v-v_c)^2} \tag{7.3}$$

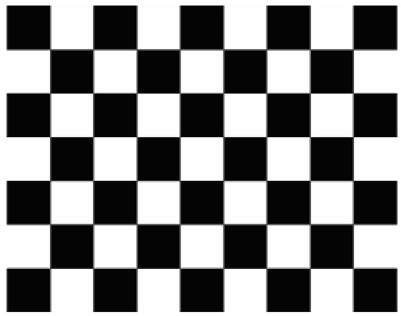

Figure 7.2 Chess board pattern

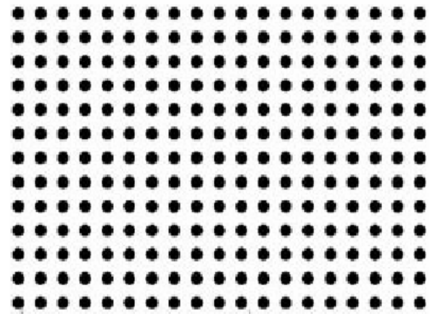

Figure 7.3 Uniform dot pattern

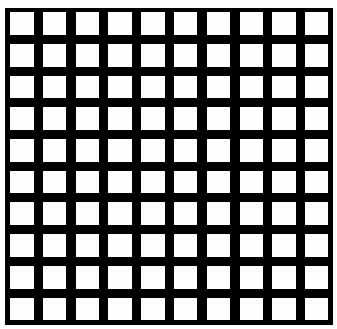

Figure 7.4 Grid pattern

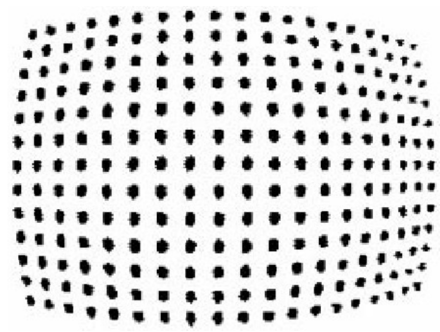

Figure 7.5 Distortion image (by dot pattern)

$$\theta = \arctan\left(\frac{v - v_c}{u - u_c}\right) \tag{7.4}$$

An expansion polynomial of degree $\overline{N}$ is defined to relate these two magnitudes

$$\rho = \sum_{i=1}^{\overline{N}} \widetilde{\lambda}_i \rho'^i \tag{7.5}$$

where $\widetilde{\lambda}_i 's$ are the expansion coefficients. Since distortion is purely radial, we assume that $\theta = \theta'$. The new pixel location in the corrected image space can be computed as

$$u = u_c + \rho \cos\theta' \tag{7.6}$$

$$v = v_c + \rho \sin\theta' \tag{7.7}$$

A. Correction based on the uniform pattern

This technique uses pattern (as Figure 7.2~7.4), on which the featured samples can be found. An example is shown in Figure 7.6, where the sample pixels are found to be the dot centers on the image on Figure 7.5, through image segmentation, labeling, and averaging operations. For chess-board and grid patterns, we can also find the samples using image processing techniques.

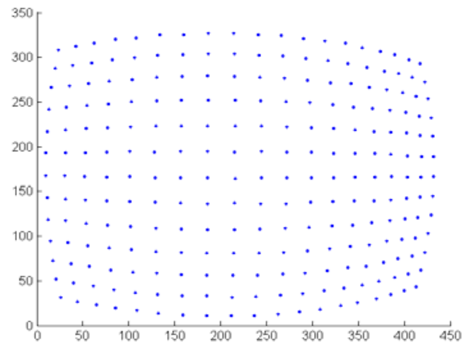

Figure 7.6 Dot center samples

For this kind of samples in Figure 7.6, Asari et al. [112] and Helferty et al. [114] proposed correction methods based on least square estimation. This method should first find the image centers in the distorted and corrected images by computing curvatures of all row and column sample curves and estimating distortion centers $(u_c^{'}, v_c^{'})$, (u_c, v_c) by interpolation. Then the expansion coefficients $\tilde{\lambda}_i$'s can be determined by using a recursive computation process until the error

$$E_\rho = \sum_{l=1}^{\overline{M}} | \rho_l - \sum_{k=1}^{\overline{N}} \tilde{\lambda}_k \rho'^k_l | \tag{7.8}$$

is smaller than a predetermined threshold, where $\overline{M}$ is the number of the samples. Figure 7.7 shows the relationship of the magnitudes ρ and ρ'. With these $\tilde{\lambda}_i$'s, and image centers (u'_c, v'_c) and (u_c, v_c), we can reconstruct the image using (7.6) and (7.7). Figure 7.8 shows the corrected image from the distortion image of Figure 7.5.

B. Correction based on circular pattern

Calibration with the dot pattern needs to estimate the image centers of the distorted and corrected images. Sometimes, it causes larger errors. So we tried to use a circular pattern. Figure 7.9 shows the segmented circles from the captured image. In the image, there is a special line (as shown in Figure 7.10), which passes through the circle center O' and also through the center C' of the distortion image, as shown in Figure 7.11. This line separates the circles into two symmetrical parts. Figure 7.10 shows the resulted symmetrical line.

Refer to the Figure 7.11 (a), "*O* " is the circle center and "*C* " the imaging center in the original image, which are corresponding to "*O'* " and "*C'* " in the distorted image Figure 7.11(b). The line AB is changed to line ED since the line passing the distortion

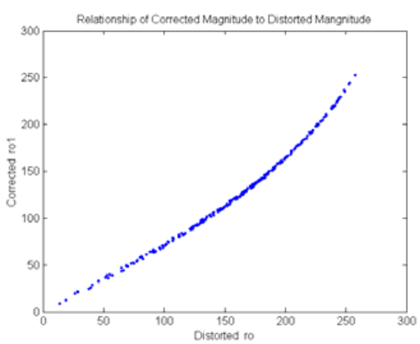

Figure 7.7 Relation of ρ and ρ'

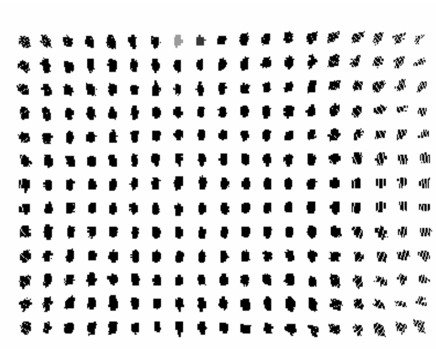

Figure 7.8 Corrected image (from Figure 7.5)

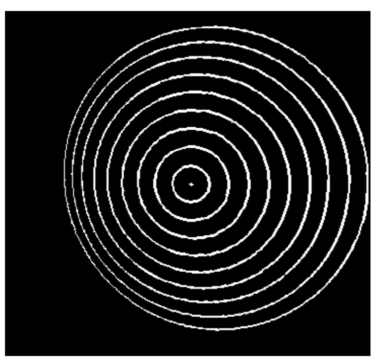

Figure 7.9 Distorted circles

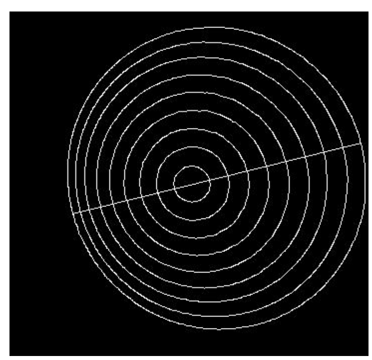

Figure 7.10 Symmetrical line

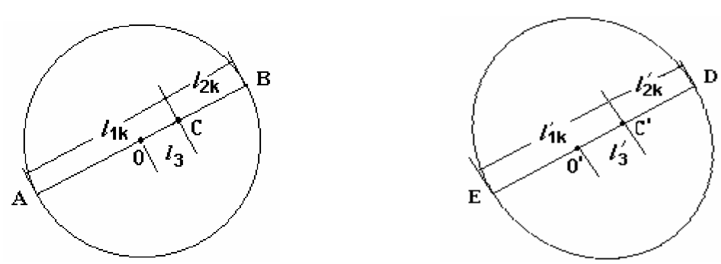

(a) Original circle (b) Distorted circle

Figure 7.11 Original and distortion circle center keeps linear. Assume that k^{th} original circle has a radius of r_k, and $AC=l_{1k}$, $CB=l_{2k}$, $OC=l_3$, $EC'=l'_{1k}$, $C'D=l'_{2k}$, $O'C'=l_3'$. We have

$$l_{1k} = \sum_{i=1}^{\overline{N}} \lambda_i \, l'^{i}_{1k} \tag{7.9}$$

$$l_{2k} = \sum_{i=1}^{\overline{N}} \widetilde{\lambda}_i \, l'^{i}_{2k} \tag{7.10}$$

$$l_3 = \sum_{i=1}^{\widetilde{N}} \widetilde{\lambda}_i \, l'^{i}_{3} \tag{7.11}$$

where $l'_{1k} - l'_3 = \hat{r}'_{1k}$ and $l'_{2k} + l'_3 = \hat{r}'_{2k}$. $\widehat{r}'_{1k}$ and $\hat{r}'_{2k}$ are known. $l_{2k} + l_3 = \hat{r}_k$ and $l_{1k} - l_3 = \hat{r}_k$. So we have

$$\sum_{i=1}^{\overline{N}} [(\hat{r}'_{2k} - l'_3)^i + l'^{i}_3] \cdot \widetilde{\lambda}_i = \hat{r}_k \tag{7.12}$$

$$\sum_{i=1}^{\overline{N}} [(\hat{r}'_{1k} + l'_3)^i - l'^{i}_3] \cdot \widetilde{\lambda}_i = \hat{r}_k \tag{7.13}$$

There are $\overline{N}+1$ unknowns, viz. $\overline{N}$ expansion coefficients ($\widetilde{\lambda}_i\text{'}s$), and l'_3 for distortion center. We can get the matrix representation:

$$\begin{bmatrix} \hat{c}_{11} & \hat{c}_{12} & \dots & \hat{c}_{1\overline{N}} \\ \hat{c}_{21} & \hat{c}_{22} & \dots & \hat{c}_{2\overline{N}} \\ \vdots & & & \\ \hat{c}_{k1} & \hat{c}_{k2} & \dots & \hat{c}_{k\overline{N}} \end{bmatrix} \begin{bmatrix} \widetilde{\lambda}_1 \\ \widetilde{\lambda}_2 \\ \vdots \\ \widetilde{\lambda}_{\overline{N}} \end{bmatrix} = \begin{bmatrix} \hat{r}_1 \\ \hat{r}_1 \\ \vdots \\ \hat{r}_k \end{bmatrix} \tag{7.14}$$

where $\hat{c}_{ji} = (r'_{2k} - l'_3)^i + l'^{i}_3$ when j is an odd, and $\hat{c}_{ji} = (r'_{1k} + l'_3)^i + l'^{i}_3$ when j is an even. Take $\overline{N}$ *+1* equations of (7.14), we can solve them for expansion coefficients $\widetilde{\lambda}_1, \hat{\lambda}_2, \dots \widetilde{\lambda}_N$, and the image center by l'_3. Figure 7.12 shows the resulted image corrected from Figure 7.9 with $\overline{N}$ =3 for expansion coefficients.

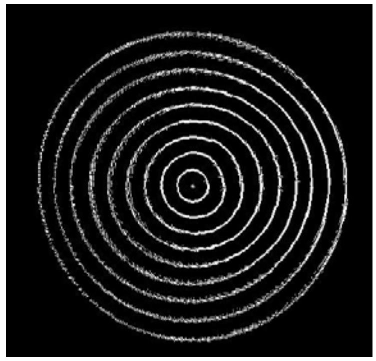

Figure 7.12 Corrected circle image

We observe that the recovered image is closer to the circles, but distortion still exists, owing to small number of samples taken along the symmetrical line, which might have some errors (noises). So for more accurate computation, a larger number of samples are required. An improved method is to use dot samples along with the circle samples as shown in Figure 7.13.

The pattern consists of circular ring, circle center, and dots with different color. Fig.14 is the captured image. Through color segmentation, we can get a dot image (Figure 7.15(a)) and a circle image (Figure 7.15(b)) from the captured sample image (Figure 7.14). With the circle image, the symmetrical line of the image can be determined such that the image center is defined in this line. With the dot image, more samples are provided so that we can compute the expansion coefficients accurately. With this method, the distortion can be corrected effectively. Figure 7.16 shows corrected image.

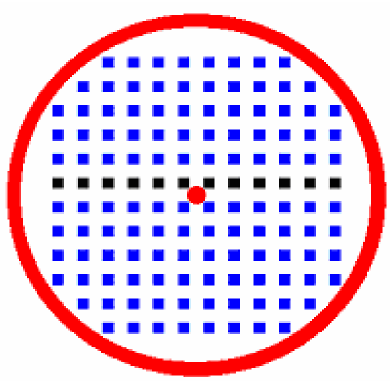

Figure 7.13 Circle-dot pattern

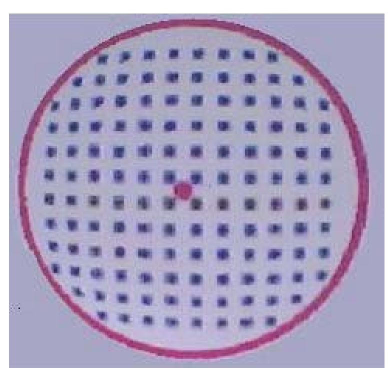

Figure 7.14 Captured image

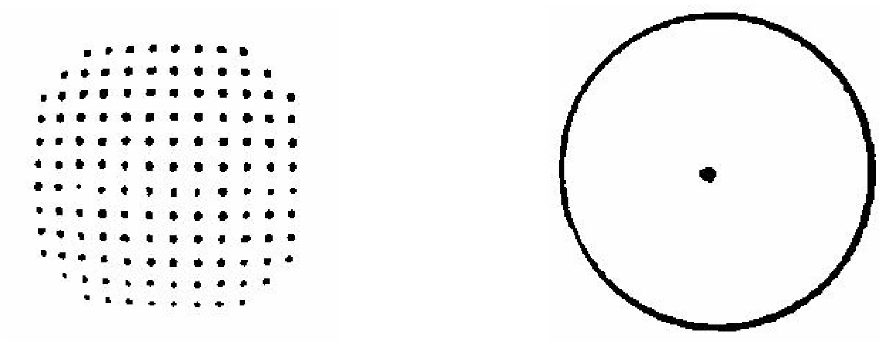

(a) Segmented dot image (b) Circle image

Figure 7.15 Circle-dot image segmentation

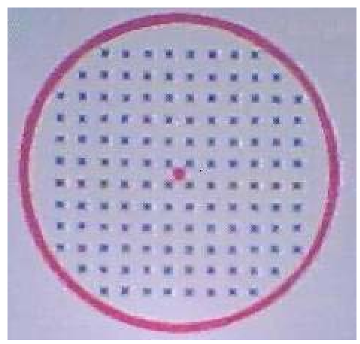

Figure 7.16 Corrected image using circle and dot pattern

7.1.3 Correction by Neural Network

Three-layer network is used so that there is only one hidden layer as Figure 7.17. There are 2 inputs, $\bar{u}$ and $\bar{v}$, the normalized coordinates of the samples in distortion image and 2 outputs, $\bar{u}'$ and $\bar{v}'$, the coordinates in the corrected image. The objective error function is defined as

$$E = \sum_{i=1}^{\bar{M}} |\bar{u}_i' - \tilde{u}_i| + |\bar{v}_i' - \tilde{v}_i| \tag{7.15}$$

where $(\bar{u}_i', \bar{v}_i')$ is the coordinates of the samples in the corrected image, and $(\tilde{u}_i, \tilde{v}_i)$ is normalized coordinates of the samples in the standard calibrated image. We need to minimize this error through the training of the neural network. For each neuron (a total of $\bar{N}$ neurons) in the hidden layer, there is an extra input 1, and the activation function is chosen with the bipolar sigmoid:

$$f(\xi) = \frac{2}{1 + \exp(\xi_k)} - 1 \tag{7.16}$$

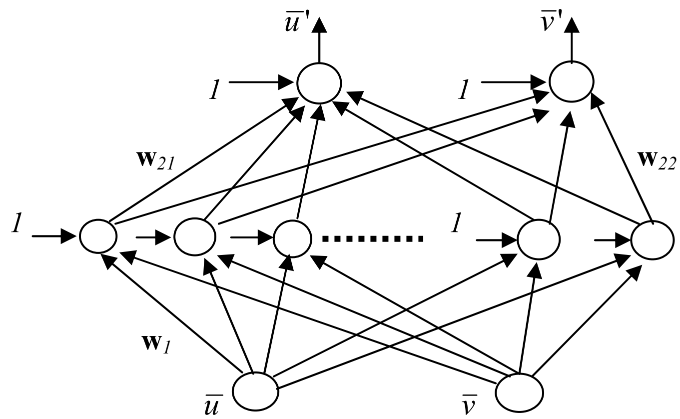

Figure 7.17 Network structure for image distortion correction

where $\xi_k = (\mathbf{w}_1)_k \cdot \mathbf{\Psi}$ (k=1, 2, ... $\overline{N}$, $\mathbf{\Psi} = (\overline{u}, \overline{v}, 1)^T$). For each neuron in the output layer, there is also an extra input 1, and the activation function could be the bipolar sigmoid. Here, we found that the error can be further minimized using following function:

$$f(\xi') = \xi' + \frac{(\xi')^3}{6} \tag{7.17}$$

where $\xi' = \mathbf{w}_2 \cdot \mathbf{h}_k$, with $\mathbf{h}_k$ representing outputs of the hidden neurons, $\mathbf{w}_2$ representing the $\mathbf{w}_{21}$, or $\mathbf{w}_{22}$, the weights from hidden neurons to output neuron $\overline{u}'$ and $\overline{v}'$. After defining the structure and the functions, we can train the network using the back-propagation learning rule. An example is the correction of distortion image of Figure 7.6. Figure 7.18 shows the training process of error vs. epochs. Figure 7.19 shows the results of error vs. neuron number. We can see the optimal neuron number is 12. And the corresponding weights are:

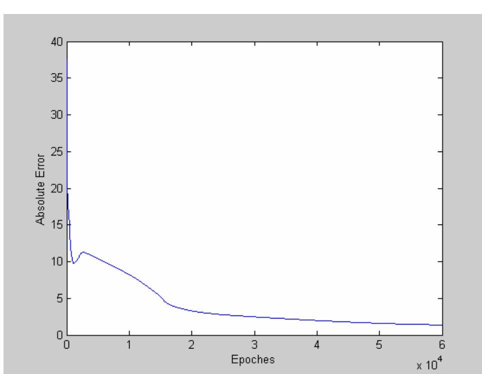

Figure 7.18 Network error vs. training epochs

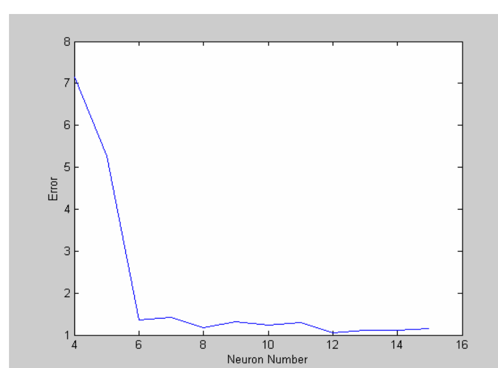

Figure 7.19 Accuracy vs. neuron number

$\mathbf{w}_1$=[-0.41 -0.029 -0.87; 8.76 -4.84 0.181; 0.76 0.107 1.14; -0.54 -0.76 -1.38;
-2.31 -0.95 -0.99; 0.87 -1.35 -0.68; -4.17 1.25 -1.49; 6.78 3.08 -0.076;
0.15 -0.02 0.508; 7.03 -3.25 -2.56; 3.67 0.75 -1.43; -0.51 -0.42 -0.43];

$\mathbf{w}_{21}$=[1.67 0.021 -3.61 -0.042 0.41 -1.27 -0.89 2.10 4.03 -0.19 -1.71 1.06 -0.18];

$\mathbf{w}_{22}$=[0.39 -0.43 -0.24 0.69 0.83 -1.11 -0.29 -2.47 -0.25 0.52 -1.28 -2.15 -0.46];

where $\mathbf{w}_1$ is a 12×3 matrix, which includes weights from inputs to hidden neurons; $\mathbf{w}_{21}$ and $\mathbf{w}_{22}$ are vectors from the hidden neurons to 2 outputs. Using these weights and determined network structure, the correction is realized. Figure 7.20 shows the corrected samples from those in Figure 7.6, and Figure 7.21 shows the corrected image from that of Figure 7.5.

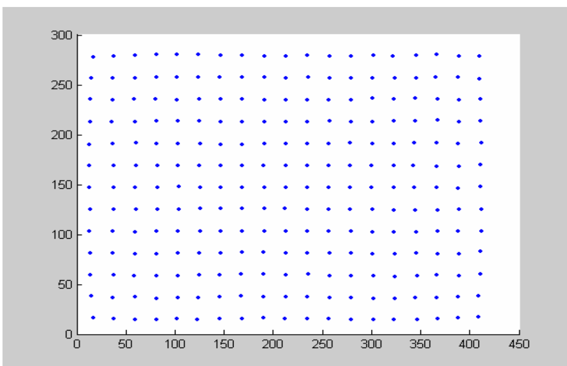

Figure 7.20 Corrected samples by NN

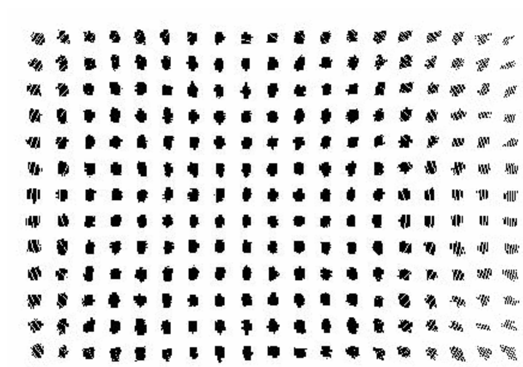

Figure 7.21 Corrected image by NN

7.2 Determining the Rotation and Transition by Image Correspondence (8-point Algorithm) [75~78, 110, 121]

Suppose a body is in motion in the half space z<0. Let $\mathbf{P}=(x, y, z)^T$ represent an arbitrary object point before motion and $\mathbf{P}'=(x', y', z')^T$ represent the same object point after motion. We have ($u=x/z$, $v=y/z$) and ($u'=x'/z'$, v'/z'), the projective coordinates of $\mathbf{P}$ and $\mathbf{P}'$ onto the image plane, where $z=f=1$, through the camera lens.

The rigid body motion equation relates $\mathbf{P}$ to $\mathbf{P}'$ is

$$\mathbf{P}'=\mathbf{R}_0\cdot\mathbf{P}+\mathbf{T}_0 \tag{7.18}$$

where R_0 is the 3×3 rotation matrix; T_0 is the translation vector $\mathbf{T}_0=[t_{x0} \ \ t_{y0} \ \ t_{z0}]^T$.

Now we can determine matrix $\mathbf{R_0}$ and unit vector $\mathbf{T}$ (collinear to $\mathbf{T_0}$) by finding correspondences in the two successive images. Here, we apply 8-point algorithm, which can be described as following steps (its proof is given in Appendix C).

A. Solve for the fundamental matrix

$$\mathbf{E} = \mathbf{T} \times \mathbf{R}_0 = \begin{bmatrix} \hat{h}_1 & \hat{h}_2 & \hat{h}_3 \\ \hat{h}_4 & \hat{h}_5 & \hat{h}_6 \\ \hat{h}_7 & \hat{h}_8 & \hat{h}_9 \end{bmatrix} \tag{7.19}$$

Denote the set of all (8 or more) observed image correspondence point pairs (u_i, v_i) $\Leftrightarrow$ ($u_i^{'}$, $v_i^{'}$), i=1,2, … , $\overline{M}$. Let

$$\boldsymbol{\omega}_i = [u_i^{'}u_i \quad u_i^{'}v_i \quad u_i^{'} \quad v_i^{'}v_i \quad v_i^{'}v_i \quad v_i^{'} \quad u_i \quad v_i \quad 1], \quad i=1,\ 2,\ \ldots 8,\ \ldots \overline{M}$$

$$\mathbf{U} = [\boldsymbol{\omega}_1 \ \boldsymbol{\omega}_2 \cdots \boldsymbol{\omega}_{\overline{M}}]^T$$

$$\mathbf{\Lambda} = [\hat{h}_1 \ \ \hat{h}_2 \ \cdots \ \hat{h}_9]^T$$

The solution of $\mathbf{\Lambda}$ is the unit eigenvector of $\mathbf{U^T U}$ associated with the smallest eigenvalue.

An important property of the fundamental matrix is its singularity in fact of rank 2. However, in most applications, the matrix $\mathbf{E}$ found by step ***A*** will not have rank 2. We can enforce the singularity constraint by correcting the $\mathbf{E}$ with $\mathbf{E}$' that minimizes the Frobenius norm $\left\| \mathbf{E} - \mathbf{E}^{'} \right\|$ subject to the condition det($\mathbf{E}'$) = 0. Thus, let $\mathbf{E} = \mathbf{V}\mathbf{D}\widetilde{\mathbf{V}}^T$ be the singular value decomposition of $\mathbf{E}$, where $\mathbf{D}$=$diag(s_1, s_2, s_3)$ satisfying $s_1 \geq s_2 \geq s_3$. Then let $\mathbf{E}^{'} = \mathbf{V} \cdot diag(s_1, s_2, 0) \cdot \widetilde{\mathbf{V}}^T$.

B. Decompose E *into transition vector* T *and rotation matrix* $\mathbf{R}_0$ (Appendix C.1)

1) The solution of $\mathbf{T}$ is a unit eigenvector of $\mathbf{E}\mathbf{E}^T$ associated with the smallest eigenvalue; and if $\sum [\mathbf{T} \times (X' \ \ Y' \ \ 1)^T]^T \cdot \mathbf{E}(X \ \ Y \ \ 1)^T < 0$, then $\mathbf{T} \leftarrow (-\mathbf{T})$.

2) If there is no noise, we have (see Appendix C.2)

$$\mathbf{R}_0 = [\mathbf{W}_2 \times \mathbf{W}_3,\ \mathbf{W}_3 \times \mathbf{W}_1,\ \mathbf{W}_1 \times \mathbf{W}_2] - \mathbf{T} \times \mathbf{E} \tag{7.20}$$

where $\mathbf{W}_1 = \mathbf{T}\times\mathbf{E}_1$, $\mathbf{W}_2 = \mathbf{T}\times\mathbf{E}_2$, $\mathbf{W}_3 = \mathbf{T}\times\mathbf{E}_3$, with $\mathbf{E}_1$, $\mathbf{E}_2$, and $\mathbf{E}_3$ being the column vector of **E.**

3) In the presence of noise, we find $\mathbf{R}_0$ such that

$$\|\mathbf{E}-[\mathbf{T}]_x\mathbf{R}_0\|_2 = \min \tag{7.21}$$

where

$$[\mathbf{T}]_x = \begin{bmatrix} 0 & -t_z & t_y \\ t_z & 0 & -t_x \\ -t_y & t_x & 0 \end{bmatrix} \tag{7.22}$$

Let $\mathbf{C} = [\mathbf{C}_1 \;\; \mathbf{C}_2 \;\; \mathbf{C}_3] = \mathbf{E}^T$, $\mathbf{D} = [\mathbf{D}_1 \;\; \mathbf{D}_2 \;\; \mathbf{D}_3] = [\mathbf{T}]_X^T$, and define 4×4 matrix **F** by

$$\mathbf{F} = \sum_{i=1}^{3}\mathbf{F}_i^T\mathbf{F}_i \tag{7.23}$$

where

$$\mathbf{F}_i = \begin{bmatrix} 0 & (\mathbf{C}_i-\mathbf{D}_i)^T \\ \mathbf{D}_i-\mathbf{C}_i & [\mathbf{D}_i+\mathbf{C}_i]_x \end{bmatrix} \tag{7.24}$$

and $[\mathbf{C}_i]_x$ and $[\mathbf{D}_i]_x$ are defined the same as that in (7.22). Let a quaternion $\mathbf{q} = (q_0 \;\; q_1 \;\; q_2 \;\; q_3)^T$ be the unit eigenvector of $\mathbf{F}$ associated with the smallest eigenvalue. The solution of $\mathbf{R}_0$ in $\|\mathbf{R}_0\mathbf{C}-\mathbf{D}\|_2 = \min$ is (see Appendix C.3)

$$\mathbf{R}_0 = \begin{bmatrix} q_0^2+q_1^2-q_2^2-q_3^2 & 2(q_1q_2-q_0q_3) & 2(q_1q_3+q_0q_2) \\ 2(q_1q_2+q_0q_3) & q_0^2-q_1^2+q_2^2-q_3^2 & 2(q_2q_3-q_0q_1) \\ 2(q_1q_3-q_0q_2) & 2(q_2q_3+q_0q_1) & q_0^2-q_1^2-q_2^2+q_3^2 \end{bmatrix} \tag{7.25}$$

7.3 Application to the real images

Using a wide view-angle camera, we got 7 images noted by "Sm1" ~ "Sm7" (Figure 7.22). Then we apply distortion correction on these images, and we obtain the seven new images "csm1"~ "csm7", shown in Fig.7.23. These images have some common spots because they originate from the same pattern. In addition, these spots have different

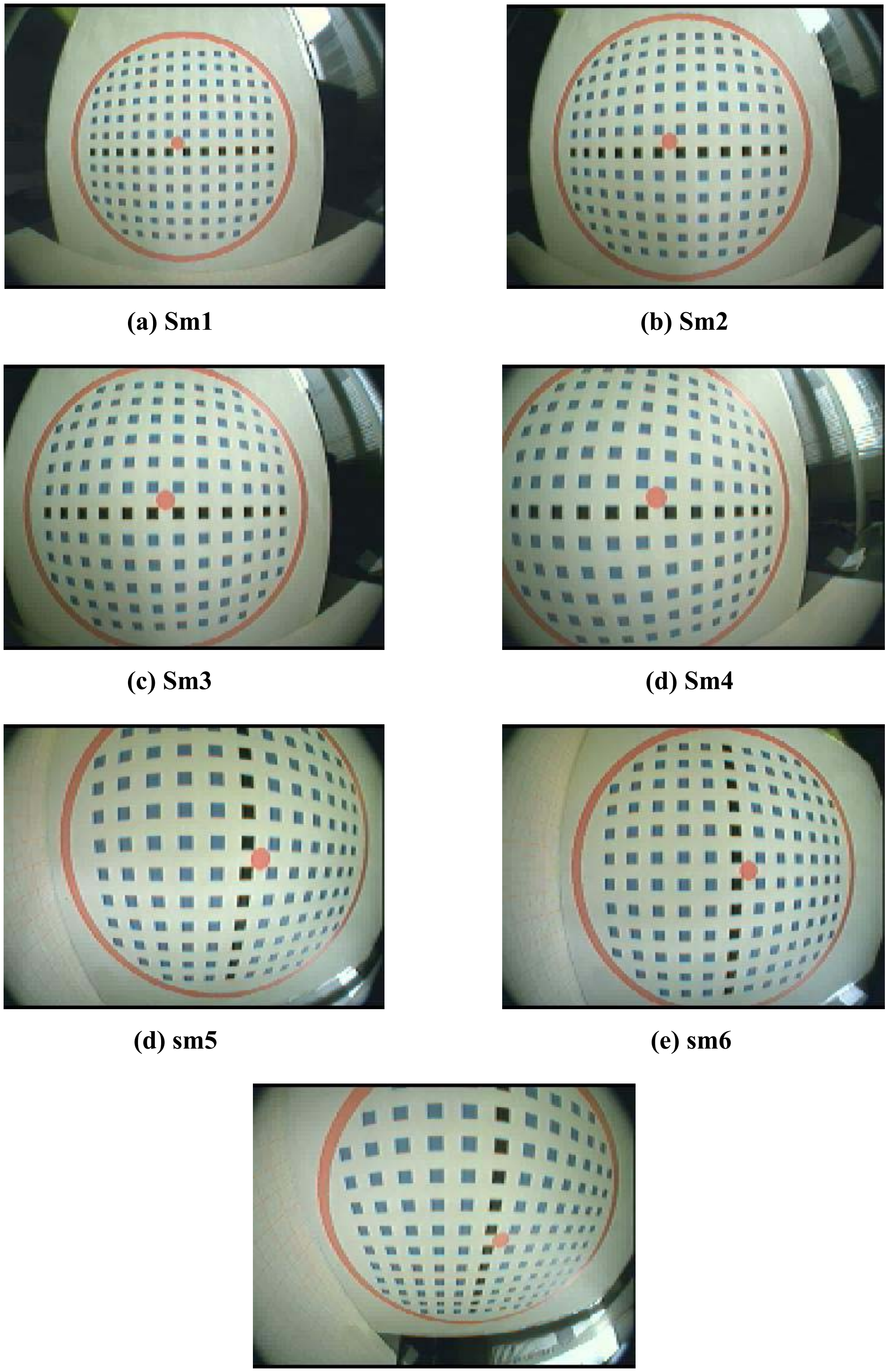

(a) Sm1 (b) Sm2

(c) Sm3 (d) Sm4

(d) sm5 (e) sm6

(g) sm7

Figure 7.22 Captured images with distortion using wide-view camera

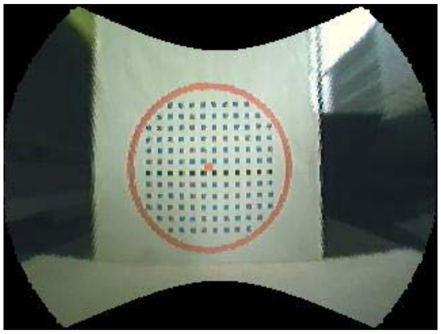

(a) Csm1

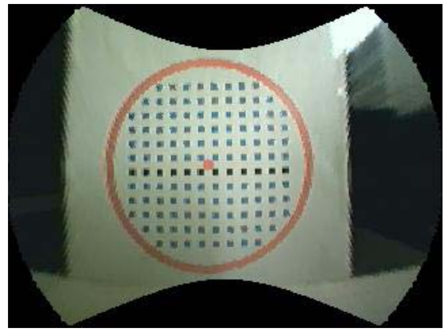

(b) Csm2

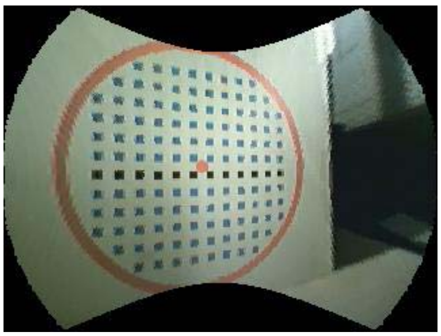

(c) Csm3

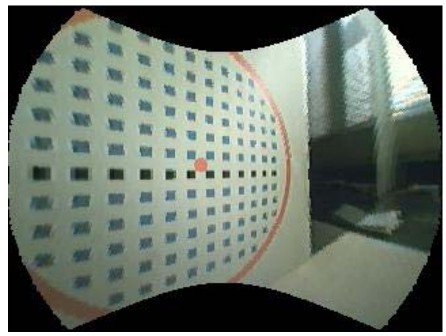

(d) Csm4

(d) Csm5

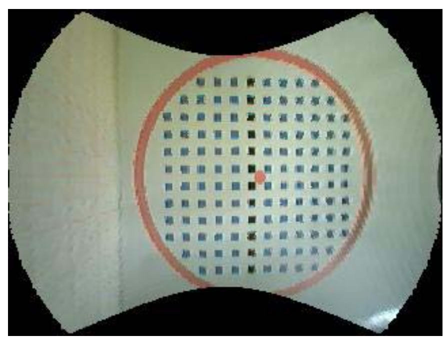

(e) Csm6

(g) Csm7

Figure 7.23 Images after distortion correction applying on “sm1”~ “sm7”

colours such that we can find corresponding spots based on the their relative locations, and determine the coordinates of the corresponding points by averaging the vertical and horizontal coordinates of all the points within the same spots. Table 7.1 shows the results, on which the datum on each cell (total 67 points, first 19 points are shown) represents the vertical and horizontal (x and y) coordinates (in pixel number) of the image. The 7 data on each row origin from a same spot, but different coordinates because there are the position shifting and rotation of the camera.

To apply the 8-point algorithm, we need to change above coordinate represented by pixel number to the coordinate relative to focal length (f=1). Figure 7.24 shows the image projection diagram. From the distortion correction algorithm, we can get the coordinate of the camera's imaging center. Then, the coordinates of the correspondence pairs can be changed to the projective coordinates onto the image plane, $z=f=1$. Since the camera has view angle θ=140º/2=70º, and the corresponding length of the imager is y_m (the pixel number corresponding to the angle θ), the relative coordinates in horizontal direction (with respect to focal length f) is

$$v = \frac{\Delta y'}{f} = \frac{y_c}{y_m}\tan(70°)$$

and the relative coordinates in vertical direction (with respect to focal length f) is

$$u = \frac{\Delta x'}{f} = \frac{x_c}{y_m}\tan(70°)$$

where $\Delta y'$ and $\Delta x'$ are the absolute horizontal (y-) and vertical (x-) coordinates with respect to the image center, y_C and x_C are the pixel coordinates corresponding to same point.

Assume that the camera moves and rotates in a procedure as "csm1" → "csm2" → "csm3" → "csm4" → "csm5" → "csm7" → "csm6", we can calculate the rotation matrices corresponding to the rotation of the successive two images, using 8-point algorithm. Table 7.2 shows the results. We can find the rotation angle of the camera along its central axis and the rotation angle of this axis using the rotation decomposition method. We first assume the initial camera's orientation be $\vec{\mathbf{r}}_1 = (m_1\ n_1\ p_1)^T$, in which the image "sm1" is captured, and also assume that the *i*-step camera's rotation can be represented by rotation angle θ_i (the rotation of the camera's central axis from $\vec{\mathbf{r}}_i = (m_i \ n_i \ p_i)^T$ to

Table 7.1 Point matching for "csm1" ~ "csm7"

Number	Co_sm1	Co_sm2	Co_sm3	Co_sm4	Co_sm5	Co_sm6	Co_sm7
1	121.0, 151.4	120.0, 147.8	119.3, 147.0	117.8, 142.6	118.8, 191.8	124.2, 185.8	129.1, 186.3
2	125.2, 156.4	125.5, 154.0	125.6, 152.6	124.9, 149.9	125.5, 185.0	130.2, 180.1	133.7, 180.2
3	125.1, 148.6	125.4, 143.0	125.5, 141.0	125.2, 136.2	110.9, 185.4	118.5, 180.0	124.5, 182.1
4	116.3, 148.2	114.4, 142.8	112.8, 140.9	110.5, 135.5	110.6 ,200.4	118.0 ,192.2	124.3, 194.6
5	116.2, 155.9	114.0, 153.5	113.0, 153.0	110.7, 149.5	125.5 ,198.9	130.2, 192.1	133.6, 191.2
6	125.0, 165.5	125.0, 163.5	125.5, 165.0	124.7, 160.9	138.8, 184.0	143.2, 180.6	142.4, 179.1
7	133.0, 165.0	135.4, 163.8	136.6, 164.4	137.4, 161.4	139.1, 170.3	143.5, 168.1	142.2, 168.1
8	134, 156	135.8, 153.5	137.8, 153.3	138.5, 149.5	126.0, 170.5	130.5, 168.5	134.0, 169.0
9	133.6, 148.6	135.6, 143.2	138.0, 141.0	139.0 ,135.5	110.5 ,171.0	118.1, 168.4	124.5 ,169.5
10	133.5 ,139.8	136, 133	138.1, 128.5	140.0 ,120.4	94.4, 171.9	105.5, 168.0	112.7, 170.6
11	125.2 ,139.7	125.6, 132.8	125.5, 128.0	125.4, 119.4	95.0 ,186.4	105.4 ,180.3	112.1, 184.4
12	116.6, 139.6	114.5, 133.0	112.9, 127.9	109.2, 120.2	94.6, 202.1	105.1, 191.6	112.9, 197.4
13	108.5, 139.5	103.9, 132.2	100.1 ,128.3	94.5, 120.6	95.3 , 218.0	105.1, 203.4	112.4 ,210.5
14	108.3 ,148.5	103.6 ,142.9	100.6, 140.9	95.8 ,136.1	111.2 ,214.1	118.6, 203.8	124.4, 205.6
15	108.6, 156.2	103.5 ,153.5	101.1, 152.6	97.5, 149.5	125.7 ,211.9	130.4, 203.7	133.6, 202.0
16	108.1 ,164.1	103.6 ,163.6	101.4, 164.4	99.5, 161.0	138.3 ,209.7	142.7 ,203.7	141.4 ,199.3
17	116.0 ,164.5	114.0 ,163.5	113.4 ,164.4	111.3, 161.0	138.8 ,196.3	143.0 ,191.6	141.4, 189.1
18	124.5 ,173.7	124.9 ,174.9	125.3 ,175.5	124.6 ,172.6	150.5 ,182.5	155.5, 180.0	149.7, 176.6
19	133.8, 173.1	135.4, 174.6	136.8, 176.0	136.7, 172.5	150.8 ,169.7	155.1, 167.9	149.3 ,168.2
…	…	…	…	…	…	…	…

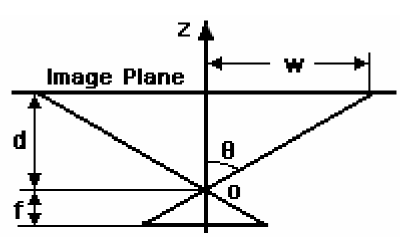

Figure 7.24 Image coordinate projection

$\vec{\mathbf{r}}_{i+1} = (m_{i+1}\ n_{i+1}\ p_{i+1})^T$) and α_i (the rotation of the camera around its central axis) for *i=1, 2, ... N*. As discussed in Section 3.3, these two angles and the $\vec{\mathbf{r}}_{i+1} = (m_{i+1}\ n_{i+1}\ p_{i+1})^T$ can be computed using quaternion method. Table 7.3 shows the results. We can see that the rotation angle α_i has relatively high accuracy, although the calculation results of θ_i are observed to have a larger error.

Table 7.2 Rotation matrices of the successive two images

Successive two images	Rotation Matrix	Transition Vector
"csm1" → "csm2"	0.9996 -0.0132 -0.0241 0.0117 0.9980 -0.0622 0.0249 0.0619 0.9978	-0.1264 -0.1536 0.9800
"csm2" → "csm3"	0.9992 0.0192 -0.0358 -0.0222 0.9960 -0.0867 0.0340 0.0875 0.9956	0.3299 0.6159 -0.7154
"csm3" → "csm4"	0.9997 0.0124 -0.0198 -0.0150 0.9904 -0.1371 0.0179 0.1373 0.9904	0.1296 0.7899 -0.5994
"csm4" → "csm5"	-0.1057 0.9772 0.1842 -0.9255 -0.1644 0.3411 0.3636 -0.1344 0.9218	0.3228 -0.5456 -0.7734
"csm5" → "csm8"	0.9816 0.1089 0.1567 -0.0969 0.9919 -0.0827 -0.1645 0.0660 0.9842	0.0154 -0.5662 -0.8242
"csm8" → "csm6"	0.9926 -0.1215 -0.0083 0.1214 0.9925 -0.0142 0.0100 0.0131 0.9999	-0.0444 0.5961 0.8017

Here our main objective is to determine the rotation angle α_i because it cannot be obtained using magnet's localization and orientation algorithm. Therefore, the results are acceptable. However, if we want improve the localization and orientation accuracy using this imaging method, there is still much work to do. Because the error is mainly from image distortion and the matching error of the corresponding points of the successive two images, we can implement the problems on:

1) Finding more reasonable calibration techniques to determine the camera parameters;

2) Combining the camera's distortion correction into the calibration algorithm to achieve better accuracy;
3) Finding an efficient matching technique to accurately determine the correspondence points on the successive images.
4) Applying appropriate signal processing algorithm to filter the noises or interferences on the image;
5) Finding some effective recursive algorithm to improve the matching algorithm.

Table 7.3 Rotation angle and orientation of the camera

Successive 2 images	Initial orientation $\vec{\mathbf{r}}_i$	θ_i (°)	Resultant orientation $\vec{\mathbf{r}}_{i+1}$	α_i (°)	Progressive Error (α_i)
"csm1" → "csm2"	[0 0 1]'	3.82	-0.024, -0.062, 0.998	0.714	0.71°
"csm2" → "csm3"	-0.024, -0.062, 0.998	5.39	-0.061, -0.148, 0.987	-1.183	-0.47°
"csm3" → "csm4"	-0.061, -0.148, 0.987	7.92	-0.082, -0.281, 0.956	-1.099	-1.57°
"csm4" → "csm5"	-0.082, -0.281, 0.956	42.98	-0.090, 0.449, 0.889	-92.65	-4.22°
"csm5" → "csm8"	-0.090, 0.449, 0.889	11.72	0.100, 0.380, 0.920	-1.514	-5.73°
"csm8" → "csm6"	0.100, 0.380, 0.920	3.15	0.046, 0.376, 0.925	6.297	0.57°

(θ_i is the rotation angle of the camera's central axis from $\vec{\mathbf{r}}_i = (m_i \ n_i \ p_i)^T$ to $\vec{\mathbf{r}}_{i+1} = (m_{i+1} \ n_{i+1} \ p_{i+1})^T$ around the axis given by $\vec{\mathbf{r}}_i \times \vec{\mathbf{r}}_{i+1}$, and α_i is the rotation around the camera's axis)

7.4 Conclusion

Realizing capsule localization and orientation by imaging methods has its advantages, which does not require additional equipment as it is realized only by the endoscopic images. In this Chapter, I present the techniques for camera distortion correction and the 8-point algorithm for determining the camera's rotation and transition.

1) For the distortion correction, I propose a calibration pattern using dots and a circle, such that the computation procedure can be simplified. While using the neural network technique, we can correct any types of image distortion, and not only the pre-assumption that the distortion is radial about the distortion center.

2) For the imaging localization and orientation, I use the 8-point algorithm. This is a linear algorithm using 8 or more correspondent points on the consecutive images. Also this is an absolute computation method which can be applied for case of the large changes of the camera's position and orientation.

Finally, the 8-point algorithm is applied to the real images taken in a sequence with different camera's position and orientation, and results show that:

1) For an acceptable accuracy, 8 correspondent points are not enough, and more 3points are preferable.
2) The result of orientation is more accurate than that of the position transition, because there are noises, distortion and calibration errors.
3) Through the rotation decomposition, we get the rotation of the camera's axis and the rotation along this axis, and we found that the latter has better accuracy. This result is satisfactory because the magnetic orientation can not provide this information, and it can be a complementary method to find true 3D rotation parameters.

Chapter 8

Conclusions and Future Work

8.1 Conclusions

To build a new robotic wireless capsule endoscope, we propose a localization and orientation system. It makes it possible to track the capsule movement in real-time mode such that the doctor can realize the external actuation and determine proper medical measures with respect to the specific endoscope location. Besides, based on the accurate localization/orientation information of the capsule, we can realize the 3D image recovery of some interesting GI tissues, so that more accurate diagnosis can be made. In this thesis, I present a localization and orientation technique using magnetic technique, which is complemented with imaging technique, and the our main work includes:

1) Proposing a magnetic localization and orientation technique [27, 55]

A magnetic localization and orientation technique has been proposed to be applied to the capsule endoscope. It is suitable for the GI test in the human body because the human body does not affect the static magnetic field created by the magnet such that high tracking accuracy can be obtained. It does not have negative effect on the human body. No internal power is required to build the magnetic field. In addition, it has very small volume, and the expense of this system is low comparing with other test machines (CT, MRI, 3D-US).

2) Finding a robust nonlinear algorithm for magnetic localization and orientation [55]

The magnetic field created by a magnet is a 5D high-order nonlinear function of the magnet's position and orientation. We can use (5 or more) magnetic sensors to measure the magnetic fluxes in the specific spatial points (out of the human body), and to compute the magnet's 5D localization and orientation parameters with an appropriate nonlinear algorithm. Several nonlinear optimization algorithms could be applied to solve such a nonlinear problem. However, the nonlinear algorithm needs predetermined initial guesses for these parameters, and the algorithm might fail to give correct results. Therefore, I tried several optimization methods, and found that Levenberg-Marquardt method (nonlinear least squares solution) is an appropriate one for its robustness against the errors in the initial guess and noises, and fast speed.

3) Proposing a linear algorithm for magnetic localization and orientation [122]

One of the most successful research that have been done is the new linear algorithm for finding the 5D position and orientation parameters of the magnet. Unlike other linear algorithms that were derived upon some approximations, our algorithm is derived from the absolute vector computation. With the data from five (or more) 3-axis magnetic sensors, this algorithm results in a solution of the position and orientation of the magnet by matrix computations. This algorithm doesn't need initial guesses for the magnet's the position and orientation, as the nonlinear algorithm does, and it could provide correct solutions in most cases (unless there is singularity). It can also provide faster speed (about 20~100 times of that in nonlinear algorithm) so that some signal processing can be applied to get higher localization accuracy. The experiment results show it reliable. I have not found such an algorithm being reported in any other paper.

4) Realization of the testing system [124]

A real magnetic sensing system was set up, which can realize real-time tracking of the capsule endoscope. I tried several types of sensors, e.g., Hall sensor, GMR sensors, and AMR sensors, and found that the Honeywell product, the 3-axis AMR sensor, HMC1053, is appropriate for the sensing system (with high sensitivity and accuracy). A sensor system, which consists of AMR sensor array, amplifier circuits, ADC, and computer, was built and some tests have been done. The results show that it is possible to obtain higher localization and orientation accuracy if there are enough sensors with appropriate calibration methods. When the magnet (Φ4.5×9 mm) moves within the area of the sensor array and 100mm over the sensor array plane, the localization error is within 10 mm and the average error is 3.3 mm, while the orientation error is within 5.7° and average error is 3.0°.

5) Localization and orientation from image processing [119, 123]

Imaging techniques can also provide localization and orientation messages. Some initial work has been done to find the camera's (2D) localization and (3D) orientation by applying distortion correction technique and the "8-point algorithm" to the correspondence points obtained in two successive images. For the image distortion correction, a calibration pattern using dots and a circle with different colors is presented, such that the computation procedure can be simplified. Also the neural network technique is applied, such that any types of image distortion can be corrected, besides the distortion that is radial about the distortion center. The imaging technique results in true 3D rotation information, while magnetic method can provide 2D orientation message relative to the rotation of the capsule's central axis. We need to fuse the sensing messages from these two techniques, and I present a method to do the rotation decomposition using quaternion, which decompose a (3D) rotation into two rotations: the rotation around the capsule's central axis and the rotation around this axis.

8.2 Future work

In this thesis, I present the localization and orientation technique for the capsule endoscope. With the proposed sensor system and corresponding algorithm, we can realize the localization and orientation of the capsule with required accuracy. However, there are still some measures to improve this technique, and much work should be done in the near future:

1) Up to now, we do the experiment using the magnet only. The next step is to include the magnet in the capsule endoscope, and its effects must be investigated on the image capture and the RF signal for radio transmission.

2) To apply this system to real endoscopic test on human bodies, we need to do more experiments on the mutual effects of the system to the human body, and vise versa.

The possible problems include: movement of the human body (or organs) on the localization and orientation accuracy, and the interferences induced by the human body and environment devices.

3) We need to find an efficient (accurate and fast) technique to determine the image correspondences. The imaging localization and orientation algorithm, i.e., the 8-points algorithm, depends on the matching accuracy of the correspondence point pairs. This is an interesting topic to investigate the characteristics of the endoscopic images, to provide some diagnosis data, e.g., the size, shape of some particular tissues. Much work should be done in this area.

4) To realize the robotic endoscope system, an external magnetic field is applied to drive the capsule (with a magnet). Obviously, we can not do magnetic localization simultaneously. Therefore, a time-sharing scheme should be proposed, such that the external actuation and localization happen in different intervals. The localization system must be compatible to the actuation system for maintaining its accuracy.

5) For the new capsule endoscope, we should develop new system to effectively fuse different sensing data: the results from magnetic technique, and those by the imaging technique. The combination of these two techniques will results in more complete, more accurate localization and orientation of the capsule endoscope. Nevertheless, another interesting application, 3D image recovery of the GI tract can be further realized, based on the accurate localization and orientation using these two techniques.

Bibliography

[1] Nimish Vakil, and Abboud Affi, "Endoscopy", Encyclopedia of Imaging Science and Technology, Vol.1, John Wiley & Sons, New York, 2002.

[2] Gavriel Iddan, Gavriel Meron, Arkady Glukhovsky, Paul Swain, "Wireless Capsule Endoscopy", Nature, Vol. 405, No. 6785, p.417, May, 2000.

[3] Koji Ikuta, Masahiro Tsukamoto, and Shigeo Hirose, "Shape Memory Alloy Servo Actuator System with Electric Resistance Feedback and Application for Active Endoscope", Proc. of IEEE Int. Conf. on Robotics and Automation, Philadelphia, PA.,USA, April 24~29,1988, pp.427~430.

[4] P. Dario et al., "A Micro Robottic System for Colonscopy", Proc. Of IEEE Int. Conf. on Robotics and Automation, Albuquerque, New Mexico, USA, April, 1997, pp.1567~1572.

[5] L. Phee, A. Arena, S. Gorini, A. Menciassi, P. Dario, Y.K. Jeong and J.O.Park,, "Development of Micro-robotic Devices for Locomotion in the Human Gastrointestinal Tract", International Conference on Computational Intelligence, Robotics and Autonomous Systems (CIRAS 2001), November 28-30, 2001, Singapore, http://robot.kist.re.kr/~ykjeong/papers/ciras20011.pdf.

[6] Paolo Dario, Pasquale Ciarletta, Arianna Menciassi, and Byungkyu Kim, "Modelling and Experimental Validation of the Locomotion of Endoscopic Robots in the Colon", http://www.iser02.unisa.it/papers/92.pdf.

[7] A. Brett Slatkin, Joel Burdick, "The Development of a Robotic Endoscope", Proceedings of the 2002 IEEE/RSJ Int. Conf. on Intelligent Robots and Systems, Aug.5~9, 1995, Pittsburgh, Pennsylvania, USA, pp2162~2171.

[8] A. Menciassi, J. H. Park, S. Lee, S. Gorini1, P. Dario1, J.O. Park, "Robotic Solutions and Mechanisms for a Semi-Autonomous Endoscope", Proceedings of the 2002 IEEE/RSJ Int. Conf. on Intelligent Robots and Systems, EPFL, Lausanne, Switzerland, October, 2002, pp. 1379~1384.

[9] S. Kumar, I. M. Kassim, and V. K. Asari, "Design of a vision-guided microrobotic colonscopy system", Advanced Robotics, Vol.14, No.2, pp87~104, 2000.

[10] Young Mo Lim, Jinhee Lee, Jisang Park, Byungkyu Kim, Jong-Oh Park, Soo Hyun Kim, and Yeh-Sun Hong, "A Self-Propelling Endoscopic System", Proceedings of the 2001 IEEE/RSJ

International Conference on Intelligent Robots and Systems Maui, Hawaii, USA, Oct. 29 - Nov. 03, 2001, pp. 1117~1122.

[11] Dominiek Reynaerts, Jan Peris, and Hendrik Van Brussel, “Shape memory micro-actuation for a gastro-intestinal intervention”. Sensors and Actuators, Vol.77, 1999, pp.157~166.

[12] J. Peris, D. Reynaerts, and H. Van Brussel, “A miniature manipulator for integration in a self-propelling endoscope”. Sensors and Actuators A, 92, 2001, pp.343~349.

[13] J. Peris, D. Reynaerts, and H. Van Brussel, “Design of miniature parallel manipulators for integration in a self-propelling endoscope”. Sensors and Actuators, 85, 2000, pp.409~417.

[14] J.D. Waye, “Small-Intestinal Endoscopy”, Endoscopy, Vol.33, No.1, 2001, pp.24~30.

[15] V. K. Zworkin, “A Radio pill”, Nature, 179**,** 898 (1957).

[16] R. S. Mackay, and B. Jacobson, “Endoradiosonde”, Nature 179**,** 1239–1240 (1957).

[17] G. D. Meron, “The Development of the swallowable video capsule (M2A)”, Gastrointestinal Endoscopy, Vol.52, No.6, Dec., 2000, pp.817~819.

[18] Arkady Glukhovsky, “Wirless capsule endoscopy”, Sensor Review; 23(2): 128~133, 2003.

[19] D. G. Adler, and C. J. Gostout, “Wirless capsule endoscopy”, Hospital Physician, May, 2003, pp.14~22.

[20] G. G. Ginsberg, A. N. Barkun, J. J. Bosco, G. A. Isenberg, C. C. Nguyen, B. T. Petersen, W. B. Silverman, A. Slivka, and G. Taitelbaum, “Wireless capsule endoscopy”, Gastrointestinal Endoscopy, Vol.56, No.5, Nov., 2002, pp.621~624.

[21] Zvi Fireman, Arkady Glukhvsky, Harold Jacob, Alexandra Lavy, Shlomo Lewkowicz, and Eitan Scapa, “Wireless Capsule Endoscopy”, IMAJ, Vol. 4, pp717-719, Sep., 2002.

[22] D. E. Fleischer, “Capsule endoscopy: The voyage is fantastic- will it change what we do?”, Gastrointestinal Endoscopy, Vol.56, No.3, 2002, pp.452~456.

[23] NORIKA3, RF Co., Ltd. T/A RF SYSTEM lab. http://www.rfnorika.com/e_system/e_system_001.html.

[24] Olympus Medical Systems Corporation, "Development of Capsule Endoscope and Peripheral Technologies for further Expansion and Progress in Endoscope Applications", http://www.olympus.co.jp/en/news/2004b/nr041130capsle.cfm.

[25] Intelligent Microsystem Center, "Endoscopic Micro-capsule", http://www.microsystem.re.kr/main_eng/menu04/sub_menu01.asp#01.

[26] F. Cepolina, and R. C. Michelini, “Robots in Medicine: A Survey of In-body Nursing AIDS. Introductory overview and concept design hints”, Proc. of ISR 2004, 35 International Symposium on Robotics, 23-26 March 2004, Paris, France.

[27] Max Q.-H. Meng, Tao Mei, Jiexin Pu, Chao Hu, Xiaona Wang, and Yawen Chan, “Wireless Robotic Capsule Endoscopy: State-of-the-Art and Challenges”, Proceedings of the 5th World Congress on Intelligent Control and Automation. Vol.6, June 15-19, 2004, pp.5561~5565.

[28] Zvi Fireman, Arkady Glukhovsky, and Eitan Scapa, “Future of capsule endoscopy”, Gastrointestinal Endoscopy Clinics of North America, 14(2004), pp.219~227.

[29] A. Menciassi, C. Stefanini, S. Gorini, G. Pernorio, P. Dario, B. Kim, and J. Park, "Legged Locomotion in the Gastrointestinal Tract", Proceedings of 2004 IEEE/RSJ International Conference on Intelligent Robots andSystems, p. 937-942, 2004.

[30] Byungkyu Kim, Sunghak Lee, Jong Heong Park, and Jong-Oh Park, “Design and Fabrication of a Locomotive Mechanism for Capsule-Type Endoscopes Using Shape Memory Alloys (SMAs)”, IEEE/ASME Transactions on Mechatronics, Vol. 10, No. 1, FEB. 2005, pp77~86.

[31] Kyoung-chul Kong, Jinhoon Cha, and Doyoung Jeon,and Dong-il Dan Cho, “A Rotational Micro Biopsy Device for the Capsule Endoscope”, 2005 IEEE/RSJ International Conference on Intelligent Robots and Systems, pp. 3057~3061, Edmonton, Canada, 2005.

[32] Feng Gong, Paul Swain, and Timothy Mills, “Wireless endoscopy”, Gastrointestinal Endoscopy, Vol.51, No.6, June, 2000, pp.725~729.

[33] C. A. Mosse, T. N. Mills, M. N. Appleyard, S. S. Kadirkamanathan, and C. P. Swain, “Electrical stimulation for propelling endoscopes”, Gastrointestinal Endoscopy, Vol.54, No.1, July, 2001, pp.79~82.

[34] Shuxiang Guo, Yasuhiro Sasaki, and Toshio Fukuda, “A New Kind of Microrobot in Pipe Using Driving Fin”, Proc. Of the 2003 IEEE/ASME Int. Conf. on Advanced Intelligent Mechatronics, Kobe, Japan, 2003, pp.697~702.

[35] Toshio Fukuda, Hidemi Hosokai, Hiroaki Ohyama, Hideki Hashimoto, and Fumihito Arai, “Giant Magnetostrictive Alloy (GMA) Application to Micro Mobile Robot as a Micro Actuator without Power Supply Cables”, Proc. Of IEEE Conf. on Microelectro Mechanical Systems, Ohio, 1990, pp.210~215.

[36] M. Sendoh, K. Ishiyama, and K.-I. Arai, “Fabrication of magnetic actuator for use in a capsule endoscope,” IEEE Trans.On Magnetics, vol.39, no.5, September 2003, pp.3232~3234.

[37] Byungkyu Kim, Sunghak Lee, Jong Heong Park, and Jong-Oh Park, "Design and Fabrication of a Locomotive Mechanism for Capsule-Type Endoscopes Using Shape Memory Alloys (SMAs)", IEEE/ASME Transactions on Mechatronics, Vol. 10, No. 1, FEB. 2005, pp77~86.

[38] M.Feldman, H. J. Smith, and T. R. Simon, "Gastric Empting of Solid Radioopaque Markers: Studies in Healthy Subjects and Diabetic Patients." Gastroenterology, vol. 87, 1984, pp. 895~902.

[39] D. Dey, D. G. Gobbi, P. J. Slomka, K. J.M. Surry, and T. M. Peters, "Automatuc Fusion of Freehand Endoscopic Brain Images to Three-Dimensional Surfaces: Creating Stereoscopic Panoramas". IEEE Trans. On Medical Imaging, Vol.21, No.1, Jan. 2002.

[40] Damini Dey, Piotr J. Slomka, David G. Gobbi, and Terence M. Peters, "Mixed Reality Merging of Endoscopic Images and 3-D surfaces", Proceedings of MICCAI 2000, Pittsburgh, USA, Oct.11~14, 2000, pp.796~803.

[41] Fabien Mourgues, Frederic Devernay, and Eve Coste-Maniere, "3D reconstruction of the operating field for image overlay in 3D-endoscopic surgery", Proceedings of the IEEE and ACM International Symposium on Augmented Reality, http://csdl.computer.org/comp/proceedings/isar/2001/1375/00/13750191.pdf.

[42] Niko Pagoulatos, Warren S. Edwards, and Yongmin Kim, "Interactive 3-D Registration of Ultrasound and Magnetic Resonance Images Based on a Magnetic Position Sensor", IEEE Trans. On Information Tech. in Biomedicine, Vol.3, No.4, Dec. 1999, pp.278~288.

[43] Liu Jie, Gao Shangkai,Gao Xiaorong,Wang Yiding, Li Zheng, Zhou Jinghao, "Calibration of 3D ultrasound imaging system based on magnetic position sensor". Qinghua Daxue Xuebao Journal of Tsinghua University. Vol.41, No.9, pp18-21, Sep. 2001.

[44] D. F. Leotta, P. R. Detmer, and R. W. Martin. "Performance of a miniature magnetic position sensor for three-dimensional ultrasound imaging". Ultrasound in Medicine & Biology, Vol.23, No.4, pp.597~609, 1997.

[45] P. R. Detmer, G. Bashein, T. Hodges, K. W. Beach, E. P. Filer, D. H. Burns, and D. E. Strandness, "3D Ultrasonic Image Feature Localization Based on Magnetic Scanhead Tracking: In Vitro Calibration and Validation", Ultrasound in Med. & Biol., Vol.20, No.9, 1994, pp.923~926.

[46] A. Fritscher-Ravens, and C. P. Swain, "The Wireless Capsule: New Light in the Darkness", Digestive Diseases, 20(02002), pp.127~133.

[47] Doron Fischer, Reuven Schreiber, Daphna Levi, and Rami Eliakim, "Capsule endoscopy: the localization system", Gastrointestinal Endoscopy Clinics of North America, 14(2004), pp.25~31.

[48] F. H. Raab, E. B. Blood, T. O. Steiner, and H. R. Jones. "Magnetic Position and Orientation Tracking System", IEEE Trans. On Aerospace and Electronic Systems, Vol.AES-15, No.5, 1979, pp.709~718.

[49] Eugene Paperno, Ichiro Sasada, and Eduard Leonovich. "A new Method for Magnetic Position and Orientation Tracking". IEEE Trans. On Magnetics, Vol.37, No.4, 2001, pp. 1938 ~1940.

[50] H. P. Kalmus, "A New Guiding and Tracking System", IRE Trans. On Aerospace and Navigational Electronics. Vol.9, March, 1962, pp.7~10.

[51] Eric Prigge, and Jonathan How, "An Indoor Absolute Positioning System with No Line of Sight Restrictions and Building-Wide Coverage", Proc. Of the 2000 IEEE International Conf. On Robotics & Automation", San Francisco, CA, April 2000, pp. 1015~1022

[52] Yoshiaki Yamada, Noriaki Yoshida, Kazuhida Kobayashi, and Kiyotaka Yamauchi, "An application of magnet and magnetic sensor: measurement system for tooth movement", IEEE Transactions on biomedical engineering, vol.37, no.10, 1990, pp.919~923.

[53] M. Akutagawa, Y. Kinouchi, H. Nagashino, "Application of neural networks to a magnetic measurement system for mandibular movement", Proceedings of the 19th annual international conference of the IEEE Engineering in Medicine and Biology Society, Vol.20, No.4, pp.1932~1935.

[54] D. F. Leotta, P. R. Detmer, and R. W. Martin. "Performance of a miniature magnetic position sensor for three-dimensional ultrasound imaging". Ultrasound in Medicine & Biology, Vol.23, No.4, ,1997, pp.597~609.

[55] Chao Hu, Max Q.- H. Meng, Mrinal Mandal, Efficient Magnetic Localization and Orientation Technique for Capsule Endoscopy. International Journal of Information Acquisition, Vol.2, No.1, March, 2005, pp. 23~36.

[56] Xiaona Wang, Max Q.-H. Meng, and Yawen Chan, **"**A low-cost tracking method based on magnetic marker for capsule endoscope**",** IEEE 2004. Proceedings. International Conference on Information Acquisition, 21-25 June 2004, pp.524 – 526.

[57] E. H. Feri, Y. B., S. Terushalmi, and F. Dreyfuss, “Measurements of the Emptying of the Stomach with a Magnetic Tracer Marterial”, IEEE Trans. On Magnetics, Vol. MAG-6, No.2, June, 1970, pp.348~349.

[58] E. Osmanoglou, O. Kosch, V. Hartmann, A. Strenzke, L. Trahms, W. Weitschies, B. Wiedenmann, and H. Mönnikes, “Magnetic marker monitoring allows to characterize effects of exogenous factors on esophageal transit of solid drug forms. Proceedings of the 13th International Conference on Biomagnetism, 2002.

[59] Weitschies W, Wedemeyer J, Stehr R, Trahms L. “Magnetic markers as a noninvasive tool to monitor gastrointestinal transit.” IEEE Trans. Biomed Eng. Feb., 1994;41(2):192-5.

[60] Werner Weitschiles, Roman Kotitz, DinoCordini, and Lutz Trahms. “High-Resolution Monitoring of the Gastrointestinal Transit of a Magnetic Marked Capsule”. Journal of Pharmaceutical Sciences, Vol. 86, No. 11, November 1997, pp. 1218~1222.

[61] W. Weitschies, M. Karaus, D. Cordini, L. Trahms, J. Breitkreutz, and W. Semmler ”Magnetic marker monitoring of disintegrating capsules”. European Journal of Pharmaceutical Scieces. July 2001;13(4):411-416.

[62] Dietmar Drung, “The PTB 83-SQUID System for Biomagnetic Applications in a Clinic”, IEEE Trans. On Applied Superconductivity, Vol. 5, No. 2, June, 1995, pp. 2112~2117.

[63] N. M. Prakash, and F. A. Spelman, “Localization of a magnetic marker for GI motility studies: an in vitro feasibility study”, Proceedings of the 19th annual international conference of the IEEE Engineering in Medicine and Biology Society, Oct.30-Nov.2, 1997, Chicago, IL. USA, pp.2394~239.

[64] V. Schlageter, P.-A. Besse, R.S. Popovic, and P. Kucera, “Tracking system with five degrees of freedom using 2D-array of Hall sensors and a permanent magnet”, Sensors and Actuators A 92 (2001), pp.37~42.

[65] E. Stathopoulos, V. Schlageter, B. Meyrat, Y. De Ribaupierre, and P. Kucera, “Magnetic Pill Tracking: a Novel Non-invasive tool for Investigation of Human Digestive Motility”. Neurogastroenterology and Motility, Vol. 17, No. 1, February 2005, pp. 148~154.

[66] Wilfried Andra, Henri Danan, Walter Kirmße, Hans-Helmar Kramer, Pieter Saupe, Rainer Schmieg, and Matthias E Bellemann, “A novel method for real-time magnetic marker monitoring in the gastrointestinal tract”, Physics in Medicine and Biology, 45 (2000) 3081–3093.

[67] D. K. Cheng. “Field and Wave Electromagnetics: Static Magnetic Fields”. Addison-Wesley Publishing. 1989.

[68] R. S. Ingarden, and A. Jamiolkowski, “Classical Electrodynamics”, Elsevier Science Publishers B.V., Poland, 1985, pp.220~222.

[69] John E. McFee, and Yogadhish Das, “Determination of the Parameters of a Dipole by Measurement of its Magnetic Field”. IEEE Trans. On Antennas and Propagation, Vol. AP-29, No. 2, March, 1981, pp. 282~287.

[70] M. Hirota, K. Nanaura, Y. Teranishi, and T. Kishigami, “SQUID Gradiometers for Fundamental Study of Underwater Magnetic Detection”. IEEE Trans. On Applied Superconductivity, Vol. 7, No. 2, June, 1997, pp. 2327~2330.

[71] R. M. Haralick, L. G. Shapiro, “Computer and Robot Vision”, Addison-Wesley Publishing Company, Inc. 1993.

[72] S. S. Beauchemin, and J.L. Barron, “The Computation of Optical Flow”, ACM Computing Surveys, Vol.27, No.3, pp. 433~467, 1995.

[73] D J. H.uncan, and T. C. Chou, “On the Detection of Motion and the Computation of Optical Flow”, IEEE Trans. On Pattern Analysis and Machine Intelligence, Vol.14, No.3, 1992, pp.346~352.

[74] R.Y. Tsai and T. S. Huang, “Uniqueness and Estimation of Three Dimensional Motion Parameters of Rigid Objects With Curved Surfaces,” IEEE Trans. On Pattern Analysis and Machine Intelligence, vol.PAMI-6, No.1, pp.13~27, 1984.

[75] H.C. Longuet-Higgins, “A Computer Algorithm for Reconstructing a Scene From Two Projections,” Nature, vol. 293, pp. 133–135, Sept 1981.

[76] R. I. Hartley, “In Defense of the Eight-Point Algorithm”, IEEE Trans. On Pattern Analysis and Machine Intelligence. Vol.19, No.6, pp580~593, June 1997.

[77] Juyang Weng, Thomas s. Huang, Narendra Ahuja, “Motion and Structure from Two Perspective Views: Algorithms, Error Analysis, and Error Estimation”, IEEE Trans. on Pattern Analysis and Machine Intelligence, vol.PAMI-11, No.5, pp.451~476, May 1989.

[78] H. Christopher Longuet-Higgins, “The Reconstruction of a Scene from Two projections-onfirmation that Defeat the 8-point Algorithm.” Proceedings of 1st Conference on Artificial Intelligence Application, Denver, pp.595~397, 1984b.

[79] Ken Shoemake, "Animating Rotation with Quaternion Curves", Computer Graphics, (Proc. Of SIGGRAPH'85), Vol. 19, No. 3, 1985, pp.245~254.

[80] Qiang Liu, and Edmond C. Prakash, "The Parameterization of Joint Rotation with the Unit Quaternion", Proc. VIIth Digital Image Computing: Techniques and Applications, 10-12 Dec. 2003, Sydney, pp.409~417.

[81] W. R. Hamilton, "Elements of Quaternions I & II ", Chelsea Publishing Company (1969).

[82] R. Mukundan, "Quaternions: From Classical Mechanics to Computer Graphics, and Beyond", Proceedings of the 7th Asian Technology Conference in Mathematics 2002. pp.97~106

[83] J. Schmidt, and H. Niemann, "Using Quaternions for Parametrizing 3–D Rotations in Unconstrained Nonlinear Optimization", VMV 2001, Stuttgart, Germany, November 21–23, 2001, pp. 399~406.

[84] Herman Bruyninckx, "Orientation and rotation", www.roble.info/pages/hbge-index.html.

[85] J. J. Craic, "Introduction to Robotics Mechanics and Control", 3rd Edition, @ 2005 Pearson Education, Inc.

[86] "Coordinate Systems", http://hyperphysics.phy-astr.gsu.edu/hbase/coord.html.

[87] R. L. Pio. "Euler angle transformations", IEEE Trans. on Automatic Control, Vol. AC-11, No. 4, October, 1966.

[88] "Numerical Recipes in C", Chapter 10. http://www.library.cornell.edu/nr/cbookcpdf.html.

[89] J. A. Nelder and R. Mead, "A simplex method for function minimization", The Computer Journal, vol.7, 1965, pp.308~313.

[90] Mattias Bjorkman and Kenneth Holmstrom, "Global Optimization Using the DIRECT Algorithm in Matlab", Advanced Modeling and Optimization, 1(2), 1999, pp.17~29.

[91] D. E. Finkel, "DIRECT Optimization Algorithm User Guide", http://www4.ncsu.edu/~definkel/research/DirectUserGuide_pdf.pdf

[92] D.R. Jones, C.D. Perttunen and B.E. Stuckman. "Lipschitzian optimization without the lipschitz constant", Journal of Optimization Theory and Application, 79(1):pp.157~181, October 1993.

[93] Waltraud Huyer, and Arnold Neumaier, "Global Optimization by Multilevel Coordinate Search", Journal of Global Otimization, 14, 1999, pp.331~355.

[94] Waltraud Huyer, “A comparison of some algorithms for bound constrained global optimization”, http://www.mat.univie.ac.at/~neum/glopt/contrib/compbound.pdf.

[95] Donald W. Marquardt, “An Algorithm for Least-Squares Estimation of Nonlinear Parameters”, Journal of the Society for Industrial and Applied Mathematics, Vol.11, No.2, 1963, pp.431~441.

[96] J.E. Lenz, “A Review of Magnetic Sensors”, Proceedings of the IEEE, vol. 78, no.6, (June 1990) 973-989.

[97] M. J. Caruso, C. H. Smith, T. Bratland, and R. Schneider, “A New Perspective on Magnetic Field Sensing”, http://www.ssec.honeywell.com/magnetic/datasheets/new_pers.pdf.

[98] “Magnetic Sensor Overview”, http://www.ssec.honeywell.com/magnetic/datasheets/magsen.pdf.

[99] NanJing New ZhongXu Microelectronic Co., Ltd. “TY Series InSb hall-effect Element”, http://www.zhongxu.com.

[100] NanJing New ZhongXu Microelectronic Co., Ltd. “CS49X Series Linear Hall-effect ICs”, http://www.zhongxu.com.

[101] M. N. Baibich , J. M. Broto, A. Fert, F. Nguyen Van Dau, F. Petroff, P. Eitenne, G. Creuzet, A. Friederich, and J. Chazelas, “Giant Magnetoresistance of (001)Fe/(001)Cr Magnetic Superlattices,” Phys. Rev. Lett., vol. 61, 2472-2475 (1988).

[102] J. Daughton, J. Brown, R. Beech, A. Pohm, and W. Kude, “Magnetic Field Sensors Using GMR Multilayer,” IEEE Trans. Magn., vol. 30, 4608-4610, (1994).

[103] P. Ciureanu, S. Middelhoek, “Thin Film Resistive Sensors”, 1992, New York: Institute of Physics Publishing.

[104] Shenzhen Huaxia Magneto-electronic Technology Development Co., Ltd., “GMR chips”, http://www.hme.com.cn

[105] Honeywell, “Solid State Hall Effect Sensors (High Performance Miniature Ratiometric Linear) SS490 Series”, http://content.honeywell.com/sensing/prodinfo/solidstate/005843_1.pdf

[106] Honeywell, “Magnetic Sensors Products”, http://www.magneticsensors.com/products.html.

[107] AdvanTech Co., “PCL-818L data acquisition card”, http://www.advantech.com/products/.

[108] Bruno Serra, and Marc Berthod, "3-D Model Localization Using High- Resolution Reconstruction of Monocular Image Sequences". IEEE Trans. On Image Processing, Vol.6, No.1, pp.175~188, Jan., 1997.

[109] Tony Jebara, Ali Azarbayejani, and Alex Pentland, "3D Structure from 2D Motion". IEEE Signal Processing Magazine, pp.66~84, May, 1999.

[110] T. S. Huang, and O. D. Faugeras, "Some Properties of the E Matrix in Two-view Motion Estimation". IEEE Trans. On Pattern Analysis and Machine Intelligence, Vol.11, No.12, pp.1310~1312, Dec.,1989.

[111] R. Y.Tsui, "A Versatile Camera Calibration Techniques for High-Accuracy 3D Machine Vision Metrology Using Off-the-shelf TV Cameras and Lenses". IEEE Journal of Robotics and Automation, Vol.RA-3, No.4, pp.323~344, August, 1987.

[112] K. V. Asari, S. Kumar, and D. Radhakrishnan, "A New Approach for Nonlinear Distortion Correction in Endoscopic Images Based on Least Squares Estimation". IEEE Trans. On Medical Imaging, Vol. 18, No. 4, April, 1999, pp.345~354.

[113] R. Shahidi, M. R. Bax, C. R. Maurer, J. A. Johnson, E. P. Wilkinson, B. Wang, J. B. West, M. J. Citardi, K. H. Manwaring, and R. Khadem, "Implementation, Calibration and Accuracy Testing of an Image-Enhanced Endoscopy System", IEEE Trans. On Medical Imaging, Vol. 21, No. 12, December 2002, pp.1524~1535.

[114] J. P. Helferty, C. Zhang, G. McLennan, and W. E. Higgins, "Videoendoscopic Distortion Correction and Its Application to Virtual Guidance of Endoscopy", IEEE Trans on Medical Imaging, Vol. 20, No. 7, July, 2001, pp.605~617.

[115] V. K. Asari, "Non-linear spatial warping of endoscopic images: an architectural perspective for real time applications". Microprocessors and Microsystems, 26 (2002), pp.161~171.

[116] K. V. Asari, S. Kumar, D. Radhakrishnan, "Technique of distortion correction in endoscopic images using a polynomial expansion". Medical & Biological Engineering & Computaing, vol.37, 1999, pp.8~12.

[117] Hideaki Haneishi, Yutaka Yagihashi, and Yoichi Miyake, "A New Method for Distortion Correction of Electronic Endoscope Images". IEEE Transactions on Medical Imaging, Vol.14, No.3, Sep., 1995, pp.548~555.

[118] W. E. Smith, N. Vakil, and S. A. Maislin, "Correction of Distortion in Endoscope Images". IEEE Trans. On Medical Imaging. Vol.11, No.1, March, 1992, pp.117~122.

[119] Chao Hu, Max Meng, Peter Xiaoping Liu, Xiang Wang, "Image distortion correction for wireless capsule endoscope". Proceedings of 2004 IEEE International Conference on Robotics and Automation, pp. 4718~4723, April, 2004, New Orleans, USA.

[120] Intel's Computer Vision Library,
http://www.intel.com/research/mrl/research/opencv/overview.htm.

[121] Xinhua Zhuang, "A Simplification to Linear Two-View Motion Algorithms", Computer Vision, Graphics, and Image Processing, Vol.46, pp.175~178, 1989.

[122] Chao Hu, Max Q.- H. Meng, and Mrinal Mandal, "Efficient Linear Algorithm for Magnetic Localization and Orientation in Capsule Endoscopy". 27th Annual International Conference of the IEEE Engineering in Medicine and Biology Society, September 1~4, 2005, Shanghai, China.

[123] Chao Hu, Max Qinghu Meng, Peter Xiaoping Liu, and Xiang Wang, "Image Representation and Compression for Capsule Endoscope Robot", Proceeding of International Conference on Control Science and Engineering 2003, Harbin, China, Dec., pp.1~6, 2003.

[124] Chao Hu, Max Q.- H. Meng, Mrinal Mandal, and Xiaona Wang, "3-Axis Magnetic Sensor Array System for Tracking Magnet's Position and Orientation", The 6th World Congress on Intelligent Control and Automation, June, 2006, Dalian, China (submitted).

Appendix A: Quaternion Algebra

Quaternions are hyper-complex numbers of rank 4, constituting a four dimensional vector space over the field of real numbers. We use the following four-tuple notation to represent a quaternion:

$$\mathbf{q} = (q_0, q_1, q_2, q_3)$$

$$= (q_0, \mathbf{w}) \tag{A.1}$$

where q_0 is the scalar component of **q**, and $\mathbf{w}=\{q_1, q_2, q_3\}$ (or $\mathbf{w} = q_1\mathbf{i} + q_2\mathbf{j} + q_3\mathbf{k}$) forms the vector part, and the entire set of **q**'s is spanned by the basis quaternions:

$$1 = (1, 0, 0, 0),\ \mathbf{i} = (0, 1, 0, 0),\ \mathbf{j} = (0, 0, 1, 0),\ \mathbf{k} = (0, 0, 0, 1). \tag{A.2}$$

The orthonormal basis components **i**, **j**, **k**, as defined above satisfy the following well-known rules:

$$\mathbf{ij} = -\mathbf{ji} = \mathbf{k} \tag{A.3}$$

$$\mathbf{jk} = -\mathbf{kj} = \mathbf{i} \tag{A.4}$$

$$\mathbf{ki} = -\mathbf{ik} = \mathbf{j} \tag{A.5}$$

$$\mathbf{i}^2 = \mathbf{jki} = -1 \tag{A.6}$$

$$\mathbf{j}^2 = \mathbf{kij} = -1 \tag{A.7}$$

$$\mathbf{k}^2 = \mathbf{ijk} = -1 \tag{A.8}$$

where it is implied that the product of any two terms in the above expressions is indeed a *quaternion product*, which is defined in the most general form for two quaternions $\mathbf{q} = (q_0, \mathbf{w}) = (q_0, q_1, q_2, q_3)$, and $\tilde{\mathbf{q}} = (\tilde{q}_0, \tilde{\mathbf{w}}) = (\tilde{q}_0, \tilde{q}_1, \tilde{q}_2, \tilde{q}_3)$ as

$$\mathbf{q}\tilde{\mathbf{q}} = (q_0\tilde{q}_0 - \mathbf{w}\cdot\tilde{\mathbf{w}},\ q_0\tilde{\mathbf{w}} + \tilde{q}_0\mathbf{w} + \mathbf{w}\times\tilde{\mathbf{w}}) \tag{A.9}$$

where $\mathbf{w}\cdot\tilde{\mathbf{w}}$ and $\mathbf{w}\times\tilde{\mathbf{w}}$ denote the familiar dot and cross products respectively, between the three-dimensional vectors $\mathbf{w}$ and $\tilde{\mathbf{w}}$. Obviously, quaternion multiplication is not commutative, since the vector cross product is not. The set of elements $\{\pm 1, \pm\mathbf{i}, \pm\mathbf{j}, \pm\mathbf{k}\}$

form a group (known as the *quaternion group*) of order 8 under multiplication. This multiplication can be also be represented by

$$\mathbf{q}\tilde{\mathbf{q}} = \begin{pmatrix} q_0\tilde{q}_0 - q_1\tilde{q}_1 - q_2\tilde{q}_2 - q_3\tilde{q}_3 \\ q_0\tilde{q}_1 + \tilde{q}_0 q_1 + q_2\tilde{q}_3 - q_3\tilde{q}_2 \\ q_0\tilde{q}_2 + \tilde{q}_0 q_2 + q_3\tilde{q}_1 - q_1\tilde{q}_3 \\ q_0\tilde{q}_3 + \tilde{q}_0 q_3 + q_1\tilde{q}_2 - q_2\tilde{q}_1 \end{pmatrix} \tag{A.10}$$

Quaternion addition is a relatively simpler operation consisting of the addition of the corresponding components.

$$\mathbf{q} + \tilde{\mathbf{q}} = (q_0 + \tilde{q}_0, \mathbf{w} + \tilde{\mathbf{w}}) \tag{A.11}$$

Quaternions also form a commutative group under addition, (0,0,0,0) being the identity element. Quaternion multiplication is associative, and distributes over addition:

$$(\mathbf{q}\tilde{\mathbf{q}})\overline{\mathbf{q}} = \mathbf{q}(\tilde{\mathbf{q}}\overline{\mathbf{q}}) \tag{A.12}$$

$$(\mathbf{q} + \tilde{\mathbf{q}})\overline{\mathbf{q}} = \mathbf{q}\overline{\mathbf{q}} + \tilde{\mathbf{q}}\overline{\mathbf{q}} \tag{A.13}$$

$$\mathbf{q}(\tilde{\mathbf{q}} + \overline{\mathbf{q}}) = \mathbf{q}\tilde{\mathbf{q}} + \mathbf{q}\overline{\mathbf{q}} \tag{A.14}$$

As in the case of ordinary complex numbers, we can define the conjugate $\mathbf{q}^*$ of a quaternion $\mathbf{q} = (q_0, \mathbf{w})$ as follows:

$$\mathbf{q}^* = (q_0, \mathbf{w}^*) = (q_0, -\mathbf{w}) = (q_0, -q_1, -q_2, -q_3) \tag{A.15}$$

The above equation allows us to define the quaternion norm $||\mathbf{q}||$ as

$$||\mathbf{q}||^2 = \mathbf{q}\mathbf{q}^* = q_0^2 + q_1^2 + q_2^2 + q_3^2 \tag{A.16}$$

In particular, a *unit quaternion* is the one for which $||\mathbf{q}|| = 1$. The components of a unit quaternion will all have an absolute value less than or equal to 1. Any quaternion $\mathbf{q}$ can be normalized by dividing by its norm, to obtain a unit quaternion. The *inverse of a quaternion* given by

$$\mathbf{q}^{-1} = \mathbf{q}^* \big/ \|\mathbf{q}\|^2 \tag{A.17}$$

satisfies the relation $\mathbf{q}\mathbf{q}^{-1} = \mathbf{q}^{-1}\mathbf{q} = 1$. Since every non-zero quaternion $\mathbf{q}$ has a multiplicative inverse, the system of quaternions forms a non-commutative division ring.

A quaternion $\mathbf{q}$ = (q_0, $\mathbf{0}$) whose vector part is zero is called a *real quaternion*. Similarly, $\mathbf{q}$ = (0, $\mathbf{w}$) whose real part is zero is called a *pure quaternion* (or *vector quaternion*). Since $\mathbf{w}$ is a three-dimensional vector, clearly there is a one-to-one correspondence between vectors in three-dimensional space and the quaternion sub-space consisting of pure quaternions. If $\mathbf{q}$ is a unit quaternion, we can write $\mathbf{q}$ in the form ($\cos(\theta/2)$, $\sin(\theta/2)\ \mathbf{w}_1$) where $\|\mathbf{w}_1\|=1$.

According to the Euler's theorem in classical mechanics, the rotation of a rigid body with a fixed point can be achieved by a single rotation about an axis through the fixed point. If $\tilde{\mathbf{w}}$ = (m, n, p) denote a vector in three-dimensional space, then a rotational transformation by an angle θ (anti-clockwise) about this vector is given by

$$\begin{pmatrix} x' \\ y' \\ z' \end{pmatrix} = \begin{pmatrix} m^2(1-\cos\theta)+\cos\theta & mn(1-\cos\theta)-p\sin\theta & pm(1-\cos\theta)+n\sin\theta \\ mn(1-\cos\theta)+p\sin\theta & n^2(1-\cos\theta)+\cos\theta & np(1-\cos\theta)-m\sin\theta \\ pm(1-\cos\theta)-n\sin\theta & np(1-\cos\theta)+m\sin\theta & p^2(1-\cos\theta)+\cos\theta \end{pmatrix} \begin{pmatrix} x \\ y \\ z \end{pmatrix} \tag{A.18}$$

Obviously, a single rotation about an equivalent axis defines the shortest path between two object orientations. The above transformation can be conveniently represented by a quaternion product:

$$\mathbf{v}' = \mathbf{q}\,\mathbf{v}\,\mathbf{q}^* \tag{A.19}$$

where $\mathbf{v}' = (0,\ x',\ y',\ z')$, $\mathbf{v} = (0,\ x,\ y,\ z)$, and $\mathbf{q} = (q_0, q_x, q_y, q_z) =$ $(\cos\frac{\theta}{2}, m\sin\frac{\theta}{2}, n\sin\frac{\theta}{2}, p\sin\frac{\theta}{2})$. It is clear that a rotation does not affect the length of a vector, and hence $\|\mathbf{v}\| = \|\mathbf{v}'\|$. Thus for a proper rotation $\mathbf{q}$ in (A.19) must be a unit vector. Also note that when $\mathbf{q}$ is a unit quaternion, we have the property $\mathbf{q}^{-1} = \mathbf{q}^*$, from (A.17). We can thus define

$$L_q(\mathbf{v}) = \mathbf{q}\,\mathbf{v}\,\mathbf{q}^* \tag{A.20}$$

as a quaternion rotation operator acting on any vector **v** in the three-dimensional space. It can be easily shown that the operator is linear, so that

$$L_q(k\mathbf{v}_1 + \mathbf{v}_2) = kL_q(\mathbf{v}_1) + L_q(\mathbf{v}_2) \tag{A.21}$$

for any constant k, and vector quaternions $\mathbf{v}_1$ and $\mathbf{v}_2$.

For rotation transformation written in matrix, we have

$$\begin{pmatrix} x' \\ y' \\ z' \end{pmatrix} = \mathbf{R} \begin{pmatrix} x \\ y \\ z \end{pmatrix} \tag{A.22}$$

where

$$\mathbf{R} = \begin{pmatrix} q_0^2 + q_x^2 - q_y^2 - q_z^2 & 2q_x q_y - 2q_0 q_z & 2q_x q_z + 2q_0 q_y \\ 2q_x q_y + 2q_0 q_z & q_0^2 - q_x^2 + q_y^2 - q_z^2 & 2q_y q_z - 2q_0 q_x \\ 2q_x q_z - 2q_0 q_y & 2q_y q_z + 2q_0 q_x & q_0^2 - q_x^2 - q_y^2 + q_z^2 \end{pmatrix} \tag{A.23}$$

Reversely, when the rotation transformation matrix is $\mathbf{R} = \begin{pmatrix} m_{11} & m_{12} & m_{13} \\ m_{21} & m_{22} & m_{23} \\ m_{31} & m_{32} & m_{33} \end{pmatrix}$, we can calculate the quaternion $\mathbf{q} = [q_0 \;\; q_x \;\; q_y \;\; q_z]^T$ with

$$q_0 = \sqrt{\frac{1 + m_{11} + m_{22} + m_{33}}{4}} \tag{A.24}$$

$$q_x = \frac{m_{32} - m_{23}}{4w} \tag{A.25}$$

$$q_y = \frac{m_{13} - m_{31}}{4w} \tag{A.26}$$

$$q_z = \frac{m_{21} - m_{12}}{4w} \tag{A.27}$$

As with matrices, quaternion rotations may be composed of multiple basic rotations:

$$\mathbf{v}' = L_{q1}(\mathbf{v}) = \mathbf{q}_1 \, \mathbf{v} \mathbf{q}_1^* \tag{A.28}$$

$$\mathbf{v}'' = L_{q2}(\mathbf{v}') = \mathbf{q}_2 \, \mathbf{v}' \mathbf{q}_2^* \tag{A.29}$$

Then

$$\mathbf{v}'' = \mathbf{q}_2 \mathbf{q}_1 \, \mathbf{v} \, \mathbf{q}_1^* \mathbf{q}_2^* \tag{A.30}$$

Since $\mathbf{q}_1^* \mathbf{q}_2^* = (\mathbf{q}_2 \mathbf{q}_1)^*$, we have

$$\mathbf{v}'' = \mathbf{q}_2 \mathbf{q}_1 \, \mathbf{v} \, (\mathbf{q}_2 \mathbf{q}_1)^* = \mathbf{q} \, \mathbf{v} \, \mathbf{q}^* \tag{A.31}$$

where $\mathbf{q} = \mathbf{q}_2 \, \mathbf{q}_1$, is the multiplication of the quaternions.

Appendix B Proof of Theorem 3.1 and 3.2

B.1 Proof of Theorem 3.1

Firstly we can see that the rotation angle $\boldsymbol{\theta}$ is always positive, because $\vec{\mathbf{r}}_1$, $\vec{\mathbf{r}}_2$ and $\vec{\mathbf{r}}_3$ follow right hand rule. Let quaternion $\mathbf{q}_1$ be the rotation (**α**) around vector $\vec{\mathbf{r}}_1$:

$$\mathbf{q}_1 = \cos(\alpha/2) + \sin(\alpha/2)\vec{\mathbf{r}}_1 = \cos(\alpha/2) + \sin(\alpha/2)(m_1\mathbf{i} + n_1\mathbf{j} + p_1\mathbf{k}) \tag{B.1}$$

Quaternion $\mathbf{q}_3$ be the rotation ($\boldsymbol{\theta}$) around vector $\vec{\mathbf{r}}_3$:

$$\mathbf{q}_3 = \cos(\theta/2) + \sin(\theta/2)\vec{\mathbf{r}}_3 = \cos(\theta/2) + \sin(\theta/2)(m_3\mathbf{i} + n_3\mathbf{j} + p_3\mathbf{k}) \tag{B.2}$$

And quaternion $\mathbf{q}_2$ be the rotation (**α**) around vector $\vec{\mathbf{r}}_2$:

$$\mathbf{q}_2 = \cos(\alpha/2) + \sin(\alpha/2)\vec{\mathbf{r}}_2 = \cos(\alpha/2) + \sin(\alpha/2)(m_2\mathbf{i} + n_2\mathbf{j} + p_2\mathbf{k}) \tag{B.3}$$

The rotation that rotates (angle **α)** around $\vec{\mathbf{r}}_1$ first and (angle $\boldsymbol{\theta}$**)** around $\vec{\mathbf{r}}_3$ second can be represented by quaternion:

$$\begin{aligned}\mathbf{q}_3\mathbf{q}_1 &= \cos(\theta/2)\cos(\alpha/2) + \cos(\theta/2)\sin(\alpha/2)\vec{\mathbf{r}}_1 \\ &+ \cos(\alpha/2)\sin(\theta/2)\vec{\mathbf{r}}_3 + \sin(\theta/2)\sin(\alpha/2)\vec{\mathbf{r}}_3 \times \vec{\mathbf{r}}_1\end{aligned} \tag{B.4}$$

Note that $\vec{\mathbf{r}}_1 \cdot \vec{\mathbf{r}}_3$=0 in deriving (B.4). The rotation that rotates (angle $\boldsymbol{\theta}$**)** around $\vec{\mathbf{r}}_3$ first and (angle **α)** around $\vec{\mathbf{r}}_2$ second can be represented by quaternion:

$$\begin{aligned}\mathbf{q}_2\mathbf{q}_3 &= \cos(\alpha/2)\cos(\theta/2) + \cos(\alpha/2)\sin(\theta/2)\vec{\mathbf{r}}_3 \\ &+ \cos(\theta/2)\sin(\alpha/2)\vec{\mathbf{r}}_2 + \sin(\alpha/2)\sin(\theta/2)\,\vec{\mathbf{r}}_2 \times \vec{\mathbf{r}}_3\end{aligned} \tag{B.5}$$

Assume that $\vec{\mathbf{r}}_1$ and $\vec{\mathbf{r}}_2$ are located in a plane shown in Figure B.1. From (3.16), we know that $\vec{\mathbf{r}}_3$ is orthogonal to this plane. Therefore $\vec{\mathbf{r}}_2 \times \vec{\mathbf{r}}_3$ must be located in this plane and orthogonal to $\vec{\mathbf{r}}_2$, and $\vec{\mathbf{r}}_3 \times \vec{\mathbf{r}}_1$ is also located in this plane and orthogonal to $\vec{\mathbf{r}}_1$. In addition, all these vectors are unit vectors. The last 2 items of (B.5) is

$$\begin{aligned}&\cos(\theta/2)\sin(\alpha/2)\vec{\mathbf{r}}_2 + \sin(\alpha/2)\sin(\theta/2)\,\vec{\mathbf{r}}_2 \times \vec{\mathbf{r}}_3 \\ &= \sin(\alpha/2)[\cos(\theta/2)\vec{\mathbf{r}}_2 + \sin(\theta/2)\,\vec{\mathbf{r}}_2 \times \vec{\mathbf{r}}_3] \\ &= \sin(\alpha/2)[\cos(\theta/2)(\cos\theta\,\vec{\mathbf{r}}_1 + \sin\theta\;\vec{\mathbf{r}}_3 \times \vec{\mathbf{r}}_1) + \sin(\theta/2)(\sin\theta\,\vec{\mathbf{r}}_1 - \cos\theta\;\vec{\mathbf{r}}_3 \times \vec{\mathbf{r}}_1)]\end{aligned}$$

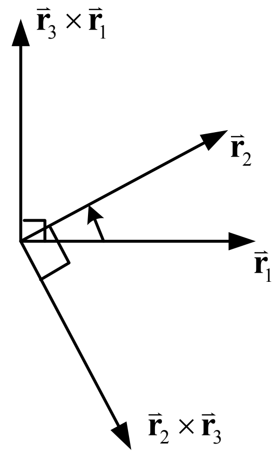

Figure B.1 The vectors $\vec{\mathbf{r}}_1$, $\vec{\mathbf{r}}_2$, $\vec{\mathbf{r}}_2 \times \vec{\mathbf{r}}_3$ and $\vec{\mathbf{r}}_3 \times \vec{\mathbf{r}}_1$ (on same plane)

$$= \sin(\alpha/2)[\cos(\theta - \theta/2)\vec{\mathbf{r}}_1 + \sin(\theta - \theta/2)\, \vec{\mathbf{r}}_3 \times \vec{\mathbf{r}}_1]$$

$$= \sin(\alpha/2)\cos(\theta/2)\vec{\mathbf{r}}_1 + \sin(\alpha/2)\sin(\theta/2)\, \vec{\mathbf{r}}_3 \times \vec{\mathbf{r}}_1$$

$\boldsymbol{\theta}$

Obviously, above 2 items are the same as the 2nd and the last items of (B.4). Comparing (B.4) with (B.5), we observe that these two equations are identical. Therefore, the rotation quaternion

$$\mathbf{q} = \mathbf{q}_3\mathbf{q}_1 = \mathbf{q}_2\mathbf{q}_3 \tag{B.6}$$

And the theorem is proved.

B. 2 Proof of Theorem 3.2

From (B.1) and (B.3), we have:

$$\mathbf{q}_1 = q_{10} + q_{1x}\mathbf{i} + q_{1y}\mathbf{j} + q_{1z}\mathbf{k} = \cos(\alpha/2) + \sin(\alpha/2)(m_1\mathbf{i} + n_1\mathbf{j} + p_1\mathbf{k}) \tag{B.7}$$

$$\mathbf{q}_2 = q_{20} + q_{2x}\mathbf{i} + q_{2y}\mathbf{j} + q_{2z}\mathbf{k} = \cos(\alpha/2) + \sin(\alpha/2)(m_2\mathbf{i} + n_2\mathbf{j} + p_2\mathbf{k}) \tag{B.8}$$

From (B.2), we have:

$$\mathbf{q}_3 = q_{30} + q_{3x}\mathbf{i} + q_{3y}\mathbf{j} + q_{3z}\mathbf{k} = \cos(\theta/2) + \sin(\theta/2)(m_3\mathbf{i} + n_3\mathbf{j} + p_3\mathbf{k}) \tag{B.9}$$

From (3.16), we have

$$\begin{pmatrix} m_3 \\ n_3 \\ p_3 \end{pmatrix} = \begin{pmatrix} n_1 p_2 - n_2 p_1 \\ p_1 m_2 - m_1 p_2 \\ m_1 n_2 - n_1 m_2 \end{pmatrix} \Bigg/ \sqrt{(n_1 p_2 - n_2 p_1)^2 + (p_1 m_2 - m_1 p_2)^2 + (m_1 n_2 - n_1 m_2)^2} \quad \text{(B.10)}$$

Since $\mathbf{q} = \mathbf{q}_3 \mathbf{q}_1$, we have:

$$\mathbf{q}_3 \mathbf{q}_1 = (q_{30} q_{10} - \mathbf{q}_{v3} \cdot \mathbf{q}_{v1}) + (q_{30} \mathbf{q}_{v1} + q_{10} \mathbf{q}_{v3} + \mathbf{q}_{v3} \times \mathbf{q}_{v1}) \quad \text{(B.11)}$$

where $\mathbf{q}_{v3} = [q_{3x} \;\; q_{3y} \;\; q_{3z}]^T$, $\mathbf{q}_{v1} = [q_{1x} \;\; q_{1y} \;\; q_{1z}]^T$. The above equation can be written as

$$\begin{pmatrix} q_0 \\ q_x \\ q_y \\ q_z \end{pmatrix} = \begin{pmatrix} q_{30} q_{10} - q_{3x} q_{1x} - q_{3y} q_{1y} - q_{3z} q_{1z} \\ q_{30} q_{1x} + q_{3x} q_{10} + q_{3y} q_{1z} - q_{3z} q_{1y} \\ q_{30} q_{1y} - q_{3x} q_{1z} + q_{3y} q_{10} + q_{3z} q_{1x} \\ q_{30} q_{1z} + q_{3x} q_{1y} - q_{3y} q_{1x} + q_{3z} q_{10} \end{pmatrix} \quad \text{(B.12)}$$

Because $\mathbf{r}_3$ is orthogonal to $\mathbf{r}_1$, $\mathbf{q}_{v3} \cdot \mathbf{q}_{v1} = q_{3x} q_{1x} + q_{3y} q_{1y} + q_{3z} q_{1z} = 0$, so

$$q_{30} q_{10} = \cos(\theta / 2) \cos(\alpha / 2) = q_0 \quad \text{(B.13)}$$

Let $\mathbf{q}_v = [q_x \;\; q_y \;\; q_z]^T$. From (B.11), we have

$$q_{30} \mathbf{q}_{v1} + q_{10} \mathbf{q}_{v3} + \mathbf{q}_{v3} \times \mathbf{q}_{v1} = \mathbf{q}_v \quad \text{(B.14)}$$

Because vector $\vec{\mathbf{r}}_1$ is orthogonal to both $\mathbf{q}_{v3}$ and $\mathbf{q}_{v3} \times \mathbf{q}_{v1}$, we get following equation by dot product of sides of (B.14)

$$q_{30} \mathbf{q}_{v1} \cdot \vec{\mathbf{r}}_1 = \mathbf{q}_v \cdot \vec{\mathbf{r}}_1 \quad \text{(B.15)}$$

That is

$$\cos(\theta / 2) \sin(\alpha / 2)(m_1^2 + n_1^2 + p_1^2) = m_1 q_x + n_1 q_y + p_1 q_z \quad \text{(B.16)}$$

The vector $\vec{\mathbf{r}}_1$ is a unit vector such that $m_1^2 + n_1^2 + p_1^2 = 1$, and

$$\cos(\theta / 2) \sin(\alpha / 2) = m_1 q_x + n_1 q_y + p_1 q_z \quad \text{(B.17)}$$

Using (B.13) and (B.17), we get $\tan(\alpha / 2) = \dfrac{m_1 q_x + n_1 q_y + p_1 q_z}{q_0}$, so

$$\alpha = 2 \tan^{-1}\left(\frac{m_1 q_x + n_1 q_y + p_1 q_z}{q_0}\right) \quad \text{(B.18)}$$

And

$$\theta = 2\cos^{-1}(q_0 / \cos(\alpha / 2)) \tag{B.19}$$

Therefore, the equations (3.17) and (3.18) in Theorem 3.2 are proved. Now, we determine the resultant axis vector $\vec{\mathbf{r}}_2 = (m_2\ n_2\ p_2)^T$ from the known quaternion $\mathbf{q}$ and the vector $\vec{\mathbf{r}}_1 = (m_1\ n_1\ p_1)^T$. From (B.12), we have

$$\begin{pmatrix} q_{3x} \\ q_{3y} \\ q_{3z} \end{pmatrix} = \begin{pmatrix} q_{10} & q_{1z} & -q_{1y} \\ -q_{1z} & q_{10} & q_{1x} \\ q_{1y} & -q_{1x} & q_{10} \end{pmatrix}^{-1} \cdot \begin{pmatrix} q_x - q_{30}q_{1x} \\ q_y - q_{30}q_{1y} \\ q_z - q_{30}q_{1z} \end{pmatrix} \tag{B.20}$$

Because $\mathbf{q} = \mathbf{q}_2\mathbf{q}_3$, we have $\begin{pmatrix} q_0 \\ q_x \\ q_y \\ q_z \end{pmatrix} = \begin{pmatrix} q_{20}q_{30} - q_{2x}q_{3x} - q_{2y}q_{3y} - q_{2z}q_{3z} \\ q_{20}q_{3x} + q_{2x}q_{30} + q_{2y}q_{3z} - q_{2z}q_{3y} \\ q_{20}q_{3y} - q_{2x}q_{3z} + q_{2y}q_{30} + q_{2z}q_{3x} \\ q_{20}q_{3z} + q_{2x}q_{3y} - q_{2y}q_{3x} + q_{2z}q_{30} \end{pmatrix}$, thus

$$\begin{pmatrix} q_{2x} \\ q_{2y} \\ q_{2z} \end{pmatrix} = \begin{pmatrix} q_{30} & q_{3z} & -q_{3y} \\ -q_{3z} & q_{30} & q_{3x} \\ q_{3y} & -q_{3x} & q_{30} \end{pmatrix}^{-1} \cdot \begin{pmatrix} q_x - q_{20}q_{3x} \\ q_y - q_{20}q_{3y} \\ q_z - q_{20}q_{3z} \end{pmatrix} \tag{B.21}$$

Finally, we get

$$\vec{\mathbf{r}}_2 = (m_2\ n_2\ p_2)^T = \frac{(q_{2x}\ \ q_{2y}\ \ q_{2z})^T}{\sin(\alpha / 2)} \tag{B.22}$$

Where $q_{30} = \cos(\theta / 2)$, $q_{10} = q_{20} = \cos(\alpha / 2)$, and $(q_{1x}\ \ q_{1y}\ \ q_{1z})^T = \sin(\alpha / 2)(m_1\ \ n_1\ \ p_1)^T$. Obviously, above three equations are the same as (3.21), (3.20), and (3.22), so Theorem 3.2 is proved.

Appendix C 8-point algorithm for solving for rotation matrix R_0 and transition vector T

C.1 8-point algorithm

C.1.1 Derivation of Two-View Motion Equation

Taking any nonzero vector **T** which is collinear with $\mathbf{T}_0$ (i.e. $\mathbf{T}\times\mathbf{T}_0=0$) and taking its cross-product with both sides of (7.18), we obtain

$$\mathbf{T}\times(x' \;\; y' \;\; z')^T = \mathbf{T}\times[\mathbf{R}_0(x \;\; y \;\; z)^T] + \mathbf{T}\times\mathbf{T}_0 \tag{C.1}$$

and

$$\frac{z'}{z}\mathbf{T}\times(u' \;\; v' \;\; 1)^T = \mathbf{T}\times[\mathbf{R}_0(u \;\; v \;\; 1)^T] \tag{C.2}$$

Since $\mathbf{T}\times(u' \;\; v' \;\; 1)^T$ is othogonal to $(u'\, v'\, 1)^T$, taking the inner product of both sides of (C.2) with $(u'\, v'\, 1)^T$, we have

$$(u' \;\; v' \;\; 1)(\mathbf{T}\times\mathbf{R}_0)(u \;\; v \;\; 1)^T = 0 \tag{C.3}$$

where $\mathbf{T}\times\mathbf{R}_0 = [\mathbf{T}\times\mathbf{r}_1 \;\; \mathbf{T}\times\mathbf{r}_2 \;\; \mathbf{T}\times\mathbf{r}_3]$ with $\mathbf{r}_1$, $\mathbf{r}_2$, $\mathbf{r}_3$ being the columns of $\mathbf{R}_0$. The motion parameter matrix **E** is defined by

$$\mathbf{E}=\mathbf{T}\times\mathbf{R}_0 \tag{C.4}$$

This matrix is called fundamental matrix. Equation (C.3) states that for any image point correspondence pair $(u,\ v)\Leftrightarrow(u'\ v')$, the 3×3 matrix **E** satisfies the following two-view motion equations which are linear and homogeneous in the nine elements of E:

$$(u' \;\; v' \;\; 1)\mathbf{E}(u \;\; v \;\; 1)^T = 0 \tag{C.5}$$

Since any $\mathbf{T}\times\mathbf{R}_0$ with $\mathbf{T}\times\mathbf{T}_0=0$ satisfies (C.5) and, moreover, such a collinear vector **T** has one degree of freedom when $\mathbf{T}_0\neq 0$ or three degrees of freedom when $\mathbf{T}_0 = 0$, the general solution of the two-view motion equation has at least one degree of freedom when $\mathbf{T}_0\neq 0$ or three degrees of freedom when $\mathbf{T}_0 = 0$.

A necessary and sufficient condition for the solution of (C.5) is related to the surface assumption [75]. The surface assumption is equivalent to that of (C.5) having a rank 8 when $\mathbf{T}_0 \neq 0$ or a rank 6 when $\mathbf{T}_0 = 0$. Thus the surface assumption must be accompanied by the number of the image point correspondence pairs ≥8 when $\mathbf{T}_0 \neq 0$ or ≥6 when $\mathbf{T}_0 = 0$. Let the origins of the camera system be O and O', respectively, before and after motion. Then the surface assumption holds if and only if the 3D points corresponding to observed image point correspondence pairs do not lie on a quadratic surface passing through O and O' when $\mathbf{T}_0 \neq 0$ or a cone with its apex at O when $\mathbf{T}_0 = 0$.

C.1.2 Solve for fundamental matrix E

Let $\mathbf{E}=\mathbf{T}\times\mathbf{R}_0$ be

$$\mathbf{E} = \begin{bmatrix} \hat{h}_1 & \hat{h}_2 & \hat{h}_3 \\ \hat{h}_4 & \hat{h}_5 & \hat{h}_6 \\ \hat{h}_7 & \hat{h}_8 & \hat{h}_9 \end{bmatrix} \tag{C.6}$$

From (C.5), we have

$$[u'u \;\; u'v \;\; u' \;\; v'u \;\; v'v \;\; v' \;\; u \;\; v \;\; 1][\hat{h}_1 \; \hat{h}_2 \; \hat{h}_3 \; \hat{h}_4 \; \hat{h}_5 \; \hat{h}_6 \; \hat{h}_7 \; \hat{h}_8 \; \hat{h}_9]^T = 0 \tag{C.7}$$

Denote the set of all (8 or more) observed image correspondence point pairs $(u_i, v_i) \Leftrightarrow (u_i^{'}, v_i^{'})$, i=1,2, … , $\overline{M}$. Let

$$\boldsymbol{\omega}_i = [u_i^{'}u_i \quad u_i^{'}v_i \quad u_i^{'} \quad v_i^{'}v_i \quad v_i^{'}v_i \quad v_i^{'} \quad u_i \quad v_i \quad 1], \quad i=1,\, 2,\, \ldots 8,\, \ldots\, \overline{M}$$

$$\mathbf{U} = [\boldsymbol{\omega}_1 \; \boldsymbol{\omega}_2 \cdots \boldsymbol{\omega}_{\overline{M}}]^T$$

$$\boldsymbol{\Lambda} = [\hat{h}_1 \;\; \hat{h}_2 \;\cdots\; \hat{h}_9]^T$$

So from (C.7), we get

$$\mathbf{U}\boldsymbol{\Lambda} = 0 \tag{C.8}$$

If the surface assumption holds for (C.5), the coefficient matrix **A** has a rank 8 when $\mathbf{T}_0 \neq 0$ and a rank 6 when $\mathbf{T}_0 = 0$. For real camera system, noises exist in the captured images. If the observed image point correspondence pairs N ≥ 9, then the matrix $\mathbf{\Lambda}$ might have a rank 9, and (C.8) might not be satisfied. In this case, we need to have

$$\| \mathbf{U\Lambda} \|_2 = min \tag{C.9}$$

Now we can solve for $\mathbf{\Lambda}$ such that (C.9) is satisfied. The solution is the unit eigenvector of $\mathbf{A}^T\mathbf{A}$ associated with the smallest eigenvalue.

C.1.3 Singularity constraint

An important property of the fundamental matrix is its singularity in fact of rank 2. However, in most applications, the matrix **E** found by solving (C.9) will not in general have rank 2. We need to take steps to enforce the singularity constraint. One convenient way is to correct the matrix **E** by the matrix **E'** that minimizes the Frobenius norm $\left\| \mathbf{E} - \mathbf{E}' \right\|$ subject to the condition det(**E**') = 0. Thus, let $\mathbf{E} = \mathbf{VD}\widetilde{\mathbf{V}}^T$ be the singular value decomposition of **E**, where $\mathbf{D}=diag(s_1, s_2, s_3)$ is a diagonal matrix satisfying $s_1 \geq s_2 \geq s_3$.. Then let $\mathbf{E}' = \mathbf{V} \cdot diag(s_1, s_2, 0) \cdot \widetilde{\mathbf{V}}^T$. This method has been proven to minimize the Frobenius norm of **E**-**E**' [121].

C.1.4 Decomposing E into transition vector T and rotation matrix $\mathbf{R}_0$

Since $\mathbf{E}=\mathbf{T}\times\mathbf{R}_0$, we have

$$\mathbf{E}^T \cdot \mathbf{T} = \begin{vmatrix} (\mathbf{T}\times\mathbf{r}_1)^T\mathbf{T} \\ (\mathbf{T}\times\mathbf{r}_2)^T\mathbf{T} \\ (\mathbf{T}\times\mathbf{r}_3)^T\mathbf{T} \end{vmatrix} = 0 \tag{C.10}$$

For easy exercise, we assume

$$\| \mathbf{E} \| = \sqrt{2} \, \| \mathbf{T} \| \tag{C.11}$$

Thus, the vector **T** could be determined by (C.10) and (C.11). The solution of **T** is a unit eigenvector of $\mathbf{EE}^T$ associated with the smallest eigenvalue.

Now we need to determine the sign of **T**. From (C.2),

$$z'\mathbf{T}\times(u' \;\; v' \;\; 1)^T = z\mathbf{T}\times[\mathbf{R}_0(u \;\; v \;\; 1)^T] = z\mathbf{E}(u \;\; v \;\; 1)^T \tag{C.12}$$

then it is clear that

$$\sum[\mathbf{T}\times(u' \;\; v' \;\; 1)^T]^T \cdot \mathbf{E}(u \;\; v \;\; 1)^T > 0 \tag{C.13}$$

since z<0, z'<0, and $\mathbf{T}\times(u' \;\; v' \;\; 1)^T$ has the same orientation as $\mathbf{E}\cdot(u \;\; v \;\; 1)^T$ and both of them are nonzero (except at most one image point correspondence pair), where the summation in (C.13) is taken over all observed image point correspondences. So if (C.13) is not satisfied, then $\mathbf{T}\leftarrow(-\mathbf{T})$.

Once $\mathbf{T}$ is determined, the true rotation $\mathbf{R}_0$ could be uniquely determined through $\mathbf{E}=\mathbf{T}\times\mathbf{R}_0$. If there is no noise, we have (see Appendix C.2)

$$\mathbf{R}_0 = [\mathbf{W}_2\times\mathbf{W}_3 \,,\, \mathbf{W}_3\times\mathbf{W}_1 \,,\, \mathbf{W}_1\times\mathbf{W}_2] - \mathbf{T}\times\mathbf{E} \tag{C.14}$$

where $\mathbf{W}_1 = \mathbf{T}\times\mathbf{E}_1$, $\mathbf{W}_2 = \mathbf{T}\times\mathbf{E}_2$, $\mathbf{W}_3 = \mathbf{T}\times\mathbf{E}_3$, with $\mathbf{E}_1$, $\mathbf{E}_2$, and $\mathbf{E}_3$ being the column vector of $\mathbf{E}$. In the presence of noise, we find $\mathbf{R}_0$ such that

$$\left\|\mathbf{E}-[\mathbf{T}]_x\mathbf{R}_0\right\|_2 = \min \tag{C.15}$$

where

$$[\mathbf{T}]_x = \begin{bmatrix} 0 & -t_z & t_y \\ t_z & 0 & -t_x \\ -t_y & t_x & 0 \end{bmatrix} \tag{C.16}$$

Since $\mathbf{R}_0^{'}\mathbf{R}_0$=1 and $det(\mathbf{R}_0)$=1, Equation (C.15) can be changed to

$$\left\|\mathbf{E}-[\mathbf{T}]_x\mathbf{R}_0\right\|_2 = \left\|\mathbf{E}\mathbf{R}_0^{'}\mathbf{R}_0-[\mathbf{T}]_x\mathbf{R}_0\right\|_2 = \left\|\mathbf{E}\mathbf{R}_0^{'}-[\mathbf{T}]_x\right\|_2 = \left\|\mathbf{R}_0\mathbf{E}^T-[\mathbf{T}]_x^T\right\|_2$$

So the above problem is changed to

$$\left\|\mathbf{R}_0\mathbf{E}^T-[\mathbf{T}]_x^T\right\|_2 = \min \tag{C.17}$$

The above equation has the form $\left\|\mathbf{R}_0\mathbf{C}-\mathbf{D}\right\| = \min$ subject to $\mathbf{R}_0$ being a rotation matrix, where $\mathbf{C}=\begin{bmatrix}\mathbf{C}_1 & \mathbf{C}_2 & \mathbf{C}_3\end{bmatrix}$ and $\mathbf{D}=\begin{bmatrix}\mathbf{D}_1 & \mathbf{D}_2 & \mathbf{D}_3\end{bmatrix}$. Obviously, $\mathbf{C}_i$ (i=1, 2, 3) is the row vectors of $\mathbf{E}$, and $\mathbf{D}_i$ (i=1, 2, 3) is the row vectors of $[\mathbf{T}]_x$.

As proved in Appendix C.3, we could find the rotation matrix $\mathbf{R}_0$ using a quaternion. Define a 4×4 matrix $\mathbf{F}$ by

$$\mathbf{F} = \sum_{i=1}^{3} \mathbf{F}_i^T \mathbf{F}_i \tag{C.18}$$

where

$$\mathbf{F}_i = \begin{bmatrix} 0 & (\mathbf{C}_i - \mathbf{D}_i)^T \\ \mathbf{D}_i - \mathbf{C}_i & [\mathbf{D}_i + \mathbf{C}_i]_x \end{bmatrix} \tag{C.19}$$

where $[\mathbf{C}_i]_x$ and $[\mathbf{D}_i]_x$ are matrices the same as that in (C.16). Let a quaternion $\mathbf{q} = (q_0 \;\; q_1 \;\; q_2 \;\; q_3)^T$ be the unit eigenvector of **F** associated with the smallest eigenvalue. The solution of the rotation matrix $\mathbf{R}_0$ in $\|\mathbf{R}_0\mathbf{C} - \mathbf{D}\|_2 = \min$ is

$$\mathbf{R}_0 = \begin{bmatrix} q_0^2 + q_1^2 - q_2^2 - q_3^2 & 2(q_1q_2 - q_0q_3) & 2(q_1q_3 + q_0q_2) \\ 2(q_1q_2 + q_0q_3) & q_0^2 - q_1^2 + q_2^2 - q_3^2 & 2(q_2q_3 - q_0q_1) \\ 2(q_1q_3 - q_0q_2) & 2(q_2q_3 + q_0q_1) & q_0^2 - q_1^2 - q_2^2 + q_3^2 \end{bmatrix} \tag{C.20}$$

C.2 Proof of Equation (C.14)

From $\mathbf{E}=\mathbf{T}\times\mathbf{R}_0$, we have

$$\mathbf{E}_1 = \mathbf{T} \times \mathbf{r}_1 \tag{C.21}$$

$$\mathbf{E}_2 = \mathbf{T} \times \mathbf{r}_2 \tag{C.22}$$

$$\mathbf{E}_3 = \mathbf{T} \times \mathbf{r}_3 \tag{C.23}$$

where $\mathbf{E}_1$, $\mathbf{E}_2$, and $\mathbf{E}_3$ are the column vectors of **E**, and $\mathbf{r_1}$, $\mathbf{r_2}$, $\mathbf{r_3}$ are the column vectors of $\mathbf{R_0}$. Since the rotation has condition $\mathbf{R_0R_0}'=1$, the matrix is normal, so we have

$$\mathbf{r}_1 = \mathbf{r}_2 \times \mathbf{r}_3 \tag{C.24}$$

By (C.21), $\mathbf{r_1}$ is orthogonal to $\mathbf{E}_1$, and therefore can be expressed as a combination of **T** and $\mathbf{E}_1\times\mathbf{T}$. We introduce new vectors

$$\mathbf{W_i} = \mathbf{T} \times \mathbf{E_i} \qquad (\, i=1, 2, 3\,) \tag{C.25}$$

And write

$$\mathbf{r_1} = a_1\mathbf{T} + b_1\mathbf{W_1} \tag{C.26}$$

Substitute into (C.21) gives

$$\mathbf{E_1} = \mathbf{T}\times(a_1\mathbf{T} + b_1\mathbf{W_1}) = b_1 (\mathbf{T}\times\mathbf{W_1}) \tag{C.27}$$

As **T** is a unit vector, and from (C.21) we know $\mathbf{E}_1$ is orthogonal to **T**, so

$$\mathbf{T}\times\mathbf{W_1} = \mathbf{T} \times(\mathbf{T}\times\mathbf{E_1}) = -\mathbf{E_1} \tag{C.28}$$

That is $b_1 = 1$. Turning to (C.24), we have

$$a_1\mathbf{T} - \mathbf{W_1} = (a_2\mathbf{T} - \mathbf{W_2}) \times (a_3\mathbf{T} - \mathbf{W_3}) = -a_2\mathbf{T} \times \mathbf{W_3} - a_3 \mathbf{W_2} \times\mathbf{T} + \mathbf{W_2} \times \mathbf{W_3} \tag{C.29}$$

because $\mathbf{W}_1$, $\mathbf{T} \times \mathbf{W_3}$ and $\mathbf{W_2} \times\mathbf{T}$ are orthogonal to **T**, whereas both $\mathbf{W_2}$ and $\mathbf{W_3}$, by (C.25), are on the plane perpendicular to **T,** $\mathbf{W_2} \times \mathbf{W_3}$ is a multiple of **T**, so we have

$$a_1\mathbf{T} = \mathbf{W_2} \times \mathbf{W_3} \tag{C.30}$$

Eq.(C.26) finally becomes

$$\mathbf{r_1} = \mathbf{W_2} \times \mathbf{W_3} - \mathbf{W_1} \tag{C.31}$$

And

$$\mathbf{r_2} = \mathbf{W_3} \times \mathbf{W_1} - \mathbf{W_2} \tag{C.32}$$

$$\mathbf{r_3} = \mathbf{W_1} \times \mathbf{W_2} - \mathbf{W_3} \tag{C.33}$$

C.3 Proof of Equations (C.20)

We first represent the rotation matrix R in terms of a unit quaternion q, and we need to prove

$$\|\mathbf{RC} - \mathbf{D}\|_2 = \mathbf{q}^T \mathbf{F}\, \mathbf{q} \tag{C.34}$$

Where **C**, **D**, and **F** are defined by (C.17)~(C.19).

A quaternion (Appendix A) consists of a scalar component q_0 and a three dimensional vector $\mathbf{w} = (\mathbf{q}_1\ \mathbf{q}_2\ \mathbf{q}_3)^T$:

$$\mathbf{q} = q_0 + \mathbf{w} \tag{C.35}$$

Assume that a rotation transform is defined as

$$\mathbf{P'} = \mathbf{RP} \tag{C.36}$$

and **v** is the quaternion representation of **P**, then the quaternion after the rotation can be represented by **v’** (the vector is **P’**)

$$\mathbf{v'} = \mathbf{qvq}^* \tag{C.37}$$

where $\mathbf{q}$ is the unit quaternion corresponding to the rotation, and $\mathbf{q}^*$ is the conjugate of $\mathbf{q}$ **($\mathbf{q}$*$\mathbf{q}^*$=1).** Here Both $\mathbf{v}$ and $\mathbf{v'}$ has only the vector part and the scalar component is zero. So we can represent

$$\mathbf{RP} = \mathbf{qP}\,\mathbf{q}^* \tag{C.38}$$

It is convenient to convert quaternion multiplication to matrix multiplication and regard a quaternion as a four dimensional column vector when it is operated with matrices. Let $\mathbf{q}$ and $\tilde{\mathbf{q}}$ be quaternions, then

$$\mathbf{q} * \tilde{\mathbf{q}} = \begin{bmatrix} q_0 \\ \mathbf{w} \end{bmatrix} * \begin{bmatrix} \tilde{q}_0 \\ \tilde{\mathbf{w}} \end{bmatrix} = \begin{bmatrix} q_0 & -\mathbf{w}^T \\ \mathbf{w} & q_0\mathbf{I} + [\mathbf{w}]_\times \end{bmatrix} \begin{bmatrix} \tilde{q}_0 \\ \tilde{\mathbf{w}} \end{bmatrix} = [\mathbf{q}]_l\, \tilde{\mathbf{q}} \tag{C.39}$$

where $[\bullet]_l$ is a mapping from a quaternion to a 4 by 4 matrix (l stands for left multiplication). Similarly, we define the mapping $[\bullet]_r$:

$$\tilde{\mathbf{q}} * \mathbf{q} = \begin{bmatrix} \tilde{q}_0 \\ \tilde{\mathbf{w}} \end{bmatrix} * \begin{bmatrix} q_0 \\ \mathbf{w} \end{bmatrix} = \begin{bmatrix} q_0 & -\mathbf{w}^T \\ \mathbf{w} & q_0\mathbf{I} - [\mathbf{w}]_\times \end{bmatrix} \begin{bmatrix} \tilde{q}_0 \\ \tilde{\mathbf{w}} \end{bmatrix} = [\mathbf{q}]_r\, \tilde{\mathbf{q}} \tag{C.40}$$

Now we prove (C.34). Using (C.38)

$$\begin{aligned}
\left\|\mathbf{RC} - \mathbf{D}\right\|_2 &= \sum_{i=1}^{n} \left\|\mathbf{D}_i - \mathbf{RC}_i\right\|_2 = \sum_{i=1}^{n} \left\|\mathbf{D}_i - \mathbf{q} * \mathbf{C}_i * \mathbf{q}^*\right\|_2 \\
&= \sum_{i=1}^{n} \left\|\mathbf{D}_i * \mathbf{q} * \mathbf{q}^* - \mathbf{q} * \mathbf{C}_i\right\|_2 \\
&= \sum_{i=1}^{n} \left\|(\mathbf{D}_i * \mathbf{q} - \mathbf{q} * \mathbf{C}_i) * \mathbf{q}^*\right\|_2 \\
&= \sum_{i=1}^{n} \left\|\mathbf{D}_i * \mathbf{q} - \mathbf{q} * \mathbf{C}_i\right\|_2
\end{aligned} \tag{C.41}$$

Using the matrix notation (C.39) and (C.40), we have

$$\mathbf{D}_i * \mathbf{q} - \mathbf{q} * \mathbf{C}_i = [\mathbf{D}_i]_l\, \mathbf{q} - [\mathbf{C}_i]_r\, \mathbf{q} = ([\mathbf{D}_i]_l - [\mathbf{C}_i]_r)\,\mathbf{q} = \mathbf{F}_i\mathbf{q} \tag{C.42}$$

where

$$\mathbf{F}_i = [\mathbf{D}_i]_l - [\mathbf{C}_i]_r = \begin{bmatrix} 0 & (\mathbf{C}_i - \mathbf{D}_i)^T \\ \mathbf{D}_i - \mathbf{C}_i & [\mathbf{D}_i]_\times + [\mathbf{C}_i]_\times \end{bmatrix} \tag{C.43}$$

Finally, we have

$$\begin{aligned} \|\mathbf{RC} - \mathbf{D}\|_2 &= \sum_{i=1}^{n} \|\mathbf{D}_i - \mathbf{RC}_i\|_2 = \sum_{i=1}^{n} \|\mathbf{F}_i \mathbf{q}\|_2 \\ &= \sum_{i=1}^{n} \mathbf{q}^T \mathbf{F}_i^T \mathbf{F}_i \mathbf{q} = \mathbf{q}^T \left(\sum_{i=1}^{n} \mathbf{F}_i^T \mathbf{F}_i \right) \mathbf{q} = \mathbf{q}^T \mathbf{F} \mathbf{q} \end{aligned} \tag{C.44}$$

Therefore, the solution of the quaternion **q** is the unit eigenvector of **F** associated with the smallest eigenvalue, and (C.20) is proved.

Appendix D: Overviews of Magnetic Sensors

There are many kinds of magnetic sensors, and here I introduce the currently conventional magnetic sensors [96~98].

1) **Search-coil magnetometer:** It is based on Faraday's law of induction that the voltage induced in a coil is proportional to the changing magnetic field in the coil. This induced voltage creates a current that is proportional to the rate of change of the field. The sensitivity of the search-coil is dependent on the permeability of the core, and the area and number of turns of the coil. However, in order for the search-coil to work, the magnetic field must either be varying, so it is not applicable to the magnet case, since the magnet produces a static field.

2) **SQUID:** The most sensitive low field sensor is the Superconducting Quantum Interference Device (SQUID). Developed around 1962 with the help of Brian J. Josephson's work that developed the point-contact junction to measure extremely low current. The SQUID magnetometer has the capability to sense field in the range of several fempto-tesla (fT) up to 9 tesla, over 15 orders of magnitude! The present designs of SQUID require cooling to liquid helium temperature (4K). This makes it difficult to be applied for magnet's localization. A cheaper and easier scheme is preferable because a magnetic sensor array is used to realize the localization and orientation of the magnet.

3) **Fluxgate:** Fluxgate magnetometers are the widely used sensor for compass navigation systems. They were developed around 1928. The most common type of fluxgate magnetometer is the second harmonic device. This device involves two coils, a primary and a secondary, wrapped around a common high-permeability ferromagnetic core. The magnetic induction of this core changes in the presence of an external magnetic field. A drive signal is applied to the primary winding at frequency f (e.g. 10 kHz) that causes the core to oscillate between saturation points. The secondary winding outputs a signal that is coupled through the core from the primary winding. This signal is affected by any change in the core permeability (slope of B-H curve) and appears as an amplitude variation in the sense coil output. By using a phase sensitive detector, the sense signal can be demodulated

and low pass filtered to retrieve the magnetic field value. Fluxgate magnetometers can sense signal in the tens of micro-gauss range, and can measure both magnitude and direction of static magnetic fields. They need a ferromagnetic core such that they tend to be bulky and difficulty be applied to the compact 3-axis sensor.

4) **Magneto-inductive magnetometers**: Magnetoinductive magnetometers are relatively new with the first patent issued in 1989. The sensor is simply a single winding coil on a ferromagnetic core that changes permeability within the Earth's field. The sense coil is the inductance element in a L/R relaxation oscillator. The frequency of the oscillator is proportional to the field being measured. A static dc current is used to bias the coil in a linear region of operation (see Figure D.1).

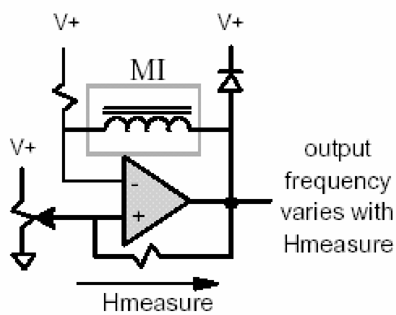

Figure D.1. Magneto-inductive (MI) sensor circuit

These magnetometers are simple in design, low cost, and low power. They are repeatable to within 4 milligauss. However, it also uses a ferromagnetic core such that they are difficulty be applied to the compact 3-axis sensor.

5) Lorentz Force Devices (Magnetoresistor and Hall sensor): There are several sensors that utilize the Lorentz force, or Hall effect, on charge carriers in a semiconductor. The Lorentz Force equation describes the force $\mathbf{F}_L$ experienced by a charged particle with charge q moving with velocity $\mathbf{V}$ in a magnetic field $\mathbf{B}$.

$$\mathbf{F}_L = q(\mathbf{V} \times \mathbf{B})$$

The Lorentz force is proportional to the cross product between the vectors representing velocity and magnetic field, so it is perpendicular to both of them. The acceleration caused by the Lorentz force is always perpendicular to the velocity of the charged particle; therefore, in the absence of any other forces, a charge carrier follows a curved path in a magnetic field. The Hall Effect is a consequence of the Lorentz force in semiconductor materials. When a voltage is applied from one end of a slab of semiconductor material to the other end, charge carriers start to flow. If at the same time a magnetic field is applied perpendicular to the slab, the current carriers are deflected to the side by the Lorentz force. Charge builds up along the side until the resulting electrical field produces a force on the charged particle sufficient to counteract the Lorentz force. This voltage across the slab perpendicular to the applied voltage is called the Hall Voltage.

The simplest of Lorentz force devices are **magnetoresistors** using semiconductors such as InSb and InAs. The effect of the magnetic field is to increase their resistance with several hundred percent in large fields. However, they are not sensitive to whether the field is positive or negative, and not applicable to the magnet's localization that requires testing both positive and negative magnetic field.

The second type of sensor, which utilizes the Lorentz force on charge carriers, is a **Hall sensor,** which uses Hall voltage**.** The Hall voltage is measured between electrodes placed at the middle of each side. This differential voltage is proportional to the magnetic field perpendicular to the slab. It also changes sign when the sign of the magnetic field changes. Hall sensor is a good choice because of its good linearity, small size, low cost and easy applicability. However, the existing Hall sensor has too low sensitivity for directly testing the magnetic field of the small magnet [99, 100], unless some magnetic concentrators are added. In 5.2, we will further discuss its applications.

6) Giant Magnetoresistive (GMR) Devices: GMR is a new and promising magnetic sensing element. Large magnetic field dependent changes in resistance are possible in thin-film ferromagnet/non-magnetic metallic multilayers. This phenomenon was first observed in France in 1988 [101, 102]. Changes in resistance with magnetic field of up to 70% were observed. The resistance of two thin ferromagnetic layers separated by a thin non-magnetic conducting layer can be altered by changing whether the moments of the ferromagnetic layers are parallel or antiparallel. These differences are shown schematically in Figure D.2. In order for spin dependent scattering to be a significant part of the total resistance, the layers must be thinner than the mean free path of electrons in the bulk material. For many ferro-magnets the mean free path is tens of nanometers, so the layers themselves must each be typically less than 10 nm (100 Å). It is not surprising, then, that GMR was only recently observed with the development of thin-film deposition systems.

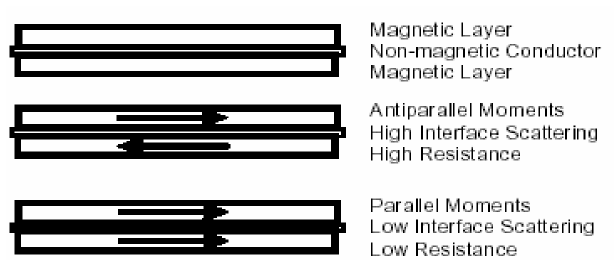

Figure D.2 Scattering from two different alignment of magnetic moments in GMR "sandwich" with two magnetic layers separated by a conducting nonmagnetic layer.

Various methods of obtaining anti-parallel magnetic alignment in thin ferromagnetic conductor multi-layers. The structures currently being used in GMR sensors are unpinned sandwiches and anti-ferromagnetic multi-layers. Figure D.3 and Figure D.4 show the typical GMR outputs (voltage and resistance) via applied magnetic field.

GMR Circuit Techniques: To date the best utilization of GMR materials for magnetic field sensors has been in Wheatstone bridge configurations, although simple GMR

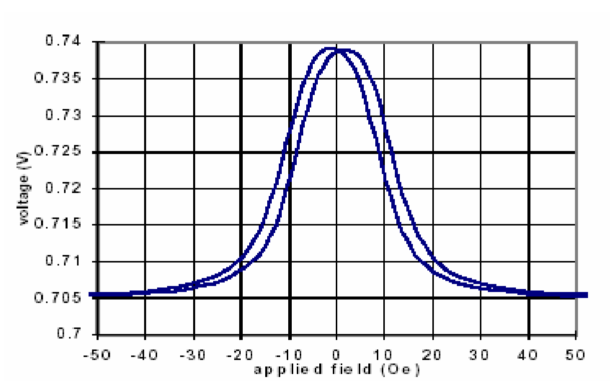

Figure D.3. Voltage vs. applied field for a 2 µm wide stripe of unpinned sandwich GMR material with 1.5 mA current. GMR = 5 %.

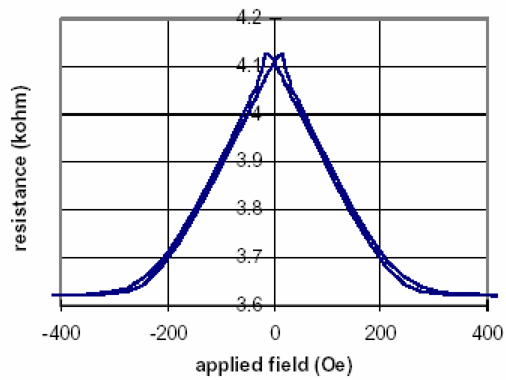

Figure D.4 Resistance vs. applied field for a 2 µm wide stripe of anti-ferromagnetically coupled multilayer GMR material. GMR = 14 %.

resistors and GMR half bridges can also be fabricated. A sensitive bridge can be fabricated from four photolithographically patterned GMR resistors, two of which are active elements. These resistors can be as narrow as 2µm allowing a serpentine 10kΩ resistor. The very narrow width also makes the resistors sensitive only to the component of magnetic field along their long dimension. Small magnetic shields are plated over two of the four equal resistors in a Wheatstone bridge protecting these resistors from the applied field and allowing them to act as reference resistors. Since they are fabricated from the same material, they have the same temperature coefficient as the active resistors. The two remaining GMR resistors are both exposed to the external field. The bridge output is therefore twice the output from a bridge with only one active resistor.

6) Anisotropic Magnetoresistive (AMR) devices: William Thompson, later Lord Kelvin [103], first observed the magnetoresistive effect in ferromagnetic metals in 1856. This discovery had to wait over 100 years before thin film technology could make a practical sensor for application use. The anisotropic magnetoresistive (AMR) sensor is one type that lends itself well to the Earth's field sensing range. AMR sensors can sense dc static fields as well as the strength and direction of the field. This sensor is made of a nickel-iron (Permalloy) thin film deposited on a silicon wafer and is patterned as a resistive strip. The properties of the AMR thin film cause it to change resistance by 2~3% in the presence of a magnetic field. Typically, four of these resistors are connected in a Wheatstone bridge configuration so that both magnitude and direction of a field along a single axis can be measured. A common bridge resistance is 1 kΩ. Figure D.5 shows the AMR output transfer curve. The key benefit of AMR sensors is that they can be bulk manufactured on silicon wafers and mounted in commercial integrated circuit packages. Low cost, high sensitivity, small size, noise immunity, and reliability are advantages over mechanical or other electrical alternatives. AMR sensors are available from Philips, HL Planar, and Honeywell.

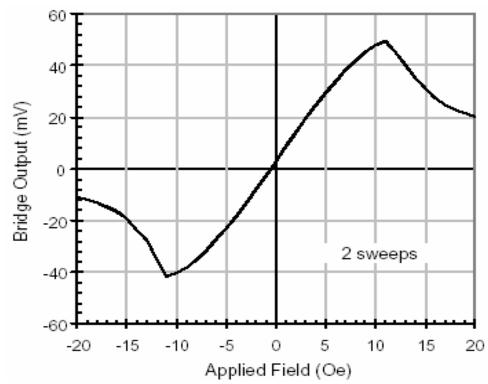

Figure D.5 AMR output transfer curve

The AMR film properties are well behaved only when the film's magnetic domains are aligned in the same direction. This assures high sensitivity and good repeatability with minimal hysteresis. As shown in Figure D.6, the **M** vector is set parallel to the length of the resistor and can be set to point in either direction, left or right, in the film. Assume for a moment that there is a current in the film flowing at a 45-degree angle to the length of the film. This creates an angle theta (θ) between the current flow and M vector. The Permalloy film has an electrical relationship between the **M** vector in the film and the current flowing through the film. Figure D.6 illustrates this property. The film resistance is the greatest when the current flows parallel to the M vector.

If an external magnetic field is applied normal to the side of the film, the Magnetization vector will rotate and change the angle θ. This will cause the resistance value to vary ($\Delta R/R$) and produce a voltage output change in the Wheatstone bridge. This change in the Permalloy is termed the magnetoresistive effect and is directly related to the angle of the current flow and the magnetization vector.

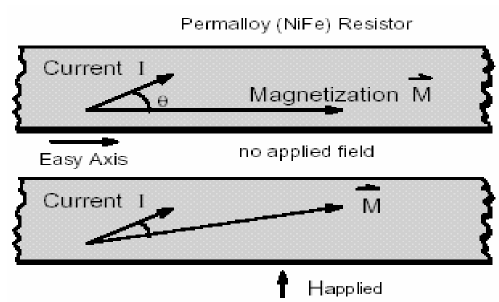

Figure D.6 Magnetoresistive effect of the AMR

Note in Figure D.7 that the ΔR/R change in resistance is symmetric about the angle θ-axis and that there is a linear region about the 45-degree angle. The method used to cause the current to flow at a 45-degree angle in the film is called barber pole biasing. This is accomplished through a layout technique by placing low resistance shorting bars across the film width. The current prefers to take the shortest path through the film, thus causing it to flow from one bar to the next at a 45-degree angle. Figure D.8 illustrated this effect for all four resistors in a simple Wheatstone bridge. By the presence of an applied magnetic field, the magnetoresistive resistor causes a resistance change (ΔR) and output voltage change (in Figure D.5) in the bridge.

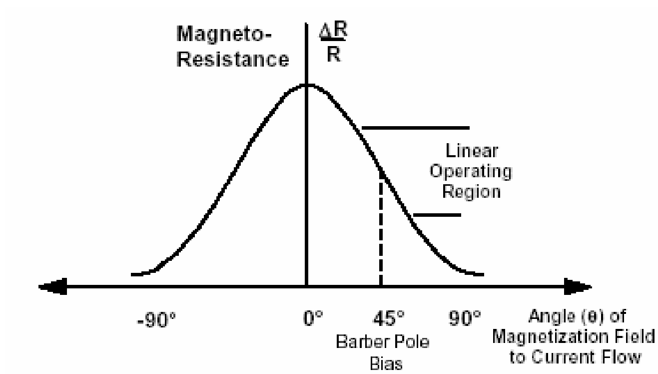

Figure D.7 Magnetoresistive variation with angle θ

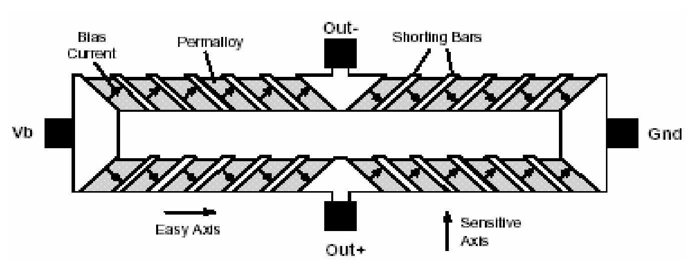

Figure D.8 AMR barber pole bias

A concern for any magnetic sensor made of ferromagnetic material is the exposure to a disturbing magnetic field. For AMR sensors, this disturbing field actually breaks down the magnetization alignment in the Permalloy film that is critical to the sensor operation. To recover the magnetic state, a strong magnetic field must be applied along the length of the Permalloy film. A common method used to realign these domains is to use a coil around the Wheatstone bridge resistors. Switching a high current pulse through the coil (Figure D.9) will create a large magnetic field of 60-100 gauss and restore the M vector. This process is referred to as flipping the magnetic domains with a set pulse. This flipping action will also take place for a pulse in the opposite direction through this external coil. In this case, the reset pulse, the domains will all point in the opposite direction along the easy axis. Honeywell's family of AMR sensor has a patented onchip strap that replaces the external coil to create the set and reset field effects.

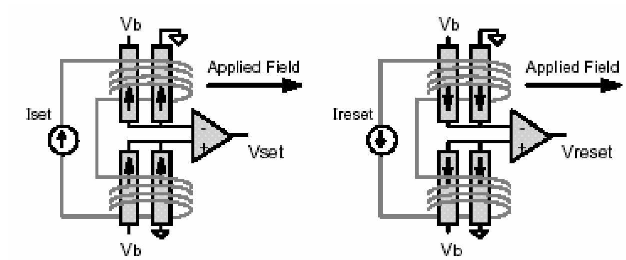

Figure D.9 Set and reset flipping circuits

Offset Reduction in AMR sensors: Specifically, undesirable effects are inherent in the sensor that may interfere with magnetic field sensing such as bridge offset voltages and temperature effects. Additional benefits to using a set/reset pulse besides restoring the sensor properties after exposure to a high magnetic field. Figure D.10 shows the transfer curves for a sensor after it has been set, and then reset, shows an inversion of the gain slope and a common crossover point on the bridge output axis. This crossover point is the zero field bridge offset voltage. For the sensor in Figure D.10, the bridge offset is around – 3 mV. This is due to the resistor mismatch during the manufacture process. This offset voltage is usually not desirable and can be reduced, or eliminated, using one of three techniques described below.

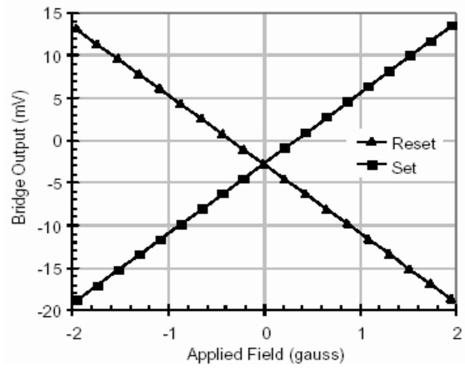

Figure D.10 Set and reset output transfer curves

OFFSET STRAP: Another method of removing the offset voltage is by using a coil to create a field in the sensitive axis direction. Static current through this coil can be set to null the bridge offset by adding or subtracting a field equal to the offset voltage. Honeywell's family of AMR sensors has a patented on-chip offset strap to accomplish offset adjustment.